UNIVERSITAT DE BARCELONA

Comparative study of nanocarriers targeted to different transport pathways into and across the endothelium for brain delivery of therapeutic enzymes

Maximilian Loeck

Doctoral Program in Biomedicine

Biomedical Engineering

Department of Biomedicine of the School of Medicine and Health Sciences

University of Barcelona

COMPARATIVE STUDY OF NANOCARRIERS TARGETED TO DIFFERENT TRANSPORT PATHWAYS INTO AND ACROSS THE ENDOTHELIUM FOR BRAIN DELIVERY OF THERAPEUTIC ENZYMES

Maximilian Loeck

Institute for Bioengineering of Catalonia (IBEC)

of the Barcelona Institute for Science and Technology (BIST)

Doctoral Thesis

July 2022

Thesis Director:

Prof. Dr. Silvia Muro Galindo

Catalan Institution for Research and Advanced Studies (ICREA) & Institute for Bioengineering of Catalonia (IBEC)

Thesis Tutor:

Prof. Dr. Pere Roca-Cusachs

University of Barcelona (UB) & Institute for Bioengineering of Catalonia (IBEC

Dedication

To my dad, who always kept me curious.

And to my mum, who taught me the power of networking.

Acknowledgements

I learned a lot during the four years of my PhD. This was a journey that I could not have done alone, which is why I would like to express my deepest appreciation to several people.

First and foremost, I would like to thank my thesis director Silvia for her exceptional supervision. I cannot begin to thank you for all your hard work and dedication, for being an inspiring scientist, and for teaching me a lot of valuable skills. Your passion for science, work ethics, and positive attitude were a great inspiration. Thank you!

I also want to thank my lab for being amazing colleagues, team players, and genuinely good people. I feel very lucky that I was able to do my PhD in such a great working environment. I would like to extend a special thanks to Marco and Marina, I could not have done it without you!

I want to thank laCaixa for giving me the opportunity to pursue my PhD in nanomedicine and for their great support during this time.

Furthermore, I want to express my gratitude to Melani Solomon from the Muro lab at the University of Maryland, who taught me several invaluable techniques I needed to complete this dissertation. Thank you for taking great care of me, for making me feel welcome in the lab, and for always greeting me with a smile.

I was lucky to work with great scientists for a collaboration with the Institute for Photonic Sciences (ICFO) in Castelldefels. Thank you Enric, Maria, and Roger for the inspiring discussions and for taking the time to answer all my questions.

I would like to express my special appreciation to IBEC's Core Facilities. Thank you for always helping me out when I had questions. It was a great to know that I could always count on you. Thanks should also go to many other installations such as *la botiga*, *el almacén, la instalación radioactiva* with a very special thanks to Pablo for all the help, *el estabulario* with a special thanks to Asun for her supervision, and, of course, Paco for all the coffee.

Más allá de la parte laboral, quiero expresar mi más sincera gratitud a varias personas que me acompañaban durante estos cuatro años aquí en Barcelona. Siempre he tenido la gran suerte de estar rodeado de gente maravillosa que me daba el soporte y la seguridad para aprender sin miedo y que me acogía cuando lo necesitaba.

Yo tuve la gran suerte de encontrar a una de las personas claves para mi vida personal justo en frente de mi laboratorio. Muchas gracias, Judith por todos los cafés, vermuts, e innumerables horas de charlas, risas y, si tocaba, lágrimas.

También les quiero agradecer a algunas personas fuera de mi ámbito laboral. Gracias, Roberto por siempre estar, en lo bueno y lo malo, por siempre alegrarme la vida y por vivir tantas locuras conmigo <3 Thanks a lot also to Yasmin, your positivity and *joie de vivre* are amazing and many a time contagious. Gràcies Elena i Josep per aguantar-me en català, ho agraeixo molt. Gracias a los mejores compañeros de piso del mundo. Ein besonderer Dank an meine Schwester, die immer für mich da ist, love you! Quiero dar las gracias a Carlos. Siempre me has trasmitido la tranquilidad y estabilidad que tanto necesito.

También gracias por dejarme escribir mi tesis en tu casa y por cocinarme. Y por último, aunque viva lejos de mí, mil gracias al amor de mi vida. Muchas gracias, Diego por todos los buenos momentos, muchos consejos, y tu apoyo. Gracias por estar en mi vida, gracias por complementarme. ¡Te quiero un montón!

Contents

List of tables

List of Figures

List of Abbreviations

^{125}I	$Iodine_{125}$
Ab	Antibody
AC	Astrocyte
ADC	Antibody-Drug conjugate
amp	Amplification
Anti-ICAM-1	Antibody targeted to intercellular adhesion molecule-1
AP	Apical
ASM	Acid sphingomyelinase
BBB	Blood-brain barrier
BL	Basolateral
BSA	Bovine serum albumin
CAM	Cell adhesion molecule
CBE	Conduritol-β-epoxide
CHO	Chinese hamster ovary
CNS	Spanish Nuclear Security Council
CNS	Central Nervous System
CPM	Counts per minute
DAPI	4',6-Diamidino-2-phenylindole
DI water	Deionized water
DLS	Dynamic light scattering
DNA	Deoxyribonucleic acid
EC	Endothelial cells
ELISA	Enzyme-linked immunosorbent assay
EMA	European Medicines Agency
EPR	European agency for medicines
ERT	Enzyme replacement therapy
EU	European Union
FBS	Fetal bovine serum
FDA	Food and Drug Administration
FELASA	Federation of European Laboratory Animal Science Associations
FITC	Fluorescein isothiocyanate
GBA	Glucocerebrosidase
GD	Gaucher disease
GlcCer	Glucosylceramide
HAse	Hyaluronidase
HBMEC	Human Brain Microvascular Endothelial Cells
HEK293	Human embryonic kidney 293
HIV-1	Human immunodeficiency virus 1
HUVEC	Human Umbilical Vein Endothelial Cells
IBEC	Institute for Bioengineering of Catalonia
ICAM-1	Intercellular adhesion molecule 1
ICFO	Institute of Catalonia for Photonic Sciences

ID	Injected dose
IgG	Immunoglobulin G
I.v.	Intra venous
kcps	Kilocounts per second
kDa	Kilodalton
LSD	Lysosomal storage diseases
L_{max}	Maximal lysosomal traffic
LR	Localisation ratio
LSD	Lysosomal storage disorders
M6PR	Mannose 6-phosphate receptor
MADLS	Multi-angle DLS
MMS	Moment scale spectrum
molec.	Molecule
MR	Mannose receptor
MW	Molecular weight
NC	Nano carrier
NORD	National Organization of Rare Disorders
NND	Nearest neighbour distance
NPD	Niemann Pick disease
NPC1 - NPC2	Intracellular cholesterol transporter 1-2
p	Pulse
PBS	Phosphate buffer saline
PC	Pericyte
PCB	Barcelona's Science Park
PD	Parkinson disease
PDI	Polydispersity index
PEG	Polyethylene glycol
PFA	Paraformaldehyde
pI	Isoelectric point
$PI(4,5)P_2$	Phosphatidylinositol 4,5.biphosphate
PLGA	Poly(lactic-co-glycolic acid)
PS	Polystyrene
PV1	Plasmalemma vesicle protein 1
QD	Quantum dot
REM	Rapid eye movement
rpm	Revolutions per minute
RT	Room temperature
sec	Seconds
SEM	Standard error of the mean
sHDL	Synthetic high-density lipoprotein
SI	Specificity index
SRT	Substrate reduction therapy
STED	Stimulated emission depletion
$t_{1/2}$	Half-time

TAT	Trans-activator protein transduction domain
TCA	Trichloroacetic acid
TfR	Transferrin receptor
TIRF microscopy	Total internal reflection microscopy
TNFα	Tumor necrosis factor alpha
U18666A	(3β)-3-[2-(Diethylamino)ethoxy]androst-5-en-17-one hydrochloride
v	Valency
VE-cadherin	Vascular endothelil cadherin

Chapter 1: Introduction

1.1. Drug Delivery to the Brain

Brain diseases can cause disability and death and pose an increasing burden on our society[1]. In 2016, neurological diseases were the leading cause of disabilities and the second leading cause of death worldwide, with a special burden for low-income and middle-income countries[1]. Whereas improvements in global health care such as vaccination programmes could reduce the frequency of infectious brain diseases such as tetanus, meningitis, and encephalitis, the total number of people who die or suffer from mostly age-related diseases such as Alzheimer's disease and other dementias has more than doubled between 1990 and 2015[2]. This is because of our growing population and because with age the prevalence of disabling disease generally increases significantly, posing a humanitarian as much as an economical challenge due to the usually high costs associated with treatments[3][14]. This is why novel and efficient treatments for CNS disorders are needed to mitigate this growing problem.

Tissues and organs rely on oxygen and nutrients for their proper functioning, producing potentially toxic CO_2 and metabolites which need to be removed. The majority of this transport is mediated by the blood *via* the general circulation[5]. The architecture of the endothelium, forming the inner lining of all blood vessels, can change between tissues and serves specific functions. E.g., in the liver, a major organ responsible for clearance, the endothelium has a discontinued structure with large gaps and incomplete basement membrane, allowing for free exchange of even larger molecules between the blood and hepatocytes, which are responsible for the neutralisation and/or excretion of certain potentially toxic metabolites and xenobiotics. In most other capillaries the endothelium is continued yet fenestrated, thus containing diaphragmed fenestrae facilitating the exchange of nutrients between the blood and the tissue[6]. However, the brain has a continuous non-fenestrated endothelial lining with special junction proteins, forming adherence junctions and tight junctions, to further seal the spaces between adjacent cells to prevent paracellular leakage across the barrier[7–9]. This is because the brain is protected by a highly selective barrier at three blood-brain interfaces, i.e. the blood and (a) the brain parenchyma (blood-brain barrier (BBB)), (b) the arachnoid epithelium (meningeal barrier),

and (c) the choroid plexus epithelium (blood-cerebrospinal fluid barrier)[10,11]. These barriers show a high complexity far beyond the tight endothelial lining, which becomes apparent when examining the BBB, the most studied of these barriers. On the basolateral side of the barrier, other cells in the brain parenchyma give biochemical and/or structural support to the barrier, including astrocytes (ACs), pericytes (PCs), microglial cells, and neurons, forming the neurovascular unit[12] (figure 1.1). The transport across the barrier is tightly controlled by endothelial cells (ECs) through transporters and active transport to protect the brain from potentially harmful endogenous proteins, metabolites, and xenobiotics[13–16]. Transporters such as glucose receptor-1, insulin receptor, and transferrin receptor are located in the plasma membrane of ECs and facilitate direct uptake of mostly selective molecules into the cytoplasm and/or out into the tissue[17,18]. Additionally, efflux transporters expulse substances from the brain, reinforcing the barrier function[19]. The importance of the BBB function is highlighted by the broad variety of major neurological disorders that associate with its impaired function, including Parkinson's disease, Alzheimer's disease, and Epilepsy[20]. Importantly, the highly selective nature of the BBB also precludes the penetration of most pharmaceutics (~98+%) into the brain, posing a formidable challenge to treat diseases affecting the CNS[18,21–23].

Nevertheless, there are different strategies for therapeutic interventions in the CNS. Probably the most invasive one is the direct injection of drugs into the brain. Less severe practices use intrathecal injections, thus between spinal cord vertebrae, to inject drugs directly into the cerebrospinal fluid. Intracranial injections are a more invasive practice that requires surgical procedures in which a hole is drilled into the cranium to directly inject in e.g., the brain parenchyma or the ventricles[23–26]. Although the blood-brain barrier can be circumvented with these practices, important therapeutic limitations have been described. For instance, intrathecal injections have been shown to release the drug rather into the blood stream than into the brain[25] and that the drug clearance from the cerebrospinal fluid is significantly higher than the drug diffusion into the brain parenchyma[27]. Additionally, sub-optimal diffusion has also been reported for injections into the CNS, with an estimated 90% of the injected drug staying within a 500 µm radius of the injection site[28]. The compromised therapeutic efficacy due to the low diffusion can be improved by increasing the injected dose, yet often leading to toxicity[29]. Another strategy to

amend the limitations of intercranial injections is the convection-enhanced diffusion device. It allows for continuous or sequential administration of drug into the brain via a catheter implanted into the brain controlled by a pump[30]. Although this method improves drug penetration into the brain, a deep penetration cannot be achieved due to the resistance of fluid flow[31]. Another concern is the potential activation of astroglia and demyelination due to an increase in intraparenchymal fluid and subsequent flow into the white matter[23]. Hence, although improving drug concentrations in the brain, these techniques show important limitations with regards to efficacy, require trained personnel and expensive equipment and procedures, and are relatively patient unfriendly[32].

Other strategies use peripheral administration after which they need to cross the BBB to penetrate the CNS. One less characterised exception is the intranasal route. This non-invasive route exploits the connection of the nasal mucosa via the perivascular channels in the lamina propia or along olfactory or trigeminal nerves into CNS or olfactory bulbs. Drug delivery to the brain via this route has been shown for some peptide hormones and small lipophilic molecules[18,33–36]. Peripheral administration is an attractive alternative to local injections as it holds the promise of showing a better drug distribution across the brain and is generally more patient friendly. Nevertheless, despite the great promise this strategy holds, CNS treatment via this approach is still hampered by important limitations such as off-target effects and often a lack of natural penetration of the drug into the brain. Nevertheless, there are different strategies trying to overcome these limitations, as will be discussed in the following.

1.2. Systemic Transport into the Brain and Transcytosis

Crossing the BBB can occur *via* two routes, (a) paracellular and (b) transcellular. The paracellular route especially restricted in the BBB, due to the lack of fenestration and the presence of junction proteins. However, transient disruption of the BBB with e.g., vasoactive agents, hyperosmotic solutions, or ultrasound, can improve brain targeting[26,27,37]. Nevertheless, this approach is non-

targeted and invasive with serious safety concerns such as albumin leakage into the brain and astrocyte toxicity, as well as chronic neuropathological changes[14,38].

Therefore, delivering drugs *via* the transcellular route is a more promising strategy. Drugs can reach the CNS on the transcellular route either by diffusion (non-saturable) or transporter-mediated (saturable). Diffusion depends largely on the physicochemical properties of the drug[18,27]. Low molecular weight below 600 Da appears to be favourable for diffusion, although exceptions have been seen[39]. Furthermore, to be able to cross the lipid bilayer without getting stuck in it, drugs need to be in the right range of lipid solubility and hydrophilicity[18]. Importantly, efflux transporters, extruding a big variety of molecules out of the BBB, limit the efficiency of this pathway[27]. The transcellular route *via* transcytosis appears the most promising strategy in terms of efficacy and safety. It is present in many cell types and virtually all ECs[40]. Transcytosis is the naturally occurring vesicular transport of relatively large cargo from one side of the cell to the other[27,32,41]. It is typically induced by receptor activation through the binding of a ligand, resulting in the engulfment of receptor and ligand into a vesicle in a process called endocytosis[27,32,41]. Then, vesicles usually reach the early endosome, a sorting station to determine their further path. From here, vesicles can either recycle back to the membrane from which they entered, reach distinct intracellular destinations such as lysosomes, or traffic to the opposite site of the cell for transcytosis[42–45]. Interestingly, not much is known about how this cellular sorting mechanism is controlled. The two main mechanisms governing this process are (a) clathrin-mediated endocytosis and (b) caveolae-mediated endocytosis. Clathrin-mediated endocytosis forms vesicles of around 100-200 nm in diameter. Vesicles are formed through a highly controlled sequence of recruitment of different endocytic proteins to the plasma membrane. These proteins form functional modules with conserved organisation between organisms, interacting with each other to drive endocytosis[46–50]. The first step is the formation of the clathrin coat. This coat, apart from clathrin, consists of adaptor proteins such as adaptor protein AP2 complex and monomeric adaptors such as clathrin assembly lymphoid myeloid leukemia protein (CALM) family and epsin, which bind to plasma membrane lipids and cargo[51–57]. The clustering of coat components through the interaction of scaffolds with each other as well as with clathrin adaptors forms the "pioneering module", which initiates the endocytic process[51]. The membrane bending that is

required to form the vesicle is thought be mediated by two processes, mediated by the coat formation, such as e.g., the assembly of clathrin into icosahedral cages, or mediated by actin filaments[51]. Then, the actin module is formed by actin filaments and regulatory components such as from the Wiskott-Aldrich syndrome protein (WASP) family, activating the nucleation of actin filaments, as well as dynamin and myosin motor proteins, involved in the next step[4858]. Proteins from the BAR domain (Bin, amphiphysin, Rvs) interact with other components such as dynamin to mediate vesicle neck constriction and scission[59]. The last step is the uncoating of the vesicle, which releases the proteins of the endocytic machinery which can then take part in another round of vesicle formation. This step is needed to free the vesicle and enable further trafficking such as fusion with early endosomes[51]. Two key mechanisms have been described in this process, breaking clathrin-clathrin interactions mediated by heat-shock protein HSC70[60] and Dephosphorilation of phosphatidylinositol 4,5.-biphosphate ($PI(4,5)P_2$), to which many endocytic adaptor proteins initially bind, thereby recruiting them to the plasma membrane and inducing the endocytic process[51]. However, despite having been studied for over five decades, the precise coordination of many different proteins involved, and their activity are still poorly understood. Clathrin-mediated transport is a crucial component for the homeostasis of the CNS, with most transport at the BBB being controlled by the clathrin-mediated pathway *via* approx. 20 receptors, including the insulin receptor, the transferrin receptor (TfR), and the lipoprotein receptor[27,61–64]. Caveolae-mediated transport is a clathrin-independent trafficking route. Caveolae are flask-shaped invaginations of up to 100 nm located in special regions with high levels of amongst others cholesterol and sphingolipids, so called lipid rafts[27,65]. Their formation essentially relies on two types of proteins, integral membrane proteins called caveolins and cytosolic cavins[66,67]. Cavins associate with caveolin-enriched membrane domains through direct binding between cavin and caveolin, as well as the binding of cavin to two membrane lipids, phosphatidylserine and $PI(4,5)P_2$, *via* specific binding sites[68–72]. There, it stabilises caveolae through formation hetero-oligomeric structures[68–72]. The function of caveolae as an endocytic carrier has long been discussed. Nevertheless, caveolae can bud of membranes mediated and internalise. To this end, EDH2 oligomerises around the neck of caveolae to confine the neck opening[73,74], whereas pacsin 2 senses or induces membrane curvature through an BAR domain which links the budding

vesicles to actin filaments[75,76] as well as recruits dynamin for caveolar fission[77]. Caveolae-mediated endocytosis was proposed to play an important role of transcytosis of cargo such as LDLs, albumin, and insulin[78–81]. However, the status of caveolae-mediated transport at the BBB is unsure, with some research suggesting that it is downregulated in healthy ECs[27,65]. Other clathrin-independent pathways also play a role for transport at the BBB, such as micropinocytosis and the CAM-pathway, as will be discussed later (section 1.4).

However, there is an increasing body of evidence that shows that factors such as age and disease can alter the transport across the BBB[26,82–84]. Those factors can have an influence on both, the paracellular and transcellular route across the BBB, e.g., by disturbing junction proteins and thus opening the usually tightly sealed endothelium, or by altering the expression of function of certain proteins involved in transcellular pathways[26,82–84]. Nevertheless, not much is known on the specific effects of disease on BBB transcytosis, especially since certain effects might be disease-specific (see Chapter 6 and Chapter 7).

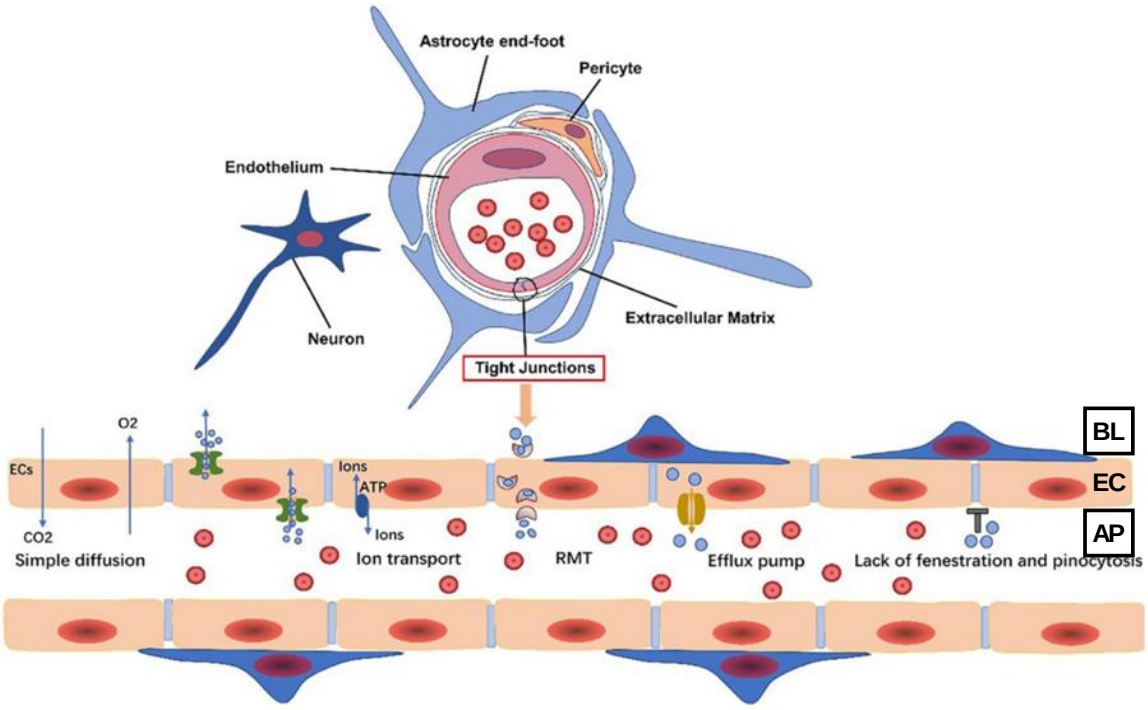

Figure 1.1 Schematic representation of the neurovascular unit. RMT = receptor-mediated transport. AP = apical side, EC = endothelial cell, BL = basolateral side. Adapted from Xiao et al.[85]

1.3. Drug Delivery Systems

Drug delivery has long been sought to be improved over the inert bioavailability of therapeutic substances to improve their efficacy. This is especially true for drug delivery to the brain, which is inaccessible for the vast majority of therapeutics (see section 1.2). This is why nanomedicine, using molecular conjugates or macromolecular assemblies in the nano-range for drug delivery, has gained increasing intention over the past decades. Nanomedicine allows to alter different properties of drugs relevant for bioavailability and thus efficacy, including drug stability, solubility, circulation, biodistribution, targeting, sub-cellular transport, and release rate[86–88].

One of the main goals of nanomedicine is to improve the local delivery to sites of interest to improve treatment efficacy while reducing off-target effects. For this, two main mechanisms can be distinguished, (a) active targeting and (b) passive targeting.

Passive targeting is mainly based on the enhanced permeability and retention (EPR) effect which leads to the passive accumulation of nano-sized particles in e.g., tumours due to their often aberrant leaky vasculature and impaired lymphatic drainage[89]. However, this approach only improves the efficient localisation at the target site, whereas it does not improve on other aspects such as uptake[89].

Active targeting refers to mostly improved bioadhesion to target cells or tissues through different means. For instance, positively charged peptides increase the affinity for the negatively charged plasma membrane[9023]. Another approach uses different targeting moieties such as peptides, sugars, or Abs that can recognise specific surface proteins or other membrane constituents. Many times, the interaction of the targeting moiety and its target leads to the internalisation and specific trafficking of the drug nano-drug, such as in the case of cell surface receptors[23,41,91]. These targeting moieties can be introduced either by direct synthesis (e.g., chimeric enzymes)[92] or chemical linkage (covalent linkage, biotin-avidin, electrostatic/hydrophobic interactions)[23,93–97].

Drug delivery has long been sought to be improved over the inert bioavailability of therapeutic substances to improve their efficacy. This is especially true for drug delivery to the brain, which is inaccessible for the vast majority of therapeutics. This is why nanomedicine, molecular

conjugates or macromolecular assemblies in the nano-range that can be used for drug delivery, has gained increasing intention over the past decades. Nanomedicine allows to alter different properties of drugs relevant for bioavailability and thus efficacy, including enhanced drug stability, solubility, circulation, biodistribution, targeting, sub-cellular transport, and release rate[86–88] (figure 1.2).

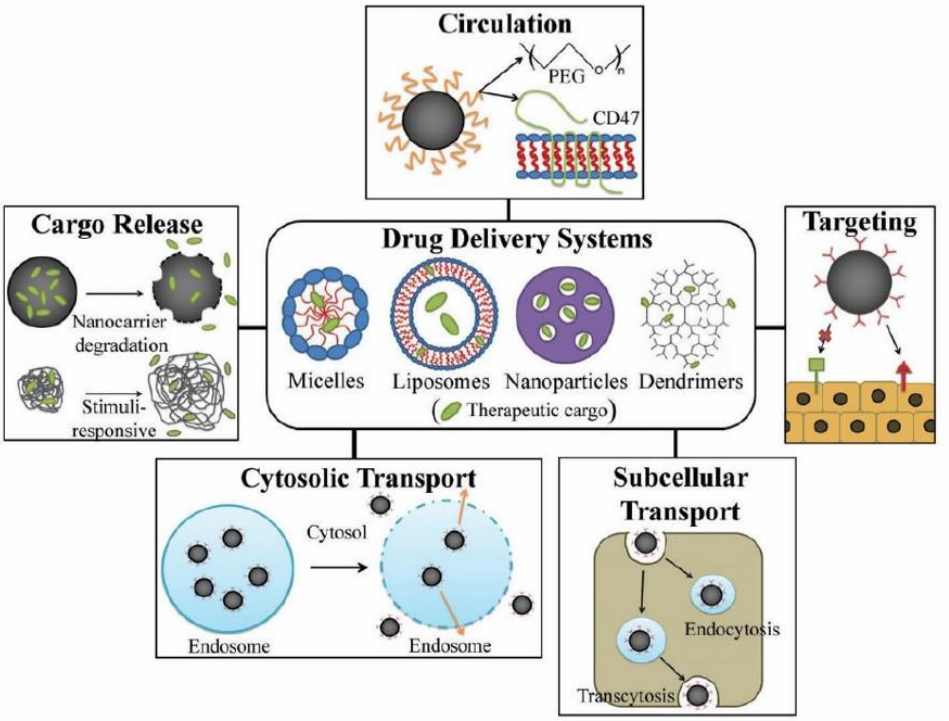

Figure 1.2 Nanomedicine structure and function. Representation of different types of drug delivery systems and their function with respect to enhanced drug delivery. Figure reproduced from Manthe et al.[98].

Nanotherapeutics can broadly be divided into lipid-based nanocarriers (NCs), polymer-based NCs, inorganic nanoparticles, viral nanoparticles, and drug conjugates (figure 1.3). Liposomes are one example for lipid-based NCs and likely the oldest and most recognised drug delivery systems. They are capsules made from natural or synthetic phospholipids with a size of around 50-300 nm, easy to prepare, and show good biocompatibility[99,100]. They allow for loading of hydrophilic drugs in aqueous core and hydrophobic drugs in lipid bilayer[101–103]. Liposomes are naturally sensitive to temperature and pH[100], the latter of which can be used to target them to tumours, whose cytoplasmic pH is often lower[104]. However, oral delivery with liposomes is challenging due to poor

stability and absorption in GI, which might be overcome by certain surface modifications, such as adding certain sugar ligands to surface[105] or Carbopol-lectin[106]. Several liposome formulations are approved for clinical use for applications such as cancer, infectious and vascular disease, and diagnostic techniques[107]. Gold nanoparticles are an example for inorganic nanoparticles. In medical applications they are 1 to 150 nm in diameter with unique chemical, physical, optical and electronical properties[108]. They are easily produced and have a low volume to surface ratio which allows for good cargo loading, are non-toxic and biocompatible[109]. Gold nanoparticles are excitable with light and emit heat, a property that can be used for phototherapy[110]. Furthermore, due to their high electron density they are easily revealed by electron microscopy, making them a valuable tool in imaging and diagnostic medicine[111]. Viral nanoparticles have versatile applications and are easily engineered to adapt their biological interactions[112]. Most viral nanoparticles can resist harsh conditions, thus allowing for manipulation and functionalisation in the lab[112]. Since viruses naturally evolved to carry and deliver cargo, viral nanoparticles show a good biocompatibility and biodegradability, are usually well-tolerated even at high doses, and therefore pose an interesting platform for drug delivery[112]. Drug conjugates are combination molecules made from a drug directly linked to one or multiple molecules such as Ab, polymer, or protein. For instance, this approach is used to produce chimeric therapeutic enzymes to allow for specific receptor targeting[113,114]. Another example in this class are antibody-drug conjugates (ADCs), combining the targeting efficiency of an Ab with the therapeutic effect of a drug[115]. Polymer-based NCs are a highly versatile group of NCs that can be made from natural or synthetic polymers that can be degradable or non-degradable[99]. Polymersomes are one example of such as NC, which is the analogue of a liposome formed by a polymer chain with hydrophobic and hydrophilic moieties, showing comparably higher stability and higher capacity for functionalisation[116,117]. One relevant example of a polymer to produce polymer NCs is poly(lactic-co-glycolic acid) (PLGA)[118]. PLGA has already been approved by the FDA and EMA for several medical applications[119,120] and is heavily investigated as a drug carrier. PLGA is a co-polymer that exists with different molar ratios of its constituents[118]. Is biocompatible and degrades in cells into lactic and glycolic acid, both of which a endogenously present in the body[88,121,122]. Both monomers possess different properties, with lactic acid being stiff, hydrophobic, and slowly

degrading, while glycolic acid is flexible, less hydrophobic, and faster degrading[123]. This is why the solubility and degradation of the NC and thus release rate can be tuned by adjusting the ratio of both acids in the co-polymer[88,122,124], with degradation rates that can vary from months up to years[125]. However, PLGA 50:50 is the exception to the rule and is hydrolysed much faster than those co-polymer containing higher proportions of one or the other acid[126]. Furthermore, polymers can end-capped with functional groups such as esters and acids, further altering their properties[127]. PLGA NCs can load a broad range of drugs and are efficiently taken up by cells[126].

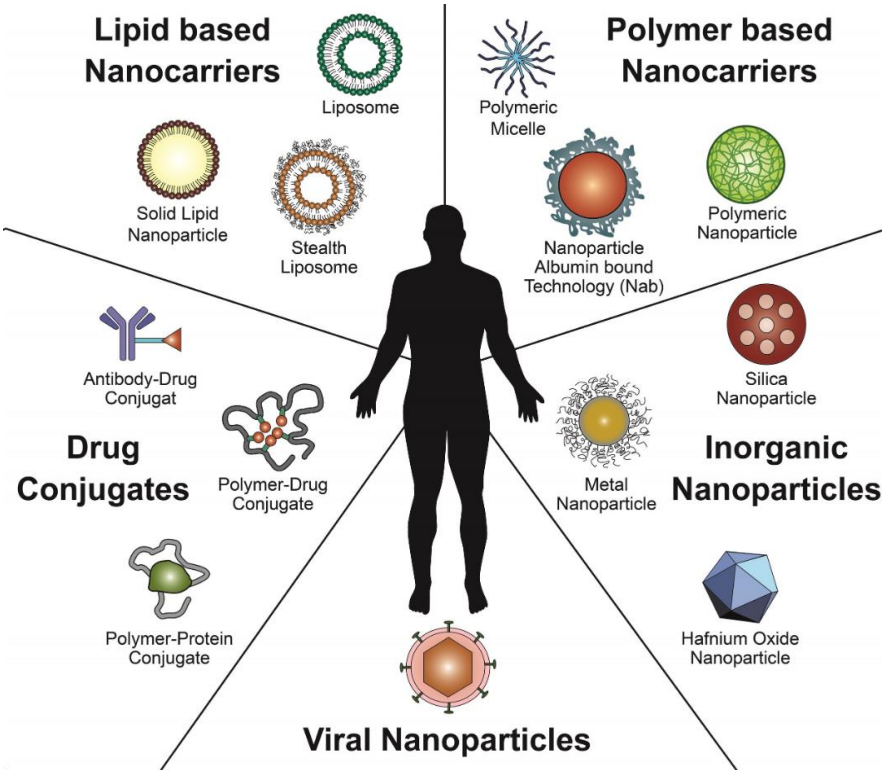

Figure 1.3 Schematic representation of established nanotherapeutic platforms. Figure reproduced from Wicki et al.[128].

Nanocarriers (NCs) are a highly versatile platform offering a myriad of advantages for the delivery of drugs. Encapsulating a drug e.g., into the matrix of a porous NC, can limit the interaction between the body and the drug until it has reached its target, thereby on the one hand protecting the drug from degradation by i.e., enzymes, or giving it additional stability and on the other hand reducing off-target effects[99,129,130]. Furthermore, the release profile of the drug from the NC can

also be tuned, helping to reduce administration frequencies and limiting dose-dependent side effects[99,129]. Other NC properties that serve to tune their behaviour include size, material, and form. For instance, NCs can be manufactured from a broad range of materials, including lipids, carbon, metals, silica, polymers and others[131–135], enabling the loading of hydrophobic and hydrophilic drugs, and even bigger biological therapeutics such as enzymes and proteins[101,136–140]. Furthermore, depending on the material properties and the chemistry used to prepare the NC, a variety of structures can be fabricated: linear, branched, or dendrimer structures, micelles, hollow capsules, porous or solid particles, etc.[101,141,142] Additionally, surface modifications can further alter the NC properties. E.g., "stealth" moieties such as polyethylene glycol (PEG) decrease the NC's interactions with complement, opsonins, phagocytic cells, and lymphocytes[102], thereby prolonging circulation time and reducing immune responses[143,144]. Coating with targeting moieties can further functionalise the NC and improve drug delivery. Here, too, tuning is possible, e.g., by using more than one kind of targeting moiety for co-targeting[145], coating with targeting Ab and CD47 to protect the targeted NC from phagocytosis[146], or varying the total number of targeting moieties (targeting valency) to influence NC properties such as avidity[147–149].

1.4. CAM-mediated endocytosis

ICAM-1 is an immunoglobulin-like transmembrane glycoprotein which is expressed in a broad range of cells, such as endothelial cells, thus lining the vessels of all organs, epithelial cells, leukocytes, muscle cells, glial cells, and neurons[150]. The expression of ICAM-1 is enhanced through different disease stimuli such as inflammation and oxidative stress[150–152], which then allows for the adhesion and extravasation of circulating leukocytes into subjacent tissue[150,153,154]. While different endothelial cell surface molecules are involved in paracellular (between cells) extravasation, ICAM is the only one mediating the transendothelial (through cells) route[153,155–157], a process similar to transcytosis. This is why the targeting to ICAM-1 is being explored for the therapeutic treatment of cancer, infection by certain pathogens, or inflammation, amongst others[150–152]. Although e.g., the binding of a class of human rhinoviruses, named the major group, to ICAM-1 was known to be required to infect cells[158], the mechanism was unknown and ICAM-1 not recognised as an endocytic receptor. However, its endocytic potential was shown later with the discovery of a novel endocytosis pathway, the CAM-mediated endocytosis, a clathrin- and caveolin-independent mechanism which is also different from micropinocytosis and

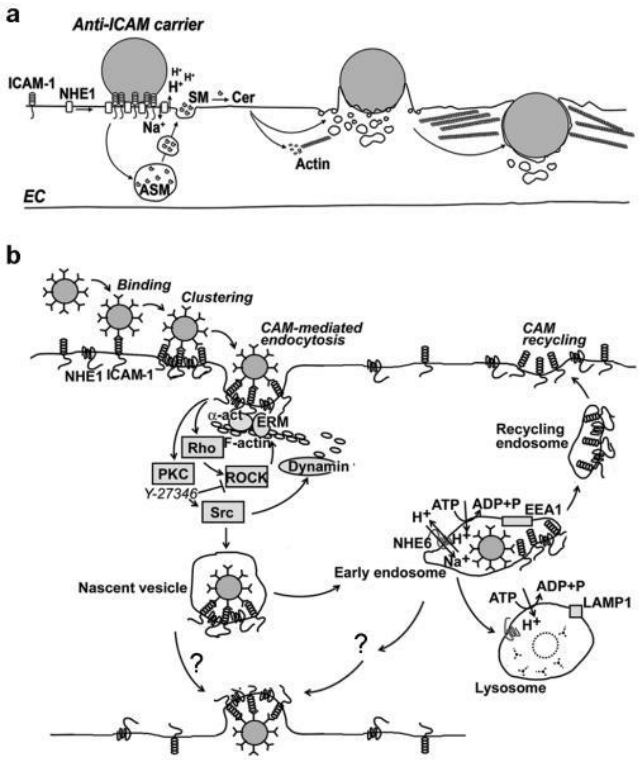

Figure 1.4 Schematic representation of the CAM-pathway for transport of therapeutic NCs. (A) The initial events of the CAM-pathway elicited by receptor engagement, sodium/proton exchanger protein NHE1 is recruited to the entry site, locally decreasing extracellular pH, followed by the recruitment of ASM resulting in ceramide generation. Ceramide facilitates the formation of invaginations and cytoskeletal rearrangements, as well as stress fibre formation, aiding endocytosis of the NC. (B) The signalling cascade of the CAM-pathway is shown, including the activation of PKA, Scr kinase, Rho, and Rho-dependent kinase (ROCK). This cascade induces the formation of endocytic structures, that pinch off the plasma membrane aided by dynamin. Then, vesicles traffic to early endosomes. Unengaged ICAM-1 traffics back to the plasma membrane, whereas carriers are transported to both, the opposite plasma membrane (transcytosis) and lysosomes. Picture taken from Muro (2012)[32].

phagocytosis[159,160]. ICAM-1 activation results in the recruitment of several endocytic partners needed for the endocytosis of cargos with sizes up to several micrometer[149]. The recruitment of sodium-hydrogen exchanger NHE-1 and perinuclear ASM to sites of endocytosis result in the local increase of plasma membrane ceramides, aiding the formation of engulfment structures and cytoskeleton rearrangemente[159,161] (figure 1.4A). Other signalling proteins involved are PKC, Src kinase and Rho kinase (ROCK) that amongst others lead to actin filament rearrangements, with ICAM-bound cargo associating with actin stress fibres[160,162]. The endocytosis process is probably progressed through the ceramide-mediated membrane curvature, forming an invagination, in filament rearrangements, and dynamin activity[159,161] (figure 1.4B). Although cell adhesion molecule (CAM) clustering was observed to be needed for internalisation[160], also non-multivalent anti-ICAM-1 Abs were found to undergo endocytosis upon binding to the receptor, probably due to binding to already clustered ICAM-1[163]. Interestingly, compared to clathrin-mediated and caveolae-mediated endocytosis with average vesicles sizes of 100-150 nm and 50-80 nm[32], respectively, endocytosis *via* the CAM-pathway appears considerably less limited by size restrictions as cargo of spherical, elongated, and irregular shapes with sizes from 100 nm – 5 µm has been seen to readily endocytose via this pathway, in line with its endogenous function of transcellular leukocyte extravasation[160,161,164]. Furthermore, ICAM-1 recycles back to the surface after endocytosis, providing a sustained target[165] (figure 1.4B).

Targeting to ICAM-1 is being explored for the therapeutic treatment of several diseases such as cancer, infection by certain pathogens, or inflammation, amongst others[150–152]. Given its wide expression pattern, ICAM-1 is accessible *via* the intravascular, intratracheal, intracerebral route[166] and due to its association to disease provides specific targeting to sites of disease as well as a sort of self-regulated targeting system, in which the specific target gets automatically downregulated following treatment success due to ICAM-1 downregulation, theoretically reducing the delivered dose to healthy tissue and redirecting it to diseased tissue that still overexpresses ICAM-1. ICAM-1 mediated transcytosis of NCs was shown across brain endothelium as well as gut epithelium, theoretically providing a broad range of application for this pathway[167,168]. ICAM-1-targeted ADCs and nanoparticles bearing therapeutic enzyme have been shown to cross barrier models without compromising the barrier integrity as measured by

an unchanged TEER value and morphologically unchanged cell junction sites, as well as a lack of albumin leakage *in vivo* in mice[163,167–170]. Furthermore, CAM-mediated trafficking does not only mediate transcytosis, but also intracellular trafficking to lysosomes[171–173]. Due to this dual trafficking, anti-ICAM-1 NCs could cross the endothelium of the lung and the brain *in vivo* in mice, where they have been shown to subsequently enter subjacent cells to which they delivered therapeutic enzyme[169–171]. Brain delivery of therapeutic enzyme on NCs has been found to be increased 3- to 7-fold for ASM, 6-fold for α-glucosidase, and 4-fold for α-galactosidase compared to free enzyme[168,172,174,175], showing the great potential for this approach for treating brain disease. Numerous works have focussed on ICAM-1 as a target for therapeutic and diagnostic strategies, including inflammatory conditions, infections, metabolic disease, cardiovascular and pulmonary pathologies, and cancer[174,176–180]. Targeting can be achieved e.g., using specific Abs or a fibrinogen-derived peptide, naturally binding to ICAM-1[174,175,180–184]. Successful targeting could be shown for a broad variety of applications, including biosensors, contrast probes, and NCs for therapeutic interventions in cell culture, animal models, and clinical trials[9,13,17–19,21–24]. Targeting ICAM-1 is an especially potent strategy for drug delivery to the lungs, with e.g., 30-fold increase of a therapeutic enzyme, ASM, compared to the free enzyme in a mouse disease model where enzyme activity could be measured in the tissue with subsequent therapeutic effect[171]. Importantly, ICAM-1 targeting provides targeting to all organs which has additional perks for multi-organ diseases such as lysosomal storage diseases, as discussed in section 1.5. Different parameters such as NC size and targeting valency, the number of targeting moieties presented on the NC surface, have been shown to affect avidity, binding, and uptake *in vitro*[149], as well as biodistribution *in vivo* in mice[168]. Nevertheless, not much is known about the specific effects of e.g., valency on the CAM-mediated intracellular trafficking, such as lysosomal trafficking and transcytosis, forming the missing link to better understand the behaviour of anti-ICAM-1 NCs.

1.5. Lysosomal Storage Diseases and Protein Therapeutics

Protein therapeutics have gained increasing interest for the treatment of many diseases. Evers since the introduction of human insulin 40 years ago[188], the number and areas of application of protein therapeutics have increased drastically[189]. Proteins are attractive therapeutics due to

their high specificity and complex function, not only improving their therapeutic efficacy but also reducing off-target effects. Whereas initially proteins were purified from natural sources, including animal pancreas and human placenta to purify insulin for diabetes treatment[190] or glucocerebrosidase (GBA) for Gaucher Disease (GD) treatment[191,192], respectively, recombinant technology increasingly made it possible to produce therapeutic proteins in a wide range of organisms including bacteria, yeast, insect cells, mammalian cells, and transgenic animals and plants[193–196]. Recombinant enzymes usually show comparable efficacy to natural proteins[188,197,198] with the benefit of a controlled production, enabling theoretically unlimited production and reducing the risk of potential pathogenic contaminants from natural sources[189,197]. Furthermore, the clinical development and FDA approval of protein therapeutics was found to be faster than for small molecules[199]. Currently, there are more than 200 therapeutic proteins approved by the FDA with hundreds of products currently under clinical development[200]. However, the successful development of novel protein therapeutics is challenged by often poor bioavailability, short half-lives, and poor permeability across biological membranes due to their physicochemical properties[201–204].

Lysosomal storage disease (LSD) are a group of around 70 inheritable genetic disorders characterised by the aberrant intracellular accumulation of undegraded macromolecules, leading to debilitating and often fatal outcome[205–207]. The general prevalence of LSDs is unknown due to a probably high level of underdiagnosis because of insufficient clinical awareness and the difficult biochemical testing necessary to diagnose the disease. Nevertheless, it is estimated to be around 1:2000-5000 in the general population, but can be much higher in some populations such as the Ashkenazi Jewish population with a prevalence as high as 1:855[208,209].

LSDs are caused by monogenetic mutations in genes mostly encoding for lysosomal enzymes, thus resulting in dysfunction and macromolecule accumulation[206,207,210]. LSDs can be classified by the type of macromolecule that they accumulate. Those include carbohydrates (Pompe disease), neutral lipids such as triglycerides (Wolman disease), glycolipids (mucolipidoses), glycans that decorate glycoproteins (glycoproteinoses), and glycosphingolipids such as sphingomyelin (glycosphingolipidoses)[211]. Additionally, secondary accumulation of other macromolecules has been observed[212]. Prominent examples of glycosphingolipidoses, the biggest group of LSDs, are

Nieman-Pick disease (NPD) type A or B, caused by a mutation in the catalytic site of acid sphingomyelinase (ASM), rendering it inactive[207] (see chapter 6), and Gaucher disease (GD), caused by a mutation leading to misfolding and degradation of glucocerebrosidase (GBA)[213] (see chapter 7) (figure 1.5). However, there are also LSDs that are not caused by the mutation of lysosomal enzymes, but rather other elements of different degradation pathways resulting in aberrant function and accumulation. For instance, mucolipidosis II/III is caused by a defect in the enzyme that phosphorylates mannose residues targeting lysosomal enzymes to be delivered to lysosomes, in turn resulting in their extracellular secretion[214], Mucolipidosis IV is caused by a defect in the mucolipin-1 channel in the lysosomal membrane, resulting in the de-regulation of lysosomal Ca^{2+} and subsequent dysfunction[215], and Niemann-Pick type C, cystinosis, and Salla disease, are caused by defective membrane transporters shuttling metabolites out of lysosomes[216,217].

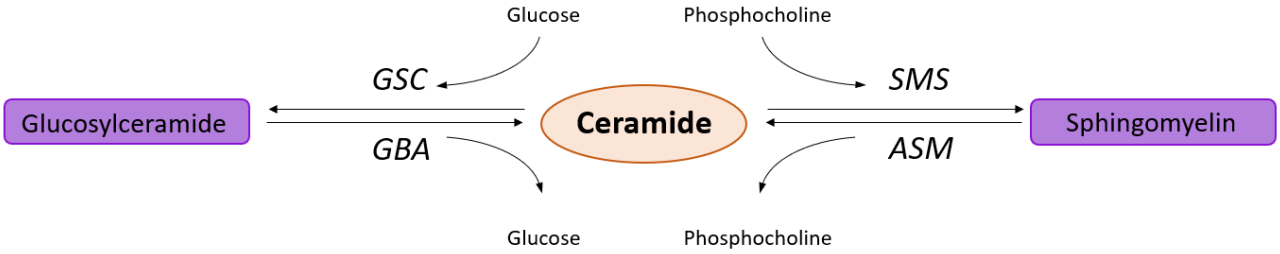

Figure 1.5 Schematic representation of part of the cellular lipid metabolism. GBA = glucocerebrosidase, GSC = glucosylceramide synthase, ASM = acid sphingomyelinase, SMS = sphingomyelinase synthase.

The aberrant storage of macromolecules can lead to cellular dysfunction and cell death through different mechanisms. A prominent mechanism is the disruption of cellular pathways. For instance, cell signalling can be affected through the disruption of lipid rafts, signalling platforms on the cell surface that are highly dependent on cholesterol and other lipids[218,219]. Furthermore, lysosomal function may be dysregulated by increased lysosomal pH, affecting many lysosomal functions including intracellular trafficking, vesicle maturation, hydrolase activity, M6PR recycling, and secretion[32,220,221], or deregulation of lysosomal Ca^{2+}, impacting vesicular transport and recycling[222], as well as an alter autophagy due to the metabolic imbalance[218]. Furthermore, lysosomal membrane permeabilization can occur as a result of aberrant storage of some materials in lysosomes, resulting in release of cathepsins into cytosol and thus induce cell

death[223]. Also, the depletion of endoplasmatic reticulum Ca^{2+}-stores, observed in some animal models of Sandoff disease, Gaucher disease, and GM1 gangliosidosis, can trigger the unfolded protein response, leading to apoptosis[224–226]. Most of these effects are specific to a certain mutation or macromolecule(s) accumulated. Less specific effects include the ”traffic jam” hypothesis, postulating that excess of undegraded material is hindering the entrance of material for degradation to lysosomes, further disturbing cellular homeostasis[227,228]. On the tissue level, LSDs can lead to impaired macrophage function (circulating and resident macrophages), resulting in ineffective or lacking clearance of apoptotic cell material, leading to inflammation, oxidative stress, and leukocyte activation[226]. Amongst damage to different cell types, alterations in cell signalling, endocytosis, and vesicular trafficking can severely damage neurons and thus cause neurodegeneration[229].

LSDs can affect a broad range of tissues since lysosomes are ubiquitously present in all cell types. The specific pathology depends on the pathway affected, but usually involves several tissues including peripheral organs as well as the CNS[228,230,231]. LSDs show very homogenous symptoms, not only between diseases but even between patients with the same disease[228,230]. Generally, LSDs can be classified depending on the age of onset; as infantile (early-onset), juvenile, or adult (late-onset) forms[228]. More than half of all LSDs associate with neuronopathic symptoms, including ataxia, dysphagia, dementia, seizures, and developmental delay, with especially severe neurodegeneration and infantile death in the infantile forms of the disease[226,231–234]. The less severe forms of LSDs affect mainly peripheral organs such as liver, spleen, bones, lungs, striated muscle, and heart[228,230].

The historically stringent development of effective treatments for rare diseases such as LSDs was incentivised by a couple of laws starting in the USA, and was later adapted by the EU, Japan, Singapore, and Australia[235–237]. Although the financial incentive provided under those laws has significantly spurred orphan drug development, the patient recruitment for clinical trials remains a major drawback due to the rarity of the diseases[236]. Nevertheless, many new products have been approved and significantly improved LSD treatment.

The treatment of LSDs can broadly be classified into two groups, namely (a) palliative treatment to alleviate disease burden and (b) disease specific intervention trying to restore biochemical alterations due to mutations. With regards to disease specific interventions, a number of strategies exist or are being investigated. For instance, gene therapy is a promising strategy to correct the monogenic mutation causing the disease or to deliver a functional gene or mRNA[238,239]. Nevertheless, remaining safety concerns and lacking efficacies still pose a problem for the clinical translation of this method. Chaperon therapy, using pharmacological or molecular chaperones to prevent protein misfolding and salvage function, is an approved therapy for some LSDs, yet large-scale screening is needed for the identification of these molecules which are mostly specific to only one disease[240–243]. Another strategy is the substrate reduction therapy (SRT), a small molecule therapy aiming to reduce aberrant accumulation by reducing the rate of biosynthesis of the accumulating molecule[244]. A major drawback of this approach is the lack of its specificity, also influencing other anabolic routes, and thus causing adverse effects[244]. This is why enzyme replacement therapy (ERT), injecting (mostly) recombinant enzyme to restore the deficient endogenous enzyme levels, has become the gold standard treatment for some LSDs[245], such as GD, the most prevalent LSD, discussed in Chapter 7. Another prominent example is NPD with recombinant ASM for ERT currently in clinical trials with promising preliminary results[246], discussed in Chapter 6.

The first marketable ERT came out in 1990 for GD and revolutionised its treatment, improving quality of life and life expectancy[234,247]. Initially, the enzyme was purified from human placenta, a process poor efficiency which required large amounts of raw material. For instance, the treatment of a single GD patient required 50,000 placentas annually, with 1/3 of the world's placentas being used for enzyme purification at the time[197]. To overcome this limitation, Chinese hamster ovary cells (CHO) were investigated to produce recombinant enzyme for ERT and proved easy handling, high product yield, and similar post-translational modifications to native enzyme[197,248], with the recombinant enzyme achieving good treatment efficacy compared to native enzyme in a comparative study[248]. This prompted the production of a whole series of different recombinant enzymes in CHO for LSD ERT[249–261]. Since then, the variety of expression systems used for the production of lysosomal enzymes has expanded and also includes bacteria,

yeast, and plant cells[262]. Thus far, 38 therapies have been approved for the treatment of different LSDs, most of which are ERTs[263].

Nevertheless, and despite their big success, current ERT treatment also face important challenges. Firstly, given the biological nature of the therapeutics used, ERT infusions can inflict immune responses, not only comprising the safety of the patients but also the treat efficacy[264–266]. To address this problem, the FDA and National Organization of Rare Disorders (NORD) have called for an improve, standardised data collection towards the development of improved monitoring assays and optimised treatment to close the current knowledge gap between predictive markers and causative mechanisms[267]. ERT can trigger two types of immune reactions, humoral immunity and/or hypersensitivity. For the humoral response the body produces Ab, mostly IgG types by plasma cells or memory B cells[266–268]. Those antibodies can post a problem for ERT treatment due to their neutralising effects when binding to the catalytic side or targeting site of the enzyme, rendering it inactive or precluding its trafficking to the lysosome, respectively. Additionally, Ab binding adds an additional binding site, the Fc region, to the enzyme, marking them for phagocytosis and thus reducing the enzyme delivery *via* the M6PR to the lysosomes of target cells[267,269–271]. With regards to hypersensitivity, they are immune-mediated and include symptoms such as hypotension, tachycardia, respiratory symptoms, rash, fever, chills, swelling, headache, nausea, etc. [272273]. Interestingly, symptoms are often more severe at the start of the treatment and decline over time, possibly due to immunotollerance[264]. Lastly, allergic reactions and anaphylactic shock are life-threatening yet uncommon[264,272–274]. Commonly, antihistamines, corticosteroids, and antipyretics are administered to alleviate symptoms, in some cases even preventively before the start of the ERT[273,275].

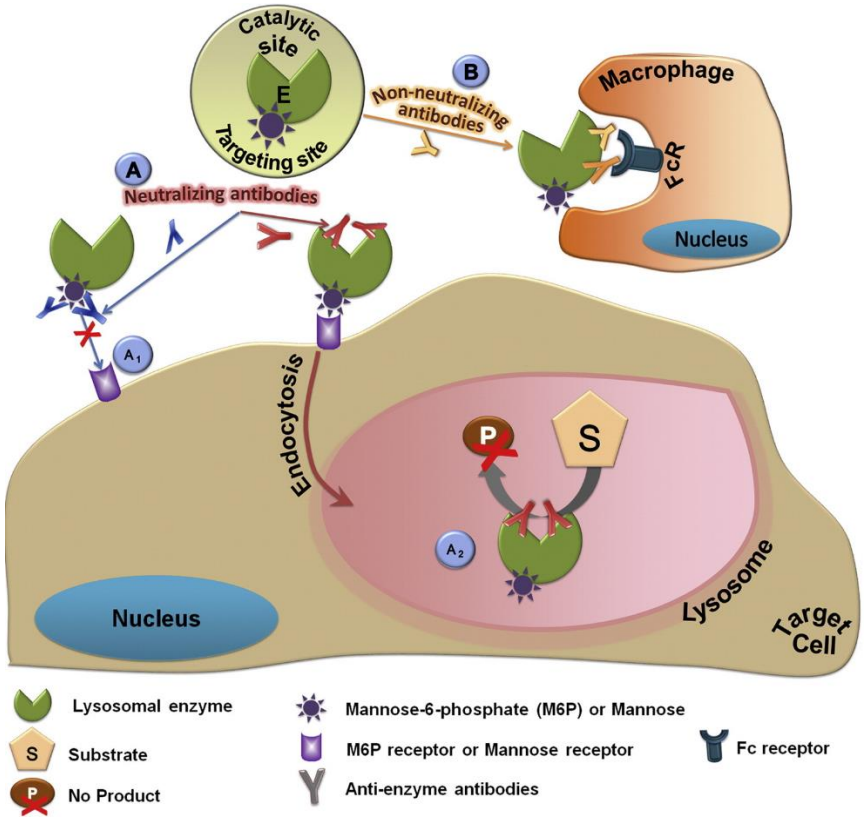

Figure 1.6 Schematic representation of the humoral immune response to therapeutic enzymes for ERT. A therapeutic enzyme with two functional sites, enzymatic and targeting, can elicit an immune response producing (A) neutralising Ab or (B) non-neutralising Ab. Neutralising Abs can bind to the targeting moiety, usually mannose or M6P, and thereby prevent binding to the receptor and thus cell entry (A_1), or to the catalytic site of the enzyme, preventing the degradation of substrate (A_2), both of which lower the efficacy of ERT. Non-neutralising Ab do not affect these functions yet increase FcR-mediated phagocytosis by macrophages (B), also lowering treatment efficacy. Graphic reproduced from Solomon and Muro (2017)[246].

Another big challenge is the poor enzyme accessibility to targets. Compared to the total number of LSDs, only a small group has an available ERT, with peripheral sites being the main target[276,277]. This is because ERT can gain rapid access the main targets for peripheral LSDs such as the liver or spleen due to their highly fenestrated endothelium[278]. In contrary, the highly selective barrier formed at the blood-brain interface, the BBB, does not allow for penetration of ERT into the brain parenchyma (see section 1.2), making treatment of neuronopathic symptoms of LSDs a major challenge with currently no effective treatment option available[24,32,226,244]. Interestingly, the M6PR, the receptor the majority of ERT rely on for entry into the cell and trafficking to lysosomes, is expressed on the BBB in neonates but downregulated soon after birth[279], precluding an efficient brain penetration of ERT *via* that pathway. Furthermore, post-translational modification

may be altered or absent depending on the expression system used. For instance, insufficient or improper glycosylation impairs the enzyme's ability to bind to the MR or M6PR on the surface of the target cell as has been reported for α-L-iduronidase for MPS I[280], β-glucuronidase for MPS VII[281282], N-acetyl-β-hexosaminidase for Sandhoff disease[283], and α-N-acetylglucosaminidase deficient in Sanfilippo syndrome[284]. One the other hand, not only alterations of the targeting moieties on the enzyme but also reduced expression of the targeted MR on e.g., macrophages in GD[285,286] or reduced MR endocytosis[287–289] have been observed, consequently reducing drug delivery. Given these challenges and limitations, new therapeutics and/or delivery systems are needed to improve the treatment of LSD, especially the more severe neuronopathic forms of the disease.

Pharmaceutical NCs provide an excellent platform to overcome aforementioned challenges to successful delivery therapeutics to target cells, additionally providing protection from degradation, immune recognition, and adverse effects by reducing off-target interactions[131,132,290]. Additionally, NCs can be functionalised with targeting moieties such as antibodies, peptides, and ligands to improve the specific delivery to organs, tissues, or cells[291–293]. NC properties are highly versatile because they can be manufactured from a broad range of materials, including liposomes, carbon, metals, silica, polymers and others[131–135]. Many polymers have been FDA approved for the delivery of therapeutic proteins and offer a broad spectrum of properties for manufacturing protein-NC formulations[99,294,295]. With respect to LSDs, various NCs have been studied to deliver different therapeutic enzymes for ERT. Albumin-silk NCs[296] and polyelectrolyte complexes of trimethyl chitosan[297] were prepared to deliver α-galactosidase (Fabry disease), NC containing guanidinylated glycosides[298] were manufactured to carry β-D-glucuronidase (Sly's syndrome) and α-L-iduronidase (Hurler, Hurler-Scheie, and Scheie syndromes), poly(butyl-cyanoacrylate) NCs[299] were prepared as carriers for arylsulfatase B (mucopolysaccharidosis VI), and brain-targeted (targeting peptides Ang2, g7, or Tf2) PLGA NCs were used to deliver galactosylceremidase (Krabbe disease)[300], whereas our group has used ICAM-1-tageted PLGA NCs and polystyrene NCs, a model carrier with comparable properties to PLGA, for the delivery of acid sphingomyelinase[170,171,175,187,301,302] (Niemann-Pick disease), α-

galactosidase[174] (Fabry disease), and α-glucosidase[172] (Pompe disease). These ICAM-1-targeted NCs have been shown to enhance enzyme delivery using a plethora of cellular models *in vitro*, as well as peripheral organs and brain *in vivo*. Therefore, targeted NCs as drug carriers offer an interesting platform for the delivery of therapeutic enzymes for ERT especially for the neuronopathic forms of LSDs, posing a special burden due to disease severity and lack of treatment, given their potential for endocytosis into and transcytosis across the BBB into the CNS[32]. Nevertheless, not much is known about the influence of the endocytosis pathway on the treatment efficacy, especially with respect to distinct LSDs, which might affect NC trafficking differently (also see *Strategies for Crossing the Blood-Brain Barrier).*

Chapter 2: Motivation and Goal

Neurological diseases are the second leading cause of death worldwide, with an increasing incidence[1]. However, despite the undoubtable burden, many of those disease lack proper treatment due to the presence of the BBB, a highly selective barrier inhibiting the passage of most therapeutics into the CNS[18,21–23]. One example of such diseases are NPD and GD, two LSDs pertaining to the sphingolipidoses, which accumulate aberrant levels of sphingolipids inside cells due to a mutation in a lysosomal enzyme, resulting in detrimental pathologies and often premature death[205–207]. Although ERT, using recombinant enzymes to restore endogenous enzyme function, is a very effective approved treatment for GD[204,21], and a comparable drug for NPD with promising results in pre-clinical studies is underway[246], the enzymes used in that therapeutic approach cannot cross the BBB and are therefore not suitable to treat the severe neuronopathic forms for the diseases[24,245].

Nanotherapeutics are a versatile platform that can be used as drug carriers, able to load a broad range of drugs, including therapeutic enzyme such as used for ERT[86–88]. Furthermore, surface modifications such as the addition of Abs allow for specific targeting to endocytosis routes, such as clathrin-mediated, caveolae-mediated, and CAM-mediated pathways, potentially increasing drug penetration by inducing transcytosis across the BBB into the brain[86–88]. However, the influence of certain surface modifications, such as targeting valency, on intracellular trafficking are not yet fully understood and have been shown to influence brain penetration. Furthermore, the influence of disease such as NPD and GD, known to alter e.g., protein expression and membrane lipid composition, potentially important for binding and uptake NCs, on NC trafficking has not yet been studied. A better mechanistic understanding of NC transport across the BBB and the specific effects of the diseases aimed to treat will be crucial towards the successful development of novel therapeutics to treat currently untreatable and deadly ailments.

In light of this information, the overall goal of this work was to enhance our understanding of NC trafficking by the BBB, to study disease-specific alterations on these trafficking events, and to identify the most promising trafficking pathway for the delivery of ERT into the brain using targeted NCs. These goals were addressed in the following specific aims:

Aim 1- Manufacture and Characterise NCs Suitable for Targeting Brain ECs. Fabricate and characterise clinically relevant PLGA and model polystyrene (PS) NCs with varying characteristics, such as number of targeting Abs exhibited on the NC surface (valency), the particular receptor being targeted to induce different RMT pathways, or the presence of enzyme cargo for delivery *in vitro* and *in vivo* in mice.

Aim 2- Study the Mechanism of CAM-mediated Transcytosis of NCs. Use a cellular model to study the mechanism of transport of anti-ICAM NCs into/across brain ECs and the influence of targeting valency on binding, uptake, lysosomal trafficking, and transcytosis.

Aim 3- Study the Effect of ASM deficiency on NC Transport for NPD ERT. Identify the best targeting route for brain ERT by assessing the interaction of NCs targeted to the three main RMT routes with brain ECs affected by ASM deficiency, characteristic of NPD. Study binding, uptake, lysosomal trafficking, and transcytosis.

Aim 4- Assess the Effect of GBA deficiency on NC Transport for GD ERT. Identify the best targeting route for brain ERT by gaining mechanistic insight into the effect of GBA deficiency, characteristic of GD and a risk factor for Parkinson's disease, on the cellular machinery involved in the interaction of brain ECs with NCs targeted to all three RMT pathways.

Chapter 3: Material and Methods

3.1. Instruments

The LSM 800 confocal microscope was from Zeiss (Jena, Germany). The SpectraMax M2e microplate spectrophotometer was purchased from Molecular Devices (San Jose, CA, USA). Zetasizer Ultra instrument was purchased from Malvern Panalytical (UK). The freeze dryer Alpha 1-4 LD was from Christ (Osterode am Harz, Germany). Polytron® PT 3100 D homogeniser and the standard dispersing aggregate knife PT-DA 20 were from Kinematica (Malters, Switzerland). Gallios flow cytometer was from Beckman Coulter (Pasadena, CA, USA). Fisherbrand™ Model 120 Sonic Dismembrator was purchased from Fisher Scientific (Hampton, NH, USA).

3.2. Materials

^{125}Iodine (^{125}I) was purchased from Perkin Elmer (Waltham, MA, USA), Pierce Iodination Tubes were from Pierce (Waltham, MA, USA), the Hidex automatic gamma counter was from Hidex (Turku, Finland), Bio-Spin P-30 Gel Tris Columns were from Bio-Rad (Hercules, CA, USA), the Allegra 6 and Avanti J-26 XP centrifuges were from Beckman Coulter (Pasadena, CA, USA), centrifuges 5810R and 5424R were from Eppendorf (Hamburg, Germany). AccuSpin Micro 17A centrifuge, gelatin, 4',6-Diamidino-2-phenylindole (DAPI), phosphate buffered saline (PBS), L-glutamine, and 10 kDa Texas Red-labelled dextran were purchased from Fisher Scientific (Hampton, NH, USA). Trehalose, hyaluronidase (HAse) from sheep testes, trichloroacetic acid (TCA), 4-methylumbelliferyl β-D-glycopyranoside, pluronic F68 surfactant, bovine serum albumin (BSA), ethyl acetate, imipramine hydrochloride, 4-methylumbelliferone, citric acid, potassium phosphate, sodium taurocholate, glycine, biotin and streptavidin, and Triton X-100 were purchased from Sigma Aldrich (St. Louis, MO, USA). M199 and RPMI 1640 basal medium, penicillin, streptomycin, TrypLE™ Express stable trypsin and secondary antibodies conjugated with Alexa Fluor were purchased from Life Technologies (Carlsbad, CA, USA). Bradford assay kit, anti-VE-cadherin, anti-clathrin, anti-caveolin-1, Amplex Red Sphingomyelinase kit, BODIPY-FlC12-sphingomyelin (Thermo Fisher Scientific), and sodium azide were purchased from Thermo Fisher (Waltham, MA, USA). Endothelial cell growth supplement (EGCS), heparin, and anti-transferrin receptor (anti-TfR) (clone: T56/14) were purchased from Merck (Darmstadt, Germany). Lactel II

copolymer was purchased from Evonik (Essen, Germany). Coverslips were purchased from Paul Marienfeld (Lauda-Koenigshofen, Germany). Fluoresbrite™ YG Microspheres 0.1 µm were purchased from Polysciences Inc. (Warrington, PA, USA). Primary HBMECs were purchased from Innoprot (Derio, Spain) and HUVECs were purchased from Cultek (Madrid, Spain). Transwell inserts 1.0 µm-pore were purchased from Corning (New York, USA). Recombinant human TNFα was purchased from Novus Biologicals (Littleton, CO, USA). Conduritol-β-epoxide (CBE) was purchased from Labclinics (Barcelona, Spain). N-hexanoyl-NBD-glucosylceramide was purchased from Matreya LLC (State College, PA, USA). Paraformaldehyde (PFA) was purchased from Aname (Madrid, Spain). Anti-ICAM Ab (clone R6.5) was produced from commercial hybridoma HB-9580 (ATCC, Manassas, VA, USA). PV1 Ab was purchased from Antibodies-online (Germany). ChromPure Mouse IgG was purchased from Vitro (Seville, Spain). Sodium chloride was purchased from Panreac (Barcelona, Spain). C57BL/6J mice were from Charles River Laboratories (Écully, France). Brain vascular pericytes and pericyte media were purchased from ScienCell Research Laboratories (Carlsbad, CA, USA). NHA astrocytes were purchased from Lonza Walkersville, Inc. (Walkersville, MD, USA).

3.3. Methods

3.3.1. Radio labelling of Antibodies and Enzymes

Where indicated, Abs (anti-ICAM, anti-TfR, anti-PV1, and control IgG) or enzyme (HAse) were labelled with ^{125}Iodine (^{125}I) for radiotracing using a gamma counter. For labelling, 100 µg protein 1mg/ml were incubated for 5 min at 4°C with 20 µCi ^{125}I using Pierce Iodination Tubes. Then, Bio-Spin P-30 Gel Tris Columns were used to remove free ^{125}I by centrifugation in an Allegra 6 Centrifuge for 4 min at 2,300 x g at room temperature (RT).

After labelling, the specific activity was assessed as follows. First, remaining free ^{125}I was separated from ^{125}I-protein using trichloroacetic acid (TCA) at a final concentration of 1 M to denature and precipitate protein for 15 min at RT, followed by centrifugation at 2,300 x g for 5 min at RT using a Centrifuge 5810R (rotor A-4-62) to separate ^{125}I-labelled protein in the pellet and free ^{125}I in the supernatant. The supernatant containing free iodine was collected and the pellet containing both fractions (Fraction A = [½ supernatant], Fraction B = [precipitate containing

^{125}I-labelled protein + ½ supernatant]) were analysed separately. In parallel, Bradford assay was used to determine the protein concentration of the ^{125}I-labelled protein solution. Then, the specific activity of ^{125}I-labelled protein was determined as the activity in counts per minute (CPM) without free ^{125}I quantified using a gamma counter, per mass protein analysed by Bradford assay (CPM/mass), as described[303].

$$Specific\ Activity = \frac{(CPM_{Fraction\ A} + CPM_{Fraction\ B}) - (CPM_{Fraction\ A} \times 2)}{Mass}$$

3.3.2. Preparation of PLGA NCs

PLGA NCs were manufactured using Lactel II copolymer (50:50 glycolic-to-lactic ratio) and Pluronic F68 surfactant.

For the encapsulation of hyaluronidase (HAse), a double emulsion/evaporation technique was used[302]. First, an aqueous solution containing 4 mg/mL protein (2:1 mass ratio HAse:bovine serum albumin (BSA) as a carrier protein) in water was added dropwise under stirring (700 rpm) to an organic solution containing 18 mg/ml Lactel II copolymer dissolved in ethyl acetate. This primary emulsion was homogenised using stirring (1,400 rpm, 30 seconds) and sonication on ice. Sonication was implemented using 10 cycles of 20 seconds on and 5 seconds off at 25% amplification, using a Fisherbrand™ Model 120 Sonic Dismembrator. Then, the formulation was added dropwise to an aqueous solution containing 2% F68 dissolved in water, under stirring (850 rpm), to form a secondary emulsion. This was followed by homogenisation by stirring (1,250 rpm, 1 min) and sonication on ice for 10 cycles of 20 seconds on, 5 seconds off. The solvent was removed by overnight evaporation under stirring (500 rpm) and NCs were collected by centrifugation at 23,800 x g for 10 min at RT using an Avanti J-26 XP (rotor: J-12)[302].

For pristine PLGA NCs without enzyme loading, Lactel II was dissolved in ethyl acetate at 10 mg/ml and added dropwise to 2% Pluronic F68 in water under stirring (1,400 rpm). This emulsion was homogenised by stirring (1,400 rpm, 1 min) and sonication on ice for 10 cycles consisting of 20 seconds on, plus 5 seconds off. Subsequently, this suspension was added dropwise under stirring (1,200 rpm) to 0.2% pluronic F68 in water and the solvent was removed by overnight

evaporation under stirring (500 rpm). NCs were collected by centrifugation at 14,100 x g for 15 min at RT using an Avanti J-26 XP (rotor: J-12). Subsequently, a second round of centrifugation at 3,000 x g for 4 min at RT was used to separate big aggregates in the pellet and NCs were collected in the supernatant.

Both types of PLGA NCs were coated with protein (anti-ICAM or 1:1 mass ratio anti-ICAM:HAse) via surface adsorption. For this, NCs were incubated with Ab at 7 x 10^{-15} µg per nm^2 of NC surface under rotation at 4 rpm using a tube rotator for 2 h at RT. Then, NCs were washed to remove non coated protein. To this end, PBS was added and NCs were collected by centrifugation at 13,500 x g for 3 min at RT using a Centrifuge 5424 R (rotor: FA-45-24-11). The NC pellet was finally resuspended in PBS[302].

3.3.3. Preparation of Coated Polystyrene (PS) NCs

FITC-like model PS beads having 100 nm diameter (Fluoresbrite™ YG Microspheres 0.1 µm) were coated with protein (either Ab alone or 1:1 Ab:HAse mass ratio) via passive surface adsorption, as described[170,171]. In brief, NCs were incubated for 1 h at RT with 2.3 x 10^{-15} µg protein (Ab or HAse) per nm^2 NC surface, washed with PBS to remove non-bound protein, and collected by centrifugation at 13,500 x g for 3 min at RT using a Centrifuge 5424 R (rotor: FA-45-24-11). NCs were resuspended in PBS containing 0.3% BSA or 1% BSA for *in vivo* experiments in mice or cell culture, respectively. Lastly, NCs were sonicated with 12 cycles of 1 second on, plus 1 second off at 25% amplification using a Fisherbrand™ Model 120 Sonic Dismembrator.

NCs with different targeting valencies were manufactured by incubation of PS beads with Ab mixtures containing different ratios of targeting Ab and untargeted IgG (1:3, 1:1, 1:0 molar ratios), thereby maintaining the total number of Ab molecules per NC to not alter NC surface properties, while only varying the number of targeting Abs, as described[149].

3.3.4. Sonication calibration

*PS NCs coated with IgG alone, as a model Ab, were characterised for p*olydispersity index *(PDI) by* dynamic light scattering *(DLS) and subsequently subjected to sonication using a* Fisherbrand™ Model 120 Sonic Dismembrator. Different protocols were tested, always using pulses of 1 second on, 1 second off, but varying sonication amplification (20%, 25%, and 75% amplification), and the number of pulses (6, 12, 25, 50), as indicated. Following sonication, NCs were analysed by DLS again to determine their PDI.

3.3.5. NC Characterisation

All NCs (PLGA and PS) were characterised using a Zetasizer Ultra instrument and analysed with the associated ZS XPLORER software. To determine the hydrodynamic size (mean diameter) and PDI, samples were diluted in PBS and analysed by backscattering. To determine NC concentration, samples were diluted in PBS and analysed by multi-angle DLS (MADLS). To determine NC ζ-potential, samples were diluted in deionised (DI) water.

3.3.6. Scanning and transmission electron microscopy

As an example of PLGA NCs, anti-ICAM-1 PLGA NCs were visualised after uranyl acetate staining using a JEOL JEM 2100 LaB6 transmission electron microscope (TEM) operating at 100 kV. As an example of PS NCs, anti-TfR NCs were visualised after uranyl acetate staining using a Tecnai Spirit transmission electron microscope operated at 120 kV.

3.3.7. Quantification of NC Encapsulation and Coating

NC encapsulation and coating efficiency were assessed using radioisotopic quantification and DLS measurements. NCs were loaded or coated with ^{125}I-labelled protein (Ab or HAse) and their resulting size, PDI, and concentration were determined by DLS, as described in section 3.3.5. Then, free ^{125}I was determined by TCA assay and corrected for, as described in 3.3.1.

The amount of protein coated or encapsulated was determined and corrected for free iodine as follows:

$$Protein\ specific\ activity = \frac{CPM_{Total} - CPM_{Free\ 125I}}{Mass}$$

$$Protein\ encapsulated\ or\ coated = \frac{(CPM_{Total} - CPM_{Free\ 125I})}{Specific\ activity}$$

$$Number\ of\ molecules$$

$$= \frac{Avogadro's\ number}{Protein\ molecular\ weight} \times protein\ mass$$

The following equations were used to determine encapsulation and coating efficiencies:

$$Encapsulation\ or\ coating\ efficiency\ (\%)$$

$$= \frac{Protein\ mass\ determined\ in\ the\ final\ formulation}{Protein\ mass\ added\ for\ encapsulation} \times 100$$

$$Encapsulated\ or\ coated\ \frac{molecules}{NC} = \frac{Number\ of\ molecules}{Number\ of\ NCs}$$

$$Protein\ \frac{molecules}{NC\ surface} = \frac{Number\ of\ molecules}{4 \times \pi \times r^2}$$

3.3.8. NC Lyophilisation

NCs formulations obtained as described in sections 3.3.2. and 3.3.3. where lyophilised at 0.1 mbar and -40 °C in a freeze dryer Alpha 1-4 LD, using 2.5% trehalose as a lyoprotectant to maintain the conformation of NCs during the removal of water. Lyophilised formulations were stored at -20 °C. Resuspension was performed in equal volume DI water as pre-lyophilisation.

NC stability under storage conditions and in complete cell medium

Coated PS NCs were stored at 4 ℃ in PBS containing 1% BSA (storage condition). At indicated time points, NCs were analysed by DLS to determine the hydrodynamic size and PDI. Alternatively, coated PS NCs were diluted in complete cell medium containing 10% fetal bovine serum (FBS) to achieve the same concentrations used in cellular experiments and incubated for 5 h. Then, NCs were analysed by DLS to determine the hydrodynamic size, PDI, and ζ-potential.

3.3.9. Cellular Brain Endothelium Model

Primary human brain microvascular endothelial cells (HBMEC) were cultured at 37°C, 5% CO_2, and 95% relative humidity in RPMI 1640 basal medium supplemented with 10% FBS, 2 mM L-glutamine, 30 µg/mL endothelial cell growth supplement (ECGS), 100 µg/mL heparin, 100 U/mL penicillin, and 100 µg/mL streptomycin.

Human umbilical vein endothelial cells (HUVEC) were cultured at 37°C, 5% CO_2, and 95% relative humidity in M199 medium supplemented with 10% FBS, 2 mM L-glutamine, 15 µg/mL ECGS, 100 µg/mL heparin, 100 U/mL penicillin, and 100 µg/mL streptomycin.

For experiments, ECs were seeded at passage 7 on glass coverslips coated with 1% gelatin in 24-well plates and grown to confluency for 3 days[149,304].

3.3.10. Cellular Blood-Brain Barrier Model

BBB models used consisted of either an HBMEC monoculture or a co-culture with other sub-endothelial cells. For the monoculture, primary HBMEC were seeded at passage 7 on the apical side of uncoated 1.0 µm-pore transwell inserts in 24-well plates. For co-culture models, astrocytes (ACs) or pericytes (PCs) were seeded on the basolateral side of the same transwell filter as HBMECs.

In all cases, to allow for barrier formation, cells were grown for 7 days at 37°C, 5% CO_2, and 95% relative humidity in RPMI 1640 basal medium supplemented with 10% FBS, 2 mM L-glutamine, 30 µg/mL ECGS, 100 µg/mL heparin, 100 U/mL penicillin, and 100 µg/mL streptomycin.

Transwells without cells were also used as controls to assess the permeability as described[170].

3.3.11. Cellular Disease Models

Inflammation model: Cells were incubated with 10 ng/mL of the inflammatory cytokine TNFα for 16-20 h prior to experiments, to mimic inflammation, a typical hallmark of LSDs[32] and other neurological diseases[305].

Niemann-Pick Disease (NPD) Model: In addition to the treatment with TNFα, as described above, cells were incubated with 20 µM imipramine for 48 h prior to experiments. Imipramine is known to induce the degradation of endogenous ASM[306] , thereby resulting in ASM deficiency and subsequent aberrant intracellular storage of sphingomyelin, such as seen in NPD[289].

Gaucher Disease (GD) model: In addition to the treatment with TNFα, described above, cells were incubated with 200 µM conduritol-β-epoxide (CBE) for 72 h prior to experiments. CBE covalently binds and inactivates glucocerebrosidase[307], leading to aberrant glucosylceramide accumulation such as seen in GD[308].

Control cells: Cells without any additional treatment were used as control.

3.3.12. Acid Sphingomyelinase (ASM) Activity

Validation of ASM deficiency model. ECs grown to confluency were incubated in control cell medium or medium containing 20 uM imipramine for 48 h as a model for ASM deficiency. Cells were lysed for 15 min at 4C in 1% Triton X-100, then 1:10 dilutions of the cell lysates were used to measure enzyme activity. This was done by incubating the diluted cell lysate for 1 h at 37 C with Amplex Red Sphingomyelinase kit. The kit contains sphingomyelin, the ASM substrate, from which ASM activity produces ceramide and phophorylcholine at pH 4.5. The kit also contains alkaline phosphatase, which dephosphorylates phosphorylcholinase into choline, and coline oxidase to form betaine and hydrogen peroxide. Finally, the kit contains 10-acethyl-3,7-dihydroxiphenoxacine (Amplex™ Red), which reacts with hydrogen peroxide to render a fluorescent compound called resorufin. Resorufin appearance was measured using a spectrofluorometer, using 571 nm excitation and 585 nm emission.

In parallel, control cells vs. cells treated as described with imipramine were incubated for 16-20 h with BODIPY-FlC12-sphingomyelin to allow this fluorescent lipid analog to incorporate into cell membranes. Then, cells were washed with PBS, fixed for 15 min with cold 2% paraformaldehyde, mounted on microscopy slides with MOWIOL and imaged by fluorescence microscopy under the green channel.

3.3.13. GBA Activity

To determine GBA activity, cells were lysed for 30 min at RT using 50 mM citric acid/PBS at pH 6, with 1% (w/v) Triton X-100, and 1% (w/v) sodium taurocholate. This cell lysate was collected by centrifugation at 20,000 x g for 20 min at 4 °C using an AccuSpin Micro 17A centrifuge. Total protein concentration was determined using a BCA assay kit following the vendors instructions. Subsequently, cell lysates were incubated for 30 min at 37 °C with 0.75 mg/ml 4-methylumbelliferyl-β-D-glycopyranoside (4-MU-β-D-Glc), a substrate of GBA, whose enzymatic cleavage releases the blue-fluorescent product 4-methylumbelliferone (4-MU). Sample fluorescence intensity was analysed using a SpectraMax M2e microplate spectrophotometer (excitation/emission 365/445 nm). A calibration curve was prepared from a range of known 4-MU concentrations and enzymatic activity was expressed as pmol product/min/µg enzyme.

3.3.14. GBA Substrate Accumulation

Cells were treated with 5 µg/mL N-hexanoyl-NBD-glucosylceramide (GlcCer), a green-fluorescent substrate for GBA. Enzymatic cleavage of GlcCer by cells results in non-fluorescent product. Therefore, loss of green fluorescence observed by microscopy is indicative of enzymatic activity. Mean fluorescence intensity was imaged by fluorescence microscopy and analysed using ImageJ.

3.3.15. VE-cadherin staining

Cells were fixed with 2% PFA for 15 min at RT, then incubated with 3 µg/mL anti-VE-cadherin in 1% BSA/PBS for 1 h at RT. Cell samples were than washed to remove non-bound Ab, incubated

with 4 µg/ml fluorescent secondary Ab for 30 min in 1% BSA/PBS, and washed again to remove non-bound Ab. Pictures were imaged by fluorescence microscopy.

3.3.16. Permeability of a cellular BBB model

Cells were incubated with Texas Red dextran (10 kDa)-free cell medium on the apical chamber and 0.5 mg/mL Texas Red dextran (10 kDa) containing cell medium on the basolateral chamber for 5, 15, 30, or 60 min. At the indicated time points, the apical cell medium was collected and analysed using a spectrophotometer (ex.: 580 nm, em.: 604 nm). Known concentrations of Texas Red dextran were used to create a calibration curve to extrapolate concentrations in samples.

3.3.17. Receptor Expression by Flow cytometry

Cells were detached using trypsin and collected by centrifugation at 4 °C and 800 x g for 5 min using a Centrifuge 5810R (rotor: A-4-62). Cells were then fixed with 2% PFA for 15 min at RT, collected again by centrifugation, and stained with 2 µg/mL Ab against ICAM-1, TfR or PV1, for 1h at 4 °C under constant rotation using a tube rotator at 4 rpm. Then, samples were washed with PBS to remove non-bound Ab and incubated for 0.5 h at 4 °C with a secondary Ab conjugated with Alexa Fluor 488 (green fluorescent) at 1.5 µg/mL under rotation at 4 rpm using a tube rotator in the dark. Subsequently, cells were washed with PBS to remove non-bound Ab, stained with 2 µg/mL DAPI for 10 min, and analysed by multilaser analysis using a flow cytometer and the associated software FlowJo.

3.3.18. Receptor Expression by Microscopy

Cells were fixed with 2% PFA for 15 min at RT and incubated with primary Ab against indicated receptors 4 µg/mL in 1% BSA/PBS for 30 min at RT. Then, cells were washed to remove non-bound Ab and incubated with 4 µg/mL fluorescent secondary Ab for 30 min at RT in the dark, washed again to remove non-bound secondary Ab and analysed by fluorescence microscopy. Analysis of sum intensity per cell – background fluorescence using ImagePro.

3.3.19. High Resolution Imagining of Receptors and Endocytic Partners

Cells were fixed and incubated with 2 µg/mL primary Ab against the indicated markers (ICAM-1, TfR, PV1, clathrin and caveolin) for 30 min in the dark. Cells were washed with PBS to remove non-bound primary Ab and incubated with secondary Abs for 1 h. ≥ 12 regions of 100 μm^2 were analysed per condition.

3.3.20. Single Molecule Tracking and TIRF Microscopy

Cells were incubated with biotinylated Abs against ICAM, washed with PBS to remove non-bound Ab, followed by incubation with QD-633-conjugated (red fluorescence) streptavidin. Subsequently, cells were washed to remove QDs and incubated in control cell medium or medium containing $3x10^{10}$ FITC-anti-ICAM:HAse NCs/mL for 5 min to allow for binding. Cells were then washed with PBS to remove non-bound NCs and imaged with total internal reflection fluorescence (TIRF) microscopy at a frame rate of 100 ms. The individual trajectories of QD-labelled receptors were recorded and represented in a histogram of immediate diffusion coefficients. The diffusion coefficients of QD fixed on glass were used to define immobility with 97% of immobilised QD being below the set threshold. Diffusion was calculated from the frequency of the moment scale spectrum (MMS) slopes for several trajectories with and without NCs and defined as <0.2 = confined, 0.2 – 0.5 = subdiffusive, and >0.5 = free. The trajectories that were analysed per condition were n = 114 trajectories (immobile QD), n = 361 trajectories from 5 cells (>32 trajectories/cell) (CBE-), and n = 442 trajectories from 4 cells (>93 trajectories/cell) (CBE+).

3.3.21. Microscopy Characterisation of NC binding to Brain ECs

Cells were incubated with $7x10^{10}$ FITC-labelled PS NCs/mL for a 30 or 60-min binding pulse, washed with PBS to remove non-bound NCs and fixed with 2% PFA for 15 min. Pictures were imaged by fluorescence microscopy. Quantification of the number of NCs/cell was assessed per cell using a custom algorithm in ImagePro, as described[309]. In brief, the algorithm recognises dot-

like fluorescent spots surrounded by background fluorescence and divides the area of these dot-like spots by the number of pixels corresponding to one NCs.

3.3.22. Radiotracing of NC Binding to Brain ECs

Cells were incubated with $7x10^{10}$ ^{125}I-labelled NCs/mL from the apical or basolateral side for a 30-min binding pulse under two different conditions: (1) Live cells at 37 °C to allow for binding under physiological conditions, or (2) fixed cells at 37 °C to inhibit endocytosis, thereby isolating binding. Then, cells were washed to remove non-bound NCs and fixed with 2% PFA (if applicable) for 15 min. Quantification of the ^{125}I-content was done using a gamma counter, the amount of NCs was calculated from the CPM in each cell fraction and the known CPM/NC, as described above.

3.3.23. Microscopy Characterisation of NC Uptake by Brain ECs

Cells were incubated with $7x10^{10}$ FITC-labelled NCs/mL for 30 min at 4 °C to inhibit endocytosis and allow for binding only, washed to remove non-bound NCs to impede further binding of NCs, and further incubated at 37 °C for 5 min, 15 min, 30 min, 1 h, 3 h, 5 h, and 24 h with NC-free medium to allow synchronized uptake. Cells were then fixed with 2% PFA for 15 min in the dark and subsequently incubated with red Alexa Fluor 555-conjugated secondary Ab targeted to the primary Ab coated on the NC surface. Secondary Ab cannot cross the cell membrane and can, therefore, only bind to NCs located in the cell surface and not internalised by cells. Hence, this method allows for differential staining of cell surface-bound NCs as yellow (green + red) and internalised NCs as green, as described[309]. Imaging of cells was done by fluorescence microscopy, NC quantification per cell (cell surface-bound + internalised NCs = total cell-associated NCs) was analysed using a customized algorithm in ImagePro, as described[309].

3.3.24. Radiotracing of NC Uptake by Brain ECs

Cells were incubated with different types of NCs bearing 2.25 µg/mL ^{125}I-labelled HAse or the same concentration free enzyme for 1 h, 3 h, or 24 h at 37 °C. When the incubation time was

reached, cells were washed to remove non-bound NCs or free enzyme. Cells were then further incubated with an elution buffer containing 0.05 M glycine and 0.1 M sodium chloride in PBS at pH 2.5, for 15 min at RT to elute and collect the cell-bound fraction of NCs or free enzyme. Then, cells were lysed with 2% Triton X-100 for 15 min at RT to lyse the cells. Intracellular NCs or free enzyme was measured using a gamma counter and the specific activity, as

3.3.25. Transcytosis of NCs Across Confluent Brain EC Monolayers

Cells were incubated with $7x10^{10}$ NCs/ml labelled with ^{125}I-Ab with indicated targeting and valency added to the apical chamber for a 30-min binding pulse at 37 °C. Early transport events into the basolateral chamber were analysed using a gamma counter. This fraction was not included in the transcytosis analysis because apart from transcytosis, NCs may also have crossed the barrier non-specifically via the paracellular route, thus leaked across the barrier. Therefore, all non-bound NCs were then removed by washing to ensure the subsequent analysis of only cell bound NCs, thereby ensuring their receptor-mediated transport. Cells were further incubated (if applicable) in NC-free medium at 37 °C until a total incubation time of 0.5 h, 1 h, 3 h, 5 h, and 24 h to allow for transcytosis. At selected time points, the basolateral fraction and cell fraction were collected, and their ^{125}I-content was quantified using a gamma counter. The number of NCs in each fraction was quantified as absolute NCs. Transcytosis was also expressed as %BL NCs / total NCs added:

$$Number\ of\ NCs = \frac{CPM\ fraction}{\frac{CPM}{NC}}$$

$$Transcytosis = \frac{Number\ of\ NCs\ in\ BL}{Total\ number\ of\ NCs}$$

3.3.26. Lysosomal Trafficking and Lysosomal Quantification

Prior to the incubation with NCs, lysosomes were stained by incubating for 40 min at 37 °C with 0.5 mg/mL 10 kDa Texas Red-labelled dextran, a polysaccharide taken up by cells *via* pinocytosis which traffics and accumulates in lysosomes as it cannot be degraded in mammalian cells[172].

Subsequently, cells were washed to remove extracellular dextran and further incubated for 60 min to allow for the complete trafficking of all dextran to lysosomes, verified by colocalisation of dextran with lysosomal marker LAMP-1[172]. Then, cells were incubated with $7x10^{10}$ FITC-labelled NCs/mL with indicated targeting and valency for either 5 min, 15 min, or 30 min continuous incubation at 37 °C followed by washing with PBS to remove non-bound NCs or a 0.5 h binding pulse followed by washing with PBS to remove non-bound NCs and further incubation in NC-free cell medium up to at 37 °C up to 45 min, 1 h, 3 h, 5 h, or 24 h total incubation. When the final incubation time was reached, cells were fixed with 2% PFA for 15 min at RT in the dark. Imaging was done by fluorescence microscopy. NC and lysosome quantification per cell using an algorithm in ImagePro, as described[309] (also see section 3.3.21.):

$$Lysosomal\ NCs = Green\ objects \cap Red\ objects$$

3.3.27. Protein Coat Loss upon Cellular Interaction

Cells were incubated with $7x10^{10}$ FITC-labelled NCs/mL for a 30 min binding pulse at 37 °C, then washed with PBS to remove non-bound NCs, and further incubated (if applicable) at 37 °C in NC-free medium up to 0.5 h, 1 h or 3 h total incubation. Then, cells were fixed with 2% PBS for 15 min at RT, permeabilised with 0.1% Triton X-100 for 15 min at RT in the dark, incubated with 4 µg/mL red-fluorescent secondary Ab against the coat proteins for 30 min at RT, and washed with PBS to remove non-bound Ab. Permeabilisation allows for the secondary antibody to enter the cells and can therefore detect the presence of coat proteins not only on cell-surface NCs but also for intracellular NCs. This method allows us to distinguish NCs with coat proteins (green + red = yellow) and without coat proteins (green only) independently from their cellular location. Analysis done by fluorescence microscopy and an algorithm in ImagePro, as described[309] (also see section 3.3.21.). The percent of NC without coat proteins at a given time was calculated using the results obtained from ImagePro:

$$\%\ \text{NCs without coating} = \text{Green objects} - (\text{Green objects} \cap \text{Red objects})$$

The percentage of NCs without protein coat was displayed over the 0.5 h base detection, assuming that at this time most NCs should not yet have reached lysosomes.

3.3.28. Cellular Degradation Pattern of Anti-ICAM-1 NCs

Cells were incubated with $7x10^{10}$ ^{125}I-Ab NCs/ml for a 30-min binding pulse from the apical side at 37 °C, then washed to remove non-bound NCs, and further incubated (if applicable) at 37 °C in NC-free complete cell medium up to 24 h. At indicated time points, cells were collected and the free ^{125}I content was determined using the TCA assay, as described above in section 3.3.1. Data were expressed relative to the overall highest value measured.

3.3.29. NC Reuptake Following Transcytosis

Cells were incubated with $7x10^{10}$ NCs FITC-labelled NCs/mL from the apical side for a 30 min binding pulse, then washed with PBS to remove non-bound NCs. Then, cells were further incubated with NC-free medium for additional 30 min. In parallel, following the wash, 0.5 mg/mL 10 kDa Texas dextran Red (red fluorescent) was added to the basolateral chamber to be able to distinguish apical and basolateral medium using fluorescence microscopy. Thus, when NCs transcytose from the apical to the basolateral side of the transwell, if they were taken up by cells again, medium containing red fluorescent dextran would enter into the same endocytic vesicle, enabling the visualisation of reuptake following transcytosis by fluorescence colocalisation (green NCs + red dextran = yellow).

3.3.30. HAse delivery to brain ECs

HUVEC were incubated with 2.25 µg/mL ^{125}I-labelled HAse either free or carried by either PLGA NCs encapsulated or coated or PS NCs (coated), as described above in sections 3.3.2. and 3.3.3. At indicated time points, cells were washed with PBS to remove non-bound HAse and incubated at RT with glycine elution buffer (0.05M glycine + 0.01M sodium chloride, pH 2.5) for 15 min to collect the cell-bound fraction, followed by lysing the cells for 15 min at RT using 2% Triton X-100 to collect the internalised fraction. The quantification of the HAse content per fraction was done using a gamma counter.

3.3.31. Fluorescence Microscopy

Images were taken using a Zeiss LSM 800 confocal microscope with an 63x / 1.4 Oil DIC M27 objective and diode lasers 405 nm, 5 mW; 488 nm, 10 mW; and 561 nm, 10 mW, all laser class 3B, two PTM Multi Alkali detectors and the associated Zen 2.3 (blue edition) imaging software. Pictures were taken as Z-stacks with varying numbers of planes, with 0.5 µm interplanar distance, to collect information across the whole hight of the cells. Images were then processed in ImageJ to compose a single 2-D image from each Z-stack using the maximum intensity Z-projections function.

3.3.32. *In vivo* biodistribution in mice

Commercial C57BL/6J mice of both sexes were weighed, anaesthetised with an intraperitoneal injection of 100 mg/kg ketamine and 1 mg/kg medetomidine and injected i.v. *via* the jugular vein with 2.3 x 10^{13} NCs/kg body weight. Injected NCs had been coated with ^{125}I-labelled 1:1 molar ratio anti-ICAM:IgG NCs (called anti-ICAM NCs thereafter) or IgG alone (called IgG NCs thereafter). In both cases, a tracer amount of ^{125}I-IgG (10% of total IgG used) was employed so that if Ab would detach from the NCs *in vivo*, then ^{125}I-IgG would not interact with the endothelium. The laboratory compares all NC biodistribution data with the biodistribution of ^{125}I-IgG, as such, as an internal control. Then, 1 min, 2 min, 5 min, 10 min, 15 min, 30 min, 45 min, 60 min, 120 min, 180 min after the injection, blood samples were extracted via the facial vein and mice were euthanised by cervical dislocation after 0.5 h, 1 h, or 3 h. Subsequently, organs were collected, weighed, and free ^{125}I was determined by homogenising organs using a Polytron® PT 3100 D homogeniser with the standard dispersing aggregate knife PT-DA 20, followed by protein precipitation using TCA, as described above, and centrifugation at 2300 x g for 5 min at RT using a centrifuge 5810R (rotor: A-4-62) to separate ^{125}I-labelled protein in the pellet and free ^{125}I in the supernatant. The ^{124}I-content was determined using a gamma counter. Data were used to calculate[174,170]:

$$Percent\ injected\ dose\ (\%ID) = \frac{CPM\ in\ blood\ or\ organ}{CPM\ total\ dose - CPM\ remaining\ in\ the\ syrringe}$$

$\%ID/g = \frac{Percent\ injected\ dose}{Gram\ organ}$, to compare organ concentrations.

$Localisation\ ratio\ (LR) = \frac{(ID\%/g)_{Organ}}{(ID\%/g)_{Blood}}$, to compare tissue-to-blood distribution.

$Specificity\ index\ (SI) = \frac{LR_{Anti-ICAM\ NC}}{LR_{IgG\ NC}}$, showing specific targeting.

3.3.33. Visualisation of Anti-ICAM NCs in Mouse Brain

Mice were injected i.v. under anaesthesia with FITC-labelled anti-ICAM NCs. At indicated time points, mice were perfused with PBS intracardially to eliminate blood and then 4% PFA to fix tissue. The brain was collected, kept in PFA overnight, and then imaged *ex vivo* by fluorescent microscopy on a PBS-wetted microscope slides.

3.3.34. Assessment of Paracellular Permeability in Mouse Brain

Mice were injected i.v. under anaesthesia with ^{125}I-labelled albumin alone (control), ^{125}I-albumin together with anti-ICAM PS NCs, or ^{125}I-albumin with TNFα. After 1 h, mice were sacrificed, blood and brain were collected, and albumin content was quantified using a gamma counter. Blood to brain leakage was calculated as:

$$Leakage = \frac{CPM_{brain}}{CPM_{blood}}$$

3.3.35. Statistics

Data were calculated as average ± standard error of the mean (SEM). For fluorescence microscopy n ≥ 3, for radiotracing n ≥ 4, for flow cytometry n = 4, for *in vivo* mice n = 5. Statistical significance was determined as $p<0.05$. Two-group comparisons by Student's t-test, multiple comparison by analysis of variance (ANOVA) followed by Tukey's test.

Chapter 4: Manufacture and Characterise NCs Suitable for Targeting Brain ECs

4.1. Introduction

LSD are a group of around 70 inheritable genetic disorders characterised by the aberrant intracellular accumulation of undegraded macromolecules (see section 1.5.)[1]. ERT, injecting recombinant enzyme to restore the deficient endogenous enzyme levels, has already become the gold standard treatment for some LSDs[310], such as GD, the most prevalent LSD, discussed in Chapter 7. Another LSD which could benefit from a protein therapeutic is NPD, discussed in Chapter 6, with recombinant ASM showing promising results in current ERT clinical trials[246311]. Nevertheless, neuronopathic forms of LSDs, often resulting in more severe forms of the disease and premature death[232–234], cannot be treated with ERT due to the lack of penetration of proteins across the BBB into the brain[312].

Nanomedicine, used to produce nano-sized drug carriers[131–135], is a versatile platform that can offer a series of advantageous properties[64,293,313]. PLGA, a synthetic co-polymer of lactic and glycolic acid, has emerged as a widely used material in nanomedicine due to its lack of toxicity, biocompatibility, and biodegradability[16]. Several PLGA-based systems are already approved by the FDA as well as the EMA for the treatment and diagnosis of diseases in the clinic[119,120]. PLGA is also being widely investigated to be used to produce NCs, capable of loading a plethora of different molecules, including hydrophilic and hydrophobic drugs[314,315], DNA[316], and proteins such as therapeutic enzymes used for ERT in LSD[148,171,300,317,318]. Therapeutic cargo can be loaded using PLGA NCs *via* different techniques, e.g. in the context of lysosomal ERT, therapeutic enzyme has been successfully loaded *via* encapsulation into the NC matrix or coating onto the NC surface[148,171,300,317,318], both showing promising results with regards to enhanced targeting, increased endocytosis, and recovery of lysosomal function[148,171,300,317,318]. Furthermore, NCs can be functionalised with targeting moieties such as antibodies, peptides, and ligands to improve the specific delivery to organs, tissues, or cells[291–293]. Targeting to cell-surface receptors to induce receptor-mediated endocytosis is a promising strategy for the delivery of NCs into and across the BBB[64]. Three distinct natural transport pathways, CAM-, clathrin-, and caveolae-mediated

endocytosis, can be targeted to induce transcytosis of NCs across the endothelium and lysosomal trafficking for the delivery of therapeutic enzyme to target cells[64,165,319–321].

The stability of a NC formulation is of importance for experimental reproducibility, safety, and efficacy[322,323]. With respect to NC-mediated ERT, NCs need to be stable under storage conditions yet release their cargo in lysosomes for good therapeutic efficacy. To this end, PLGA NCs have the favourable characteristic of being degraded to lactic and glycolic acid in lysosomes[324,325], breaking up the NC structure and thus helping to release its therapeutic cargo at the target site, the lumen of the lysosome, while also helping to restore the abnormal pH, affected in several LSDs, by the release of these acidic monomers[326]. In fact, the release of therapeutic enzyme from PLGA NCs was found to be minimal under storage conditions and in model physiological fluids for up to 72 h, in line with only minimal changes in hydrodynamic size and PDI under storage conditions at 4 °C for up to 8 weeks[302], whereas an enhanced release has been observed under lysosomal-like conditions[172,174]. Thus, targeted PLGA NCs offer an interesting platform for the delivery of therapeutic enzymes for LSD treatment, particularly neuronopathic symptoms.

Although beneficial to drug release, lysosomal degradation of PLGA NCs is a confounding factor when studying intracellular trafficking. Therefore, other non-degradable polymers such as PS NCs, offering similar behaviour to PLGA NCs, have to be used as a model NCs to study trafficking[148,171,175,301]. For example, our group had used ICAM-1-tageted PLGA NCs and polystyrene NCs for the delivery of acid sphingomyelinase[170,171,175,187,301,302] (Niemann-Pick disease), α-galactosidase[174] (Fabry disease), and α-glucosidase[172] (Pompe disease). These ICAM-1-targeted NCs have been shown to enhance enzyme delivery using a plethora of cellular models *in vitro*, as well as peripheral organs and brain *in vivo* in mouse models[21,37-43].

As such, the aim of this chapter was to fabricate targeted NCs able to carry and deliver therapeutic enzyme for LSD treatment, particularly neuronopathic symptoms that requires BBB transcytosis, but also targeting to peripheric tissues which are also affected in LSDs[1,2]. NCs characteristics such as the selection of the receptor being targeted and the NC targeting valency were varied without affecting other physicochemical properties of NCs, and NC stability and therapeutic enzyme delivery were studied *in vitro* and *in vivo* in mice to test and verify transport

results mentioned above. Ultimately, NCs produced for this chapter served as a tool to study the remaining research questions of this thesis.

Note: Results obtained in this chapter have been partially published in an article where I have been a co-author (in bold): Muntimadugu E., Silva-Abreu M., Vives G., **Loeck M.**, Pham V., Del Moral M., Solomon M., Muro S. Comparison between Nanoparticle Encapsulation and Surface Loading for Lysosomal Enzyme Replacement Therapy. *Int. J. Mol. Sci.* **23**, 4034 (2022).

4.2. Results and Discussion

4.2.1. NC Preparation and Characterisation

To produce polymeric NCs, PLGA was chosen as a material due to its FDA approval for medical applications[126]. PLGA NCs with or without therapeutic enzyme were prepared using an emulsion-evaporation technique (see section 3.3.2.) and characterised by DLS (table 3.1). Pristine PLGA NCs showed a diameter of 147.6 nm, with a PDI of 0.09, and a ζ-potential of -34.7 mV. The diameter of NCs observed under SEM was in agreement with DLS data (figure 4.1). The size was in a suitable range for nanotherapeutic applications, the PDI below the desired threshold of 0.2 to prevent quick agglomeration, and the negative surface charge favourable for colloidal stability, comparable to NCs described elsewhere[148,171,175,301]. Therefore, these pristine PLGA NCs were considered suitable for further functionalisation.

For instance, these PLGA NCs were coated with protein via passive surface adsorption, a method also commonly applied in the preparation of ELISA plates, using established protocols[149,160,174,187,301,327]. Firstly, coating with a therapeutic enzyme, HAse, served to load the protein cargo onto the NC. HAse is deficient in mucopolysaccharidosis IX[328] and also serves as a model for enzymes that are deficient in LSDs, due to comparable molecular weight (MW = 55 kDa), isoelectric point (pI = 4.9), and activity peak at pH 4.5-6.0[329]. Secondly, coating with anti-ICAM-1 Ab was used to functionalise NCs for active targeting. For the functionalisation, the orientation of the Ab is paramount as only an exposed functional variable region will be able to interact with the receptor and hence lead to specific targeting. Such exposure due to “vertical”

orientation (Fc on the NC surface) of the coating Abs has been demonstrated for concentrations used in the present study[330]. Importantly, surface functionalisation via surface adsorption of Abs is a simple and valuable method to produce stable and functional NCs for proof-of-concept investigation[172,174,302], yet is not intended for translational development. NCs were coated with a 50:50 HAse:anti-ICAM-1 mass ratio as this was found to be the optimal ratio for protein delivery to the brain[170]. Sonication was used to form a more homogeneous solution after protein coating of NCs and was optimised to yield NC with a PDI < 0.2, suggesting relatively low levels of aggregation. To calibrate this process, Ab coated NCs were prepared and treated with variations of percent sonication amplification (amp) and number of pulses, followed by DLS measurement to determine NC PDI. Before sonication, Ab coated NCs showed a PDI of 0.98, representing a high degree of aggregation and therefore clearly indicating the need for sonication. A sonication amp of 20% with 6, 12, 25, and 50 pulses gave rise to NC formulations with PDIs of 0.25, 0.20, 0.14, 0.13, respectively. An amp of 25% with 12 pulses resulted in a NC formulation with a PDI of 0.18, and an amp of 75% with 12 pulses produced a NC formulation with a PDI of 0.12 (figure 4.2). Since PDI is a physicochemical parameter that does not provide any functional information about the Ab coat which might be affected by sonication, the least intense setting producing coated NCs with PDI ≤ 0.2 was chosen to minimise potential negative effects of sonication on NC coating.

Table 3.1 Characterisation of poly (lactic-co-glycolic acid) (PLGA) and polystyrene (PS) NCs.

Formulation		Diameter (nm)	PDI	ζ-potential	HAse molec./NC
Pristine	**PLGA NCs**	147.60 ± 4.48	0.09 ± 0.01	-34.70 ± 0.80	-
	PS NCs	114.00* ± 0.58	0.03* ± 0.00	-25.20* ± 0.84	-
Coated (50:50 mass ratio anti-ICAM-1:HAse)	**PLGA NCs**	172.13 ± 14.94	0.15 ± 0.01	-26.43 ± 3.14	291.60 ± 54.10
	PS NCs	191.50 ± 2.33	0.17 ± 0.01	-16.80 ± 2.46	338.89 ± 7.20
Encapsulating Hase + Coating anti-ICAM-1	**PLGA NCs**	236.10* ± 30.20	0.21* ± 0.02	-36.57* ± 1.46	538.00* ± 68.00

Pristine = no coating or cargo; PLGA = poly(lactic-co-glycolic acid); PS = polystyrene; PDI = polydispersity index; molec. = molecule; data are average ± SEM, statistics: *p<0.05 by Student's t-test, comparing PLGA NCs *vs* PS NCs of same group or PLGA NCs coated *vs* encapsulated, n ≥ 3.

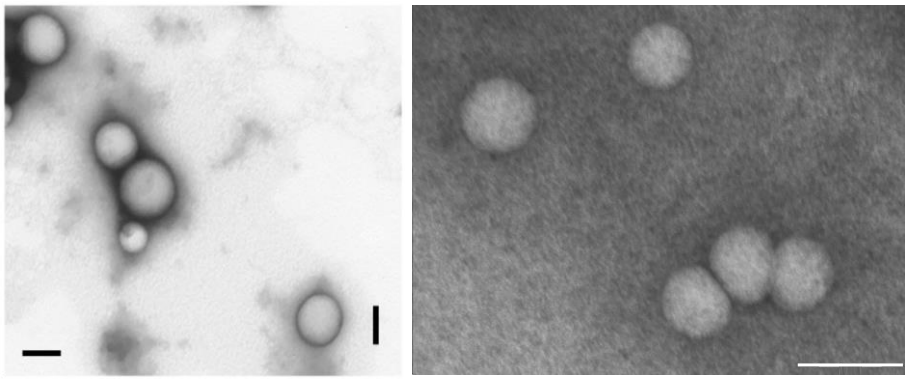

Figure 4.1 Electron microscopy of Ab coated NCs. (Left) Representative transmission electron microscopy images of Ab coated PLGA NCs counterstained with uranyl acetate. Scale bar = 100 µm. (Right) Representative transmission electron microscopy images of Ab coated PS NCs counterstained with uranyl acetate. Scale bar = 200 µm

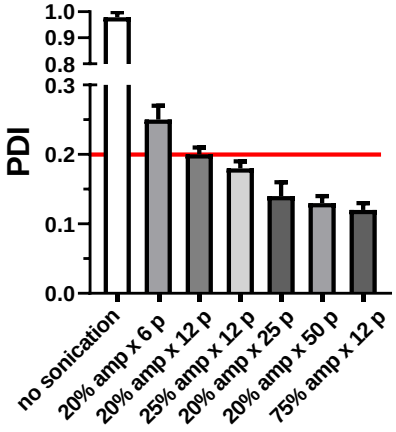

Figure 4.2 Effect of different sonication protocols on the PDI of Ab coated NCs. The protocol is defined by the amplification of the longitudinal vibration of the converter (%amp) multiplied by the number of pulses (p) (1 sec on, 1 sec off) applied. The red line marks the maximum of the desired PDI ≤ 0.2. Data are average ± SEM. n = 3.

After coating, PLGA NCs increased their diameter to 172.1 nm, the PDI to 0.15, and the ζ-potential to -26.4 mV (table 3.1). The increased size indicates the addition of a protein coat, the slight increase in PDI suggests an increase in population heterogeneity as a result of coating[331], whereas the more neutral surface charge can be explained by the addition of coating protein. Thus, all these parameters suggest the successful coating of PLGA NCs with protein, whereas the increase of all parameters is within the acceptable range for nanotherapeutic application[174,187,301,327]. Also, the negative ζ-potential is favourable for drug delivery since cationic NCs have been shown to induce cytotoxicity *in vitro* and *in vivo*, amongst other reasons due to inflicting membrane damage by electrostatic interactions[332–334].

Additionally, the coating with HAse was quantified using ^{125}I-HAse and radiotracing measurements and showed a loading capacity of 292 HAse molecules per NC (table 3.1), verifying successful coating. Additionally, PLGA NCs could be loaded by encapsulating HAse using a double emulsion-evaporation technique followed by coating with anti-ICAM-1 Ab alone, resulting in NCs with a diameter of 236.1 nm, a PDI of 0.21, a ζ-potential of -36.6 mV, and a loading capacity of 538 HAse molecules per NC (table 3.1). Thus, encapsulation significantly increased the enzyme loading capacity, in line with the significant increase in hydrodynamic size. These NCs were also coated with targeting Ab (anti-ICAM-1), rendering 122 Ab molecules/NC (not shown). Thus, this set of data shows that PLGA NCs can be produced and loaded with a therapeutic enzyme via two distinct loading methods.

Furthermore, given the well-known degradation of PLGA to lactic and glycolic acid in water and physiological fluids[324,325], non-degradable polystyrene (PS) NCs were used as a model NC for subsequent trafficking studies to avoid confounding results. Although statistically different before coating, PS NCs were comparable to PLGA NCs after coating with 50:50 anti-ICAM-1:HAse mass ratio, with a diameter of 191.5 nm, PDI to 0.17, and ζ-potential of -16.8 mV, and a loading capacity of 338.9 HAse molecules per NC (table 3.1). The size of Ab coated PS NCs was confirmed by electron microscopy (figure 4.1). Given these results and the fact that previous studies had confirmed that anti-ICAM-1 PLGA NCs and anti-ICAM-1 PS NCs behave similarly with regards to specific binding, endocytosis, and therapeutic effect of cargo *in vitro*, as well as biodistribution *in vivo* in mice[148,171,175,301], PS NCs were regarded a suitable model for PLGA NCs.

Additionally, NC properties such as size, surface charge, and targeting valency (the number of targeting molecules on the surface of a NC) are known to influence NC transport[149,335]. To be able to study the effect of targeting valency on the relatively uncharacterized CAM transcytosis, anti-ICAM-1 NCs with different valencies were prepared. Importantly, the total number of Ab molecules/NC was kept constant to not affect other surface properties which might impact NC transport. To achieve this, NCs were coated with different ratios of anti-ICAM-1 Ab and non-

specific IgG, keeping the total number of coating Abs constant. Three distinct targeting valencies (v1, v2, and v3; table 3.2) were prepared using an earlier optimised protocol[336,337]. NCs of all valencies showed comparable physicochemical properties, with size of 198.9 – 211.3 nm, PDI of 0.15 – 0.16, and a ζ-potential of -26.9 – -21.7 mV, with solely the number of targeting Abs on the surface varying: i.e., 45.5, 97.6, and 191.6 anti-ICAM-1 molecules/NC for v1, v2, and v3 formulations, respectively, as intended (table 3.2). Non-targeted NCs with a full IgG coat (v3) were prepared as control and showed comparable physicochemical properties to v3 anti-ICAM-1 NCs, as expected, since they had comparable Ab coating. This suggests comparable adsorption of both Abs (anti-ICAM-1 and IgG) to the NC surface (table 3.2). Thus, using this protocol the effect of targeting valency on the interaction (e.g.: binding, uptake, and intracellular trafficking) of anti-ICAM-1 PS NCs with brain ECs can be studied without the influence of other physicochemical properties.

Table 3.2 Characterisation of anti-ICAM-1 PS NCs with different targeting valencies.

Formulation	Targeting valency	Size	PDI	ζ-potential	Targeting Ab molec./NC
Anti-ICAM-1 NC	**v1**	198.89 ± 5.66	0.16 ± 0.02	-23.78 ± 3.02	45.48 ± 0.89
	v2	207.30 ± 4.37	0.16 ± 0.01	-21.68 ± 1.92	97.57 ± 6.83
	v3	211.25 ± 2.19	0.15 ± 0.00	-26.88 ± 2.69	191.61 ± 15.44
IgG NC	**v3**	199.50 ± 13.85	0.18 ± 0.02	-19.35 ± 0.35	200.22 ± 5.52

Ab = antibody; PDI = polydispersity index; molec. = molecule; v = valency; NC = nanocarrier; data are average ± SEM, n ≥ 4, statistics: *p<0.05 by Student's t-test, missing symbol indicates not significant result.

For the purpose of comparing the CAM-, clathrin-, and caveolae-mediated pathways (used in Chapter 6 and Chapter 7), v2 formulations coated with anti-TfR (clathrin) and anti-PV1 (caveolae) were produced using the same protocol (table 3.2). All v2 formulations showed comparable physicochemical properties independently from targeting, with size 180.2 – 207.3 nm, a PDI of 0.14 – 0.16, and ζ-potential of -20.6 – -23.8 mV (table 3.3), although size was statistically smaller for anti-PV1 NCs (table 3.3). However, given the comparable total number of approx. 90 targeting Abs per NCs this slight difference in size is irrelevant (table 3.3). Thus, using this protocol the

effect of distinct endocytosis pathways as well as the interaction (e.g.: binding, uptake, and intracellular trafficking) of NCs with brain ECs can be studied.

Table 3.3 Characterisation of PS NCs targeted to the three main endocytosis pathways.

Formulations	Size	PDI	ζ-potential	Targeting Ab mol./NC
Anti-ICAM-1 NCs (v2)	207.30 ± 4.37	0.16 ± 0.01	-21.68 ± 1.92	97.57 ± 6.83
Anti-TfR NCs (v2)	195.78 ± 4.44	0.15 ± 0.01	-20.57 ± 2.72	81.69 ± 3.15
Anti-PV1 NCs (v2)	180.22 ± 3.06	0.14 ± 0.01	-23.83 ± 2.07	85.56 ± 6.78

Ab = antibody; PDI = polydispersity index; mol. = molecule; v = valency; NC = nanocarrier; data are average ± SEM, n ≥ 9, statistics: *p<0.05 by Student's t-test, missing symbol indicates not significant result.

In conclusion, I was able to produce PLGA NCs as drug carriers for therapeutic enzymes. Furthermore, undegradable PS NCs were found to be similar to PLGA NCs with regards to physicochemical properties, Ab coating, and drug loading, and can therefore be used as a model for transport and biodistribution studies without confounding degradation. Lastly, surface modifications such as targeting valency and receptor-targeting were varied without affecting the overall physicochemical properties of the NCs, enabling the study of the specific effect of these modifications on the NC-cell interactions.

4.2.2. NC Stability

NCs stability is an important parameter not only for the translation into the clinic with regards to shelf-life, the time a formulation can be stored after preparation, but also to be able to properly work with the formulations experimentally. For instance, a good stability at storage conditions ensures the quality of NCs formulations throughout the waiting period between NC preparation and the beginning of the experiment, either in-house or when shipped to collaborators, as well as the possibility for long-term storage and multiple testing from the same batch. Stability at experimental conditions is important to gain insight into the state of the NCs when they interact with cells. This effect of experimental conditions on NC stability is an often-overlooked parameter and can have a great impact on NC performance such as impaired targeting through loss of targeting moieties or corona formation[338,339].

Different surface functionalisation and drug loading of PLGA NCs and PS NCs have been shown to yield targeted NCs with comparable physicochemical properties able to load a therapeutic enzyme (see Section 1.2.1). PLGA NCs have been shown to degrade to lactic and glycolic acid in physiological millieu[324,325], thus disappearing and impeding tracing, which makes PS NCs the preferred choice for subsequent transport studies due to their non-degradable nature. Therefore, to ensure the good quality for experimental work, the stability of targeted PS NCs was assessed under different, relevant conditions.

First, the stability of the anti-ICAM PS NCs was tested under storage conditions, at 4 °C in PBS containing 1% BSA, used to improve colloidal stability. At indicated time points, the hydrodynamic size and PDI were analysed by DLS. The size remained stable with only minor changes with an increase from 209.0 nm at day 0 to 216.7 nm at day 21 of storage (figure 4.3A), while the PDI increased slightly but constantly from 0.17 at day 0 to 0.23 at day 21 of storage (figure 4.3B). The colloidal stability of anti-ICAM PS NCs is in accord with results in the literature that found a relative coat stability at 4 °C for up to 72 h[172,174] and an acceptable stability with regards to hydrodynamic size and PDI at 4 °C up to 8 weeks[302] for comparable formulations.

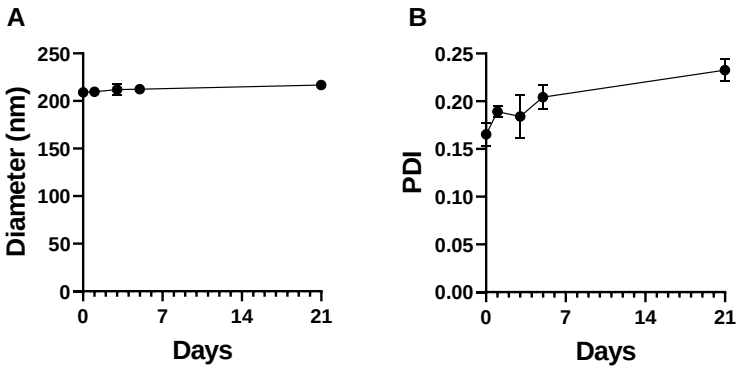

Figure 4.3 Anti-ICAM-1 PS NC (v3) stability in PBS containing 1% BSA at 4 °C. Coated NCs (v3) were stored in PBS (pH 7.4) containing 1% BSA at 4 °C for up to 21 days. At indicated time points their physicochemical properties were determined by DLS, for instance (A) size and (B) PDI. Data are average ± SEM. Some error bars are hidden by symbols.

Thus, it could be confirmed that coated NCs used in the present work do not quickly aggregate. Furthermore, although still within an acceptable range at 21 days after NC preparation, PDI values continuously increased during 21 days at 4 °C, surpassing the set limit of PDI≤0.2 at day 7, suggesting slow aggregation. Thus, experimental performance of the formulation might be compromised at some point which was sought to be improved using lyophilisation.

Lyophilisation, the extraction of water from a frozen sample under vacuum, is a common method to improve the stability of colloidal NCs[340]. Anti-ICAM-1:HAse NCs were lyophilised with trehalose as a stabiliser, whose high glass transition temperature has been shown to avoid irreversible aggregation of NCs during lyophilisation[341] and to give structural protection to proteins via hydrogen bonds[342,343]. Lyophilised formulations were stored at -20 °C, resuspended with the sample's original volume (pre-lyophilisation), and then (a) analysed by DLS to assess the effect of lyophilisation on physicochemical properties and (b) incubated with brain ECs to study binding and uptake to assess the effect of lyophilisation on the functional properties of the NCs with a relevant target cell. To this end, green-fluorescent anti-ICAM-1 NCs were incubated before and after lyophilisation with brain ECs for 1 h and then cell-surface NCs were counterstained in red to be able to distinguish between extracellular NCs (green + red = yellow) and intracellular NCs

A

NC parameters	% of pre-lyophilisation
Diameter	98.41% ± 0.04
PDI	102.78% ± 0.08
ζ-pot.	98.99% ± 0.12
Ab molec./NC	91.41% ± 0.08

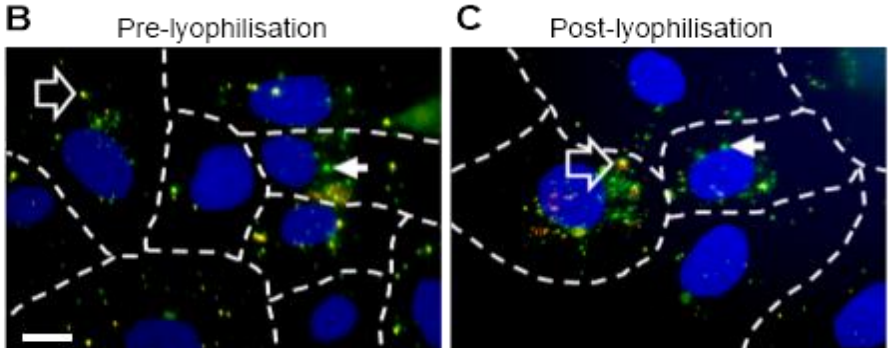

Figure 4.4 Comparison of pre- and post-lyophilisation of anti-ICAM-1 NCs. Anti-ICAM-1 PS NCs in PBS containing 1% BSA and 2.5% trehalose were lyophilised, stored at -20 °C, and resuspended in deionised water matching volumes prior to lyophilisation. (A) Comparison of indicated characteristics of anti-ICAM-1 PS NCs post-lyophilisation as percent of pre-lyophilisation values, statistics: Student's t-test, *p<0.05, non-significant results lack symbol. (B-C) Representative confocal microscopy pictures of a binding and uptake experiment with (B) NCs pre-lyophilisation (C) and NCs post-lyophilisation. (B-C) Brain ECs were grown to confluency on coverslips and treated with 10 ng/mL TNFα (20 h treatment). Cells were incubated with FITC-labelled (green fluorescent) anti-ICAM-1 NCs (pre- or post-lyophilisation) for a 30-min binding pulse, washed to remove non-bound NCs, further incubated in NC-free medium up to 1 h, fixed, and counterstained with red secondary Ab to distinguish between intracellular NCs (green only, arrows) and cell-bound NCs (green + red = yellow, open arrows). Blue = nuclei, scale bar = 10 µm.

(green only) (see section 3.3.23.; figure 4.4). Lyophilisation of anti-ICAM-1 NCs did not significantly affect their hydrodynamic size, PDI, and ζ-potential, nor the number of targeting moieties displayed on the surface of each NC (figure 4.4A), in line with similar results for binding and uptake of anti-ICAM-1 NCs pre-lyophilisation *vs.* post-lyophilisation (figure 4.4B-C). Thus,

lyophilisation poses a suitable technique to enable NC shipment and long-term storage at -20 °C as no negative effect on relevant NC properties were observed.

Another important parameter is the stability at more physiological conditions such as in complete cell medium supplemented with serum. The presence of serum in the medium where the interaction of NCs and cells take place, containing more than 1000 components including lipids and protein, might affect Ab coated NCs, for instance, through the formation of a protein corona blocking the targeting moieties, resulting in decreased targeting or NC aggregation. Thus, assessing physicochemical properties of a NC formulation in the storage buffer does not necessarily reflect the physicochemical properties of the same NC in complete cell medium and, thus, during the interaction with cells. Therefore, the colloidal stability of anti-ICAM-1 NCs was assessed in complete cell medium. To this end, anti-ICAM-1 NCs were first characterised by DLS in storage condition, then added to complete medium, incubated for 5 h to allow for interaction between NCs and medium constituents, and characterised again by DLS (figure 4.5).

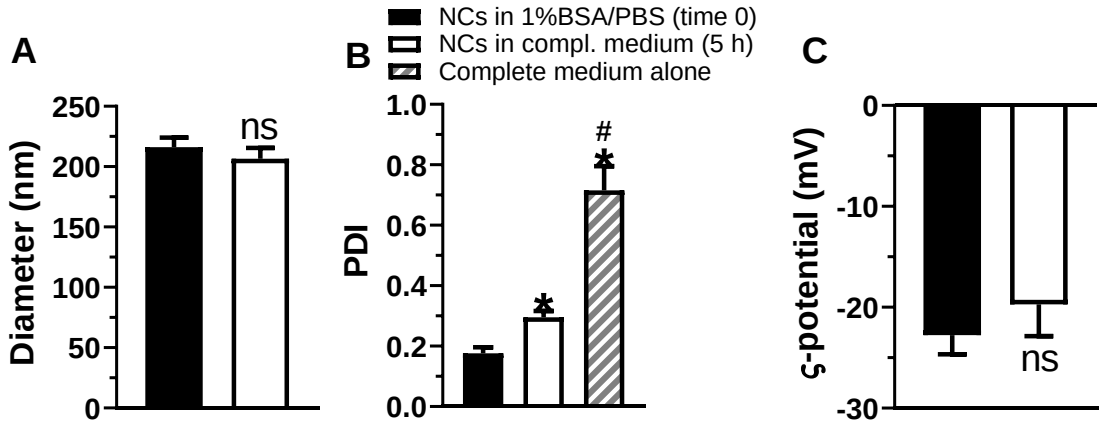

Figure 4.5 NC stability in complete cell medium. (A) Hydrodynamic size, (B) PDI, and (C) ζ-potential of anti-ICAM-1 PS NCs (v3) were assessed by DLS first in PBS containing 1% BSA, and then after 5 h incubation in complete cell medium containing 10% FBS. (B) Additionally, the PDI of complete cell medium containing 10% FBS was assessed by DLS. Data are average ± SEM, n ≥ 3, *compared to NCs in 1%BSA/PBS (TIME 0), #compared to NCs in complete medium (5 h), by Student´s t-test ($p<0.05$), n.s. = not significant.

The incubation in complete medium did not significantly affect particle size or ζ-potential, whereas the PDI of the formulation was significantly increased from 0.18 to 0.3 (figure 4.5). The unchanged size and ζ-potential of anti-ICAM-1 NCs after 5 h incubation in complete cell medium suggests that the serum constituents do not greatly interact with anti-ICAM-1 NCs. The loss of weakly attached coat proteins due to time or increased interaction with serum proteins is possible. For instance, the loss of approx. 7% of the coated protein of comparable NCs after 5 h in complete medium at 37 °C has been reported[174]. Nevertheless, the loss refers to loss of initially used coating protein and does not specify whether the total number of coating proteins decreases or whether the initially used coating proteins are removed and substituted by other molecules such as serum proteins, thus not reducing the overall size of the coat. Independently of the loss or exchange of coating protein, the reported minimal effect of complete medium on the coat, maintaining 93% of the original coating proteins after 5 h[174], is in line with the unaffected size and ζ-potential (figure 4.5). Given these results, it is unlikely that the increased PDI originates from changes to the NCs. Alternatively, the PDI of complete cell medium alone was assessed by DLS and found to be 0.72 (figure 4.5B), likely the result of differently sized populations such as amino acids, lipids, and proteins in complete medium. Thus, the presence of such diverse populations of molecules in complete medium is likely the reason for the observed increased PDI of the NC formulation, without actually interacting with the NCs. These results should be corroborated with further radiotracing measurements to better assess the state of the Ab coating rather than rely on physicochemical properties alone.

Given the favourable physicochemical properties of anti-ICAM-1 NCs in complete medium after 5 h, taking into account that the longest *in vitro* incubation of NCs in complete medium in the present study is 1 h and given the quick disappearance of anti-ICAM-1 NCs from the general circulations after less than 5 min (figure 4.7A), the stability of Ab coated NCs was considered to be good under experimental conditions.

4.2.3. Intracellular delivery of a therapeutic enzyme using anti-ICAM-1 NCs

Thus far, PLGA and PS NCs could be successfully prepared, loaded with a therapeutic enzyme, and targeted to markers of different endocytosis pathways. Furthermore, targeted NCs showed good stability at storage and experimental conditions, enabling their use for further experimentation. The suitability of the NCs prepared in this study, targeted PLGA NCs and targeted PS NCs, to deliver a therapeutic enzyme to a relevant target cell was assessed as a proof-of-concept using ICAM-1 as a target. To this end, the delivery of ^{125}I-HAse to brain ECs by anti-ICAM-1 PLGA NCs loaded via two distinct techniques (encapsulation or coating) and anti-ICAM-1 PS NCs (coating) (table 3.1) was assessed by radiotracing and compared to the delivery of free ^{125}I-HAse (figure 4.6).

Brain ECs were activated with TNFα to simulate ICAM-1 expression in disease situations and then incubated with equal amounts of radiolabelled HAse carrier by anti-ICAM-1 PLGA NCs either by encapsulation or coating, on anti-ICAM-1 PS NCs coated with HAse, or free enzyme. Following 1, 3, or 24 h of incubation, the cell-bound and internalised fraction of HAse were separated by acide glycine elution[344] and quantified using a gamma counter. HAse was delivered in significantly higher amounts to brain ECs when carrier by any of the NC formulations compared to free enzyme, with only little if any differences in the cell-bound fractions (figure 4.6A-D). This is in line with reports in the literature using comparable NCs *in vitro* and *in vivo*[171,172,174,187,302] and can be attributed to the specific effects of ICAM-1-targeting, such as receptor targeting and receptor-mediated endocytosis. Furthermore, significantly more HAse was delivered to cells when encapsulating the enzyme compared to coating it onto PLGA NCs. For instance, PLGA encapsulating HAse delivered 5.6 x 10^{11}, 7.0 x 10^{11}, and 7.5 x 10^{11} HAse molecules per well at 1, 3, and 24 h, respectively (figure 4.6A), whereas PLGA NCs coated with HAse delivered 1.3 x 10^{11}, 1.2 x 10^{11}, and 1.8 x 10^{11} HAse molecules per well at respective times (figure 4.6B).

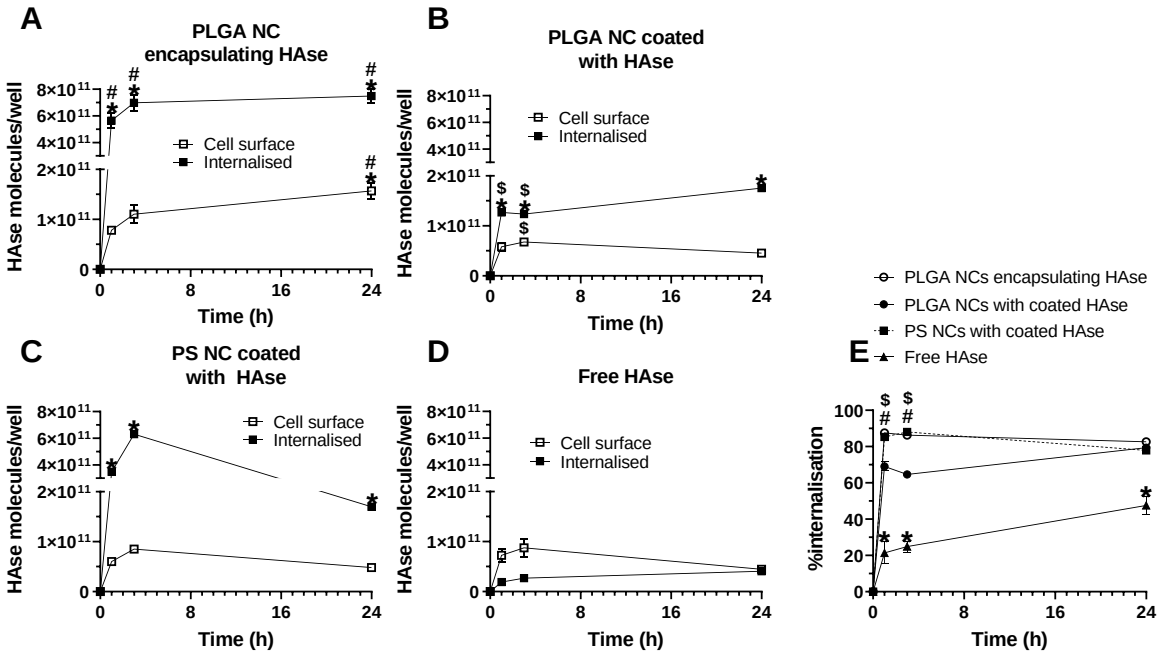

Figure 4.6 Delivery of a therapeutic enzyme to brain ECs using different NC formulations. Brain ECs were grown to confluency on coverslips and treated with 10 ng/mL TNFα (20 h treatment). Then, cells were incubated up to 24 h with 2.25 µg/mL ^{125}I-labelled HAse carried by indicated preparations targeted to ICAM-1. At indicated time points, cells were washed to remove non-bound HAse, incubated with pH 2.5 glycine elution buffer to collect cell-bound HAse, and lysed with Triton X-100 to collect internalised HAse. The amount of ^{125}I-labelled HAse in each fraction was quantified using a gamma counter. (A) PLGA NC with encapsulated HAse, coated with anti-ICAM-1, (B) PLGA NCs coated with 50:50 HAse:anti-ICAM-1 mass ratio, (C) PS NC coated with 50:50 HAse:anti-ICAM-1 mass ratio, (D) Free = HAse without NC. (E) Percent internalisation of all HAse that interacted with cells. Data are average ± SEM. Non-visible error bars are hidden behind the data sign. Statistics: Student's t-test, $p<0.05$, *data point was compared to free HAse, #compared PLGA NCs coated with HAse to PLGA NC with encapsulated HAse, $ PLGA NCs coated with HAse to PS NC coated with HAse. n = 4.

The observed differences in HAse delivery when either encapsulated into or coated onto anti-ICAM-1 PLGA NCs might be explained by several distinct properties of both formulations. Firstly, the enzyme loading capacities of both formulations are different, with 538 and 292 HAse molecules per NC, respectively (table 3.1). Thus, equal binding and uptake of both NCs would result in a higher cargo delivery with the encapsulating NCs. Secondly, encapsulating formulations have a full anti-ICAM-1 coat (valency v3) as compared to the 50:50 mass ratio coating with anti-ICAM-1 and HAse of the coated formulation (valency v2). Although the co-presence of enzyme together with targeting Abs on the NC coat was not expected to greatly interfere with binding and uptake, as described[174,301], it reduces the targeting valency which has

a direct impact on binding and uptake[170]. Hence, the higher valency of encapsulating anti-ICAM-1 PLGA NCs might further favour the enzyme delivery.

Furthermore, significantly more HAse was delivered to cells when coated onto PS NCs compared to PLGA NCs at 1 h and 3 h with 3.5 x 10^{11} and 6.3 x 10^{11} (figure 4.6C), and 1.3 x 10^{11} and 1.2 x 10^{11} (figure 4.6B) HAse molecules per well, respectively, whereas the total delivery after 24 h is comparable between both formulations, around 1.8 x 10^{11} HAse molecules per well. Interestingly, HAse delivery with PS NCs showed an initial steep increase up to 3 h, followed by a decrease up to 24 h (figure 4.6C), whereas PLGA NCs show a steep but comparatively lower increase up to 1 h, followed by a moderate increase up to 24 h (figure 4.6B). The observed differences regarding enzyme delivery by anti-ICAM-1 PS NCs *vs.* anti-ICAM-1 PLGA NCs might result from the difference in degradability of both materials. PLGA NCs can be degraded[324,325], thereby releasing its cargo before reaching intracellular compartments or into the lumen of endosomes and lysosome, and making it more accessible for intracellular cargo degradation. In contrast, polystyrene NCs cannot be degraded, and thus likely releases its cargo by gradual detachment from the NC surface comparatively slower than PLGA NCs. Speculatively, this means that when HAse is delivered to lysosomes on PLGA NCs, a balance between enzyme influx and enzyme degradation may establish quickly, whereas in the case of PS NCs the initial influx might be quicker than the degradation of the enzyme, resulting in a peak delivery at early time points. Furthermore, whereas PLGA NCs can be degraded, PS NCs slowly accumulate in lysosomes over 24 h, likely saturating this compartment, with unknown consequences for NC binding, uptake, and lysosomal delivery, probably partly explaining the decreased enzyme delivery after 24 h. Lastly, although not significantly different, a tendency for higher enzyme loading of PS NCs compared to PLGA NCs might also play a role in the higher HAse delivery with anti-ICAM-1 PS NCs compared to anti-ICAM-1 PLGA NCs (table 3.1). Nevertheless, despite the observed differences, both formulations showed successful enzyme delivery to brain EC superior to free enzyme, supporting the viability of PS NCs as a model for PLGA NCs.

This experiment was designed to verify the use of the prepared targeted NCs for the trafficking of a therapeutic enzyme, HAse. In conclusion, the delivery of HAse was significantly higher when delivered on NC formulations compared to free enzyme. Although showing distinct enzyme

delivery patterns likely due to their distinct material characteristics, undegradable PS NCs can be regarded a useful model for PLGA NCs.

4.2.4. Anti-ICAM-1 NC biodistribution and brain targeting in mice in vivo

After having verified the suitability of anti-ICAM-1 NCs to deliver therapeutic enzyme to brain ECs *in vitro*, NC biodistribution was assessed in a more relevant *in vivo* mouse model, to study their general behaviour and the possibility of using these NCs for the delivery of therapeutic enzyme across the BBB, for future treatment of neuronopathic symptoms in LSDs.

ICAM-1 targeting was chosen as a relevant proof-of-concept in line with *in vitro* experiments shown above and because it is upregulated during the neuroinflammation that associates with LSDs[345]. All animal experiments were approved and done under regulatory compliance (see Appendix, Ethical & Regulatory Compliances). Thus, using PS NCs to avoid confounding results from degradation, we examined the biodistribution of ^{125}I-labelled anti-ICAM-1 NCs after i.v. injection in mice. Anti-ICAM NCs and control NCs were both labelled with ^{125}I-IgG for radiotracing experiments to preclude confounding results in the case of Ab detachment from the NCs. This is because if ^{125}I-IgG detached from the NCs it would behave as free ^{125}I-IgG alone and no differences could be observed between both NC formulations. Over the period of 1 h blood samples were taken at indicated time points to assess NC circulation and organs were harvested after sacrifice at 1 h to quantify NC content. Firstly, the BBB function in an inflammation mouse model was assessed by measuring albumin leakage into the brain and was found to be increased 1.7-fold over control condition (figure 4.7). Therefore, untreated mice were used to not confound the results of the brain penetration of anti-ICAM-1 NCs.

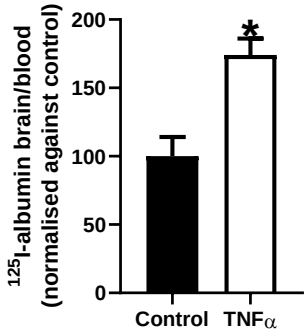

Figure 4.7 *In vivo* albumin brain leakage. Commercial C57BL/6J mice were anaesthetised and injected with ^{125}I-albumin alone (control), or ^{125}I-albumin and TNFα. At 1 h, mice were sacrificed, blood and brain were collected, and ^{125}I-albumin quantified using a gamma counter. The leakage of albumin into the brain was calculated as the ratio of albumin in brain to blood, normalised to control. Data are average ± SEM. Statistics: Student's t-test, *p<0.05. Figure adapted from Manthe et al. (2020)[170].

In untreated mice, anti-ICAM-1 NCs and control IgG NCs disappeared from the general circulation very quickly, yet anti-ICAM-1 NCs disappeared quicker than IgG NC with half-times of 18 sec *vs.* 48 sec, respectively, with both formulations equally plateauing at 7.5% ID after 10 min (figure 4.8A). The quick disappearance of both NC formulations is in line with previous finding[172,175] and likely the result of fast clearance of NCs based on sheer size mostly by liver-resident Kupffer cells and also spleen macrophages[346,347], also explaining the comparable plateau levels for both formulations (figure 4.8A). However, the quicker disappearance of anti-ICAM-1 NCs was likely the result of their specific binding of anti- to ICAM-1-positive tissue. The organ accumulation at 1 h was normalised to the relative amount of NCs in circulation ((%ID/g tissue)/(%ID/g circulation)), a parameter called localisation ratio (LR), to assess the tissue-to-blood distribution. Brain, heart, and kidney showed relatively low LR of 0.12, 0.4, 0.77, respectively, while liver, spleen, and the lungs showed a higher LR of 5.00, 11.51, and 12.21, respectively (figure 4.8B). The relatively high LRs of liver and spleen can be explained by the predominant clearance of nano-sized materials by these organs. Furthermore, the relatively high LR of the lungs is in line with earlier findings and was expected because of (a) the big surface area of the lung, containing 20-30% of the body's endothelium and highly expressed ICAM-1[172,174,175], (b) lungs receiving the undivided cardiac output, and (c) the lungs having a first pass effect regarding i.v. injected NCs. The low LR of the brain highlights the difficulty of targeting this organ (figure 4.8B). Furthermore, to assess the specific targeting the LR of anti-ICAM-1 PS NCs was normalised to the LR of IgG PS NCs, a parameter called specificity index (SI) which reflects improvement modified by targeting. The SI showed enhanced delivery compared to IgG NCs. This increase was comparable for brain, heart, kidney, liver, and spleen with 1.53, 1.39, 1.69, 1.35, and 1.38 SI, respectively. Furthermore, ICAM-

1-mediated targeting to the lungs proved to be especially specific with an SI of 12.81, highlighting the potential of anti-ICAM-1 NCs for therapeutic targeting of this organ (figure 4.8C). Thus, although moderate, the targeting of anti-ICAM-1 NCs to the brain was specific despite this being a non-disease model, thus only exhibiting baseline ICAM-1 expression. Since ICAM-1 expression associates with inflammation[68-70], higher brain delivery can be expected in disease conditions associating with neuroinflammation such as Parkinson's disease or LSDs[345,348]. Additionally, an upregulated expression of ICAM-1 also allows for extravasation of white blood cells (see section 1.4) which have been reported to be able to scavenger lung endothelium-bound anti-ICAM-1 NCs and deliver them to the brain parenchyma *via* the general circulation, further increasing brain delivery[72]. Hence, this holds potential as an approach to deliver therapeutic enzyme for ERT to treat neuronopathic symptoms of LSD.

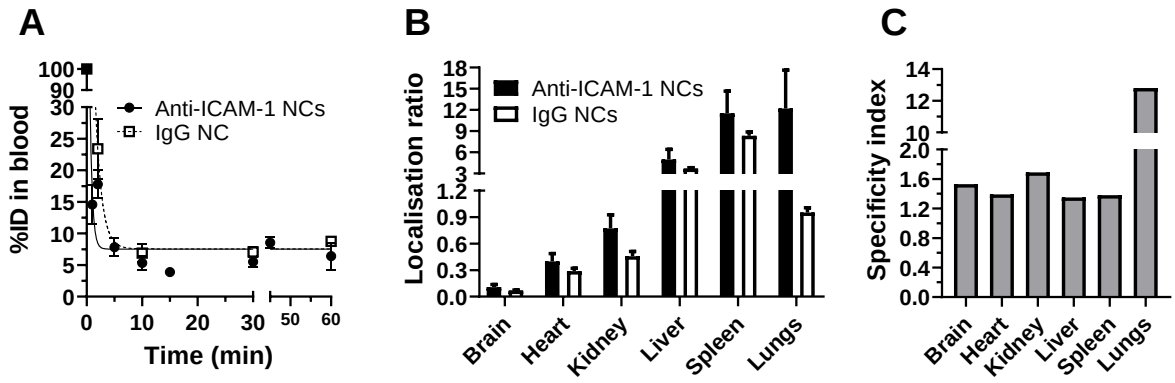

Figure 4.8 Biodistribution of anti-ICAM-1 PS NCs in mice. Commercial C57BL/6J mice were anaesthetised and i.v. injected with anti-ICAM-1/^{125}I-IgG PS NCs (v2) or ^{125}I-IgG PS NCs. At indicated time points, blood samples were taken. After 60 min, mice were sacrificed, and organs were collected. The level of ^{125}I in each sample was quantified using a gamma counter. (A) Percent of injected dose (%ID) in blood. (B) Localisation ratio (LR) of anti-ICAM-1 NCs in different organs to compare the tissue-to-blood distribution. (C) Specificity index comparing the LR of anti-ICAM-1 NCs to IgG NCs to show specific targeting. Data are average ± SEM. Non-visible error bars are hidden behind the data sign.

Then, for a better understanding of the biodistribution of the anti-ICAM-1 NCs, this was assessed at 0.5, 1, and 3 h. The rather short time period was chosen because here I aimed to assess the behaviour of the NC, not the therapeutic enzyme, up to the point of drug delivery. Given the very low half-life of anti-ICAM-1 NCs of only seconds in the circulation (figure 4.8A) and the possible

degradation of the ^{125}I-tracer protein used for analysis, longer time periods might be more irrelevant to assess biodistribution by this method.

The lungs showed a significant reduction of the LR from 59.3 to 12.2 (79%) from 0.5 h to 1 h, whereas no significant change was seen for any other organ at that time (figure 4.9A). However, there was a significant reduction of the LR of liver and spleen from 5.0 to 1.5 (70%) and 11.1 to 4.6 (59%) from 0.5 h to 3 h, respectively, whereas the LR of the lungs did not decrease further compared to 1 h (figure 4.9A). The relatively high LR of liver and spleen are in line with the clearance function of NC in these organs[346,347]. NC degradation by macrophages in liver and spleen further explain the reduction of the LR after 3 h. In contrast, the high LR of the lungs results from the extensive binding of anti-ICAM-1 NCs to the lung endothelium, as discussed before. The fast LR reduction in this organ may be due to fast endocytosis by lung endothelial cells[171], which may result in intracellular degradation of the tracer. In addition, a recent work has shown that anti-ICAM NCs can be picked up by circulating leukocytes and be transported from the lung to the brain[72]. To gain a better understanding of the degradation of anti-ICAM-1 NCs, the levels of free iodine were assessed using an established method that uses TCA to precipitate proteins and separate free ^{125}I[73] that may result from degradation (see methods). The reduction of free iodine levels over time in most organs indicates the clearance of ^{125}I from the general circulation by glomerular filtration and excretion in the urine[349], in line with constant relatively high levels in the kidneys (figure 4.9C). Free iodine was initially highest in the liver with 115.4% of background free iodine at 0.5 h and significantly less with 44.0% at 3 h (figure 4.9B). The overall high levels of free iodine in the liver are in line with its clearance function[347] and sheer size of the organ. In comparison, the spleen, the other major organ involved in NC clearance[346], showed lower levels of free iodine, comparable at all time points with only a slight tendency for reduction with 13.0% at 0.5 h and 8% at 3 h (figure 4.9B), likely the result of the comparably small size of the organ. The lungs contained 32.7% of background free iodine at 30 min and significantly less with 13.6% of background free iodine at 1 h and 15.4% of background free iodine at 3 h (figure 4.9B), in line with the quick removal of NCs from that organ. Interestingly, there was no decrease observed in the brain at any time point (figure 4.9A), which might be the result of NC influx from the lungs as

well as tracer degradation in this organ. In line with this, the brain showed comparable free iodine levels at all time points with 1.4% at 0.5 h and 1.7% at 3 h (figure 4.9B).

To further gain insight into the trafficking of NCs into the brain, the transcytosis of fluorescent anti-ICAM-1 NCs *in vivo* in mouse cortical brain capillaries was also visualised post-mortem using confocal microscopy. While non-targeted IgG NCs did not show any significant binding, as expected, anti-ICAM-1 NCs showed abundant attachment to the brain endothelium 30 min after injection, a time also used to allow for binding in cellular models in the present work (figure 4.10A). Microscopy pictures give the idea of three distinct locations of cell-associated NCs; on the surface of ECs (arrows), in perinuclear ring-like structures which might be transcytosing or lysosomal NCs (closed arrowheads), and basolateral-like location (open arrowheads), yet no visible NCs were observed beyond blood vessels. Penetration into the brain parenchyma is a relevant property for a more successful delivery of therapeutic enzyme to brain cells such as neurons which can subsequently endocytose NCs. Nevertheless, brain penetration has been seen to be incomplete likely due to insufficient detachment of NCs following transcytosis[350].However, visible penetration of anti-ICAM-1 NCs into the brain parenchyma was detected 3 h after injection (figure 4.10A). To verify that the observed crossing of the BBB was not the result of paracellular leakage, 66.5 kDa ^{125}I-albumin was co-injected with anti-ICAM-1 NCs and remained in circulation similar to albumin injected alone, suggesting that anti-ICAM-1 NCs do not impair BBB function, unlike TNFα tested in figure 4.7, and that anti-ICAM-1 NCs cross the BBB by transcytosis (figure 4.10B).

These results show that anti-ICAM-1 NCs interact specifically with mouse endothelium and disappear quickly from the general circulation following i.v. injection. Furthermore, the delivery of NCs to all organs improves through ICAM-1 targeting, with a relevant and high increase for lung targeting, but also brain targeting, although to a limited extent in the control (not diseased) mouse model. Nevertheless, disease is expected to increase brain targeting[72]. Lastly, anti-ICAM-1 NCs were shown to penetrate into the brain parenchyma at 3 h, relevant for successful drug delivery to brain cells such as neurons, without compromising BBB function. Furthermore, intracarotid injection of targeted NCs might further increase the targeting to the brain[351]. Thus,

using receptor-targeted NC to deliver therapeutic enzyme across the BBB is a promising strategy for the treatment of neuronopathic symptoms of LSDs.

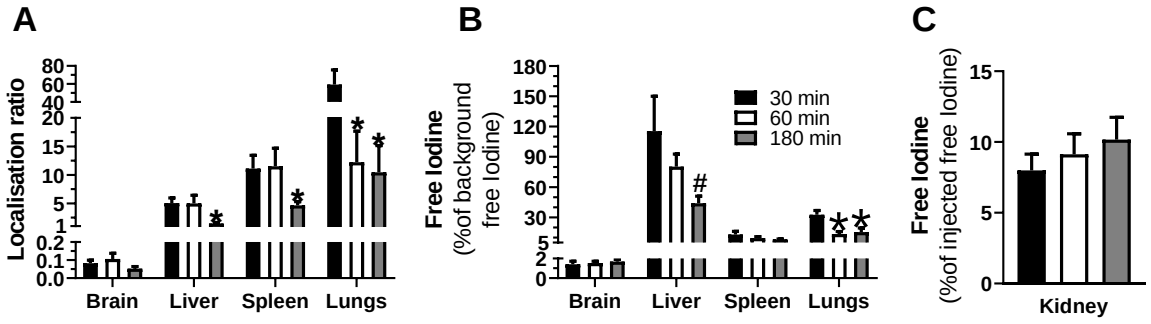

Figure 4.9 Biodistribution of anti-ICAM-1 PS NCs at different time points. Commercial C57BL/6J mice were anaesthetised and injected i.v. with anti-ICAM-1/^{125}I-IgG NCs. At indicated time points, mice were sacrificed, and organs were collected. The amount of ^{125}I-NCs in each sample was quantified using a gamma counter. (A) Localisation ratio of anti-ICAM-1 NCs in different organs to compare the tissue-to-blood distribution. (B, C) Free iodine as percent of injected free iodine. Data are average ± SEM. Statistics: Student's t-test, $p<0.05$, *compared data point to 30 min, #compared data point to 60 min.

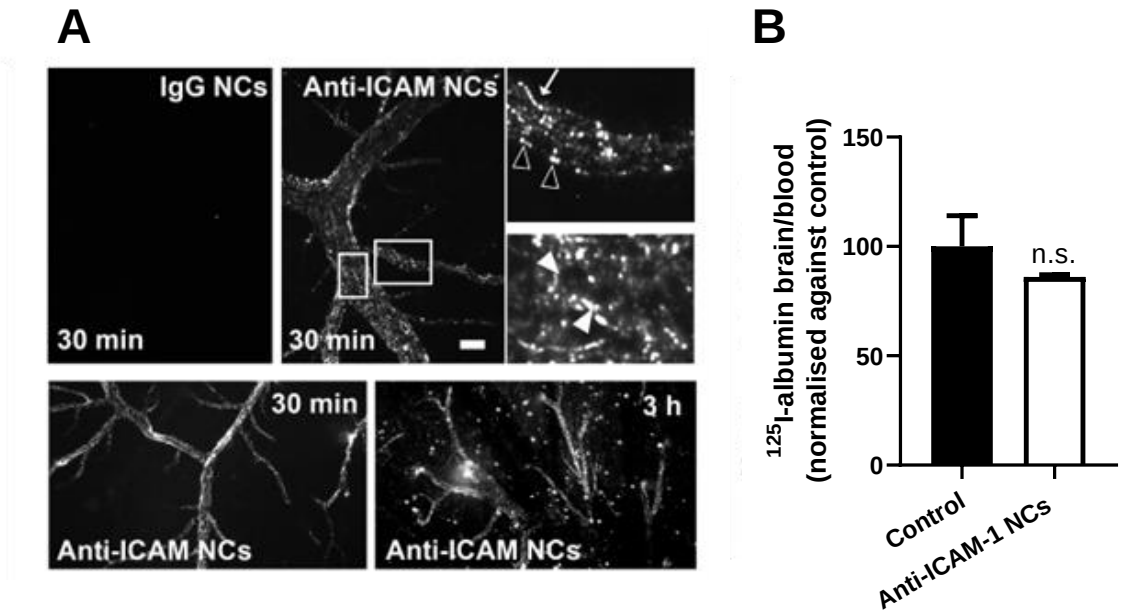

Figure 4.10 Transcytosis of anti-ICAM-1 NCs by brain endothelium in mice. (A) Mice were anaesthetised and injected i.v. with FITC-labelled anti-ICAM-1 NCs or FITC-labelled IgG NCs (v3). At indicated time points, mice were

subjected to intracardial perfusion first with PBS to eliminate blood and then with paraformaldehyde to fix tissue. The brain was collected and imaged *ex vivo* by fluorescence microscopy. Scale bar = 10 µm. Boxes = regions magnified 3x in right panels. Arrows = NCs on apical surface of ECs, closed arrowheads = intracellular NCs, open arrowheads = NCs on basolateral surface of ECs. (B) Mice were anaesthetised and injected with ^{125}I-albumin alone (control or ^{125}I-labelled albumin and anti-ICAM-1 NCs. At 1 h, blood and brain were collected, and ^{125}I-albumin quantified using a gamma counter. The leakage of albumin into the brain was calculated as the ratio of albumin in brain to blood, normalised to control. Data are average ± SEM. Statistics: Student's t-test, *p<0.05, n.s. = not significant. Figure adapted from Manthe et al. (2020)[170].

4.3. Conclusion

Enzymes have gained increasing attention as therapeutic drugs in recent years, yet their applications are limited by protein characteristics such as size, charge, and stability, impeding e.g., their penetration across the BBB into the brain, such as in the case of ERT for LSD[1,7]. NCs offer a versatile and promising platform for the delivery of therapeutic enzymes that might help overcome such limitations[13,15]. In this chapter, I aimed to prepare targeted polymeric NCs capable of loading and delivering therapeutic enzyme into and across brain ECs. I was able to prepare targeted NCs capable of loading therapeutic enzyme made from clinically relevant PLGA or non-degradable PS as a model for transport studies. I modified targeting valency and I also produced NCs targeted to markers of different endocytic routes, ICAM-1 (CAM-mediated endocytosis), TfR (clathrin-mediated endocytosis), or PV1 (caveolae-mediated endocytosis), without affecting the overall physicochemical properties. Moreover, NC physicochemical properties were not negatively affected either under storage conditions or physiological-like conditions during times experimentally relevant. Furthermore, ICAM-1 targeted NCs, used as a relevant model, were shown to be able to deliver therapeutic enzyme to brain ECs *in vitro* and also reach the brain *in vivo* in a mouse model. Thus, polymeric NCs targeted to receptor-mediated transport mechanisms pose a promising vehicle for the delivery of therapeutic enzyme across and into the BBB for ERT to treat neuronopathic symptoms of LSDs.

Chapter 5: Study the Mechanism of CAM-mediated Transcytosis of NCs

5.1. Introduction

The lack of fenestration of and highly selective transport across the BBB are a formidable challenge for the treatment of diseases affecting the CNS (see section 1.1.). NCs offer a promising platform to overcome this hurdle by exploiting natural transport mechanisms across the BBB into the CNS[64,293,313]. One of these transport routes is transcytosis, a naturally occurring mechanism where cargo is transported between the blood and the tissue side in membranous vesicles that cross barrier cells[352]. Transcytosis can be induced by targeting receptors associated with the clathrin-, caveolae-, or CAM-mediated pathways[32,303,353–355]. Nevertheless, cargo can also be delivered to other destinations than the opposite site of the cell via transcytosis, such as lysosomes, mitochondria, or recycling back to the site of entry[164,356,357]. The mechanism by which the brain ECs decides the trafficking route of cargo upon receptor activation is poorly understood. Other interactions of NCs with target cells such as binding, uptake, and intracellular trafficking, as well as circulation, biodistribution, and clearance are impacted by NC properties such as size, surface charge, shape, elasticity, etc.[149,164,358–362] and might, thus, also influence NC trafficking by brain ECs. Therefore, a better understanding of the effect of NC properties on trafficking is paramount for the successful delivery of therapeutics into and across the BBB[293,363].

The transport behaviour of NCs can be influenced by targeting moieties displayed on their surface[149,168,336,364–367]. A well-studied example for receptor-mediated transcytosis across the BBB is targeting the TfR[368,369]. Nevertheless, insufficient brain penetration due to trapping of Ab, Ab-drug conjugates, and TfR-targeted NCs in and around brain capillaries has been observed, for which insufficient abluminal release due to high Ab avidity likely played a role[350,370–375]. Different studies have shown that Ab affinity, influencing avidity, plays a crucial role for brain penetration. In this regard, lowering the affinity for TfR increases the brain penetration of anti-TfR Ab[373–375], as well as Ab-drug conjugates[374,375] . Interestingly, brain penetration and Ab affinity do not show a linear relationship, as an experiment with affinities from 5 nM (high affinity) to 76 nM and 108 nM (intermediate affinity), down to 174 nM (low affinity) shows a bell-shaped relationship of

affinity and brain exposure of Abs with and without cross-linked drug, where high Ab affinity results in low brain exposure due to Ab trapping in and around blood vessels, intermediate Ab affinity increases brain exposure because it favours transcytosis across the BBB, yet low affinity results in decreased brain exposure likely due to poor engagement with the brain endothelium[375]. Importantly, these findings could be confirmed in a non-human primate, highlighting the relevance of this mechanism across species[376].

Furthermore, Ab affinity does not only affect transcytosis but also lysosomal trafficking. High affinity (20 nM) anti-TfR Abs cause a dose-dependent reduction of TfR levels *in vivo*, in line with higher lysosomal degradation *in vitro* and *in vivo* compared to low affinity (600 nM) anti-TfR Ab[377]. Comparable results have been found when, instead of decreasing the affinity, the avidity of anti-TfR Ab to TfR was decreased by decreasing the pH, resulting in higher transcytosis as compared to lysosomal trafficking at physiological pH[378]. Interestingly, lysosomal trafficking does not either show a linear but a bell-shaped relationship with affinity. A study assessing the trafficking of anti-TfR Ab with different affinities across the BBB shows that anti-TfR Abs with high (5 nM) and low (174 nM) affinity preferentially traffic to lysosomes, whereas anti-TfR Abs with intermediate (76 nM and 108 nM) affinity associate more with recycling endosomes, likely destined for exocytosis, while also showing efficient release of intermediate affinity Abs on the basolateral side of brain ECs *in vitro*[379], in line with abovementioned findings of increased brain exposure for Abs with identical (intermediate) affinities[375].

Valency, the number of targeting moieties, is another factor that influences avidity and has been shown to affect Ab transport. Ab with monovalent, thus less strong, engagement to TfR show higher brain exposure compared to Ab with bivalent, thus stronger, engagement[380]. Comparable results have been described for Ab-drug conjugates, showing higher penetration and drug activity in the brain for monovalent *vs* bivalent anti-TfR Abs cross-linked to a therapeutic enzyme[381]. Comparable to the effects of affinity on lysosomal trafficking, a lower valency increases transcytosis whereas a higher valency increases lysosomal trafficking, as shown for mono- *vs.* bi-valent interactions of anti-TfR Ab with its receptor[355].

Given the importance of overall affinity of Abs, determined by affinity itself or by valency and thus avidity, the importance of this parameter for NCs and their transport needs to be considered. For instance, NC targeting valency, the number of targeting moieties displayed on the NC surface, influences NC binding, downstream signalling, and uptake[147,149,365,382–384]. Since most studies use adherent cell models that only permit trafficking to intracellular destinations such as lysosomes but not transcytosis[147,149,365,382–384], the effect of valency on trafficking destination is poorly understood with only few studies addressing the matter. For example, it has been shown that lower valency is advantageous for transcytosis efficiency of polymersomes targeted to LRP1 with angiopep-2 compared to high valency or monovalent interactions *in vitro*, *in vivo* and *in silico*[385]*.* Furthermore, polymersomes with the valency resulting in the most efficient transcytosis associate less with lysosomal marker rab5 compared to those with higher valency rendering less efficient transcytosis, suggesting an inverted relationship of valency with lysosomal degradation[385]. In another study, polymeric micelles with different valencies of glucose molecules to target GLUT1 have shown a bell-shaped relationship of valency and transcytosis efficiency *in vivo,* with intermediate valency showing the highest transcytosis efficiency compared to low and high valency. Furthermore, high valency micelles were trapped in and around the blood vessels[386], as described for high affinity anti-TfR Abs[350,370–375], likely due to insufficient release of NCs from the basolateral side of the cell.

Similarly, in one of our recent studies, we have used polymeric NCs targeted to ICAM-1 with different valencies of anti-ICAM-1 Ab to assess NC transport[170]. Firstly, we could verify earlier findings[149,170] of the direct relationship of binding and uptake of NCs with targeting valency[170]. With regards to transcytosis, we found a bell-shaped relationship between targeting valency with transcytosis, with an intermediate valency NCs rendering the most efficient transcytosis[170]. Interestingly, we showed that matrix metalloprotease 9 (MMP9) is involved in the release of NCs from the basolateral side of cells by cleaving ICAM-1, enabling the detachment of transcytosed NCs[170], suggesting the importance of this step for transcytosis. Lastly, NCs could also be delivered to lysosomes, yet this was analysed in brain ECs grown on coverslips, thus not allowing for transcytosis which might have altered natural trafficking behaviour[170].

However, the mechanistic relationship between valency, transcytosis, and lysosomal trafficking remains unknown. For instance, the existence of lysosomal trafficking concomitantly with transcytosis of NCs in brain ECs remains uncertain, such as the influence of targeting valency on that process. Furthermore, the fate of NCs bound to the basolateral side of cells is undefined. Therefore, in this chapter, we aimed to use a BBB model to study the mechanism of transport of anti-ICAM-1 NCs into/across brain ECs, focusing on lysosomal trafficking, the effect of targeting valency, and the fate of NCs attached to the basolateral side of brain ECs.

Note: Results obtained in this chapter have been partially published in an article where I have been a co-author (in bold): Manthe, R. L., **Loeck, M.,** Bhowmick, T., Solomon, M. & Muro, S. Intertwined mechanisms define transport of anti-ICAM-1 nanocarriers across the endothelium and brain delivery of a therapeutic enzyme. *J. Control. Release* **324**, 181–193 (2020).

5.2. Results and Discussion

5.2.1. Validation of the brain EC barrier model to study NC trafficking

To be able to study NC transport at the BBB in a more realistic setting, human brain microvasculature endothelial cells (HBMEC) were grown on transwell filters to form a cellular monolayer, separating an apical and a basolateral chamber, to allow for NC transcytosis to occur. As a first step, different aspects of the brain EC barrier model were verified to assess the suitability of this model to address the questions in this chapter.

Firstly, cells were treated with the inflammatory cytokine TNFα to induce ICAM-1 expression, due to its known association with inflammation[150–152], which was found to be increased by 4.4-fold (figure 5.1A). Then, the interaction of anti-ICAM-1 NCs with brain ECs was assessed. In line with the enhanced expression of ICAM-1, NCs targeted to that receptor showed significantly increased binding by 2.5-fold in TNFα-activated compared to untreated cells (figure 5.1B), which was furthermore found to be specific over non-targeted IgG NCs, with 4.6-fold increase (figure 5.1B), as expected.

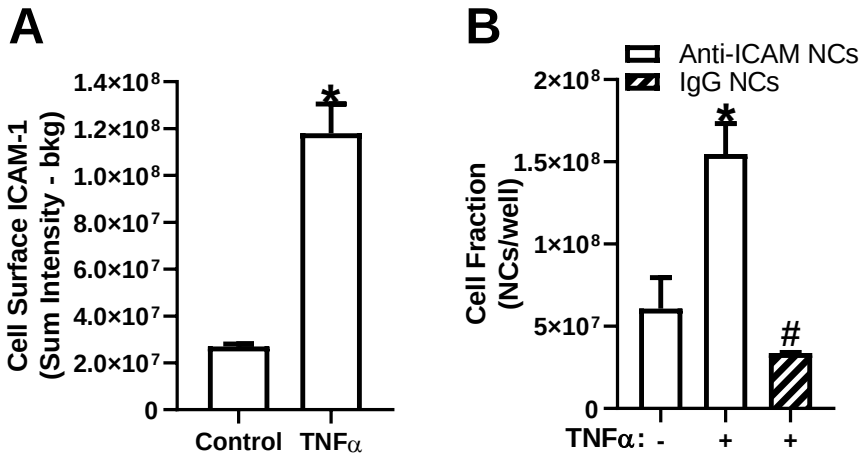

Figure 5.1 ICAM-1 expression and targeting to brain ECs. (A) The relative expression of ICAM-1 was assessed. Human brain microvasculature ECs (HBMECs) were grown on transwells and treated with 10 ng/mL TNFα (20 h treatment) in simulated inflammation or left untreated as control, fixed, immunostained using anti-ICAM-1 and FITC-labelled secondary antibodies, and analysed by fluorescence microscopy. Sum fluorescence minus background is shown. (B) Cells were treated like in (A) and incubated with ^{125}I-labelled anti-ICAM-1 NCs or control IgG NCs for a 30-min binding pulse, washed to remove non-bound NCs, and analysed using radiotracing. The graph shows the number of NCs associated with cells. Data are average ± SEM. Statistics: Student's t-test, $p<0.05$, *compared TNFα (+) to TNFα (-) cells, #compared IgG NCs to anti-ICAM-1 NCs.

Then, the formation of a cellular barrier was confirmed to further verify the model. To this end, anti-ICAM-1 NCs were added to the apical chamber of confluent cell monolayers and incubated for 30 min. Then, the distribution of the NCs across cells from the apical chamber to the basolateral chamber was quantified. After 30 min incubation, 97.6% of all NCs remained in the apical chamber and 1.5% of all NCs passed into the basolateral chamber (figure 5.2A). In comparison, 23.61% of all NCs crossed a control transwell filter without any cells (data not shown), indicating that the cell monolayer acts as barrier separating apical and basolateral compartments. Furthermore, fluorescence microscopy was used to obtain structural information of the cell monolayer (figure 5.2B), showing the formation of a confluent lining as well as the expression of VE-cadherin, a pivotal protein for BBB integrity[387], at the cell-cell junctions between adjacent cells (figure 5.2B). Additionally, to eliminate any leakage which might confound transcytosis results, all experiments performed thereafter used a pulse-chase incubation. To this end, cells are incubated with NCs for a 30-min binding pulse, allowing for NC binding to cell-surface receptors, followed by washing to remove all non-bound NCs in the apical as well as the basolateral chamber. Finally, cells were incubated in NC-free cell medium to only trace NCs pre-

bound to receptors. Using this protocol, the NC transcytosis by brain ECs was assessed in the absence or presence of other relevant BBB cells such as astrocytes (ACs) and pericytes (PCs)[352]. It was observed that the co-culture of brain ECs with other relevant BBB cells did not have a significant influence on NC transcytosis, whereas transcytosis was possible and not that different in all cases (figure 5.2C). Therefore, the brain EC monoculture model was used to address the remaining questions in this work, since the goal was to focus on NC trafficking by brain ECs alone.

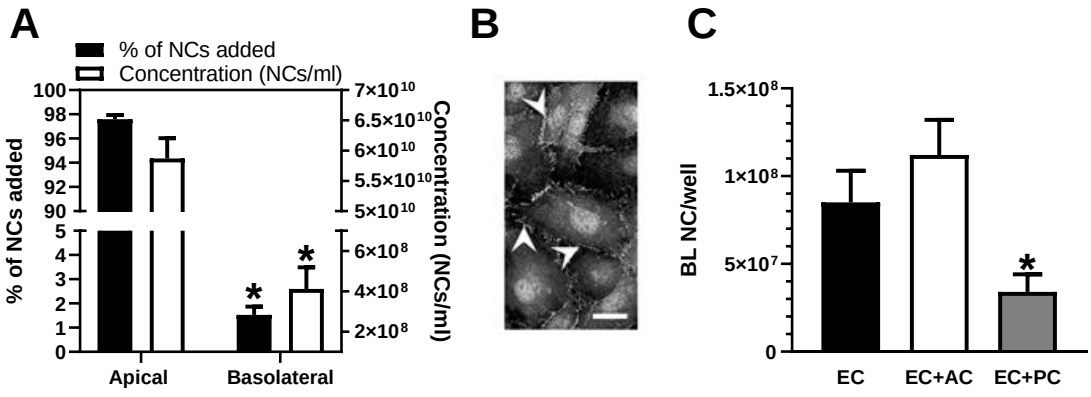

Figure 5.2 Barrier integrity of the EC monolayer used for transcytosis. (A) Brain ECs were grown on transwells and treated with 10 ng/mL TNFα (20 h treatment) to simulate inflammation. Then, I^{125}-labelled anti-ICAM-1 NCs were added to the apical chamber and incubated for a 30-min binding pulse, washed to remove non-bound NCs, and fixed. The number of NCs in the apical and basolateral chambers were determined as percent of total NCs added (left axis) and as concentration (NCs/mL) (right axis). Data are average ± SEM. (B) Representative microscopy picture of a confluent brain ECs monolayer grown on a transwell. Cells were fixed, permeabilised, and immunostained for VE-cadherin. Visualisation by fluorescence microscopy. Scale bar = 10 µm, arrow heads = VE-cadherin at cell-cell junctions. (C) Brain ECs were grown on transwells, either as a monoculture or co-culture with ACs or PCs on the basolateral side of the same transwells. Experimental procedure like in (A), but after washing cells were further incubated in NC-free medium up to 5 h. The graph shows the absolute number of NCs transcytosed per well into the basolateral chamber. EC = endothelial cell, AC = astrocyte, PC = pericyte. Data are mean ± SEM. Statistics: Student's t-test, *p<0.05.

Then, the radiotracing technique was verified. To measure the transcytosis across the BBB model, radiolabelled Abs are coated onto the targeted NCs used for radiotracing quantification. A limitation of this method might be the detachment of labelled coating proteins, thereby confounding trafficking results. Therefore, the integrity of the coated NCs and, thus, suitability of the method was assessed. To this end, cells were incubated with either ^{125}I-anti-ICAM:IgG NCs or anti-ICAM:^{125}I-IgG NCs added to the apical side to compare the trafficking of both formulations. There was no significant difference between the interaction of cells with NCs with either label. NCs bound to cells in comparable total numbers, with approximately $2.8 \times 10^8 - 3.1 \times 10^8$ NCs/well

after 30 min. The number of cell-bound NCs decreased over 24 h to approximately 1.3 x 10^8 – 1.9 x 10^8 NCs/well, while it significantly increased in the basolateral fraction from 0.8 x 10^8 – 1.0 x 10^8 NCs/well after 3 h to 1.6 x 10^8 – 2.1 x 10^8 NCs/well after 24 h (figure 5.3A). The comparable trafficking of both NCs indicates the stability of the NC coating. This is because in the case of stable NC coating, both Abs could be transported together on the same NC, leading to equal NC numbers independent from which Ab carries the ^{125}I-label. On the other hand, if Ab detached from the NC, "free" Ab would be expected to be transported (anti-ICAM[163,388]) or not (IgG), as in figure 5.1 (figure 5.3B).

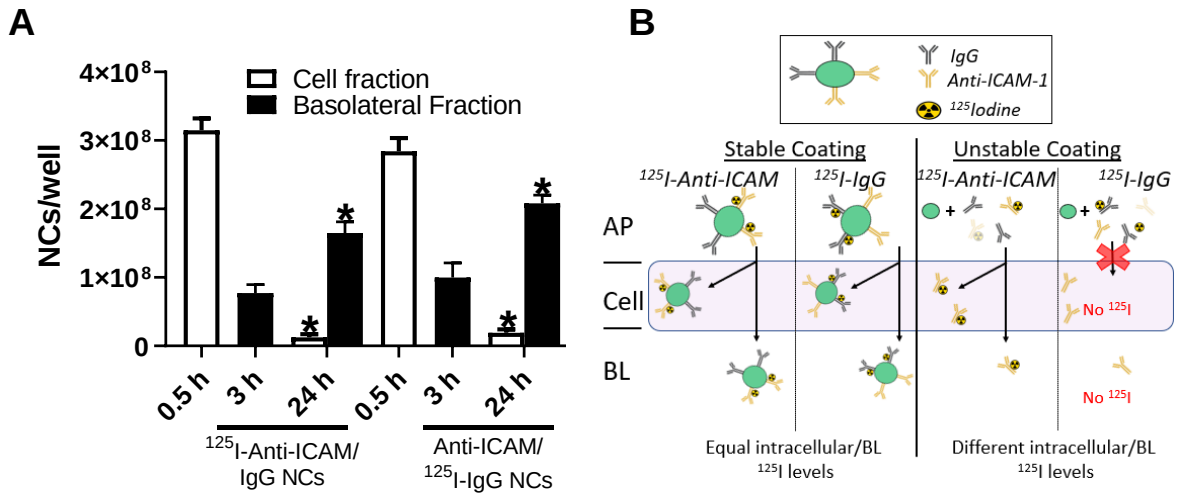

Figure 5.3 Verifying NC Radiotracing. Set-up like in figure 5.2A. Cells were incubated with anti-ICAM:^{125}I-IgG NCs or ^{125}I-anti-ICAM:IgG NCs using the pulse-chase method. Then, cellular, and basolateral fractions were collected for radiotracing using a gamma counter. (A) Quantification of NCs in the cell and basolateral fraction per well comparing ^{125}I-anti-ICAM-1/IgG NCs and anti-ICAM-1/^{125}I-IgG NCs. (B) A model to explain the differential transport of intermediate valency anti-ICAM-1 NCs and free Abs. Data are shown as average ± SEM. Stats: Student's t-test, $p<0.05$, *compared to previous time point of respective fraction and same NC, #compared to the same time point of respective fraction and the other NC (Student's t-test, $p<0.05$).

Lastly, cells were incubated with anti-ICAM-1 NCs of two distinct targeting valencies (v2 and v3; table 3.2) and their binding and uptake were compared (figure 5.4). After 30 min of incubation, significantly more NCs of the v3 formulation compared to the v2 formulation had bound to cells, with 828 *vs.* 591 NCs/cell, as well as been taken up into cells, with 493 *vs.* 267 NCs/cell, respectively (figure 5.4). This validated previous results on the valency dependency of binding and uptake and, thus, the model used[149,170].

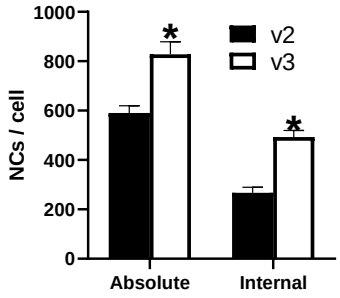

Figure 5.4 Binding and uptake of anti-ICAM-1 NCs by brain EC grown on transwell. Cells were TNFα-activated and incubated with FITC-labelled anti-ICAM-1 for 30 min, washed to remove non-bound NCs, fixed, and counterstained with red secondary Ab to distinguish between intracellular NCs (green only) and cell-bound NCs (green + red = yellow). The pictures were analysed by fluorescence microscopy. Data are average ± SEM. Statistics: Student's t-test, $p<0.05$, *compared v3 to v2.

In conclusion, brain EC monolayers grown to confluency on transwells behaved similarly to beforementioned brain EC monolayers described in literature with regards to ICAM-1 expression in control and inflammation, as well as regarding their interaction with anti-ICAM-1 NCs. Furthermore, the NC quantification by radiotracing was validated and the brain EC monolayer was shown to form a proper barrier for NCs used in the present work. Thus, this model was used in the following experiments to address the questions regarding NC trafficking at the BBB.

5.2.2. The Valency Dependency of Lysosomal Trafficking of NCs

Following uptake, NCs can embark on different intracellular routes. A common intracellular destination for cargo are lysosomes, whereas barrier cells such as brain ECs also transport cargo from the apical side (general circulation) to the basolateral side (CNS) and *vice versa*, circumventing lysosomal degradation[352].

With respect to anti-ICAM-1 NCs, lysosomal trafficking as well as transcytosis have been observed by ECs, nevertheless, lysosomal trafficking has typically been studied in cells grown on coverslips, thus not allowing for transcytosis to occur simultaneously as in the BBB[167,170,172,303]. Thus, it was unknown whether the lysosomal trafficking observed in ECs grown on coverslips was an artifact due to e.g., a cellular coping mechanism given the impossibility of NC transcytosis, or whether these two trafficking events do happen simultaneously in a barrier set-up. To this end, the intracellular trafficking of anti-ICAM-1 NCs was studied in a parallel experiment examining

lysosomal trafficking by using FITC-labelled NCs and fluorescent microscopy and transcytosis by using ^{125}I-labelled NCs and a gamma counter. Both trafficking events were found to happen simultaneously in brain ECs, with 58.5% of all NCs initially bound to cells in the basolateral fraction (figure 5.5A) and 45.0% of all NCs associated with cells at that time point in lysosomes (figure 5.5B) at 24 h. Interestingly, the lysosomal colocalisation of anti-ICAM-1 NCs measured in the present work differed significantly from that of ECs grown on coverslips with 28% to >65% after 3 h[159,172,174,187,388], respectively, probably due to the lack of transcytosis function of cells when grown on coverslips. This highlights the importance of culture conditions when studying trafficking pathways.

Furthermore, when assessing the cellular retention of NCs using radiotracing, a gradual reduction of NCs was observed (figure 5.5A), in line with concomitant transcytosis. Nevertheless, the percent of NCs in the cellular fraction diminished far beyond what might have been expected due to the results obtained for lysosomal trafficking, with only 2.7% of originally bound NCs in that fraction at 24 h (figure 5.5A). This is because ^{125}I-Ab on the NC coat, used for radiotracing, is degraded in lysosomes, just as previous observed in other studies[159], producing free ^{125}I that can escape the cell perhaps through ion channels independently from the NC. This is then a further prove for the lysosomal trafficking of a fraction of NCs. However, the PS NCs used to assess intracellular trafficking cannot be degraded by cells, for which this material was chosen over PLGA, enabling lysosomal tracing by fluorescence microscopy (see Chapter 4).

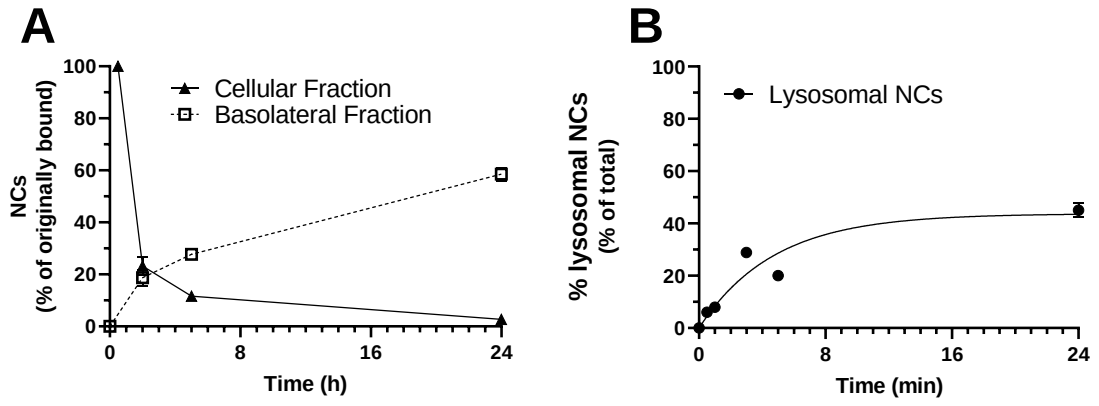

Figure 5.5 Simultaneous transport of anti-ICAM-1 NCs to lysosomes and across the brain EC monolayer. Cells were TNFα-activated and incubated with anti-ICAM-1 NCs *via* the pulse-chase method. (A) Cells were incubated with ^{125}I-

labelled anti-ICAM-1 NCs. Then, the cellular fraction and basolateral fraction were collected and NCs quantified using a gamma counter. (B) Lysosomes were pre-stained with Texas Red dextran (10 kDa), washed to remove extracellular dextran, and further incubated to allow for complete lysosomal trafficking of dextran. Then, cells were incubated with FITC-labelled anti-ICAM-1 NCs. Lysosomal trafficking was determined by fluorescence microscopy as colocalisation of green NCs with red lysosomes (green + red = yellow). Data are shown as average ± SEM. Invisible error bars are hidden behind data symbols.

Thus, following endocytosis by brain ECs, anti-ICAM-1 NCs embark on lysosomal trafficking and transcytosis concomitantly. However, the mechanism that decides which pathway the cargo embarks on is poorly understood. For instance, cargo avidity for receptors (defined by either receptor affinity or targeting valency) has been observed to impact transcytosis, whereby cargo with intermediate avidity to a receptor has shown higher transcytosis than cargo with low and high avidity (see section 2.1). This is why the valency dependency on lysosomal trafficking was also assessed. To this end, cells were incubated with anti-ICAM-1 NCs of three valencies (v1, v2, v3; table 3.2) and their lysosomal trafficking was assessed for up to 60 minutes to isolate this trafficking process without the potential influence of simultaneously transcytosis. Slopes of linear regressions were 0.135x, 0.153x, and 0.186x for v1, v2, and v3 formulations, respectively (figure 5.6A), suggesting a direct relationship of lysosomal trafficking with valency.

This result was further supported by quantifying the disappearance of Ab coating from anti-ICAM-1 NCs using immunofluorescence. This method used the abovementioned lysosomal degradation of coating Ab[159] as a measure to quantify lysosomal trafficking. For this purpose, following the incubation of cells with green-fluorescent anti-ICAM-1 of different valencies, cells were fixed and permeabilised to allow the red-fluorescent secondary Ab targeted against coating Ab to enter the cell, double-staining all cell-associated NCs, extracellular or intracellular, with intact Ab coating (green + red = yellow), whereas NCs without Ab coating appear as green only (figure 5.7B). Given the fact that complete coat degradation upon entry into lysosomes might not be immediate, the time of analysis was prolonged to 3 h to study early events. The disappearance of Ab coating from anti-ICAM-1 NCs also showed a valency dependency (figure 5.7B), in line with trafficking results.

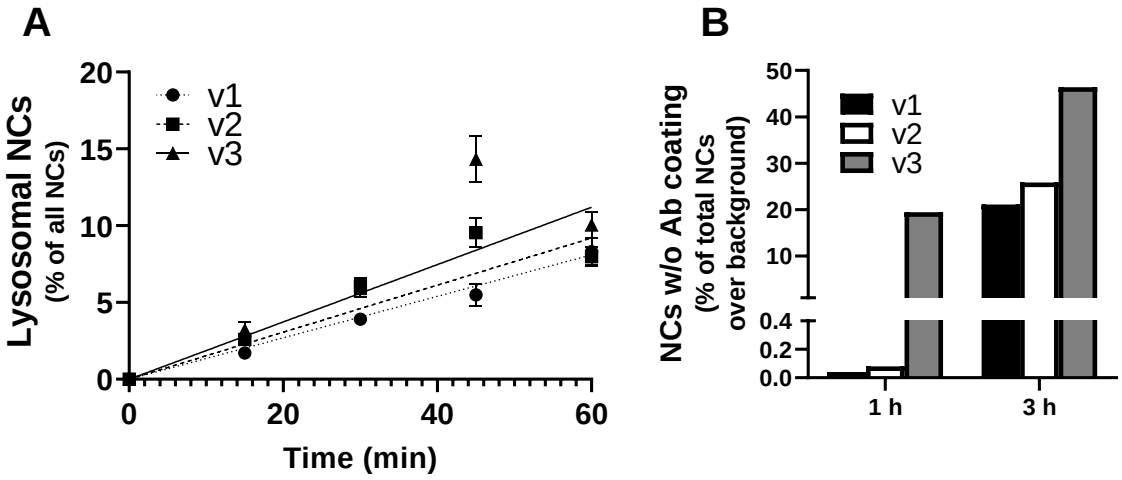

Figure 5.6 Early lysosomal trafficking and Ab coat degradation of anti-ICAM-1 NCs by brain ECs. (A) Cells were TNFα-activated and lysosomes pre-stained with dextran, as described (figure 5.5). Then, cells were incubated with FITC-labelled anti-ICAM-1 NCs of different valencies using the pulse-chase method. Lysosomal trafficking was determined by fluorescence microscopy as colocalisation of green NCs with red lysosomes (green + red = yellow). Data are shown as average ± SEM. Invisible error bars are hidden behind data symbols. (B) Cells were TNFα-activated and incubated with FITC-labelled anti-ICAM-1 NCs of different valencies using the pulse-chase method. Then, cells were fixed, permeabilised to allow Ab to cross the cell membrane, and incubated with red secondary Ab against anti-ICAM-1, which is located on the NC coat. This method allows to distinguish NCs with Ab coating (green + red = yellow) and without Ab coating (green). Data are percent of all NC without Ab coating over background from averaged data (see methods).

5.2.3. Basolateral reuptake of transcytosed anti-ICAM-1 NCs

Several studies have postulated that an insufficient detachment from the basolateral side of brain ECs might be the reason for the lower transcytosis efficiency of high-avidity cargo compared to intermediate-avidity cargo[170,350,370–375]. Furthermore, the Muro lab described a cellular mechanism consisting of the proteolytic cleavage of ICAM-1 to be involved in the detachment of anti-ICAM-1 NCs from brain ECs after transcytosis[170]. Given the existence of a cellular mechanism to help cargo detachment from the basolateral side, this poses the questions of what happens at the basolateral side of brain ECs to cargo that does not efficiently detach, such as observed for high-avidity NCs that accumulates in and around blood vessels In the brain following i.v. injection in mice[375,386]. Because in such a case cargo, such as targeted NCs, is entrapped at the basolateral side of cells through the engagement with respective receptor, such as ICAM-1 in this case, it was postulated that reuptake by endocytosis can occur[170].

As a first step towards exploring this hypothesis, anti-ICAM-1 NCs were added to the basolateral chamber of a brain EC monolayer to assess the possibility of binding and uptake from that side of cells (figure 5.7). Binding was found to be possible, yet approx. 14-fold reduced compared to binding to the apical side with 1.2 x 10^7 and 1.7 x 10^8 NCs/well, respectively (figure 5.7A). This reduction was unsurprising given the presence of the transwell filter between the cells and the basolateral chamber, reducing the contact area of the NC-containing medium with the cell surface to only the openings of the filter pores. Furthermore, the uptake of anti-ICAM-1 NCs from the basolateral side was assessed and compared to the apical uptake (figure 5.7B). The uptake of anti-ICAM-1 NCs from the basolateral side of brain ECs was confirmed and shown to be slightly faster compared to apical uptake, with 61.6% *vs.* 49.6% of all NCs internalised at 0.5 h (figure 5.7B). The possibility of uptake from the basolateral side of ECs via the CAM-pathway is in line with observations of reverse trans-endothelial migration of different white blood cells from tissue into the blood stream, including neutrophils, leukocytes, and monocytes following initial extravasation[389]. Although the mechanism of the reverse trans-endothelial migration remains to be defined, ICAM-1 has been shown to be involved in the basolateral to apical migration of monocytes across the endothelium[389]. The involvement of ICAM-1 in this process is unsurprising given its pivotal function for trans-endothelial migration of leukocytes during extravasation[153,155–157].

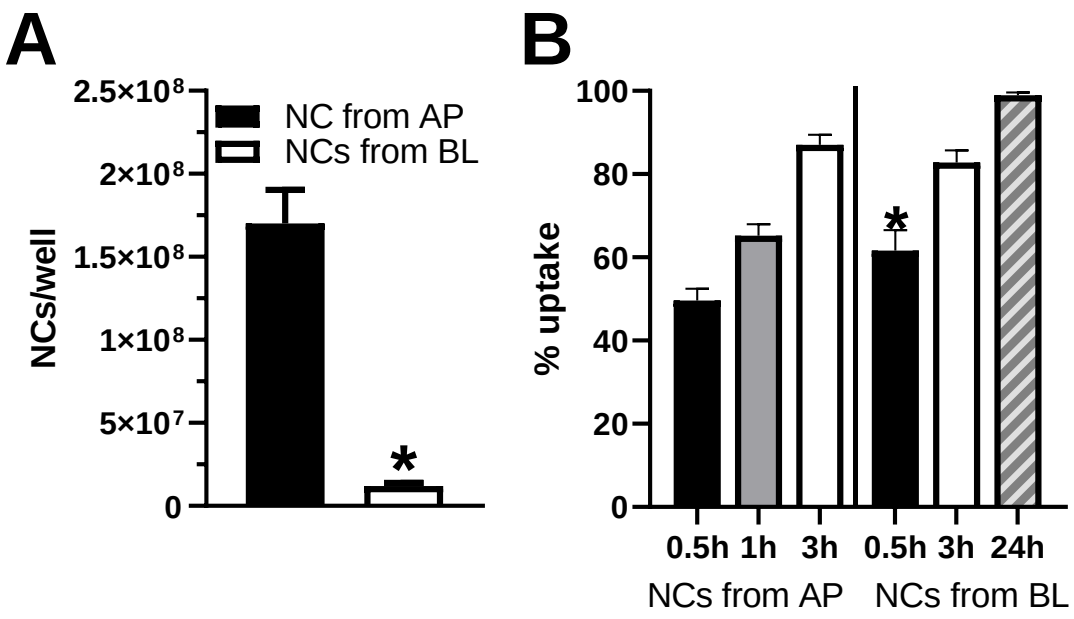

Figure 5.7 NC binding and uptake rate from the apical VS basolateral side of brain ECs. Cells were TNFα-activated and incubated with anti-ICAM-1 NCs using the pulse-chase method. (A) ^{125}I-anti-ICAM-1 NCs were used for quantification of binding. Cells were incubated either from the apical or basolateral side of the barrier. After 30 min the cellular fraction was collected and NCs were quantified using a gamma counter. (B) FITC-labelled anti-ICAM NCs were used to assess uptake. Cells were incubated either from the apical or basolateral side of the barrier. Uptake was quantified as described (figure 5.4). AP = apical, BL = basolateral. Data are shown as average ± SEM. Statistics: Student's t-test, $p<0.05$, *compared basolateral to apical of same time point.

Although the previous result showed NC uptake from the basolateral side of brain ECs, NCs had been added to that chamber and, thus, this only suggests but does not prove NC reuptake post-transcytosis. To precisely verify this, cells were incubated with green-fluorescent anti-ICAM-1 NCs added to the apical side for 30 min to allow for binding and washed to remove non-bound NCs. Then, NC-free medium was added to the apical chamber and NC-free medium containing red-fluorescent dextran, a fluid phase marker, was added to the basolateral chamber. In that way, when NCs transcytose to the basolateral side of the cell monolayer and subsequently re-enter into the cell, the cell medium that enters into the vesicle upon reuptake contains red-fluorescent dextran, marking those vesicles visible in two colours (green + red = yellow), enabling the quantification of reuptake by fluorescence microscopy (figure 5.8A). NC reuptake was confirmed for anti-ICAM-1 NCs, with 39.8% of all cell-associated NCs being colocalised with dextran 30 min after simultaneous incubation (30 min pulse + 30 min chase = 1 h total transport time for NCs)

(figure 5.8B). This colocalisation was in fact the result of the simultaneous uptake of NCs and dextran in the same basolateral vesicle and not the due to intracellular fusion of separately internalised vesicles, given the following results. When cells were first incubated with dextran, then washed and finally NCs were added, only 8% of all cell-associated NCs colocalised with dextran containing vesicles (figure 5.8B). Furthermore, no leakage of dextran was detected from the basolateral to the apical chamber, i.e., <2% after similar time (30 min), validating the method (figure 5.8C). Lastly, anti-ICAM NC reuptake at the basolateral side after transcytosis showed a dependency on NC targeting valency, with higher targeting valency NCs (v3 formulation) showing higher reuptake rate than intermediate targeting valency NCs (v2 formulation), with 53.0% *vs.* 45.1% of all NCs in reuptake after 1 h, respectively (figure 5.8D). This finding is in line with the valency dependency of binding and uptake from the apical side of ECs (figure 5.4) and supports the idea of insufficient detachment playing a role in the process.

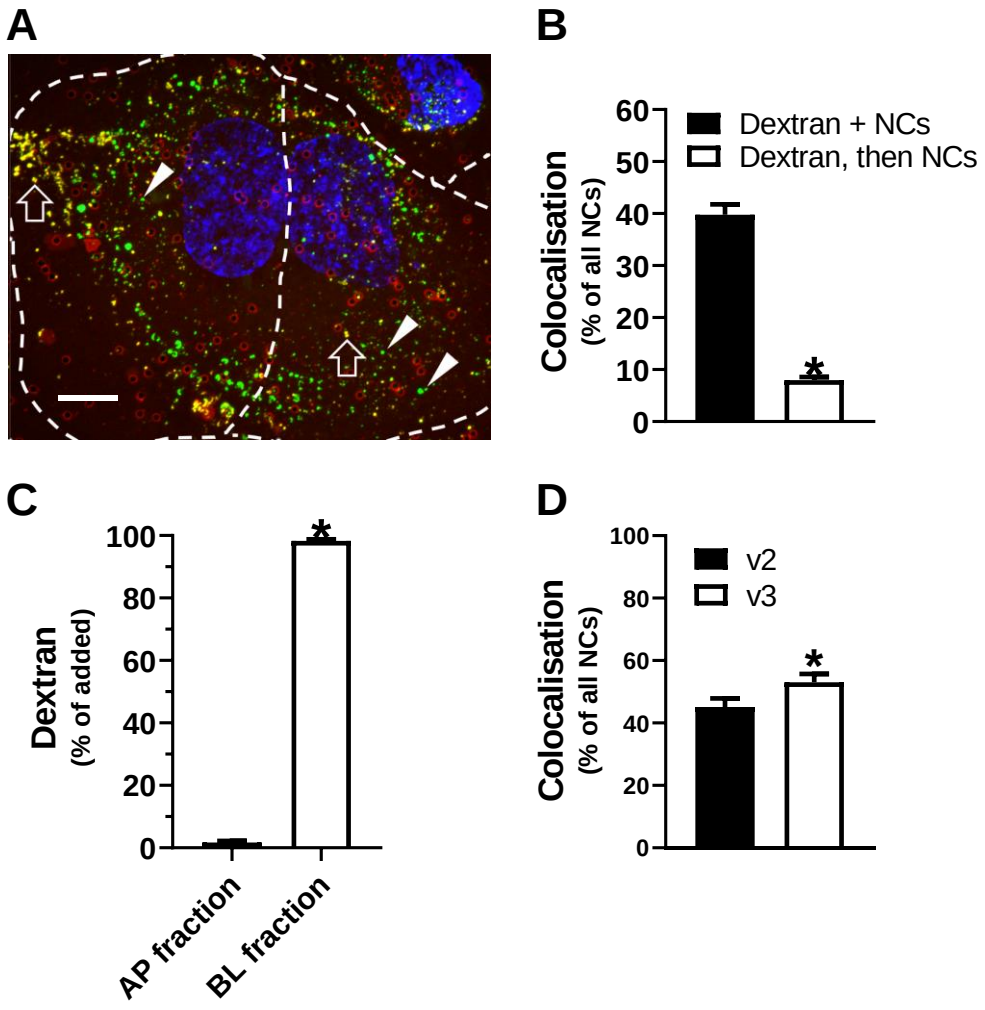

Figure 5.8 Reuptake of anti-ICAM-1 NCs by brain ECs. Cells were TNFα-activated and incubated with FITC-labelled anti-ICAM-1 NCs from the apical side for a 30-min binding pulse, washed to remove non-bound NCs, and further incubated for 30 min with NC-free medium with Texas Red dextran as a fluid phase marker in the basolateral chamber. In this way, NCs that transcytosed to the basolateral chamber and re-enter the cell colocalise with the fluid phase marker in the basolateral medium (green + red = yellow). Pictures were analysed by fluorescence microscopy. (A) Representative confocal microscopy image. Green = NCs not in reuptake (arrow heads), yellow = NCs in reuptake (open arrows). Scale bar = 10 µm. (B) Percent colocalisation of all NCs after 1 h of total incubation with NCs in the presence of dextran (dextran + NCs) compared to the percent colocalisation of all NCs after 1 h of total incubation after the removal of dextran (dextran, then NCs) (see method figure 5.5B). (C) Quantification of the leakage of dextran from the basolateral chamber into the apical chamber after 30 min. (D) Comparison of the percent colocalisation of all NCs after 1 h of total incubation with NCs in the presence of dextran (dextran + NCs) between anti-ICAM-1 NCs v2 formulation and v3 formulation. AP = apical, BL = basolateral. Data are shown as average ± SEM. Statistics: Student's t-test, *p<0.05.

5.2.4. The Effect of NC Reuptake on Lysosomal Trafficking

Given the observed reuptake following transcytosis, the question arose about the subsequent intracellular transport of those NCs. To address this question, cells were incubated with green-fluorescent anti-ICAM-1 NCs added to either the apical or the basolateral sides of the barrier, using the pulse-chase method described and the lysosomal trafficking was quantified (figure 5.9). Lysosomal trafficking was significantly faster from the basolateral side compared to the apical side of the barrier, with half-times of 2.4 h *vs.* 3.4 h, respectively (figure 5.9). Furthermore, compared to the apical side, trafficking to lysosomes from the basolateral side was not only faster, but also a higher percentage of all NCs interacting with cells ended up in lysosomes (figure 5.9), suggesting that lysosomal degradation is the preferred route from that side and therefore likely the preferred route following basolateral reuptake of transcytosed NCs.

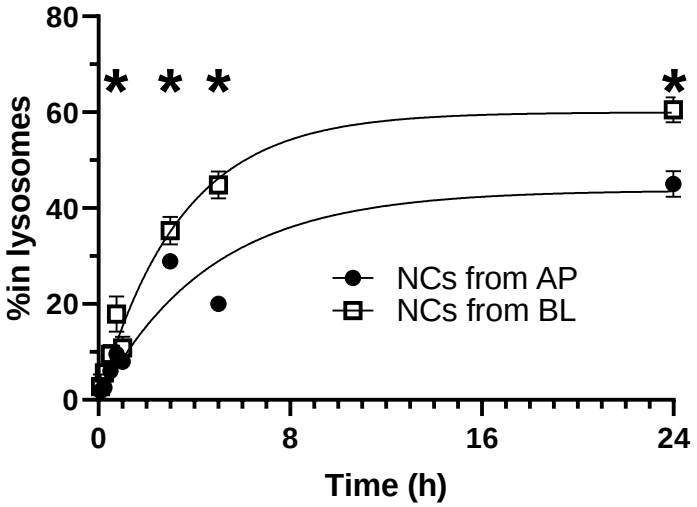

Figure 5.9 Comparison of the lysosomal trafficking of anti-ICAM-1 NCs from the apical or basolateral side of brain ECs. Cells were TNFα-activated and pre-treated with Texas Red dextran, as described (figure 5.6). Then, cells were incubated with FITC-labelled NCs from either the apical or basolateral side of cells using the pulse-chase method. Then, lysosomal trafficking was assessed by colocalisation using fluorescence microscopy (figure 5.6). AP = apical and BL = basolateral. Data are average ± SEM. Statistics: Student's t-test, $p<0.05$, *compared BL to AP.

Thus, NCs that embark on the transcytosis route have been shown to undergo reuptake and quickly traffic to lysosomes. This means that the kinetics of the transcytosis pathway have an influence on the kinetics of the lysosomal trafficking pathway. Since NCs on the transcytosis pathway first need to cross the cell and subsequently re-enter before they traffic to lysosomes,

the influence of that route is likely to impact the lysosomal route at later time points than earlier tested (up to 1 h) where a direct relationship between trafficking valency and lysosomal trafficking was observed (figure 5.6). To address this, the lysosomal trafficking of anti-ICAM-1 NCs of different valencies (v1, v2, or v3) was assessed up to 24 h (figure 5.10). Interestingly, an inverted bell-shaped relationship between targeting valency and lysosomal trafficking speed was found, with half times of 159, 193, and 138 min for v1, v2, and v3 formulations, respectively (figure 5.10A). This is in line with the finding of a bell-shaped relationship between targeting valency and transcytosis[170]. This is because since lysosomal trafficking and transcytosis are prominent final destinations in brain ECs (figure 5.5) and because they are mutually exclusive, their kinetics were expected to be inverted. Additionally, lysosomal degradation was determined following the incubation with cells with ^{125}I-anti-ICAM-1 NCs of different valencies (v2 or v3) by measuring free ^{125}I in the cellular fraction, since free ^{125}I should be produced upon lysosomal degradation of ^{125}I-coating Abs[159] (figure 5.10B). In line with valency dependency of early events of lysosomal trafficking (figure 5.6), free iodine peaked earlier for v3 formulations than v2 formulations. Interestingly, in contrast to v2 formulations, v3 formulations showed a secondary increase in lysosomal degradation at later time points, in line with the significantly higher reuptake of that targeting valency and subsequent "second round" of lysosomal trafficking.

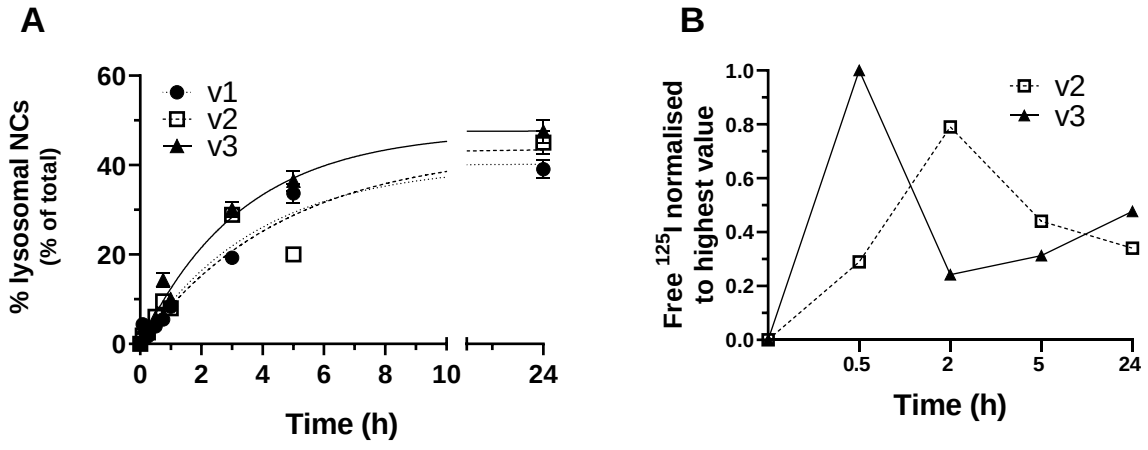

Figure 5.10 Valency dependency of anti-ICAM-1 NC lysosomal colocalisation by brain ECs. Cells we TNFα-activated and incubated from the apical chamber with NCs using the pulse-chase method. (A) Lysosomes were pre-stained with Texas Red dextran and incubated with FITC-labelled NCs up to 24 h, as described (figure 5.5B). Lysosomal

trafficking was assessed as colocalisation (green + red = yellow) by fluorescence microscopy. Data are average ± SEM. (B) Cells were incubated with ^{125}I-NCs. At indicated time points, the cellular fraction was collected and free ^{125}I determined using the TCA assay (see section 3.3.1). Data are normalised averages.

5.3. Conclusion

The brain endothelium is the primary lining of the BBB and therefore plays a vital role in controlling all transport into and out of the CNS, inhibiting the passage of most therapeutics into the brain[352]. Using active transport across that barrier is a promising strategy for therapeutic intervention for the CNS and has gained increasing attention over the past decades. However, the mechanisms of cargo trafficking at the BBB are poorly understood. Here we studied NC trafficking by brain EC monolayers *via* the ICAM-1-mediated pathway (figure 5.11). NCs were found to simultaneously traffic from the apical to the basolateral side of cells (transcytosis), as well as to lysosomes, with early lysosomal trafficking showing direct targeting valency dependency. Interestingly, we saw that a fraction of the NCs that embarked on the transcytosis route could re-enter the cell from the basolateral side, probably due to insufficient detachment of the NC from the cell, although entrapment between the cell monolayer and the filter at areas without pore may also contribute to this. Furthermore, targeting valency-dependent reuptake from the basolateral side of cells was found, with higher valencies inducing higher reuptake, just as the case for apical uptake. Lastly, NCs that entered the cell from the basolateral side of the monolayer were confirmed to traffic to lysosomes, suggesting that the same pathway might be taken by NCs after reuptake. In line with this, the lysosomal trafficking rate over 24 h was shown to have an inverted bell-shaped relationship with valency, likely resulting from the influence of early apical and later basolateral events in the whole kinetics. These results highlight the intricate interplay of concomitant trafficking events and their importance for drug delivery intro and across the BBB.

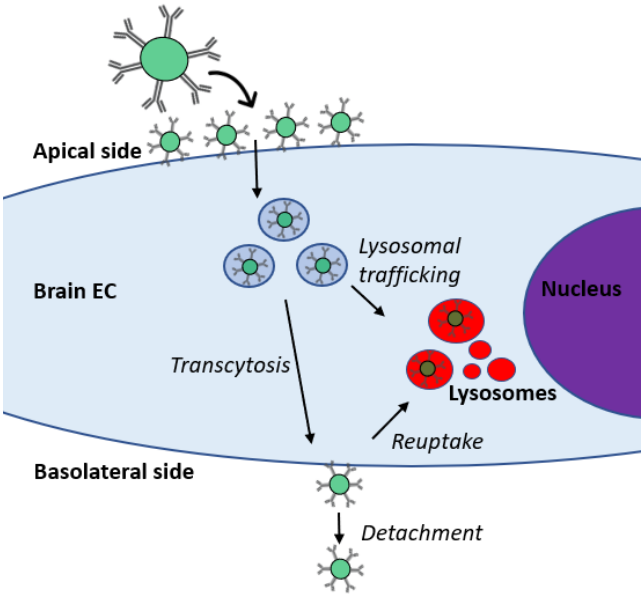

Figure 5.11 Cartoon of anti-ICAM-1 NC trafficking by brain EC cells. Following binding and uptake, NCs can embark on either the lysosomal trafficking route or the transcytosis route. Interestingly, a fraction of the NCs on the transcytosis route re-enters the cell (reuptake), probably due to insufficient detachment of the NCs from the basolateral side of cells, followed by secondary lysosomal trafficking.

Chapter 6: Study the Effect of ASM Deficiency on NC Transport for NPD ERT

6.1. Introduction

Acid sphingomyelinase (ASM) deficiency, also called Niemann-Pick disease type A or B, (NPD, OMIM #257200, #607616)[390,391], is a rare genetic disorder belonging to the lipidosis type of lysosomal storage diseases (LSD), which results in the aberrant accumulation of undegraded sphingomyelin in lysosomes[392]. Historically, NPD also referred to current type C (NPC), which is characterised by an aberrant cholesterol transport due to mutations in transporter proteins Niemann Pick C1 (NPC1) or NPC2[393,394], with clinically comparable symptoms to ASM deficiency. Nevertheless, here we will focus on ASM deficiency, thus NPD type A or B only.

NPD type A or B are both caused by mutations in the *SMPD1* gene encoding for ASM. ASM is a lysosomal enzyme that cleaves sphingomyelin with an optimal activity at a pH of 5, a major component of cell membranes[395], into ceramide and phosphocholine and is, therefore, crucial for maintaining sphingolipid homeostasis and participating in membrane turnover[396,397]. NPD type A has an early onset and is usually diagnosed within the first 6 months of life[232]. Symptoms include hepatosplenomegaly and respiratory failure, and rapid neurodegeneration, often resulting in early mortality before 3 years of life[232]. NPD type B shows greater variability regarding age of diagnosis, with patients ranging from childhood to late adulthood[398–400]. Symptoms include hepatosplenomegaly and frequently involve complications in the lungs, such as impaired gas exchange and some degree of interstitial lung disease, yet no involvement of the CNS[398–400]. Although less severe than type A, NPD type B is a life-threatening disease with significant mortality and morbidity, especially in the paediatric population[401]. There is a broad phenotypic variability within NPD types A and B patients, with an intermediate NPD type A-B also described[402,403].

There is a lack of proper studies to quantify the economical and psychological burden of patients with NPD types A or B. However, some information can be derived from case reports[404]. For patients with NPD type A irritability and general discomfort has been described, resulting in the need for around-the-clock care, physical and occupational therapy, and frequent hospitalisation,

negatively impacting not only the patient's but also caregiver's quality of live[404]. For patients with NPD type B the quality of life is also negatively impacted, yet less severe[404]. Apart from reduced physical functioning and general health, patients suffer from social isolation and peer rejection due to growth and developmental delay and chronic fatigue[404].

As a primary consequence of ASM deficiency, sphingomyelin accumulates in lysosomes. Additionally, secondary accumulation of cholesterol, lyso-sphingomyelin, glycolipids such as glucosylceramide, and gangliosides GM2 and GM3 has been observed[212,405]. ASM deficiency-induced cellular lipid disbalance is likely to have a myriad of downstream effects due to the key role of these membrane lipids on normal cell function[406–408]. Some of these changes are of utmost interest and importance for the treatment of NPD, such as changes in target receptor expression or intracellular trafficking, which have been shown to have major effect on drug delivery and thus treatment efficacy[288], some of which have been described in the literature[23-28]. For instance, in ASM deficiency, endocytosis has been reported to be reduced *via* the clathrin-, caveolae-, and macropinocytosis pathways, which might affect ERT as this typically relies on clathrin mediated endocytosis *via* the M6PR[288,289,409,410]. Furthermore, the intracellular trafficking of lactosylceramide, a membrane lipid taken up via caveolae-mediated endocytosis, has been shown to change from Golgi to predominantly lysosomal trafficking in ASM deficient cells, a property which is interestingly shared among many LSDs and has been linked to a cellular cholesterol imbalance such as seen in NPD[411–413].

Currently, there is no effective treatment for restoring ASM deficiency. Enzyme replacement therapy (ERT), the delivery of exogenous enzyme to deficient cells, is already the gold standard for several LSDs (e.g., see GD, chapter 7) but is not yet approved for NPD types A or B. Nevertheless, Genzyme/Sanofi are developing the first ERT for NPD type B, Olipudase Alpha[414], which has scored favourable results in an ongoing clinical trial[246].

Due to the lack of an effective and approved treatment for NPD types A or B and the undoubtable disease burden, there is a need for novel therapeutics addressing this issue. Interestingly, a series of animal studies have shown therapeutic efficacy in the brain following high-dose ERT for some enzymes, which might cross the BBB although at a low degree through pinocytosis[245,415–425].

Nevertheless, this strategy remains rather ineffective given its non-specific transport mechanism and, additionally, such high doses pose a high risk for immunogenicity[245,415,424,425,416–423]. Therefore, although the development of a potentially life-saving ERT for NPD type B is underway[246], since enzymes cannot adequately cross the BBB and penetrate into the CNS, severe neurodegeneration in NPD type A will most likely remain untreated even after approval of Olipudase Alpha[273].

Nanomedicine, using nanosized drug delivery systems to deliver drugs, offers an interesting platform to create new therapeutics or improve on already existing ones. Different nano-sized therapeutics have been investigated for the use in ASM deficiency. The Muro laboratory was first to test and demonstrate the potential that targeted NCs hold for NPD ERT[44]. In an initial study, anti-ICAM-1 NCs were shown to successfully deliver ASM to NPD fibroblasts *in vitro*, resulting in lysosomal trafficking, stable enzyme activity, and lipid storage reduction[187]. As a next step, the laboratory reported the improved delivery *in vivo* in mice of ASM to all major peripheral organs when the enzyme was delivered by NCs targeted to ICAM-1, either by using anti-ICAM-1 Ab or a peptide derived from the fibrinogen region that naturally binds to ICAM-1, compared to common practice consisting of injecting naked enzyme without a carrier [175,301]. Then, transcytosis of anti-ICAM-1 NCs was described *in vitro* as well as *in vivo* in mice, showing efficient brain targeting[171,303], highlighting the potential for this approach to be used in ERT for neuronopathic NPD type A. Furthermore, other nanoparticles have been investigated as macromolecule scavengers to reduce substrate in substrate reduction therapy (SRT). For instance, synthetic high-density lipoprotein (sHDL) particles, originally designed for cardiovascular disease with currently ongoing phase III clinical trial[426], have been shown to rescue the sphingolipid storage in NPD type A patients' fibroblasts in cell culture[50]. Nevertheless, when this strategy was used in an animal model for NPC with similar neuropathology, no improvement of motor symptoms was observed, suggesting poor CNS penetration[427]. Lastly, in an early clinical trial, the novel not yet approved ERT Olipudase Alpha[246] had been shown to induce dose-dependent adverse effects when injected as free enzyme without a carrier, due to the rapid systemic increase of ceramide[414], a catabolite of accumulated sphingomyelin (figure 1.5)[428]. Using liposomes for the delivery of Olipudase Alpha has not only been shown to enhance sphingomyelin reduction in lysosomes of

NPD type B patient's fibroblasts compared to naked enzyme, but also to reduce extracellular sphingomyelin degradation by preventing the interaction of encapsulated enzyme with sphingomyelin on the cell surface, in turn reducing rapid ceramide production and thus side effects[429], further demonstrating the potential of nanomedicine for ERT.

Nevertheless, not much is known about the interactions of multivalent NCs with diseased brain ECs at the BBB. Therefore, in this study, NCs targeted to the three main routes associated with endothelial transcytosis clathrin-, caveolae-, and CAM-mediated pathways were assessed and compared in ASM-deficient brain ECs to determine the most promising candidate to deliver ERT to the CNS in NPD.

6.2. Results and Discussion

6.2.1. Validation of ASM Deficiency Model and Receptor Expression

Firstly, imipramine was used to induce ASM deficiency in human brain ECs, since no other BBB model for this disease is readily available. This drug inhibits ASM irreversibly by degradation and has been used previously by the Muro laboratory to mimic ASM deficiency in cell culture[44]. In this study, treatment of brain ECs for 48 h with this agent lowered by 4-fold ASM activity measured *in vitro* using respective cell lysates (figure 6.1A) and this clearly increased the accumulation of a fluorescent sphingomyelin analog in cells (figure 6.1B), as expected given that this is an ASM substrate.

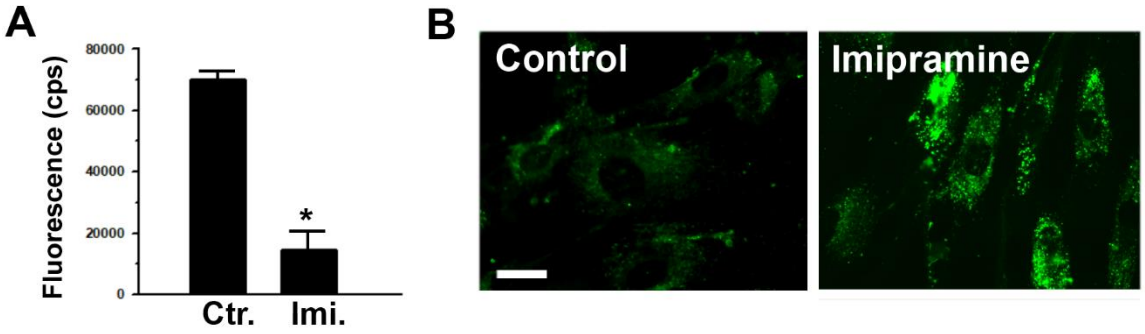

Figure 6.1. Model for ASM deficient ECs. ECs were incubated at 37 °C in control (Ctr) medium or medium containing 20 µM imipramine for 48 h as a model for ASM deficiency. (A) cells were lysed, and samples were incubated with for

1 h at 37 °C with Amplex Red Sphingomyelinase kit, which measures enzyme activity by rendering fluorescent resorufin, measured by spectrofluorometry. Scale bar = 10 um. * $p < 0.5$ by Student's t test (n=3). (B) Cells were incubated overnight with BODIPY-FlC12-sphingomyelin, then washed, fixed, and imaged by fluorescence microscopy under the green channel.

Then, the expression of ICAM-1, TfR, and PV1 was analysed under different conditions by flow cytometry (figure 6.2A). Under control conditions (referred to as no treatment in the figure), ICAM-1 and TfR showed comparable and relatively low expression levels, whereas PV1 showed no expression over IgG control. These findings are in line with the literature on ICAM-1 baseline expression in ECs under control conditions[430], the vital function of TfR for the iron homeostasis of the brain[431], and the known downregulation of caveolae-mediated transport at healthy BBB[27,65]. Furthermore, under inflammation-like conditions simulated by treating cells with TNFα (referred to as imipramine (imip) – in the figure), the receptor expression increased the most for ICAM-1, then TfR, and no change was observed for PV1 (figure 6.2A). This was expected because ICAM-1 has a well-known association with inflammation[150–152], whereas the effects of TNFα on TfR expression appear to be more dependent on the cell type. For instance, TNFα has been reported to reduce the expression of TfR in lung epithelium[432], to not affect the TfR expression in kidney cells[433], and to increase TfR expression in human fibroblasts[434], K562 lymphoblast leukaemia cells[435], enterocytes[436], and human umbilical vein endothelial cells (HUVEC)[437]. Given the close relatedness of HUVEC used in the literature[65] and HBMEC used in the present experiment, both being ECs, the present results were not surprising. Furthermore, TNFα has been shown to slightly reduce the transcription of PV1[438], whereas not much is known about its expression levels. Thus, the very low baseline expression might mask the minimal effect that TNFα has on the expression of PV1, or the increased transcription of the gene does not translate to receptor expression. On the other hand, caveolae-mediated transport has been reported to be upregulated in different diseases[24,25,83], yet not much is known about the underlying mechanisms which might be too complex to be recapitulated in this monocellular model. Lastly, in ASM deficiency, the expression of ICAM-1 was further increased compared to inflammation condition, whereas TfR remained unaffected (figure 6.2). Interestingly, PV1 expression was increased in ASM deficiency (figure 6.2A).

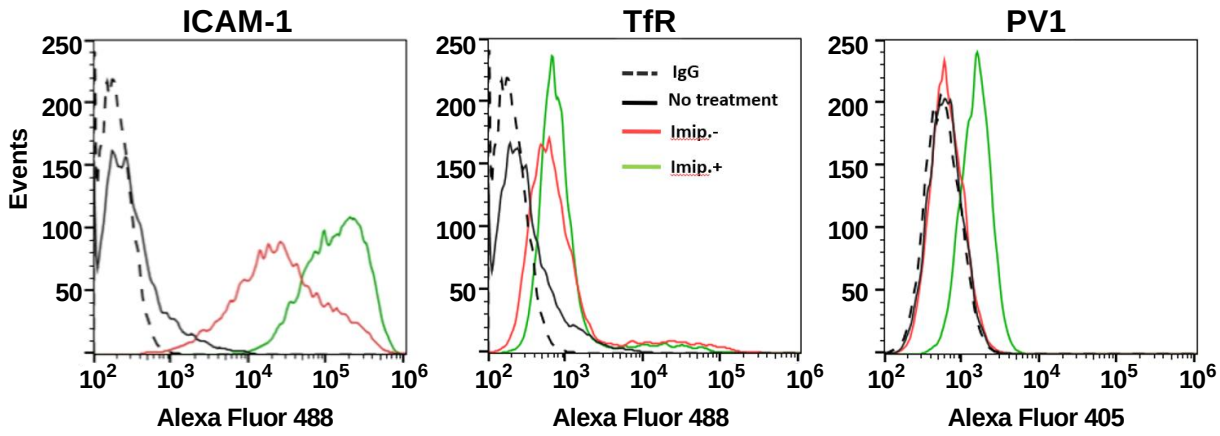

Figure 6.2 Receptor expression. Flow cytometry quantification of receptor expression on brain ECs. Brain ECs were incubated in control medium (called no treatment), cell medium containing 10 ng/mL TNFα (20 h) and 20 µM imipramine (48 h treatment) to simulate ASM deficiency (called Imip.+) or 10 ng/mL TNFα for 20 h (Imip.-) as an ASM-normal control. Cells were then detached using trypsin and stained with either anti-ICAM-1, anti-TfR, or anti-PV1 followed by fluorescent secondary Ab, and analysed by flow cytometry. IgG was used as a control.

These results were intriguing since not much is known about the effect of ASM deficiency on receptor expression. Nevertheless, this condition has been reported to affect gene expression[439] as well as receptor expression[440].

6.2.2. The Effect of ASM Deficiency on NC Binding and Uptake

After model validation and receptor expression, the specific binding of the targeted NCs was assessed (figure 6.3). NCs could be fabricated with similar physicochemical properties, only varying the targeting Ab (table 3.3). Furthermore, all formulations were prepared using PS NCs due to their non-degradability, important for subsequent trafficking studies, (see Chapter 4) and had the same targeting valency (v2; table 3.3).

The targeting of all NCs to brain ECs was specific over IgG control NCs. The highest specificity was achieved with anti-ICAM-1 NCs, followed by anti-TfR NCs and then anti-PV1 NCs, with 61.1-, 16.3-, and 2.7-fold increase over IgG NCs, respectively (figure 6.3), likely related to the level of respective receptor expression previously observed. Hence, all formulations were specific and, therefore, adequate for the following studies.

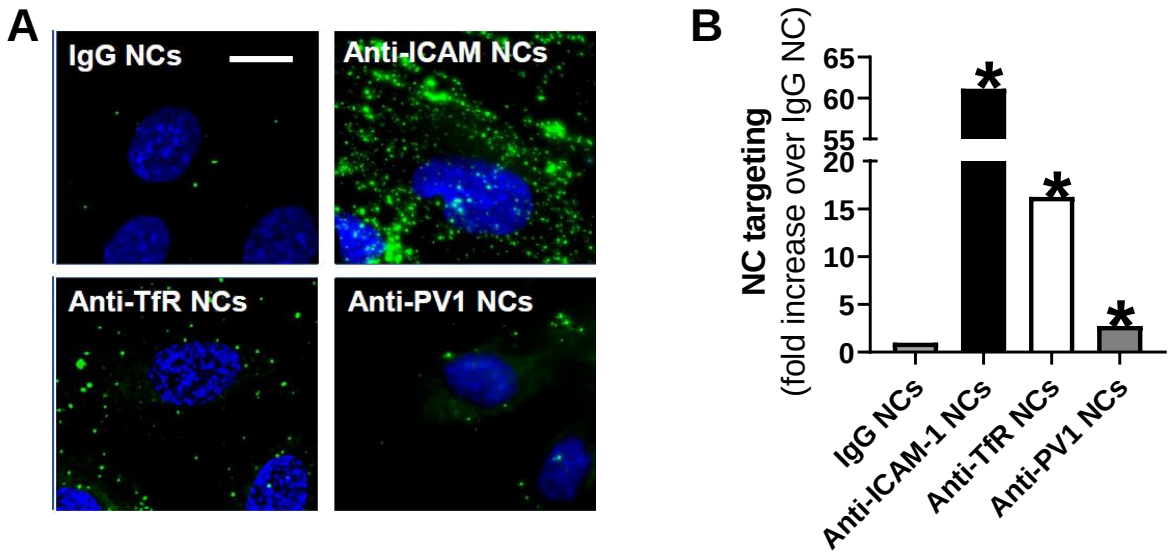

Figure 6.3 NC targeting specificity. (A) Brain ECs were treated with 10 ng/mL TNFα (20 h treatment). Then, cells were incubated for 1 h with FITC-labelled PS NCs targeted to either ICAM-1, TfR, or PV1 or non-targeted IgG NCs, as indicated, washed with PBS to remove non-bound NCs, fixed, and analysed by fluorescence microscopy. (B) Quantification of NC targeting as fold increase over IgG NCs. Data are averages. Stats: Student's t-test, $p<0.05$, *compared to IgG NCs.

In addition, the role of disease on the binding of NCs was tested (figure 6.4A). Under control condition, anti-ICAM-1 NCs and anti-TfR NCs bound to cells comparably, with 99.0 and 89.3 NCs per cell, respectively, whereas anti-PV1 NCs bound significantly less, with 39.9 NCs per cell (figure 6.4B), in line with receptor expression (figure 6.2). Then, inflammation significantly increased the total binding of anti-ICAM-1 NCs and anti-TfR NCs over control condition by 5-fold and 1.5-fold, respectively, whereas it did not significantly affect the binding of anti-PV1 NCs (figure 6.4C). Therefore, under inflammation the binding was significantly different between all three NCs with total binding of 494.3, 131.4, and 42,4 NCs per cell for anti-ICAM-1 NCs, anti-TfR NCs, and anti-PV1 NCs, respectively (figure 6.4D), which was also in line with the receptor expression levels (figure 6.2A). This was in line with earlier studies using HUVECs grown on coverslips, which had also shown an increased binding of similar anti-ICAM-1 NCs under inflammation conditions[304], confirmed here for HBMEC on transwells. Contrary to the present results, the same study found overall less NCs per cell and a small but significant difference between the binding of anti-ICAM-

1 NCs and anti-TfR NCs under control conditions, and lacked an increased binding of anti-TfR NCs under inflammation[304]. This discrepancy might result from differences in the cell type (macrovasculature *vs.* microvasculature ECs) and growth condition (coverslip *vs.* transwell) used. For instance, protein expression has been found to be affected by growth conditions[441] and might therefore also affect receptor expression.

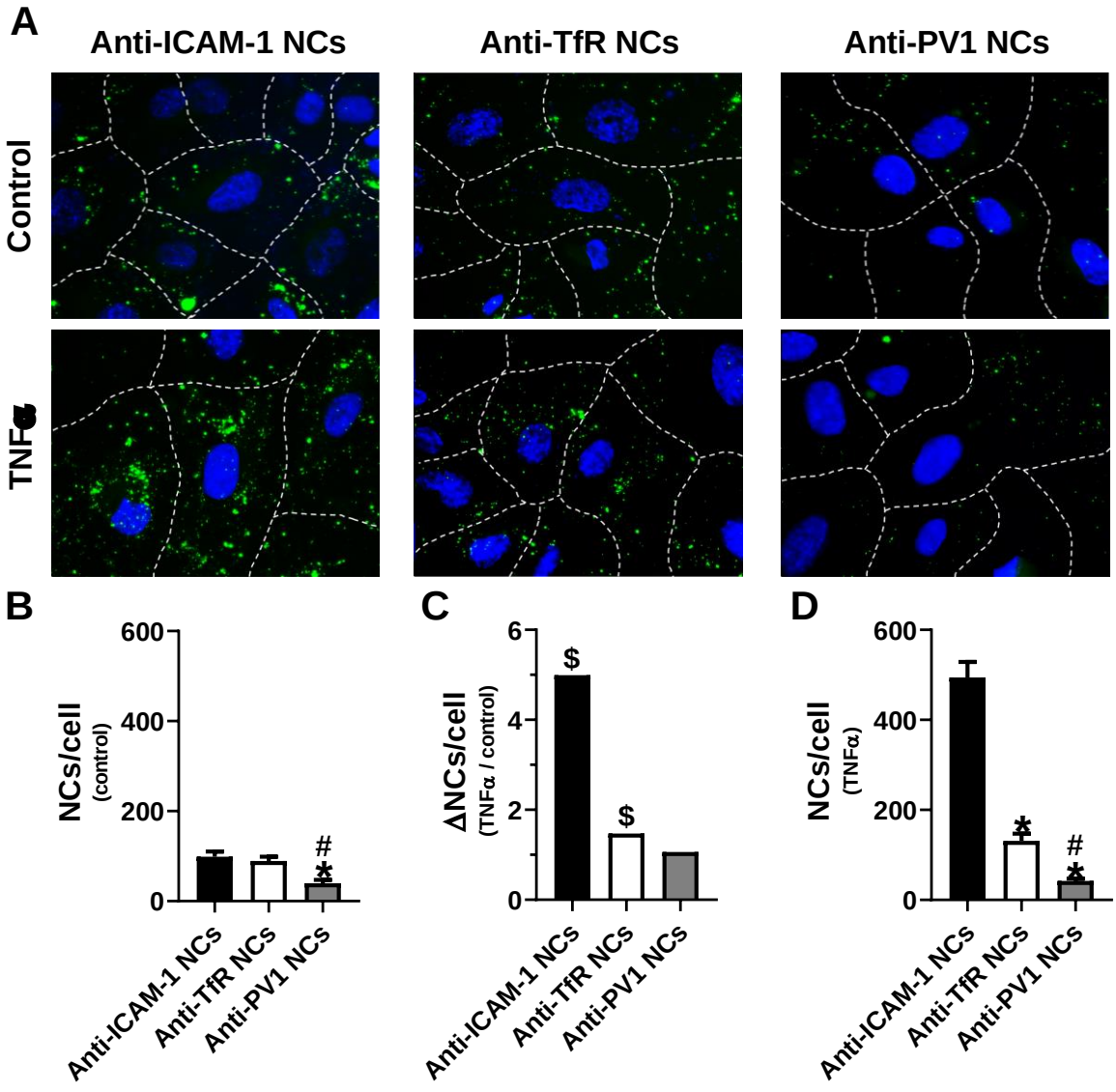

Figure 6.4 NC binding to brain ECs under control and inflammation conditions. Brain ECs were grown to confluency on transwells and not treated (control) or incubated with 10 ng/mL TNFα (20 h treatment) to mimic inflammation. Then, cells were incubated for 1 h with FITC-labelled NCs targeted to either ICAM-1, TfR, or PV1, as indicated, washed with PBS to remove non-bound NCs fixed, and analysed by fluorescence microscopy. (A) Representative microscopy images. Green = NCs, blue = nuclei. Dashed lines = cell borders. Scale bar = 10 µm. (B) Quantification of NCs bound per cell under control condition. (C) Fold change (Δ) between NCs bound per cell under inflammation condition and

NCs bound per cell under control condition. (D) Quantification of NCs bound per cell under inflammation condition. Data are average ± SEM. Stats: Student's t-test, p<0.05, *compared to anti-ICAM-1 NCs, #compared to anti-TfR NCs, $analysed significance of fold change.

Then, additionally to TNFα, cells were treated with imipramine[442] (figure 6.5A) to mimic NPD . In this model, the binding of anti-ICAM-1 NCs and anti-TfR NCs was significantly increased by 7.3-fold and 1.8-fold, respectively, compared to control condition (figure 6.5B), in line with receptor expression, whereas the binding of anti-PV1 NCs was not affected, with a 1.1-fold change compared to control, despite the observed increase in PV1 receptor expression (figure 6.2). Nevertheless, given the significant changes in lipid composition induced by ASM deficiency, which have a special structural importance for lipid-rafts in which caveolae are situated, it is likely that, despite the increased expression of PV1, its presentation and accessibility for NC binding are sub-optimal[443–445]. Hence, to assess the specific effect of ASM deficiency on this increase, the binding of all three NCs under NPD condition (inflammation + ASM deficiency) was compared to inflammation alone (figure 6.5C). Solely the binding of anti-ICAM-1 NCs increased significantly by 1.5-fold, in line with receptor expression (figure 6.2), whereas anti-TfR NCs and anti-PV1 NCs were unaffected by ASM deficiency, with 1.2-fold and 1.1-fold change, respectively (figure 6.5C). Hence, in NPD, there was a significant difference regarding the binding among all three NCs tested, with 726.7, 162.2, and 45.2 NCs per cell for anti-ICAM-1 NCs, anti-TfR NCs, and anti-PV1 NCs, respectively (figure 6.5D).

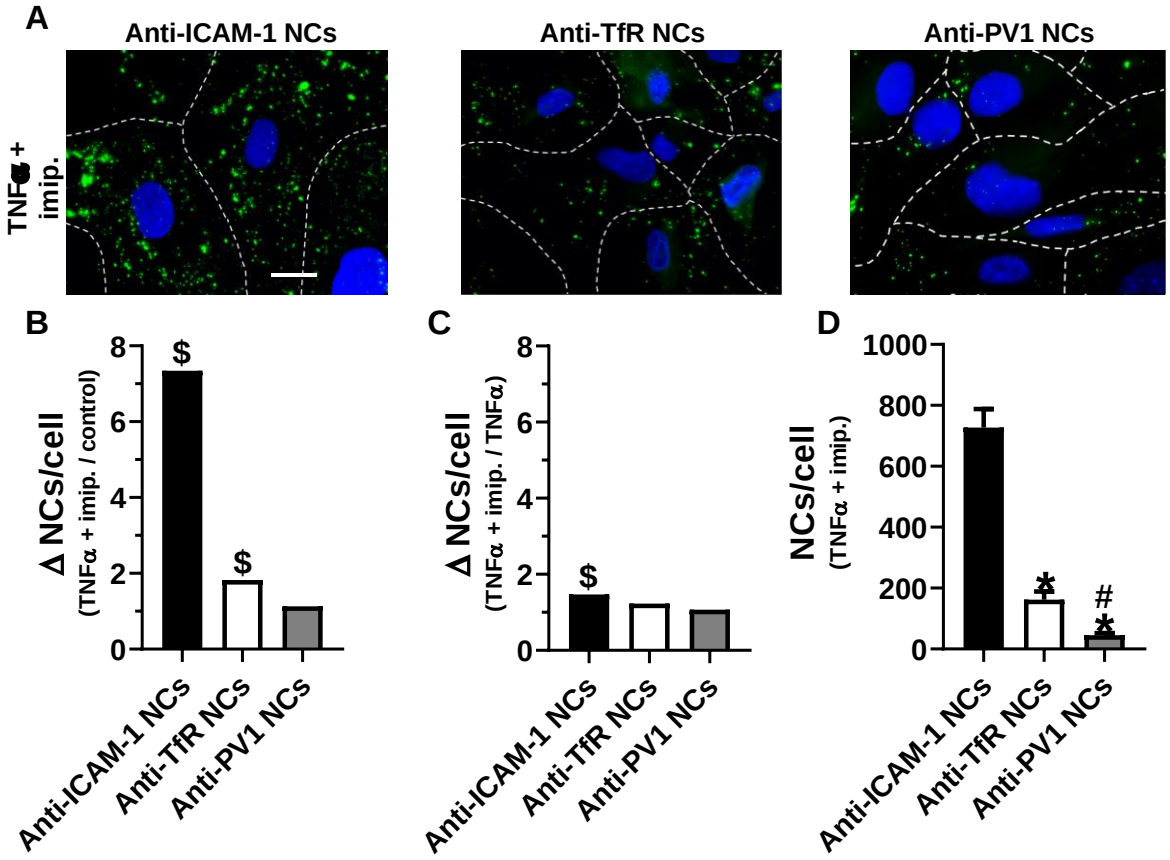

Figure 6.5 Effect of ASM deficiency on NC binding to brain ECs. Cells were grown to confluency on transwells and incubated with 10 ng/mL TNFα (20 h treatment) and 20 µM imipramine (48 h treatment) to simulate ASM deficiency. Then, cells were incubated for 1 h with FITC-labelled NCs targeted to either ICAM-1, TfR, or PV1, as indicated, washed with PBS to remove non-bound NCs, fixed, and analysed by fluorescence microscopy. (A) Representative microscopy images. Green = NCs, blue = nuclei. Dashed lines = cell borders. Scale bar = 10 µm. (B) Fold change (Δ) between NCs bound per cell under ASM deficiency and control condition. (C) Fold change (Δ) between NCs bound per cell under ASM deficiency and inflammation condition. (D) Quantification of NCs bound per cell under NPD condition. Data are average ± SEM (D) or average (B, C). Stats: Student's t-test, $p<0.05$, *compared to anti-ICAM-1 NCs, #compared to anti-TfR NCs, $compared significance of change.

Furthermore, apart from NC binding to cells, NC uptake by cells upon receptor targeting has been reported for all three receptors tested in the current work[160,446,447] and is an important parameter for drug delivery into and across the BBB. Therefore, the uptake of anti-ICAM-1 NCs, anti-TfR NCs, and anti-PV1 NCs was assessed and compared in brain ECs under control and inflammation condition (figure 6.6A).

Firstly, under control conditions, there was no significant difference between the uptake of anti-ICAM-1 NCs and anti-TfR NCS, with 30.7% and 36.3% of all NCs being internalised, respectively,

whereas anti-PV1 NCs were taken up significantly more, with 50.5% of all NCs being internalised (figure 6.6B). Inflammation did not significantly affect the uptake rate of any of the three NCs tested (figure 6.6C), resulting in comparable uptake rates in inflammation and control conditions (figure 6.6D). Thus, inflammation does not have a direct influence on the efficiency of the uptake mechanism.

On the other hand, when looking at the absolute number of internalised NCs per cell, inflammation significantly increased this parameter for anti-ICAM-1 NCs by 6.2-fold, from 28.0 to 174.6 NCs per cell, whereas it did not significantly increase the absolute number of internalised anti-TfR NCs or anti-PV1 NCs, with 45.6 and 22.2 NCs per cell, respectively (figure 6.6E-G). Taken together, the increased absolute number of anti-ICAM-1 NCs is not the result of an inflammation-enhanced uptake rate, but rather the result of an inflammation-induced upregulation of ICAM-1 expression (figure 6.2) and subsequently increased binding of NCs (figure 6.4C). Despite the increased overall engagement of NCs per cell, the uptake was not expected to be altered through saturation of the internalisation pathway, as the uptake has been reported to be dependent on the number of engagements per NC, governed by NC valency, and not to be affected by the overall engagement of receptors per cell, thus being independent from the total number of NCs bound[149], in line with present results.

When analysing the total number of NCs internalised, there was a significant difference among anti-ICAM-1 NCs, anti-TfR NCs, and anti-PV1 NCs, with 174.6, 45.6, and 22.2 NCs per cell in inflammation condition, respectively (figure 6.6E), in accordance with receptor expression (figure 6.2) and NC binding (figure 6.4D). Importantly, despite the significantly higher uptake rate of anti-PV1 NCs compared to anti-ICAM-1 NCs and anti-TfR NCs under inflammation condition (figure 6.6D), the stark differences in receptor expression and NC binding (figure 6.2 and figure 6.4D) remained the defining factor for the total internalised NCs.

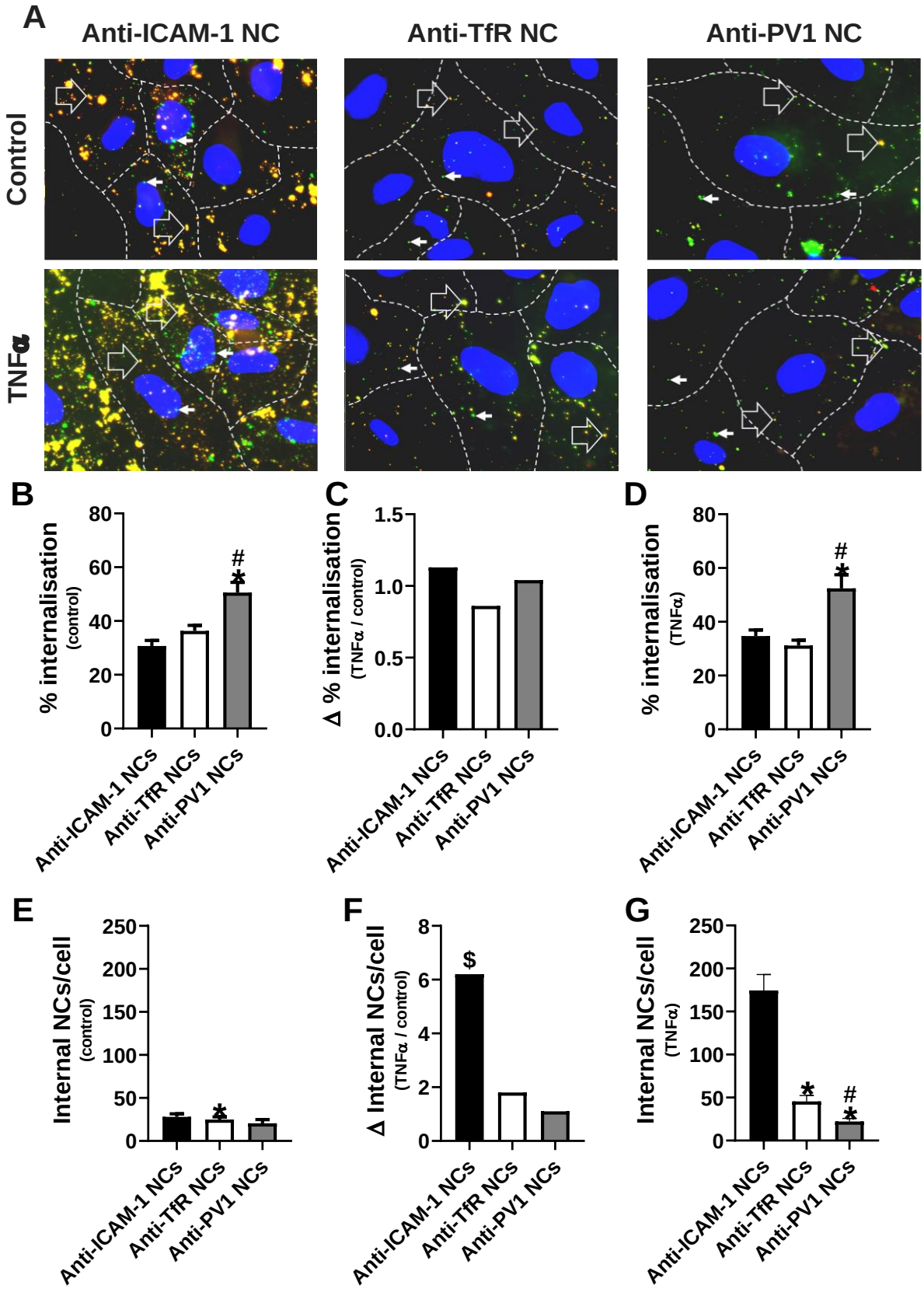
A
Anti-ICAM-1 NC
Anti-TfR NC
Anti-PV1 NC
Control
TNFα
B
% internalisation (control)
C
Δ % internalisation (TNFα / control)
D
% internalisation (TNFα)
E
Internal NCs/cell (control)
F
Δ Internal NCs/cell (TNFα / control)
G
Internal NCs/cell (TNFα)
Anti-ICAM-1 NCs
Anti-TfR NCs
Anti-PV1 NCs

Figure 6.6 Effect of inflammation on NC uptake by brain ECs. Cells were grown to confluency on transwells and not treated (control) or incubated with 10 ng/mL TNFα (20 h treatment) to simulate inflammation. Then, cells were incubated for 1 h with FITC-labelled NCs targeted to either ICAM-1, TfR, or PV1, as indicated, washed with PBS to remove non-bound NCs, fixed, and counterstained with red secondary Ab against the coat protein located on the NC. Secondary Ab does not cross the cell membrane and therefore allows to distinguish internalised (green) from cell-bound (green + red = yellow) NCs. Pictures were analysed by fluorescence microscopy. (A) Representative microscopy images. Green = internalised NCs (small white arrows), yellow = cell-bound NCs (green + red; large open arrows), blue = nuclei. Dashed lines = cell borders. Scale bar = 10 µm. (B) Quantification of the percent NC internalisation of all NCs bound to cells in control condition, (C) Fold change (Δ) between percent NC internalisation of all NCs bound to cells in inflammation and control condition. (D) Quantification of the percent NC internalisation of all NCs bound to cells in inflammation condition. (E) Quantification of total numbers of NCs internalised per cell in control condition. (F) Fold change (Δ) between total NC internalisation per cell in inflammation and control condition. (G) Quantification of the total NC internalisation per cell in inflammation condition. Data are average ± SEM. Statistics: Student's t-test, $p<0.05$, *compared to anti-ICAM-1 NCs, #compared to anti-TfR NCs, $compared significance of change. Lack of symbol indicates non-significant result.

Interestingly, uptake rates in the current study were considerably lower compared to an earlier study comparing anti-ICAM-1 NCs and anti-TfR NCs performed with HUVECs cultured on coverslips[304]. As discussed earlier, apart from the obvious reason of micro- *vs.* macrovasculature origin of the cell lines used, the growth condition might heavily influence the findings. While in the present work cells were grown as a barrier allowing for transcytosis, the other study[304] used a non-barrier model to study uptake, thus not allowing for transcytosis (see chapter 5). This might favour the permanent intracellular location of endocytosed NCs, whereas the barrier model allows for exocytosis on the basolateral side of the cell as part of the transcytosis process, probably lowering the perceived uptake rate because transcytosed NCs which may be located between the cell and the filter likely have an Ab coat which can be detected by counterstaining, thereby marking them appear as surface located NCs despite the fact that they have been internalised previously at the apical side. Importantly, one method is not better than the other depending on what conclusions are sought to be drawn from the results. It is likely that transcytosis cannot occur in the non-barrier model, which makes that model more suited to estimate the absolute uptake of NCs due to the inclusion of NCs that might otherwise have embarked on the transcytosis route. Instead, the barrier model provides a more realistic estimate of the total number of internalised NCs at any given time, permanent or in transit, since it allows for transcytosis to happen, not accumulating all internalised NCs inside cells. Thus, in summary, inflammation did not directly affect internalisation rate of NCs, yet significantly increased the

total numbers of internalised anti-ICAM-1 NCs as a result of increased ICAM-1 expression and anti-ICAM-1 NC binding.

Then, after having determined the effect of inflammation, the additional effect of NPD on NC uptake was assessed (figure 6.7A). The NPD model did not significantly change the uptake rate of any of the three NCs tested compared to control condition (figure 6.7B). However, when comparing the uptake rate in NPD to inflammation condition, a significant decrease of anti-ICAM-1 NCs by 20% could be observed. This was expected due to the involvement of ASM activity in the CAM-pathway[161], where ASM-mediated generation of ceramide at sites of the cell membrane where anti-ICAM-1 NCs bind has been shown to promote NC engulfment and cytoskeletal re-organizations necessary for CAM-mediated endocytosis[80]. Instead, the uptake rate for other two formulations did not change significantly by ASM deficiency (figure 6.7C).

With regards to the absolute number of NCs internalised per cell, this increased for the NPD model for anti-ICAM-1 NCs by 7.4-fold compared to control condition, likely as a result of TNFα-induced ICAM-1 expression (6.2-fold in TNFα compared to control; figure 6.6F). When comparing NPD to inflammation condition to determine the specific effect of ASM deficiency, no significant difference was found (figure 6.7F). This was likely the result of two counteracting events, an increased NC binding (figure 6.5C) due to an increased receptor expression (figure 6.2), and a decreased uptake rate due to ASM deficiency (figure 6.7C). Furthermore, the absolute numbers of anti-TfR NCs and anti-PV1 NCs were not affected by any disease condition (figure 6.7E-F). Ultimately, the internalisation level was different among anti-ICAM-1 NCs, anti-TfR NCs, and anti-PV1 NCs, with 207.2, 57.8, and 29.5 NCs per cell internalised in the NPD model, respectively (figure 6.7G), in accordance with receptor expression (figure 6.2) and NC binding (figure 6.4D). Importantly, as mentioned for inflammation condition, also in ASM deficiency the significantly higher uptake rate of anti-PV1 NCs compared to anti-ICAM-1 NCs and anti-TfR NCs under inflammation condition (figure 6.7D) could not compensate for the stark differences in receptor expression and NC binding (figure 6.2 and figure 6.4D, which ultimately defined the absolute levels of NC internalisation.

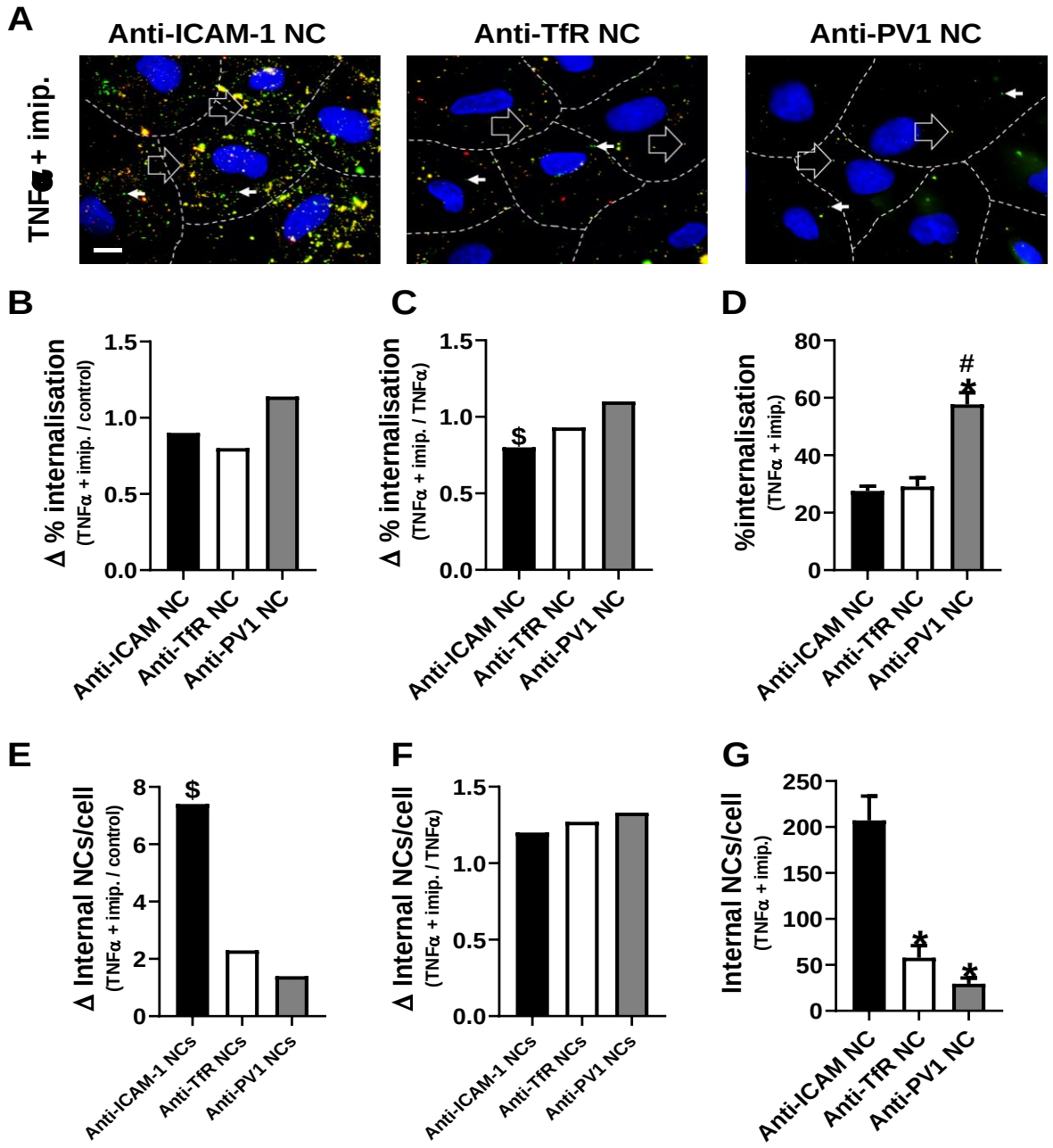

Figure 6.7 Effect of ASM deficiency on NC uptake by brain ECs. Cells were grown to confluency on transwells and incubated with 10 ng/mL TNFα (20 h treatment) and 20 µM imipramine (48 h treatment) to simulate NPD. Then, cells were incubated for 1 h with FITC-labelled NCs targeted to either ICAM-1, TfR, or PV1, as indicated, washed to remove non-bound NCs, fixed, and counterstained with red secondary Ab against the coat protein located on the NC. Secondary Ab does not cross the cell membrane and therefore allows to distinguish internalised (green) from cell-bound (green + red = yellow) NCs. Pictures were analysed by fluorescence microscopy. (A) Representative microscopy images. Green = internalised NCs (small white arrows), yellow = cell-bound NCs (green + red; large open arrows), blue = nuclei. Dashed lines = cell borders. Scale bar = 10 µm. (B) Fold change (Δ) between percent NC internalisation of all NCs bound to cells in ASM deficiency and control condition. (C) Fold change (Δ) between percent

NC internalisation of all NCs bound to cells in ASM deficiency and inflammation condition. (D) Quantification of the percent NC internalisation of all NCs bound to cells in ASM deficiency. (E) Fold change (Δ) between total numbers internalised NCs per cell in ASM deficiency and control condition. (F) Fold change (Δ) between total numbers internalised NCs per cell in ASM deficiency and inflammation condition. (G) Quantification of total numbers of NCs internalised per cell in ASM deficiency. Data are average ± SEM. Statistics: Student's t-test, $p<0.05$, *compared to anti-ICAM-1 NCs, #compared to anti-TfR NCs, $compared significance of change. Lack of symbol indicates non-significant result.

Thus, under both disease conditions, inflammation and NPD, the total binding of NCs was highest when targeting ICAM-1, followed by TfR, and lastly PV1. In line with these results, the total number of internalised NCs was also highest for ICAM-1, then TfR, and lastly PV1 targeting, governed by the sheer difference of total binding under the disease conditions and in spite of minor specific effects that the disease conditions might have on the uptake rate. Interestingly, present results do not fully confirm earlier findings in the literature. The reduction of clathrin-, caveolae-, and macropinocitosis-mediated pathways, the latter being another example for a clathrin-independent endocytosis route, such as CAM-mediated endocytosis, have been reported in NPD macrophages and fibroblasts[288,289,409]. However, cited studies are different to the present one in several important aspects. Firstly, studies in the literature have investigated endocytosis using natural ligands, such as transferrin for the TfR and cholera toxin B for caveolae, whereas the present study assessed endocytosis of NCs, which might be inherently different due to differences in valency and size. Secondly, the cell types used for the experiments are different, focusing on macrophages[288] or fibroblasts[289,409] *vs.* brain ECs in the present study, which all serve different biological functions. For instance, macrophages and fibroblasts are not barrier cells and thus unlikely to transport cargo *via* transcytosis, whereas brain ECs transport cargo *via* this mechanism as a supply to the underlining tissue cells. Furthermore, different cell types might be affected differently in disease, such as earlier discussed for the expression of TfR, further explaining the difference in results.

In conclusion, judging from targeting and internalisation results of NCs in brain ECs forming a barrier model, anti-ICAM-1 NCs appear to provide an advantage for drug delivery to brain ECs under both disease conditions due to the potential for an overall higher drug delivery.

6.2.3. The Effect of ASM Deficiency on NC Lysosomal Trafficking

Intracellular trafficking subsequent to binding and uptake defines NC distribution and, therefore, is important to be assessed. In brain ECs, there are two relevant trafficking routes: lysosomal trafficking in charge of cargo degradation and transcytosis, a route that circumvents lysosomal degradation[170] and delivers cargo across the cellular barrier[55,56]. Although both dependent on vesicular transport, these two processes fulfil very different functions and, thus, have distinct effects on drug delivery and distribution.

First, we assessed lysosomal trafficking of NCs. This is important for NPD ERT because is represents the final destination of for ERT delivery into cells of target tissues and because brain ECs are also affected by ASM deficiency in NPD, thus necessitate enzyme being delivered to lysosomes in parallel to transporting enzyme to transcytosis for brain delivery. To this end, lysosomes were stained with Texas Red dextran, followed by incubation with NCs and colocalisation analysis by fluorescence microscopy in different conditions (figure 6.8A). Importantly, dextran has been previously demonstrated to traffic rapidly to lysosomes and reside there for significant periods of time, since mammalian cells lack dextranase[24,25,44].

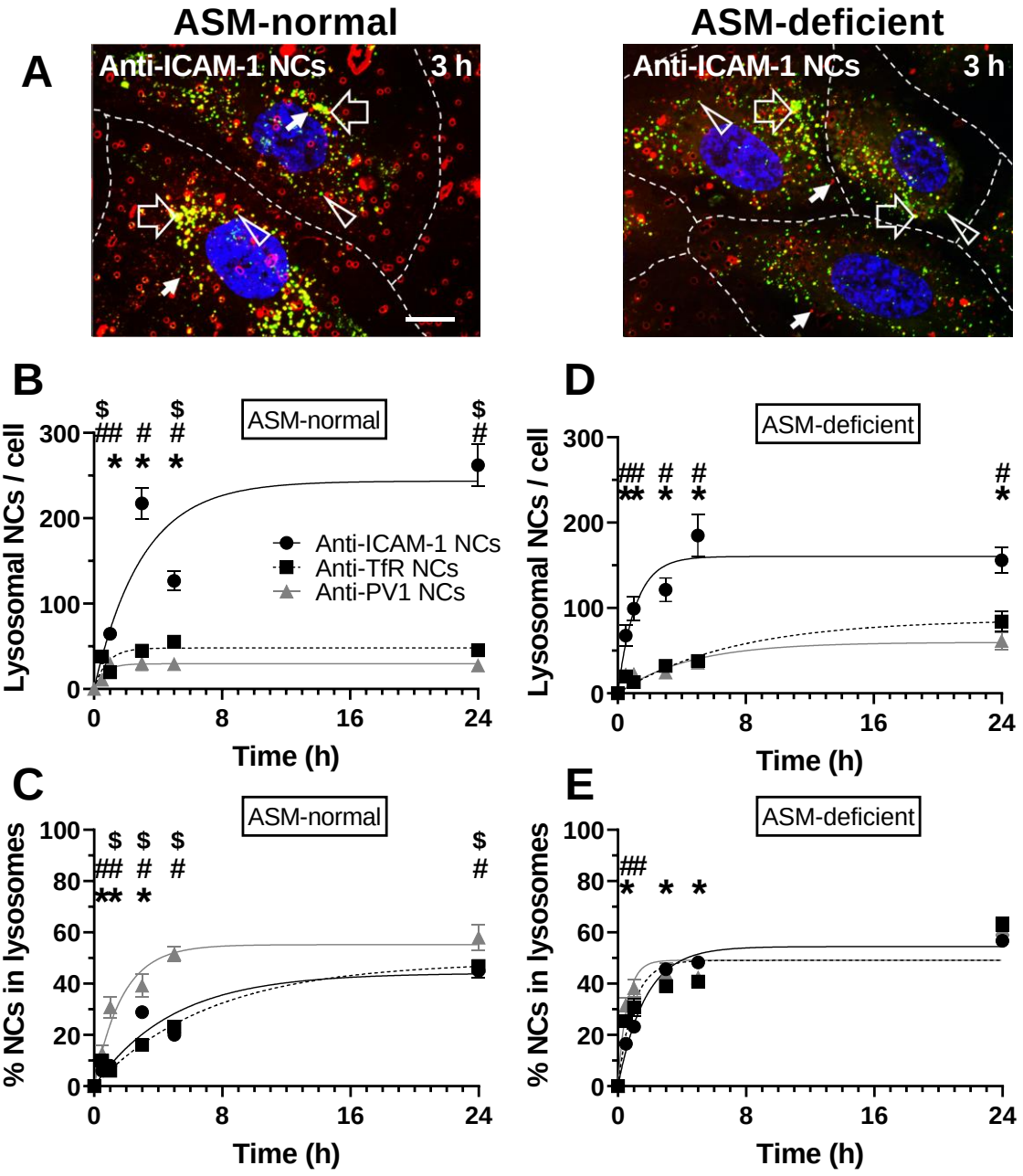

Figure 6.8 Comparative lysosomal transport of NCs in ASM-normal vs. ASM-deficient brain ECs. Cells were treated with 10 ng/mL TNFα (20 h treatment) and 20 µM imipramine (48 h treatment) to simulate ASM deficiency or 10 ng/mL TNFα (20 h treatment) as an ASM-normal control. Prior to the incubation with NCs, cells were incubated with 0.5 mg/mL Texas Red dextran (10 kDa) for 30 min, washed to remove excess dextran, and further incubated in dextran-free medium for 1 h to ensure the localisation of dextran in lysosomes. Then, cells were incubated with FITC-labelled NCs targeted to either ICAM-1, TfR, or PV1, for a 30-min binding pulse, washed to remove non-bound NCs, and further incubated (if applicable) in NC-free medium up to 24 h. Cells were then fixed and analysed by fluorescence microscopy. (A) Representative microscopy pictures of lysosomal colocalisation of anti-ICAM-1 NCs. NCs are green (arrowheads), lysosomes are red (small-closed arrows), and NCs colocalised with lysosomes are green + red = yellow (large open arrows). Blue = nuclei, dashed lines = cell borders. Scale bar = 10 µm. (B) Absolute number of NCs colocalised with lysosomes in ASM-normal cells or ASM-deficient cells. (C) Percent NCs colocalised with

lysosomes in ASM-normal cells or ASM-deficient cells. Data are average ± SEM. Stats: Student's t-test, $p<0.05$, *compared anti-ICAM-1 NCs to anti-TfR NCs, #compared anti-ICAM-1 NCs to anti-PV1 NCs, $compared anti-TfR NCs to anti-PV1 NCs.

In ASM-normal cells, the absolute level of NC trafficking to lysosomes was highest for targeting to ICAM-1, followed by TfR, and lastly PV1, with maximum number of NCs in lysosomes at saturation (L_{max}) of 243.5, 48.0, and 29.5 NCs, respectively (figure 6.8B). This difference between anti-ICAM-1 NCs *vs.* anti-TfR NCs and anti-PV1 NCs is in line with receptor expression (figure 6.2) and binding (figure 6.4D). Furthermore, the trafficking rate was faster for anti-PV1 NCs compared to anti-ICAM-1 NCs and anti-TfR NCs, with half-times of 1.2 h *vs.* 3.4 h and 5.0 h, respectively (figure 6.8C). This is in line with the significantly faster uptake of anti-PV1 NCs (figure 6.6D). This might have been driven by the abundant presence of albumin, the main component of serum present in the cell medium. For instance, albumin influx into the brain has been shown to be caveolin-1 dependent[448,449]. Furthermore, vesicles containing albumin have been reported to end up in the endosomal system, for instance in late endosomes or lysosomes[450]. Thus, caveolae-targeted anti-PV1 NCs might have predominantly been co-transported with albumin, offering a possible explanation for their rapid transport to lysosomes.

In ASM-deficient cells, the absolute level of NC trafficking to lysosomes was also highest for targeting to ICAM-1, followed by TfR, and lastly PV1, with L_{max} of 160.3, 86.5, and 59.8 NCs in lysosomes, respectively (figure 6.8D). Thus, ASM deficiency did not change the relationship among all formulations with regards to lysosomal trafficking. Nevertheless, ASM deficiency mostly diminished the differences among all formulations with regards to trafficking rate, with half-times of 0.4 h, 1.2 h, 0.7 h for anti-PV1 NCs, anti-ICAM-1 NCs, and anti-TfR NCs, respectively (figure 6.8E), which might be the result of a stark increase in lysosomal trafficking of all NCs alike (as discussed in the following figure 6.9) to comparable levels.

In conclusion, the total delivery of NCs into lysosomes was highest for anti-ICAM-1 NCs, followed by anti-TfR NCs and anti-PV1 NCs in ASM-normal as well as ASM-deficient brain ECs, in line with receptor expression and binding, whereas the trafficking speed was surprisingly quickest for PV1 in ASM-normal cells, a property mostly lost in ASM deficiency.

To better understand the effect of ASM deficiency on each formulation, lysosomal trafficking was compared between ASM-normal and ASM-deficient cells (figure 6.9). The effect of ASM deficiency on the absolute number of NCs being trafficked to lysosomes varied among formulations. For instance, the L_{max} for anti-ICAM-1 NCs was reduced by 1.5-fold, from 243.5 to 160.3 NCs in lysosomes (figure 6.9A), in line with the decreased uptake of this formulation in ASM deficiency (figure 6.7C). The L_{max} for anti-TfR NCs increased by 1.8-fold, from 27.5 to 49.1 NCs in lysosomes (figure 6.9C), in line with the increased lysosomal trafficking rate observed (figure 6.9D), in combination with no significant effect of ASM deficiency on neither binding nor uptake (figure 6.5C, 3.7C). The L_{max} for anti-PV1 NCs deceased by 1.4-fold from 82.4 to 59.8 NCs in lysosomes (figure 6.9E).

Furthermore, lysosomal trafficking of NCs was significantly faster in ASM deficiency compared to ASM-normal cells for all pathways tested, with half-times decreasing by 2.8-fold from 3.3 h to 1.2 h for anti-ICAM-1 NCs (figure 6.9B), 3.3-fold from 3 h to 0.6 h for anti-TfR NCs (figure 6.9D), and 2.3-fold from 0.9 h to 0.4 h for anti-PV1 NCs (figure 6.9F).

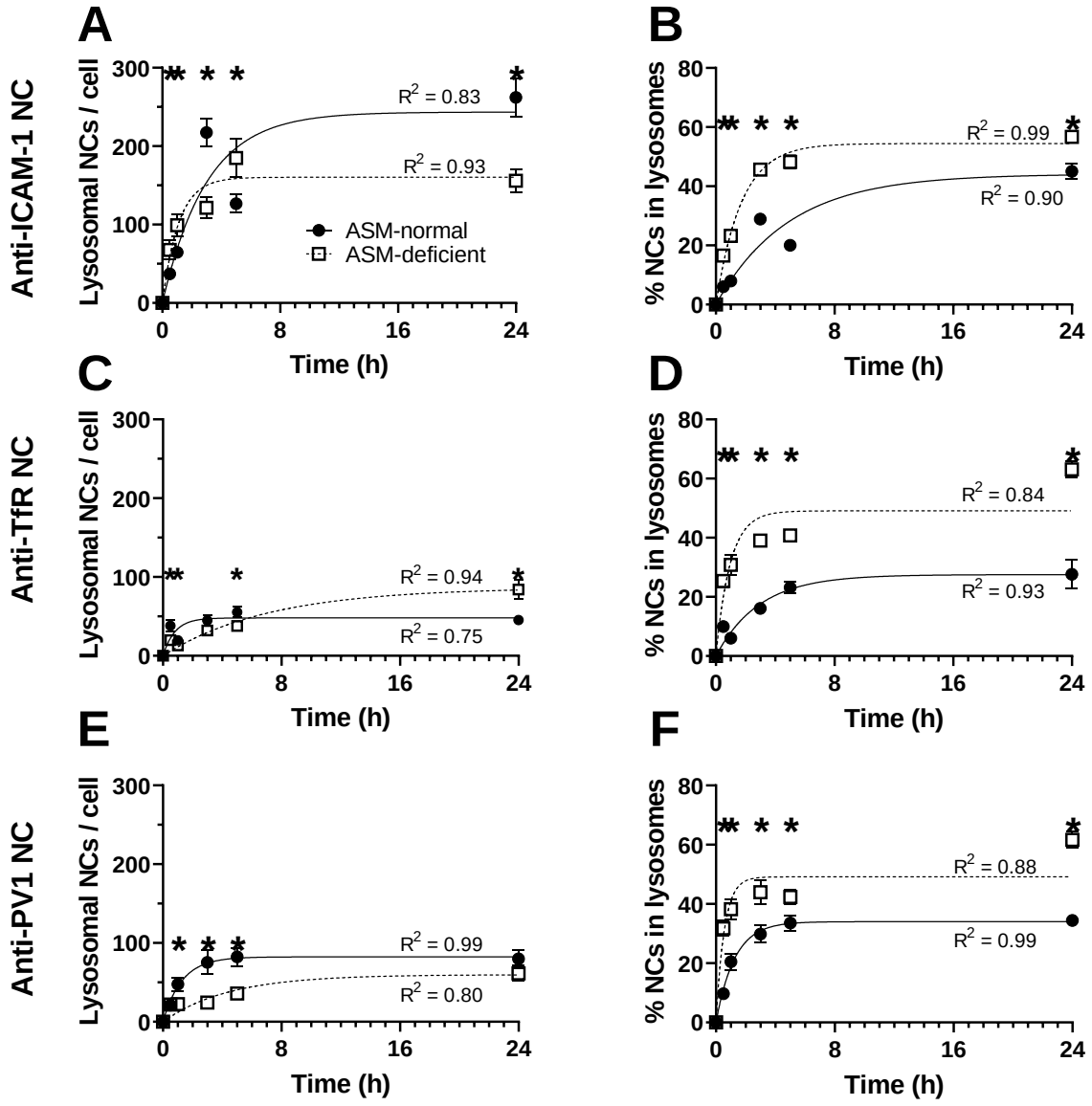

Figure 6.9 Effect of ASM deficiency on lysosomal transport of NCs by brain ECs. Cells were treated and analysed as above (figure 6.8). (A, C, E) Absolute numbers of respective NCs colocalising with lysosomes. (B, D, F) Percent of respective NCs in lysosomes of total NCs interacting with cells. Data are average ± SEM. Statistics: Student's t-test, $p<0.05$, *compared inflammation to NPD condition.

In general, aberrant intracellular trafficking in NPD has been described for different endocytosis pathways. For instance, the caveolae-mediated transport marker caveolin-1 accumulates in lysosomes upon progesterone- or U18666A-induced accumulation of cholesterol in lysosomes, the source of lipoprotein-derived cholesterol for the cell[451]. In turn, this results in a depletion of

cholesterol in the cell surface membrane, which also occurs when treating cells with low levels of cyclodextrin[452]. As well, cholera toxin B, a marker for caveolae-mediated transport, has been shown to change intracellular distribution upon endocytosis by NPD type A patient´s fibroblasts, from the Golgi apparatus to more endosomal localisation[410]. Similarly, lactosylceramide trafficking *via* caveolae-mediated transport has been found to be altered from a predominant uptake and recycling pathway to lysosomal trafficking in fibroblasts from NPD type A and C patients, as well as in NPC1-null CHO cells and chemically induced NPD type C macrophages (treated with U18666A or progesterone)[453,454]. Furthermore, the same study found that the trafficking of transferrin, usually also predominantly embarking on an uptake and recycling pathway *via* clathrin-mediated transport, had also been perturbed in fibroblasts from NPD type A and C patients, yet with unknown consequences for lysosomal trafficking[453]. These changes go hand in hand with a significant 1.7-fold increase in the total number of lysosomes per cell (measured in this study; data not shown) and are likely the result of the ample accumulation of a plethora of lipids (see introduction), which has been associate especially to aberrant cholesterol levels in several studies[409,412,452–455].

Thus, the underlying mechanism orchestrating the increase in lysosomal trafficking does not appear to be pathway specific, nor to be dependent on mono- *vs.* multi-valent interaction of cargo and receptor. In conclusion, ASM deficiency significantly increased the rate of NC lysosomal trafficking independently from the endocytosis pathway, similarly to aberrant trafficking of non-multivalent cargos such as lactosylceramide to lysosomes.

6.2.4. The Effect of ASM Deficiency on NC Transcytosis

Whereas lysosomal trafficking is important for the intracellular delivery of ERT, transcytosis plays an essential role at the BBB to deliver therapeutic NCs from the general circulation into the CNS. This is the reason why the effect of ASM deficiency on transcytosis by brain ECs was assessed.

Firstly, the barrier integrity in ASM deficiency was assessed to scrutinise the model used (figure 6.10). To this end, the transport of NCs across the BBB into the basolateral chamber after 30 min was quantified using a gamma counter. The barrier function was maintained in ASM deficiency with 8.6%, 2.2%, and 5.9% of all NCs added to the apical side having crossed the barrier after 30

min for anti-ICAM-1 NCs, anti-TfR NCs, and anti-PV1 NCs, respectively (figure 6.10). Although the values for anti-ICAM-1 NCs and anti-PV1-NCs were minimally enhanced by ASM deficiency compared to inflammation (figure 5.2A), further studies of transcytosis described below showed this may be due to enhanced transcytosis under this condition for these two formulations. In any case, all values stayed far below transport levels of NCs across a cell-free transwell, where 23.6% of all NCs were found in the basolateral chamber after 30 min (result not shown). Nevertheless, to avoid any confounding results, experiments were executed using the pulse-chase method described in Chapter 5. To this end, cells were incubated with NCs for 30 min to allow for binding, then washed to remove non-bound NCs from the apical chamber and also NCs in the basolateral chamber, and finally only cell-bound NCs were traced in the transcytosis experiments (see section 3.3.25.).

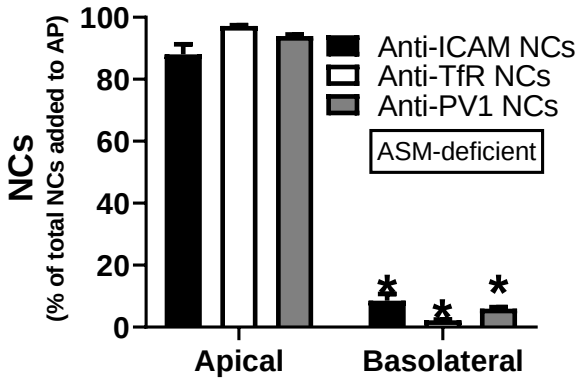

Figure 6.10 Barrier integrity of endothelial model used for transcytosis in ASM-deficient brain ECs. Cells were treated with 10 ng/mL TNFα (20 h treatment) and 20 µM imipramine (48 h treatment) to simulate ASM deficiency. To assess barrier integrity, ^{125}I-labelled NCs targeted to either ICAM-1, TfR, or PV1, were added to the apical side over the cells for 30 min. Then, the number of NCs in the apical and basolateral fraction were quantified using a gamma counter. Data are average ± SEM. Statistics: Student's t-test, $p<0.05$, *compared apical to basolateral.

All NCs tested were transcytosed across the BBB model in inflammation and NPD condition (figure 6.11). In inflammation, anti-ICAM-1 NCs were transcytosed in significantly higher numbers compared to anti-TfR NCs and anti-PV1 NCs, with 4.3×10^7 *vs.* 2×10^7 and 2.0×10^7 NCs per well, respectively at 5 h, and 9.7×10^7 *vs.* 3.5×10^7 and 4.8×10^7 NCs per well, respectively at 24 h (figure 6.11A), in line with receptor expression and binding observed above. Nevertheless, the transcytosis rates were comparable between all NCs tested (figure 6.11B). In NPD condition, anti-

ICAM-1 NCs remained the highest transcytosed NC compared to anti-TfR NCs and anti-PV1 NCs with 5.8 x 10^7 *vs.* 2.9 x 10^7 and 1.3 x 10^7 NCs per well, respectively at 2h, and 6.8 x 10^7 *vs.* 3.6 x 10^7 and 1.7 x 10^7 NCs per well, respectively at 24 h (figure 6.11C). Interestingly, the transcytosis rate in NPD condition was significantly higher for anti-PV1 NCs compared to anti-ICAM-1 NCs and anti-TfR NCs, with 51.1% *vs.* 23.0% and 30.2%, respectively (figure 6.11D). Nevertheless, given the comparably overall very low binding previously observed for anti-PV1 NCs, this significant difference did not have a great impact on total numbers of NCs transcytosed (figure 6.11C).

Given the relatively comparable transcytosis rates of all pathways tested in inflammation as well as NPD condition, the total number of NCs transcytosed was governed by binding and uptake observed above. For instance, in inflammation condition, anti-ICAM-1 NCs showed a great advantage in binding (figure 6.4D) which was reflected in transcytosis (figure 6.11A). Nevertheless, in ASM deficiency, the negative effects on anti-ICAM-1 NC uptake (figure 6.5C) diminished the difference of total NC transcytosis compared to other formulations after 24 h, although anti-ICAM-1 NCs still offered the most favourable transcytosis overall in both conditions.

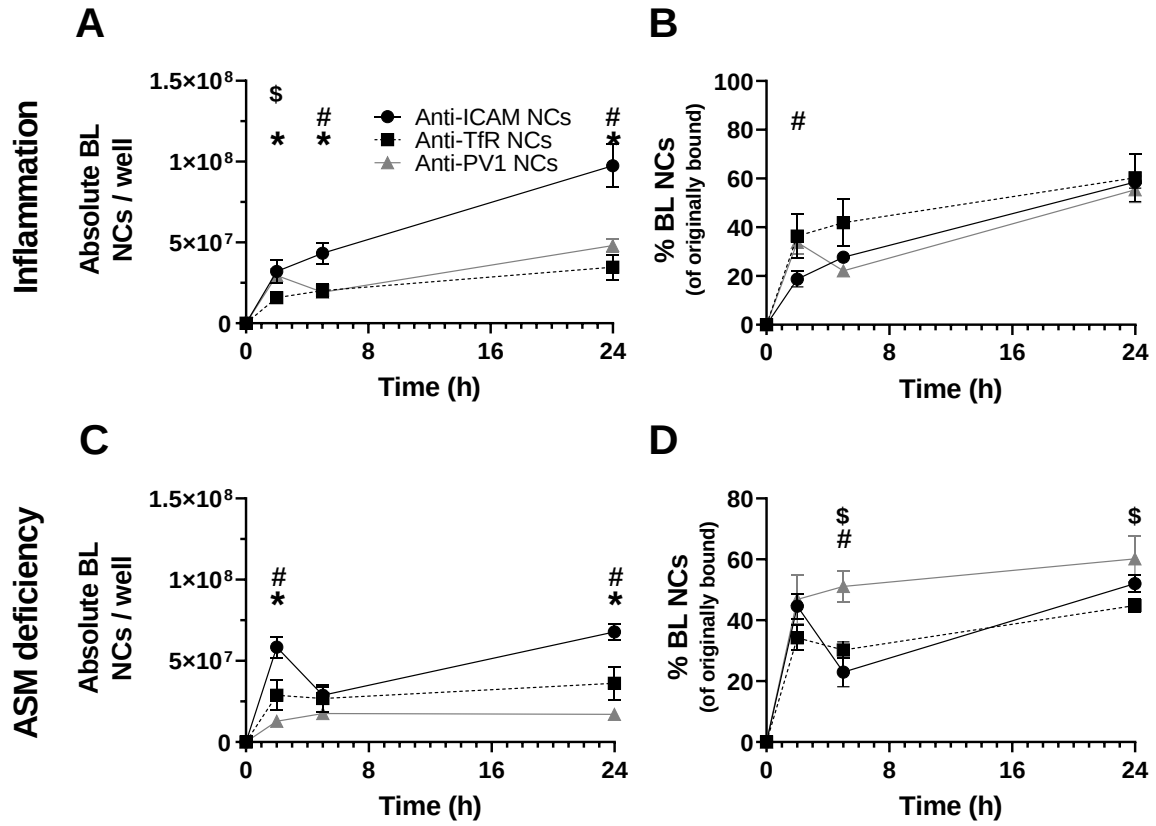

Figure 6.11 Comparative transcytosis of NCs targeted to different markers under inflammation or ASM deficiency. Brain ECs were treated with 10 ng/mL TNFα (20 h treatment) and 20 µM imipramine (48 h treatment) to simulate ASM deficiency or 10 ng/mL TNFα (20 h treatment) as an ASM-normal control. To assess transcytosis, ^{125}I-labelled NCs targeted to either ICAM-1, TfR, or PV1, were added to the apical chamber for a 30-min binding pulse, washed to remove non-bound NCs, and further incubated (if applicable) with NC-free medium for the indicated chase time. Then, the number of NCs in the basolateral fraction was assessed using a gamma counter. (A, C) Total NCs in the basolateral fraction per well in (A) inflammation or (B) ASM deficiency, (B, C) percent basolateral NCs of originally bound NCs in (A) inflammation or (B) ASM deficiency. Data are average ± SEM. Statistics: Student's t-test, $p<0.05$, *compared anti-ICAM-1 NCs to anti-TfR NCs, #compared anti-ICAM-1 NCs to anti-PV1 NCs, $compared anti-TfR NCs to anti-PV1 NCs.

To then gain a better understanding of the specific effect of NPD over inflammation alone, thus due to ASM deficiency, the transport of anti-ICAM-1 NCs, anti-TfR NCs, and anti-PV1 NCs was compared in these two models (figure 6.12). The absolute number of anti-ICAM-1 NC transcytosed over the 24 h testing period was significantly lower in NPD condition compared to inflammation condition, with 9.7 x 10^7 *vs.* 6.1 x 10^7 NCs transcytosed per well (figure 6.12A). However, transcytosis rate was faster for this formulation under ASM deficiency compared to inflammation alone, e.g., 44.6% *vs.* 18.7% of originally cell bound NCs were transcytosed,

respectively by 2 h (figure 6.12B). Although an opposite tendency was seen for anti-TfR NCs, no statistically significant differences were found for under these disease conditions (figure 6.12 C-D). Anti-PV1 NCs showed a similar trend to anti-ICAM NCs, where total transcytosis was significantly decreased in NPD condition compared to inflammation condition, e.g., from 4.8 x 10^7 to 1.7 x 10^7 NCs per well at 24 h, with a faster transcytosis rate for NPD, e.g., 51.1% *vs.* 22.1%, respectively (figure 6.12E-F).

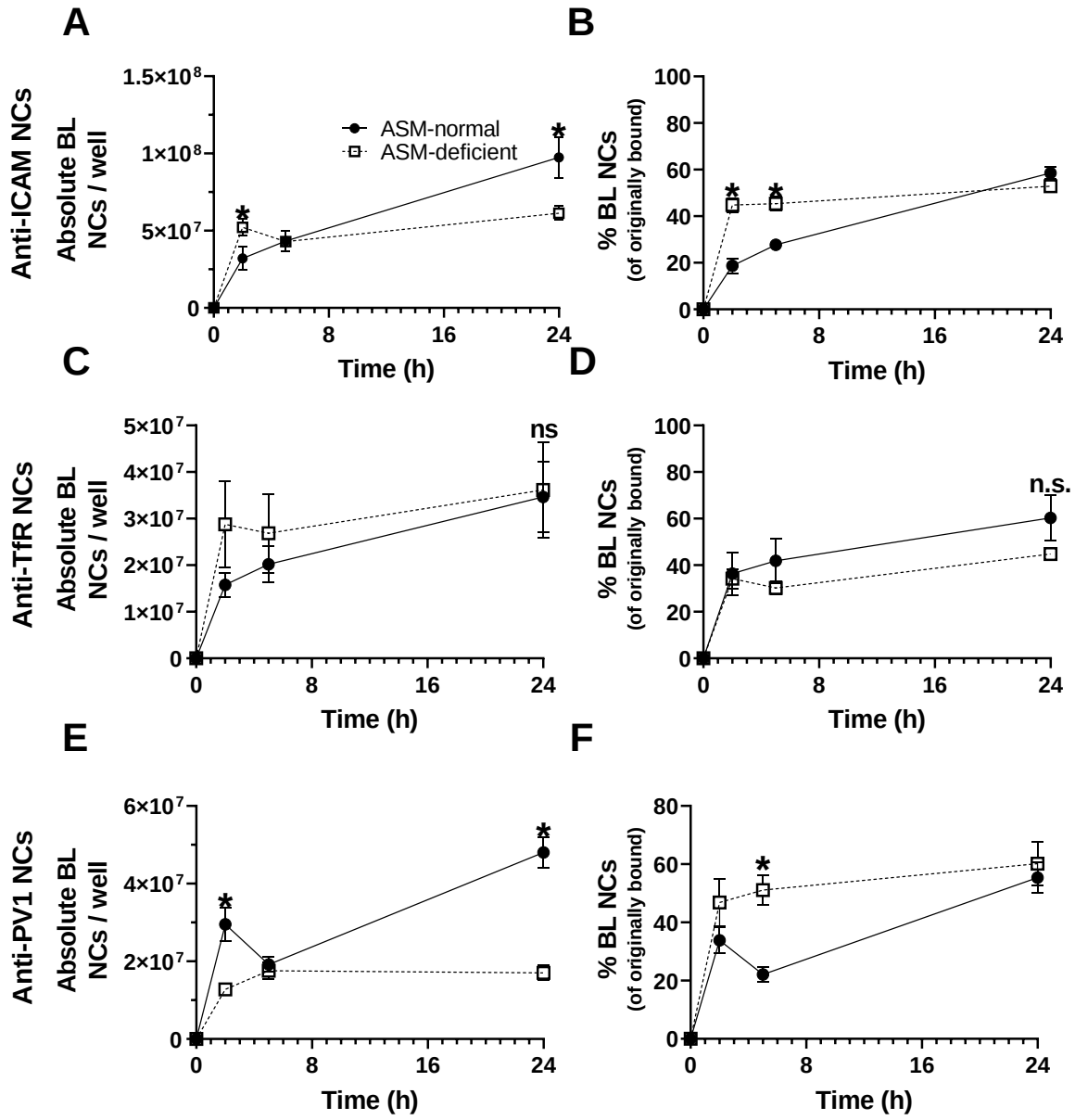

Figure 6.12 Effect of ASM deficiency on NC transcytosis by brain ECs. Cells were treated with 10 ng/mL TNFα (20 h treatment) and 20 μM imipramine (48 h treatment) to simulate ASM deficiency or 10 ng/mL TNFα (20 h treatment)

as an ASM-normal control. To assess transcytosis, ^{125}I-labelled NCs targeted to either ICAM-1, TfR, or PV1, were added to the apical chamber for a 30-min binding pulse, washed to remove non-bound NCs, and further incubated (if applicable) with NC-free medium for the indicated chase time. Then, the number of NCs in the basolateral fraction was assessed using a gamma counter. (A, C, E) Comparing absolute numbers of anti-ICAM-1 NCs (A), anti-TfR NCs (C), or anti-PV1 NCs (E) in the basolateral chamber in ASM-normal *vs.* ASM-deficient cells. (B, D, F) Comparing percent NCs of originally bound of anti-ICAM-1 NCs (B), anti-TfR NCs (D), or anti-PV1 NCs (F) in the basolateral chamber in ASM-normal *vs.* ASM-deficient cells. Data are average ± SEM. Statistics: Student's t-test, $p<0.05$, *compared ASM-normal to ASM-deficient.

Finally, to better understand the increased rate of transcytosis for anti-ICAM-1 NCs in NPD condition despite their reduced endocytosis rate (figure 6.7C), uptake from the basolateral side of brain ECs was assessed (figure 6.13). Similarly, to reduced uptake rate from the apical side, the rate of basolateral uptake of this formulation was decreased, which would explain that NCs that were transported to the basolateral side of brain ECs would more efficiency cross into the basolateral chamber due to lesser re-uptake by cells at this side (see Chapter 5).

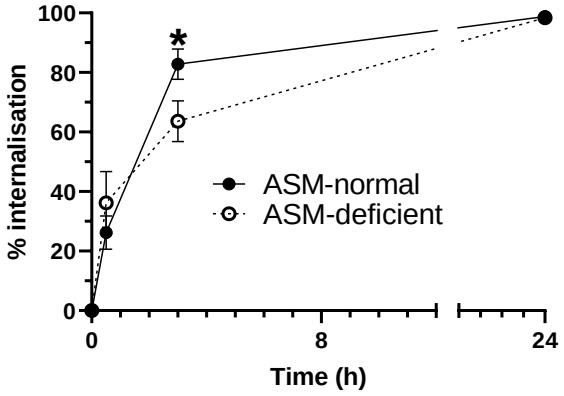

Figure 6.13 Internalisation of anti-ICAM-1 NCs from the basolateral side of ASM-normal *vs.* ASM-deficient brain ECs. Cells were incubated at 37 °C with 10 ng/mL TNFα (overnight treatment) and 20 µM imipramine (48 h treatment) to stimulate ASM deficiency or 10 ng/mL TNFα (overnight treatment) alone to simulate inflammation as control. Then, cells were incubated with FITC-labelled anti-ICAM-1 NCs (v2) for a 30-min binding pulse, washed to remove non-bound NCs, fixed, and counterstained with red secondary Ab to distinguish intracellular (green only) from cell-bound (green + red = yellow) NCs. Analysis was done by fluorescence microscopy as for figure 6.6. Data are average ± SEM. Statistics: Student's t-test, *$p<0.05$.

In summary (figure 6.14), with regards to absolute NC levels, ASM deficiency increased binding of anti-ICAM-1, whereas the other two formulations were not affected, according with receptor expression changes. Furthermore, NC uptake rate was unchanged for anti-TfR NCs and anti-PV1 NCs, for which the absolute level of NCs internalized by brain ECs by these routes did not vary.

However, the rate of uptake of anti-ICAM-1 NCs was decreased, as previously shown for other cell types, was compensated by the increased NC binding, resulting in no variation in the number of total NCs internalized by brain ECs. Interestingly, ASM deficiency increased the rate of lysosomal trafficking for all formulations, which may be related to the fact that lysosomes are typically engorged and widespread in cells affected by LSDs[33]. However, this condition affected absolute lysosomal trafficking differently for all formulations, with anti-ICAM-1 NCs showing a decrease, anti-TfR NCs showing an increase, and anti-PV1 NCs showing no change. In the case of anti-ICAM-1 NCs, this could be due to the fact that the rate of uptake of NCs from the basolateral side of brain ECs was also reduced. Since this was shown in Chapter 5 to also feed NCs to lysosomes, reduced basolateral uptake may result in reduced lysosomal trafficking in absolute values. In the case and anti-TfR NCs, since binding and uptake did not change by ASM deficiency, but the rate of lysosomal trafficking increased, this explains the increased absolute trafficking to this compartment. In the case of anti-PV1 NCs, binding and uptake were not affected, and the rate of lysosomal trafficking did, as for anti-TfR NCs; yet this does not result in enhanced absolute levels of lysosomal colocalization. Since transcytosis takes places in the same cells concomitantly to lysosomal transport, this difference could be due to different intertwined interactions between these two destinations. For instance, the rate and absolute transcytosis of anti-TfR NCs did not change in ASM deficiency, for which the enhanced lysosomal transport rate would result in more NCs ending up in this destination. However, for anti-PV1 NCs for the transcytosis rate and lysosomal transport rates increased, so this competing enhancement resulted in no variation in the absolute lysosomal colocalization. Nevertheless, this would be expected to increase the absolute number of NCs being transcytosed, but this value rather decreased. While there is no current explanation for this phenomenon, perhaps increased trafficking to other intracellular compartment or recycling back to the apical side could take place. This was similar for the case of anti-ICAM-1 NCs, where increased transcytosis rate led to decreased absolute transcytosis. Since this occurred concomitantly to decreased absolute lysosomal transport, these NCs may also reside in other intracellular compartment of recycle apically.

Absolute NC levels	Targeting		
	ICAM-1	TfR	PV1
Binding	↑	↔	↔
Uptake	↔	↔	↔
Lysosomal trafficking	↓	↑	↔
Transcytosis	↓	↔	↓

Trafficking rates	Targeting		
	ICAM-1	TfR	PV1
Binding	-	-	-
Uptake	AP: ↓ BL: ↓	↔ -	↔ -
Lysosomal trafficking	↑	↑	↑
Transcytosis	↑	↔	↑

Figure 6.14 Cartoon summarising the effects of ASM deficiency on NC trafficking by brain ECs compared to inflammation. Data represented compares TNFα+Imipramine condition vs. TNFα alone. AP = apical; BL = basolateral.

In conclusion, ASM deficiency had different effects on the brain EC interaction of anti-ICAM-1 NCs, anti-TfR NCs and anti-PV1 NCs. Anti-ICAM-1 NCs offered the overall most favourable results due to the highest number of NCs being transcytosed across this barrier and also delivered to EC lysosomes, both necessary NPD targets, therefore representing the most promising formulation out of the three tested in this study for the delivery of ERT in neuronopathic NPD.

6.3. Conclusion

NPD is a severe disease with up to date very few treatment options[246,392]. Although a novel ERT, the gold standard for the treatment of LSDs such as NPD, is currently in clinical trials, free enzyme cannot cross the BBB and is therefore ineffective in treating neuronopathic forms of NPD[245,246,273]. Nanomedicine, using NCs to deliver ERT, pose an interesting option to cross the BBB and deliver ERT into the CNS[245]. Nevertheless, ASM deficiency, hallmark of NPD, is known to alter several cellular functions which might affect the NC's interaction with target cells and intracellular trafficking[288,289,409–411]. Therefore, establishing the effects of ASM deficiency on those parameters is paramount for the development of ERT for NPD. In this study, NCs were targeted to markers of different endocytosis pathways for comparative purposes. Anti-ICAM-1 NCs were selected as the most promising candidate due to the highest receptor expression resulting in significantly

higher NC binding to cells, as well as absolute level of NC delivery both to EC lysosomes and across brain ECs. This dual targeting to lysosomes and across the BBB is favourable in NPD because not only the CNS but also the brain endothelium both need to be treated.

In addition, ASM deficiency increased the binding of anti-ICAM-1 NCs to brain ECs (figure 6.15), in agreement with receptor expression changes. The rate of NC uptake was decreased, as previously found for other cell types[80], while the absolute number of NCs internalized per cell did not vary, likely because of the increased binding found. Furthermore, NC uptake rate from the basolateral side was also decreased, just as apical rate was decreased, since it depends on the same CAM-mediated mechanism. As a consequence of the lower reuptake, NC transcytosis rate was significantly increased under NPD condition, as NCs would be able to traffic more efficiency to the basolateral chamber. Yet, absolute number of transcytosed NCs was lower in NPD. This was surprising because the absolute lysosomal trafficking of NCs was also lower in NPD. Hence, NCs may be trafficking to other intracellular compartments or recycled back to the apical chamber. The lysosomal trafficking rate was increased in NPD, perhaps because less NCs inside cells favour this kinetics.

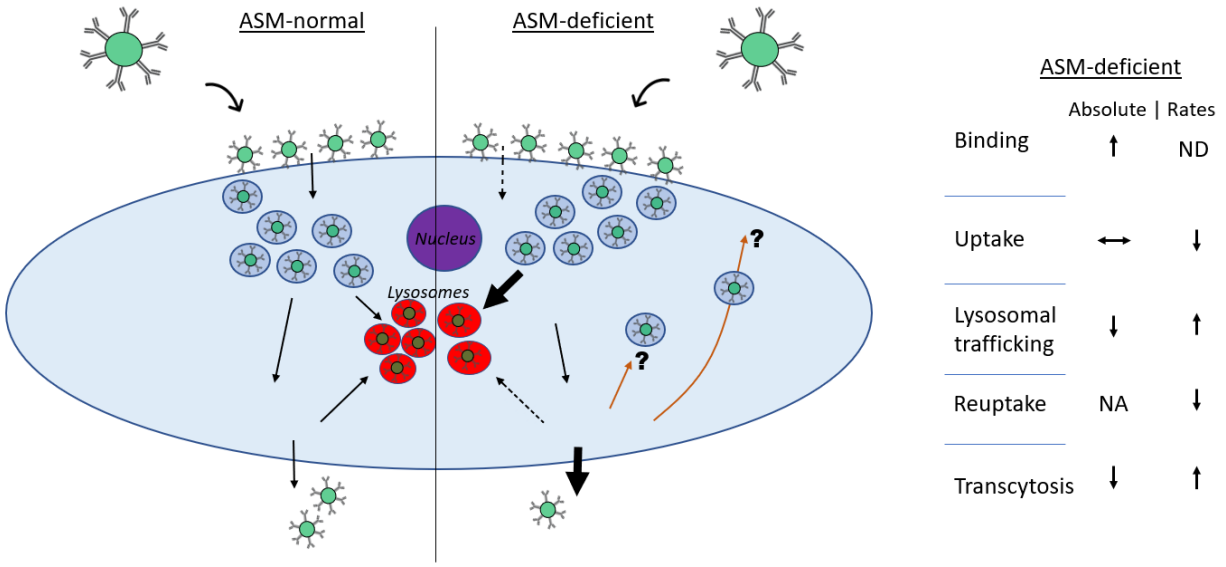

Figure 6.15 Cartoon summarising the effects of ASM deficiency on anti-ICAM-1 NCs as the most promising candidate for ERT. Arrows indicate trafficking rates. Thin arrow = unchanged rate, dashed arrow = decreased rate, thick arrow = increased rate. Brown arrows with question marks indicate uncertainty of existence of trafficking route. NA = not applicable, ND = not determined.

Chapter 7: Assess the Effect of GBA Deficiency on NC Transport for Gaucher Disease Enzyme Replacement Therapy.

7.1. INTRODUCTION

Deficiency of glucocerebrosidase (GBA), a lysosomal enzyme that degrades glucosylceramide (GlcCer), is the hallmark of Gaucher disease (GD, OMIM#230800,#230900,#231000)[456–458] and a major risk factor for Parkinson's disease[459]. GD is a rare genetic disorder belonging to the LSD group that results in the aberrant accumulation of the membrane glycosphingolipid GlcCer[460].

The prevalence of GD lies around 0.7 to 1.75 per 100,000 births in the general population and is as high as 118 per 100,000 in the Ashkenazi Jewish population[461]. Clinically, GD can be divided into 3 sub-types; non-neuronopathic type 1, infantile acute neuronopathic type 2, and subacute/chronic neuronopathic type 3 GD[460]. Disease onset varies between sub-types, with type 1 showing childhood or adult onset, type 2 showing infant onset, and type 3 childhood or adolescence onset[460]. To measure severity, tools have been developed for GD type 1[462,463] and type 3[464], usually leading to fatality in childhood or adulthood and childhood or adolescence, respectively, whereas no tools have been developed for infantile type 2 given patient's median life expectancy of only 9 months[233,234].Symptoms are highly variable not only among sub-types but also patients within the same group. Symptoms include hepato-splenomegaly, anaemia, and bone disease, and in the case of type 2 and 3, additional neurological deterioration[460,233]. Left untreated GD has life threatening consequences; however, treatments include EMA approved enzyme replacement therapy (ERT) drugs Cerezyme®[465], VPRIV®[466], and (not yet in the European Union) Elelyso®[467], as well as substrate reduction therapies (SRT) Zavesca®[468] and Cerdelga®[469], which generally work well and decrease disease severity[234,247,470,471]. Nevertheless, SRT is not the first choice therapy and rather used for those patients that cannot receive ERT[468,469].

ERT aims to restore intracellular enzyme levels via i.v. infusions of exogenous GBA, targeting the mannose-6-phosphate receptor to deliver the enzyme to lysosomes[191](also see section 1.5.). ERT has been used successfully since the 1990[191] and revolutionised GD treatment, improving quality of life and life expectancy[234,247]. Since exogenous enzyme is degraded over time, ERT is a chronic biweekly treatment to continuously restore enzyme levels with yearly costs around €124,000 and

€258,000 per patient[472,473].Despite successful treatment of visceral symptoms, ERT for GD is not an option for the treatment of neuronopathic symptoms of Gaucher type 2 and 3 because i.v. injected enzyme cannot penetrate the CNS due to the highly selective BBB[474–476] (see section 1.2.). Currently, there is no effective treatment available to treat GD type 2, whereas GD type 3 receive ERT to treat visceral symptoms, with currently no standardised treatment to address neurological symptoms of GD type 3[477]. Nevertheless, miglustat (Zaveska®) can cross the BBB and has been shown to be a promising alternative used for SRT in combination with ERT to improve the neurological manifestations of the disease of some GD type 3 patients (case studies[478–480]), whereas a randomised, controlled trial including 30 patients did not find significant improvements[481].

Given the lack of an effective treatment option for neuronopathic GD patients, there is a need for novel approaches to address this issue. Nanomedicine, using nanosized drug delivery systems to deliver drugs, can offer advantages such as protection of therapeutic cargo, improvement of cargo half-life in plasma, and specific targeting, such as into and across the BBB to improve pharmaco-distribution[31,32]. Hence, nanomedicine has great potential to improve ERT for neuronopathic LSDs[245,32] (see section 1.5.). Some nano-formulations have been designed and tested for GD specifically. PLGA nanoparticles of 50-100 nm diameter were shown to interact with and internalise into PD patient's fibroblasts with GBA mutations *in vitro,* where they could slightly restore the abnormal pH of lysosomes and consequently some pathological changes due to abnormal lysosomal functions[326]. Another study used calcium alginate microspheres to encapsulate GBA for localised delivery to bone[482]. Microspheres were shown to successfully encapsulate the enzyme without negatively affecting its biological activity and to release it in a sustained manner under physiological conditions[482]. Furthermore, GBA released from microspheres could be taken up by GD patient's fibroblasts *in vitro*[482]. In another approach, engineered exosomes loaded with GBA were produced in the human cell line HEK293[34]. Exosomes could be purified and retained their activity and were shown to be able to target endocytic compartments when incubated with their parent cell, HEK293[483]. Although intriguing, this study is still limited by the lack of characterization of GBA activity and targeting and drug delivery properties when used with more relevant cells such as GD patient material or chemically

induced GD models[483]. In addition, based on the limitation that most ERTs are dependent on the lysosomal delivery by the mannose-6-phosphate receptor (M6PR), one research group developed various fusion protein linking GBA and HIV-1 trans-activator protein transduction domain (TAT) [484]. This fusion protein was shown to retain its specific activity and to be able to enter GD patient's fibroblasts *in vitro* in a receptor-independent manner[484]. Yet, whilst being independent from M6PR, this approach also showed cytosolic delivery without lysosomal specificity, likely reducing the therapeutic efficacy of the treatment[484]. In yet another study, lysosome-targeted liposomes were used to deliver the ERT drug VPRIV® to monocyte-derived macrophages with chemically induced GD and GD patient's fibroblasts *in vitro*[485,486]. Liposomes modified with octadecyl-rhodamine B, previously shown to induce lysosome targeting[485], increased lysosomal trafficking of VPRIV® and significantly increased lysosomal substrate degradation in cells compared to free enzyme or plain liposomes[486]. Hence, nanomedicine shows potential for ERT to treat GD but to date it remains relatively unexplored.

Furthermore, given the natural lysosomal targeting of many receptor-mediated endocytosis pathways and the decreased lysosomal targeting when circumventing receptor-mediated endocytosis, such as in the TAT case[484], vesicular endocytosis upon receptor targeting remains a promising strategy to deliver GBA to lysosomes. Additionally, cargo cannot only be targeted to lysosomes upon receptor-mediated endocytosis, but also across biological barriers such as the BBB via the transcytosis pathway (see section 1.2.)[21,38]. The three major receptor-mediated transcytosis routes are CAM-, clathrin-, and caveolae-mediated pathways, all of which have been subject to investigation to be exploited for drug delivery[41,487,488]. Therefore, by exploiting these transport routes, NCs targeted to specific receptors on brain ECs could offer an alternative approach to deliver GBA for ERT across and into the BBB for the treatment of neuronopathic GD.

Parkinson's disease (PD) is a relatively common, age-related neurodegenerative disease (find a comprehensive review here[489]). The burden of PD is continuously rising, with 6.1 million cases in 2016 compared to 2.5 million cases in 1990, partly due to our aging population[2,490]. PD can be caused by single mutations, environmental factors, or a combination of several genetic and environmental factors[491,492]. Generally, PD is linked to dysfunction of vesicular transport,

lysosomes, mitochondria, synaptic transport, and neuroinflammation, resulting in the death of primarily dopaminergic neurons and causing motor symptoms[489]. Not only the cause but also the clinical symptoms, disease progression, and prognosis in PD show high heterogeneity, even in patients with identical underlying causes[489]. Symptoms include motor alterations, such as manifestations of dreamed movements in the REM phase and involuntary movements, as well as non-motor symptoms like depression and constipation[492,493]. PD patients have a decreased life expectancy, yet the disease progression is slow and patients generally live a long time with the disease[489,494]. Treatments are available and include continuous dopaminergic pharmacotherapy[495–498] and various treatments of non-motor symptoms such as depression[489]. Treatment costs vary depending on disease severity and treatment and are estimated to be between 10,000€ and 34,000€ per year per patient[499]. Interestingly, mutations in the GBA gene are a common risk factor for PD, found in 8.5% of all PD patients with multi-ethnic backgrounds[500]. Moreover, PD patients with GBA mutations show earlier onset of disease and more severe motor-symptoms, faster disease progression, and reduced survival[501]. This is why GBA is considered a novel target for potential PD treatment. For instance, Miglustat, a GlcCer synthase inhibitor used for SRT in GD, has shown protective properties against PD neurotoxicity[502] and increasing the levels of GBA expression by gene therapy in a GBA-associated PD mouse models could ameliorate PD symptoms and delay disease progression[503,504]. This is why novel therapies to treat neuronopathic GD may not only ameliorate neuronopathic GD but also delay the development of GBA-associated or idiopathic PD[505,506].

However, the effect of GBA deficiency, impacting both GD and PD, on transcytosis pathways between the circulation and the CNS remains poorly understood and could alter brain access of nanomedicine-based ERTs. This is because the accumulation of macromolecules in GBA deficiency is not restricted to lysosomes. For instance, in GD the initial accumulation of GlcCer happens primarily in lysosomes, but then it evenly distributes over all cellular membranes as accumulation increases[507,508], with mostly unknown consequences. On the plasma membrane, GlcCer primarily accumulates in lipid raft-like domains where it leads to decreased membrane fluidity and the formation of gel-like phase regions[509–513]. The expansion of raft-like domains was hypothesised to decrease the mobility of non-raft associated membrane constituents such as

TfR[509]. Furthermore, morphological changes and tubular-like structures on the plasma membrane have been observed, likely due to the accumulation of lipids with membrane bending properties, affecting cellular interactions[509,511,514]. Additionally, GBA deficiency has been shown to also affect intracellular trafficking. Clathrin-mediated endocytosis decreases in GBA-deficient macrophages[509] and, although not statistically significant, shows a similar tendency in fibroblasts from GD patients[409]. On the other hand, caveolae-mediated endocytosis seems unaffected in GBA-deficient macrophages[509] and was not substantially altered in fibroblasts from GD patients[409]. Lastly, GBA deficiency also alters vesicular transport. For instance, lactosylceramide, a substrate that is usually targeted to the Golgi apparatus upon endocytosis, was shown to be mistargeted to lysosomes in GBA-deficient fibroblasts and macrophages[515].

The current lack of effective treatment for neuronopathic symptoms of GD, with potential application for PD, requires novel solution to deliver ERT across the BBB into the CNS. Yet, given the described alterations in cell physiology and vesicular transport, GBA deficiency is likely to also alter NC-cell interaction and subsequent NC vesicular transport. However, the effect of GBA deficiency on NC transport has yet to be studied in brain ECs.

Therefore, in this chapter I aimed to study the effects of GBA deficiency on expression and display of endocytic machinery, ICAM-1 lateral mobility and interaction with NC, NC binding and uptake, lysosomal trafficking of NCs, and transcytosis of NCs. This is relevant as a better understanding of NC-cell interaction and transport into and across the BBB is paramount to develop novel therapeutic NCs and to identify the most amenable routes for an efficient delivery of therapeutic enzyme to GBA-deficient cells for ERT in GD, especially important for the more severe neuronopathic types A and C.

7.2. RESULTS AND DISCUSSION

7.2.1 Verification of Chemical Induced GBA Deficiency in Brain ECs as a GD Model

A chemical GD model was used in the present work due to the lack of commercially available brain ECs from GD patients. The model consisted of treating human brain microvascular endothelial cells with conduritol-β-epoxide (CBE), which covalently binds and inactivates GBA[307], thereby resulting in the aberrant accumulation of GlcCer such as seen in GD[308]. In fact, CBE has already been used to induce GBA deficiency *in vitro*[516–518] and *in vivo*[519,520] to study GD. Firstly, the suitability of using CBE to induce GBA deficiency to produce a GD model was assessed. In the present work, GBA deficiency was studied in brain ECs incubated with 200 µM CBE for 72 h (see section 3.3.11.).

To validate the model, the Muro lab at the University of Maryland (USA) used cell lysates from control and CBE-treated brain ECs and incubated it with 4-methylumbellliferyl-β-glycopyranoside, a GBA substrate, to assess the activity of the enzyme. Samples from cells that were treated with CBE showed significantly less enzyme activity when incubated with this substrate compared to control cells (figure 7.1A). Furthermore, in line with these findings, a significant 2.8-fold increase of intracellular GBA substrate (analogue N-hexanoyl-NBD-glucosylceramide) accumulation was measured in cells treated with CBE compared to control cells (figure 7.1B). Therefore, these findings validate the pharmacological model of GBA deficient human brain ECs.

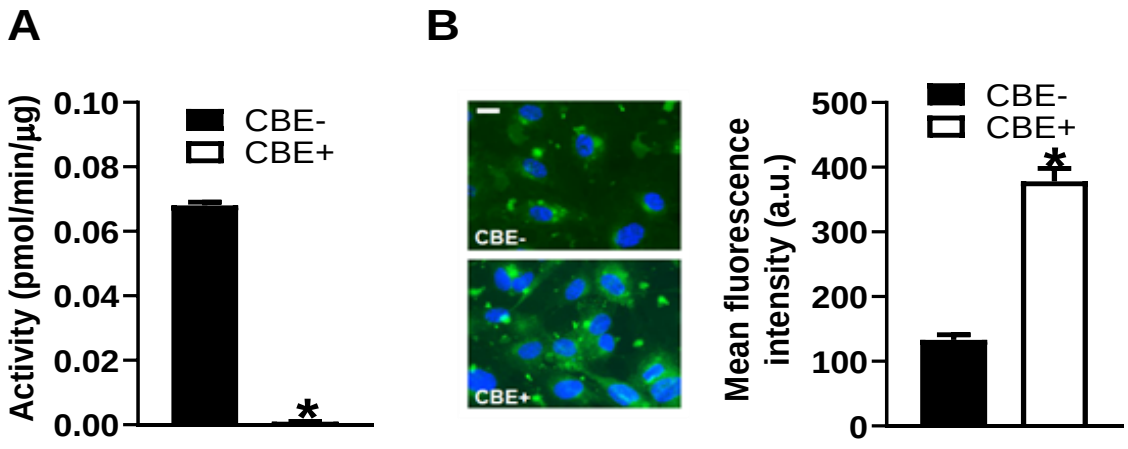

Figure 7.1 Model for GBA deficient human brain ECs. Human brain ECs were incubated at 37 °C with 10 ng/mL TNFα (overnight treatment) and 200 µM CBE (72 h treatment) to simulate GBA deficiency, or 10 ng/mL TNFα (overnight treatment) alone to simulate inflammation as GBA-normal control. (A) Cells were lysed, and samples were incubated

for 30 min at 37 °C with a GBA substrate, 4-methylumbellliferyl-β-glycopyranoside, whose enzymatic cleavage results in a blue-fluorescent product, measured by spectrophotometry. (B) Cells were incubated with 5 μg/mL of green-fluorescent N-hexanoyl-NBD-glucosylceramide (GlcCer), a GBA substrate, for 48 h after the first 24 h of the CBE treatment. (Left) Micrographs, (right) quantification of mean fluorescent intensity per cell. Scale bar = 10 μm; green = GlcCer; blue = cell nucleus stained with DAPI. (A, B) Data are mean ± SEM. (*p<0.05, Student's t-test). Performed by the Muro lab at the University of Maryland (USA).

7.2.1. The Effect of GBA Deficiency on Expression and Display of Endocytosis Machinery in Brain ECs

The number of receptors displayed on the surface of cells is an important parameter to determine the interaction of a receptor-targeted NCs with the target cell. Higher receptor expression usually increases NC binding due to the higher number of connections able to form between the NC surface and the cell, which increases the binding avidity[521,522]. Yet, up to date, not much is known about how GBA deficiency affects cell surface receptors and endocytic partners in brain ECs. Hence, this was therefore assessed next using the validated model for GBA deficiency.

As a first step towards understanding the effect of GBA deficiency on NC transport, expression of the target receptors was analysed by flow cytometry (figure 7.2). Since the effect of inflammation (TNFα treatment) had been evaluated in Chapter 6, here we focussed on the additional role of GBA deficiency using CBE. ICAM-1 was the most highly expressed of the three markers as observed from flow cytometry data, followed by TfR and then PV1 (figure 7.2). Inducing GBA deficiency showed a minimal increase in ICAM-1 expression and no observable effects on TfR or PV1 (figure 7.2). GBA deficiency-induced alteration of receptor expression is possible based on literature, since altered protein expression in GD cells has been previously reported[285,523]. For instance, a decrease in soluble TfR, indicative of cellular TfR expression, has been observed along with other therapeutic effects in GD patients following the ERT[524], suggesting that this receptor was upregulated in GBA deficiency. Nevertheless, the mechanistic relation between GlcCer accumulation and altered receptor expression remains elusive.

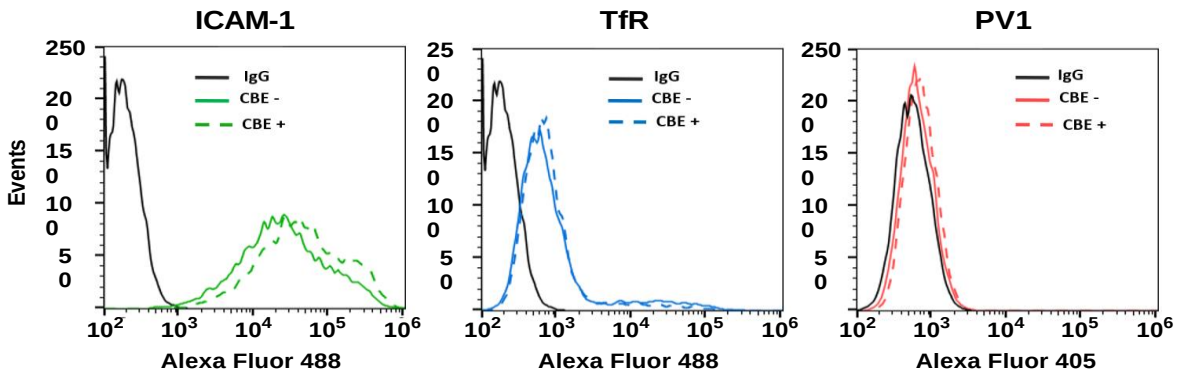

Figure 7.2 Receptor expression in GBA deficient brain ECs. Human brain ECs were incubated at 37 °C with 10 ng/mL TNFα (overnight treatment) and 200 µM CBE (72 h treatment) to simulate GD, or 10 ng/mL TNFα (overnight treatment) alone to simulate inflammation as GBA control. Then, cells were detached using trypsin, collected by centrifugation, and fixed using PFA. Subsequently, cells were stained at 4 °C with primary Ab to label surface receptors, as indicated, washed to remove non-bound Ab, and then stained at 4 °C with green-fluorescent secondary Ab against the primary Ab, and DAPI to stain the nuclei. The expression levels of the indicated surface receptors were quantified by multilaser analysis using a flow cytometer and associated FlowJo software.

Nevertheless, receptor expression is not the only factor determining NC binding and uptake. Receptor distribution and colocalization with endocytic elements are also important parameters that might influence the interaction of multivalent NCs with cells. Whereas receptor expression levels have been shown to influence NC binding and uptake as a function of receptor density[521,522], receptor distribution on different regions of the plasma membrane can influence ligand affinity and binding, e.g., through differences in spatial segregation and localised areas of receptor crowding[525,526]. Furthermore, other endocytic elements are paramount for endocytosis upon receptor activation. For instance, clathrin and caveolin-1 are structural proteins involved in the formation of vesicles[527,528]. Many uptake routes rely on the presence of such endocytic elements for the internalisation of receptor-bound cargo and a lack of colocalisation of a receptor with its intracellular partner may allow for binding but diminishes uptake. Therefore, the effect of GBA deficiency both on receptor distribution and their partners was assessed. This was performed by Dr. Enric Gutierrez Martinez in Prof. Maria Garcia-Parajo's laboratory at the Institute of Catalonia for Photonic Sciences (ICFO), Barcelona.

Using super resolution microscopy, GBA deficiency was observed to significantly decrease the amount of caveolin-1 nanodomains, whereas it did not affect ICAM-1, TfR, PV1 (figure 7.3A),

expected because of the minimal changes seen by flow cytometry (figure 7.2) or clathrin density (figure 7.3A). Consequently, when analysing the nearest neighbour distance (NND), which indicates the distance of a given receptor domain to the nearest given endocytic partner, GBA deficiency was shown to increase the average distance of each receptor with caveolin-1, in line with its decreased number of nanodomains (figure 7.3A), whereas the NND with clathrin was unaffected (figure 7.3C), in line with unaffected clathrin nanodomains (figure 7.3A).

Due to the pivotal role of caveolin-1 in the formation of caveolae[527], the reduced number of caveolin-1 nanodomains and thus availability of caveolin-1 in GBA deficiency are likely to affect NC transport when targeting this pathway. Furthermore, the receptor domain density was highest for ICAM-1, then TfR, and lastly PV1 (figure 7.3A), in line with receptor expression seen by flow cytometry (see figure 7.2). Also, the colocalisation of each receptor with the endocytic partners clathrin and caveolin-1 was not significantly affected by GBA deficiency (figure 7.3B). For instance, as expected, ICAM-1 showed no colocalisation with either clathrin or caveolin-1, due the CAM-pathway's independence from classical endocytosis routes[160], whereas TfR colocalised more with clathrin than caveolin-1, and PV1 colocalised more with caveolin-1 than clathrin (figure 7.3B), expected since they are their respective endocytic partners[529,530]. In conclusion, GBA deficiency did not significantly affect elements of the cell machinery needed for the endocytosis of anti-ICAM-1 NCs[86] and anti-TfR NCs[87], whereas the reduction of caveolin-1 nanodomains near the cell surface might affect the trafficking of anti-PV1 NCs[88].

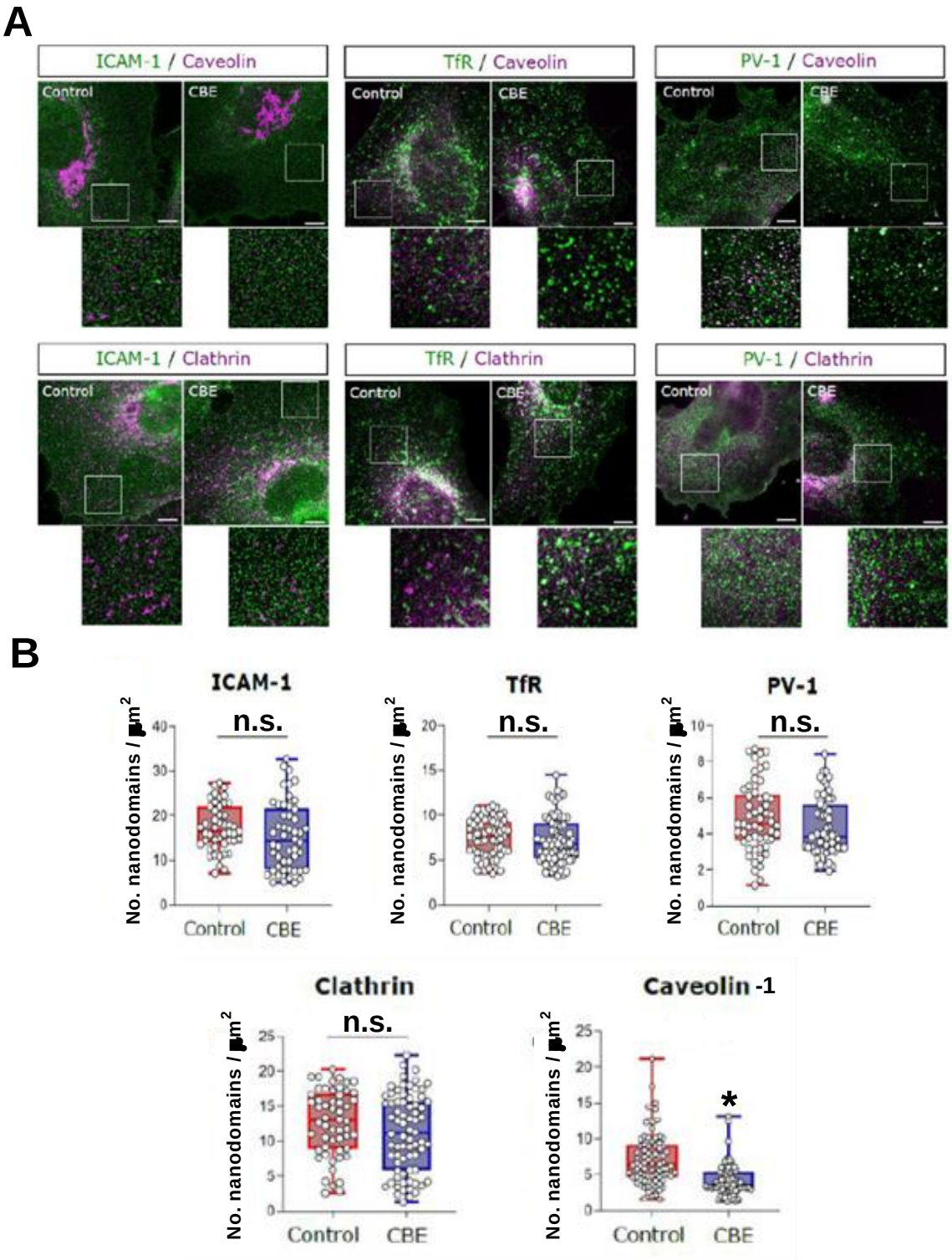

Figure **7.3 Display of receptors and other endocytic elements in GBA deficiency.** Brain ECs were incubated at 37 ℃ with 10 ng/mL TNFα (overnight treatment) and 200 µM CBE (72 h treatment) to simulate GBA deficiency, or 10 ng/mL TNFα (overnight treatment) alone as GBA-normal control. (A) Representative stimulated emission depletion

(STED) microscopy images of cells immunostained for ICAM-1, TfR, or PV1 together with clathrin and caveolin-1 (top). (B) Quantification of nanodomain density for the different markers stated above. Each dot represents the average nanodomain density per cell. (*p<0.05, Student's t-test; n.s. = not significant) (bottom). This experiment was performed by Dr Enric Gutierrez Martinez in Prof Maria Garcia-Parajo's laboratory at the Institute of Catalonia for Photonic Sciences (ICFO), Barcelona.

7.2.2. The Effect of GBA Deficiency on NC Transcytosis in Brain ECs

Due to the pathological similarities between GD and NPD, both showing aberrant accumulation of undegraded lipids in lysosomes, and given the results obtained for NPD in Chapter 6 showing that binding and uptake were mostly governed by the stark differences in receptor expression levels in spite of little pathology-specific changes, the focus for GD was directly set on transcytosis of NCs targeted to these three routes to identify the most suitable pathway for ERT in GD. A GBA-deficient BBB model was used to study the specific effect of GBA deficiency on NC transcytosis via three distinct endocytosis routes, whereas a BBB inflammation model (GBA normal) served as a control due to the common association of GD with inflammation[531,532] (figure 7.5 and figure 7.6).

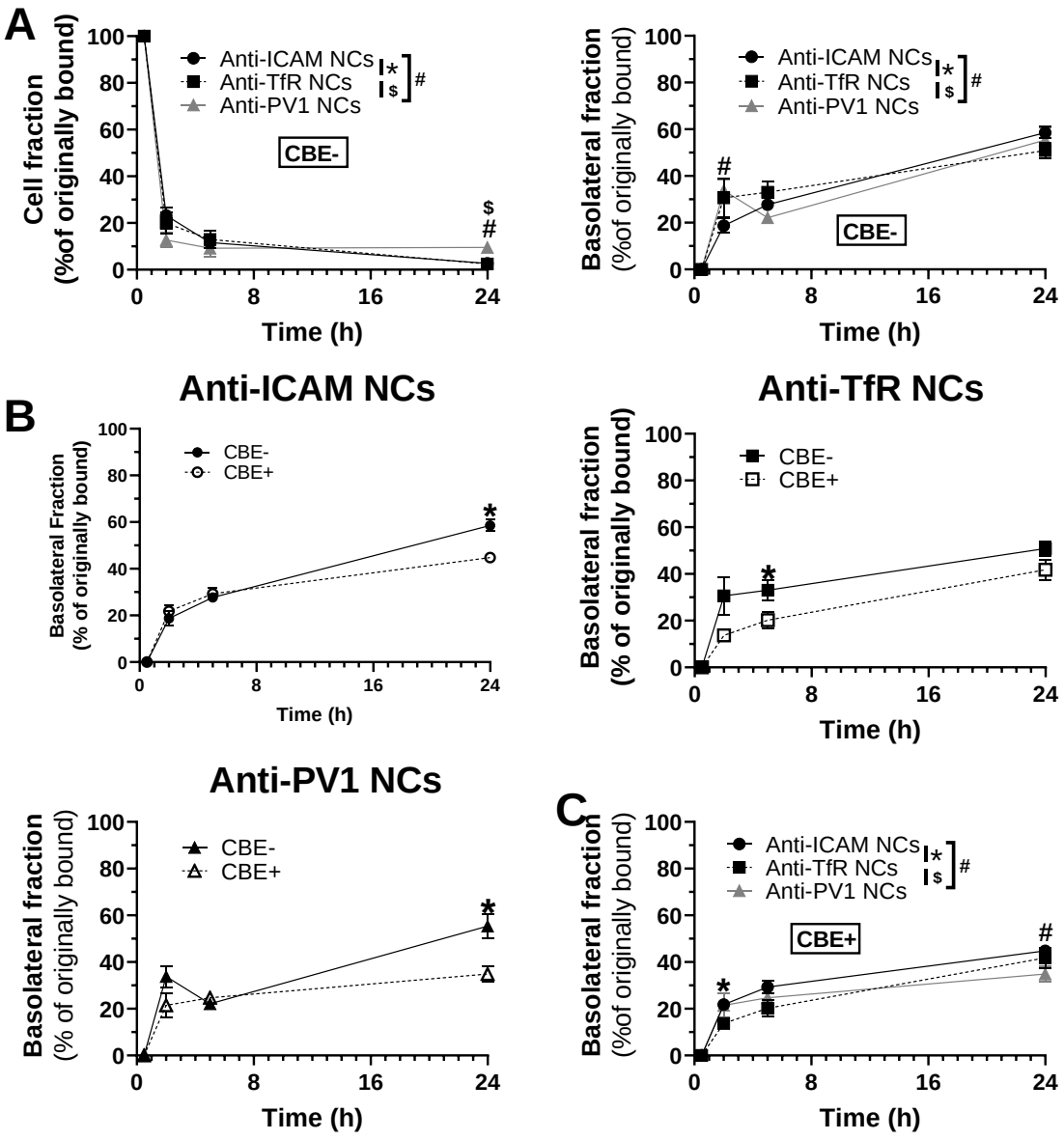

Figure 7.5 Transcytosis rates for targeted NCs in GBA-normal *vs.* GBA-deficient brain ECs. Brain ECs were incubated at 37 °C with 10 ng/mL TNFα (overnight treatment) and 200 μM CBE (72 h treatment) to simulate GBA deficiency, or 10 ng/mL TNFα (overnight treatment) alone as GBA-normal control. To assess transcytosis, ^{125}I-labelled NCs (v2) were added to the apical chamber above cells for a 30-min binding pulse, washed to remove unbound NCs, and cells were further incubated with NC-free medium for the indicated chase time. Then, the amount of NCs in the cell and basolateral fractions were measured using a gamma counter and expressed as percent of NCs originally bound to cells, illustrating transport rates. (A) Cell association (left) and transcytosis (right) of NCs targeted to each route in GBA-normal cells. (B) Transcytosis rates comparing GBA-normal *vs.* GBA-deficient cells. (C) Comparative transcytosis of different NCs targeted to each endocytosis route in GBA-deficient cells. Data are average ± SEM. Statistics: Student's t-test, $p<0.05$, *compared anti-ICAM-1 NCs to anti-TfR NCs (A, C); #compared anti-ICAM-1 NCs to anti-PV1 (A, C); $compared anti-TfR NCs to anti-PV1 NCs (A, C); *compared GBA-normal to GBA deficiency (B).

In the GBA-normal model, all NCs disappeared from cells at comparable rates, with anti-PV1 NCs showing a slightly higher cell retention after 24 h with 9.5%, *vs.* 2.7% and 2.4% cell levels for anti-ICAM-1 NCs and anti-TfR NCs, respectively (figure 7.5A left). Concomitantly, NCs targeted to either pathway appeared progressively in the basolateral chamber at comparable rates around 50-60% at 24 h, indicating the potential of all NCs tested for transcytosis (figure 7.5A right). In terms of absolute number of NCs (figure 7.6), anti-ICAM-1 NCs showed significantly higher levels associated with cells compared to anti-TfR NCs and anti-PV1 NCs, with 1.7 x 10^8 *vs.* 6.8 x 10^7 and 8.7 x 10^7 NCs/well, respectively, at 0.5 h, and 3.8 x 10^7 *vs.* 1.7 x 10^7 and 1.1 x 10^7 NCs/well, respectively, at 2 h. Whereafter cell retention was relatively similar for all formulations except for anti-PV1 NCs which showed slightly higher levels at 24 h compared to anti-TfR NCs (figure 7.6A). The significantly higher cell retention of anti-ICAM-1 NCs up to 2 h is likely the result of significantly more binding compared to anti-TfR NCs and anti-PV1 NCs, as suggested by receptor expression levels (figure 7.2) and receptor density (figure 7.3A). Furthermore, the significantly higher cell retention of anti-PV1 NCs in GBA-normal cells at 24 h is in line with the lower disappearance rate at that time point (figure 7.5A). Whereas this difference manifested itself between anti-TfR NCs and anti-PV1 NCs (figure 7.6A), the lower cell retention rates of anti-ICAM-1 NCs (figure 7.5A) is likely compensated by significantly higher interaction of those NCs with cells compared to anti-PV1 NCs (figure 7.6A), leading to comparable total amount of both formulations in cells at 24 h (figure 7.6A).

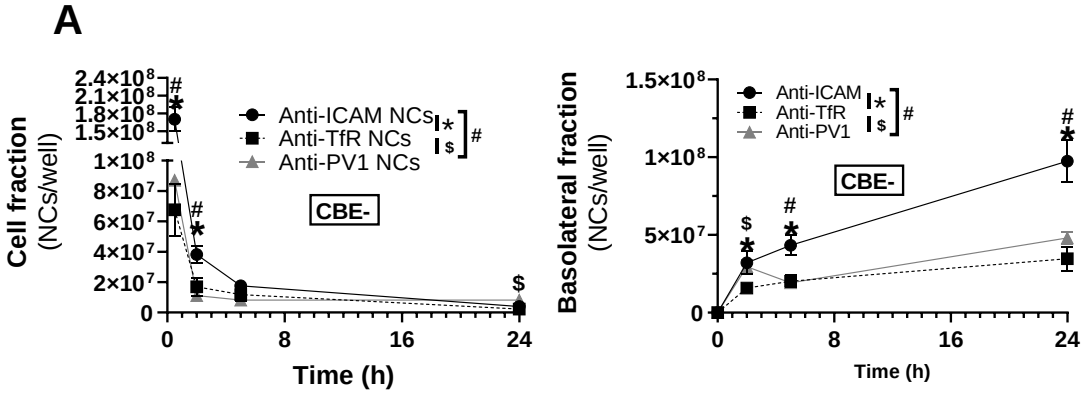

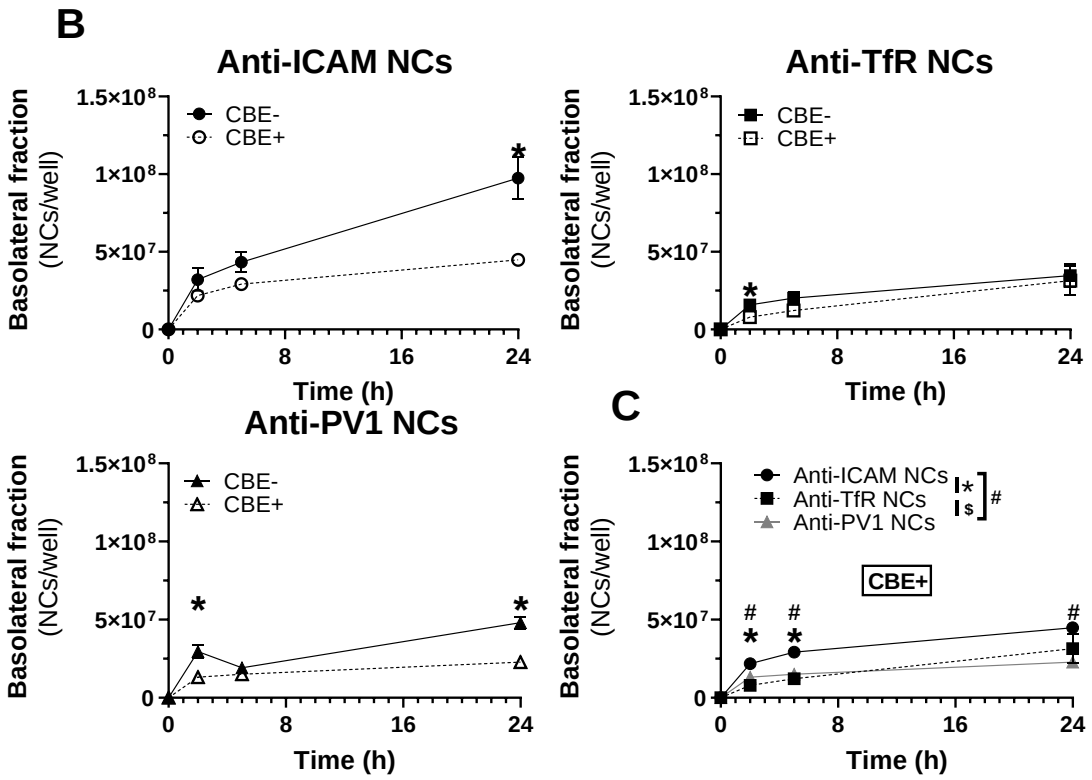

Figure 7.6 Absolute numbers of NCs associated with cells and transcytosed in GBA-normal *vs.* GBA-deficient brain ECs. Brain ECs were incubated at 37 °C with 10 ng/mL TNFα (overnight treatment) and 200 µM CBE (72 h treatment) to simulate GBA deficiency, or 10 ng/mL TNFα (overnight treatment) alone as GBA-normal control. To assess transcytosis, ^{125}I-labelled NCs (v2) were added to the apical chamber for a 30-min binding pulse, washed to remove unbound NCs, and further incubated (if applicable) with NC-free medium for indicated chase time. Then, the amount of NCs in the cell and basolateral fraction was assessed by radiotracing as total NCs in the indicated fraction. (A) Comparison of cell association and transcytosis of NCs targeted to all uptake routes per well in GBA-normal cells. (B) Comparison of transcytosis in GBA-normal *vs.* GBA-deficient cells. (C) Comparison of transcytosis of NCs targeted to all routes in GBA-deficient cells. Data are average ± SEM, ($p<0.05$, Student's t-test, *comparing anti-ICAM-1 NCs to anti-TfR NCs (A, C) *compared GBA-normal to GBA deficiency (B), #compared anti-ICAM-1 NCs to anti-PV1, $compared anti-TfR NCs to anti-PV1 NCs.).

The absolute transcytosis of NCs in GBA-normal cells was highest for anti-ICAM-1 NCs compared to anti-TfR NCs and anti-PV1 NCs, with 4.3 x 10^7 *vs.* 2.0 x 10^7 and 1.9 x 10^7 NCs/well, respectively, at 2 h and 9.7 x 10^7 *vs.* 3.5 x 10^7 and 4.8 x 10^7 NCs/well, respectively, at 24 h (figure 7.6A right). This result is in line with comparable transcytosis rates for all NCs tested (figure 7.5A) in combination with significantly higher ICAM receptor expression (figure 7.2).

Then, the effect of GBA deficiency on NC transcytosis was assessed (figure 7.5B and figure 7.6B). GBA deficient cells showed decreased transcytosis rates and total numbers for all NCs, yet to

different degrees. For instance, the transcytosis rates of anti-ICAM-1 NCs and anti-PV1 NCs significantly decreased at 24 h, whereas anti-TfR rather showed a tendency for decreasing at all time points yet was only significant at 5 h (figure 7.5B). In line with these results, the absolute amount of transcytosed NCs was also decreased for all NCs tested: e.g., for anti-ICAM-1 NCs and anti-PV1 NCs by 54% and 53%, respectively, at 24 h, whereas anti-TfR NCs showed the most significant decrease of 50% at 2 h (figure 7.6B).

Ultimately, the transcytosis of all NCs was compared in GBA-deficient cells to identify the most suitable route. Transcytosis rates were comparable among all NCs with only little differences (figure 7.5C). For instance, the rate for anti-TfR NCs was initially lower and continuously approached the rate of anti-ICAM-1 NCs, whereas the rate of anti-PV1 NCs was initially comparable to anti-ICAM-1 NCs but saturated earlier. Hence, anti-ICAM-1 NCs showed a higher transcytosis rate compared to anti-TfR NCs at 2 h, whereas it showed a significantly higher transcytosis rate compared to anti-PV1 NCs at 24 h (figure 7.5C). In terms of absolute levels, anti-ICAM-1 NCs were transcytosed the most compared to anti-TfR NCs and anti-PV1 NCs, with 2.2 x 10^7 *vs.* 7.9 x 10^6 and 1.3 x 10^7 NCs/well, respectively, at 2 h and 2.9 x 10^7 *vs.* 1.2 x 10^7 and 1.5 x 10^7 NCs/well, respectively, at 5 h. At 24 h, anti-ICAM-1 NCs were still transcytosed significantly more than anti-PV1 NCs, whereas there was only a trend for higher transcytosis compared to anti-TfR NCs due to highly variable results for anti-TfR NCs at this time point (figure 7.6C).

Interestingly, GBA deficiency decreased the transcytosis rate and total numbers of all NCs, yet at different time points. This might indicate a generic effect of GBA deficiency on transcytosis, yet different pathways may react in a specific manner to the pathological alterations. Furthermore, there was no specific effect of the decreased caveolin-1 on PV1-mediated transport observed, which suggests that either there is still sufficient caveolin-1 available for caveolae-mediated endocytosis despite its downregulation, or that anti-PV1 NCs are partly internalised through compensating mechanisms, such as *via* clathrin-mediated endocytosis, as described elsewhere[533].

In conclusion, GBA-deficiency decreased the transcytosis rates of NCs independently from the pathway targeted, resulting in comparable transcytosis rates for all NCs, whereas anti-ICAM-1 NCs showed the highest overall absolute transcytosis, in line with receptor expression, thus making this the most promising pathway for ERT across the BBB in GBA deficiency.

7.2.3. The Effect of GBA Deficiency on Binding and Uptake of anti-ICAM-1 NCs in Brain ECs

Next, to better understand the trafficking results, i.e., the reduction in transcytosis rates and/or absolute NCs transcytosed across GBA-deficient brain ECs in spite of unchanged receptor expression and density (figures 7.2 and 7.3A), the effect of GBA deficiency on preceding events, such as uptake and binding, were assessed. This was investigated focusing on the most promising candidate defined above, anti-ICAM-1 NCs.

To synchronise NC uptake and separate this process from binding, GBA-normal and GBA-deficient brain ECs were first incubated with anti-ICAM-1 NCs for 30 min at 4 °C to allow for binding without uptake. Then, cells were washed to remove non-bound NCs and further incubated at 37 °C, allowing for "synchronosed" uptake. The uptake rates of anti-ICAM-1 NCs by GBA-normal and GBA-deficient brain ECs were comparable at 15 min with 48% and 50% of all cell-associated NCs being internalised, respectively. Uptake increased in both cell models at 30 min, with GBA-deficient cells showing a tendency for a slightly higher uptake rate. At 60 min, there was a significantly higher uptake rate of anti-ICAM-1 NCs by GBA-deficient brain ECs compared to GBA-normal cell, with 86% compared to 69 % uptake, respectively (figure 7.7A). This result could be explained because GBA deficiency results in the accumulation of GlcCer and other phospho- and sphingolipids in the detergent-insoluble domains on the plasma membrane[507,510,512,513]. There are three properties of GlcCer that might help to understand the observed increase in CAM-mediated endocytosis. Firstly, the accumulation of GlcCer has been shown to increase the release of Ca^{2+}, which is shown to be involved in CAM-mediated endocytosis[159,534], from the endoplasmatic reticulum upon stimulation[224]. Secondly, GBA deficiency might increase ASM-mediated production of ceramide, crucial for CAM-mediated uptake[161]. This is because both enzymes, GBA and ASM, are involved in different pathways for ceramide production[535]. It can be hypothesised

that the downregulation of one of those pathways due to GBA deficiency might result in the upregulation of another route, such as the ASM pathway, e.g., by increasing expression of ASM or inducing of ASM enzyme activity. Thirdly, increased GlcCer levels in GBA deficiency have been shown to lead to the formation of flexible structures that protrude from model membranes[511] and to facilitate the formation of membrane nanotubes in macrophages[509]. Interestingly, similar tubular protrusions have been observed at engulfment sites for CAM-mediated endocytosis[161,388]. Thus, a GlcCer-facilitated formation of membrane protrusions in GBA deficient cells might aid cargo engulfment and endocytosis.

Nevertheless, since the increased uptake was contradictory to the observed decreased transcytosis of anti-ICAM-1 NCs (figures 7.5B and 7.6B), NC binding was also compared for GBA-normal *vs.* GBA-deficient cells to infer whether this parameter may be altered and, thus, render a different transport outcome. To this end, GBA-normal or GBA-deficient cells were fixed with PFA to preclude NC uptake, yet allow for binding, and then incubated for 30 min with anti-ICAM-1 NCs. However, the amount of anti-ICAM-1 NCs bound to cells did not differ depending on GBA deficiency (figure 7.7B), in line with the lack of an effect of GBA deficiency on ICAM-1 expression (figure 7.2) or nanodomain display (figure 7.3A).

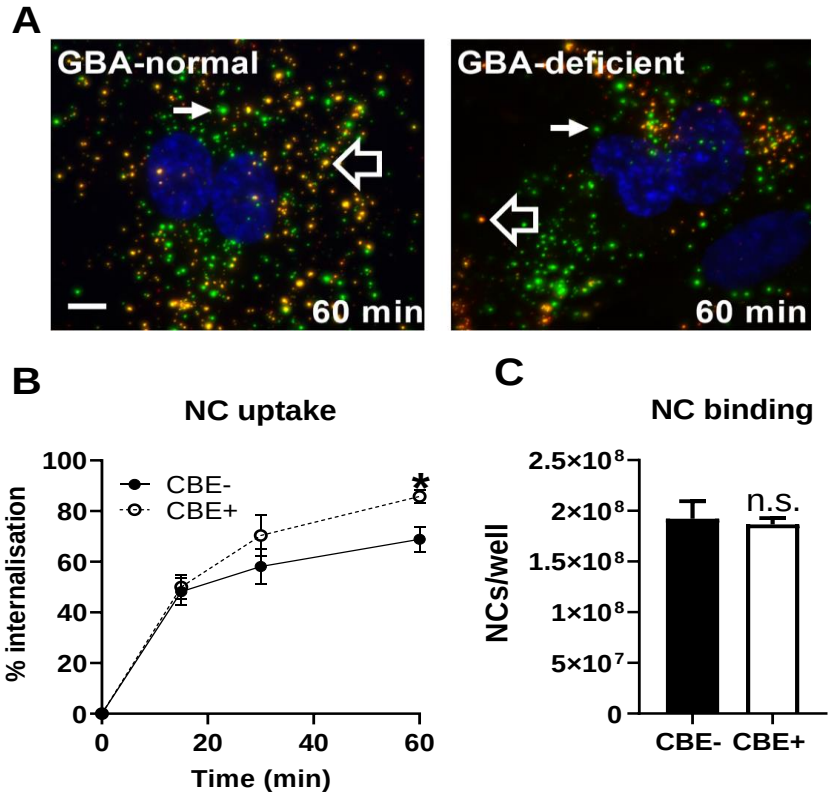

Figure 7.7 Effect of GBA deficiency on binding and uptake of anti-ICAM-1 NCs by brain ECs. Brain ECs were incubated at 37 °C with 10 ng/mL TNFα (overnight treatment) and 200 µM CBE (72 h treatment) to simulate GBA deficiency, or 10 ng/mL TNFα (overnight treatment) alone as GBA-normal control. (A-B) Cells were incubated with FITC-labelled anti-ICAM-1 NCs (v2) at 4°C for 30 min to allow for binding without uptake. Then, cells were washed to remove unbound NCs and further incubated at 37°C in NC-free medium to enable NC uptake up to the indicated times. Then, cells were fixed and immunostained with red-labelled secondary antibody to distinguish between cell-bound (green + red = yellow, open arrows) and intracellular (only green, arrows) NCs by fluorescence microscopy and quantify the percentage of internalized NCs from all cell-associated ones. (A) Representative images at 60 min, scale bar = 10 µm, (B) quantification of percent internalisation. (C) Cells were fixed with PFA to preclude uptake and then incubated with ^{125}I-labelled anti-ICAM-1 NCs (v2) for 30 min at 37 °C to allow for binding without uptake. Then, cells were washed to remove unbound NCs and analysed using a gamma counter to quantify the number of NCs per well. Data are average ± SEM. (*p<0.05, Student's t-test, n.s. = not significant).

In conclusion, GBA deficiency did not affect the binding of anti-ICAM-1 NCs to brain ECs, expected because of similar ICAM expression (figure 7.2) and number of nanodomains (figure 7.3A), whereas it significantly increased NC uptake by brain ECs, which is in contradiction with the observed decay in transcytosis.

7.2.4. The Effect of GBA Deficiency on ICAM-1 Lateral Mobility and Interaction with NCs in Brain ECs

We then sought to investigate the discrepancy encountered. As said, GBA deficiency is known to change the lipid composition of the plasma membrane due to the accumulation of GlcCer and other sphingolipids[507,510,512,513]. Given the importance of plasma membrane composition for its fluidity, vesicle formation and thus, endocytosis, changes in lipid composition might play a role in the increased NC uptake. To this end, using super resolution microscopy and total internal reflection (TIRF) microscopy, the mobility of ICAM-1 was assessed in GBA-normal and GBA-deficient brain ECs in the presence and absence of anti-ICAM-1 NCs. This was performed by Dr. Enric Gutierrez Martinez in Prof. Maria Garcia-Parajo's laboratory at the Institute of Catalonia for Photonic Sciences (ICFO), Barcelona.

In the absence of anti-ICAM-1 NCs, ICAM-1 lateral mobility was significantly increased in GBA-deficient cells compared to GBA-normal cells (figure 7.8A-B), in line with an observed decreased immobile fraction (figure 7.8C). On the other hand, GBA deficiency increased the fraction of confined ICAM-1 following the addition of anti-ICAM-1 NCs (figure 7.8D).

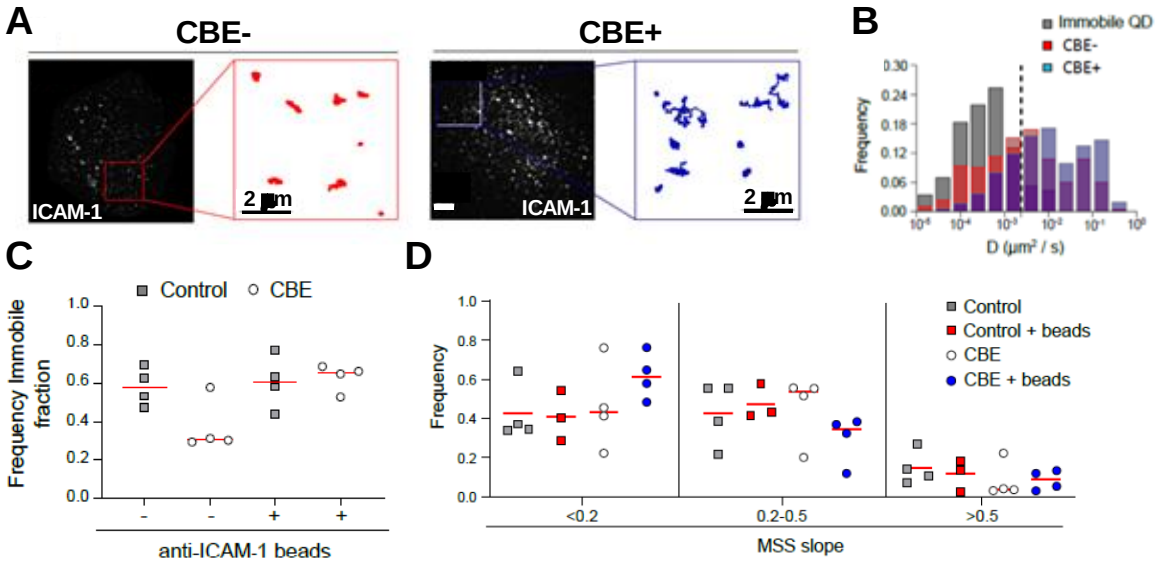

Figure 7.8 Lateral ICAM-1 diffusion on the plasmalemma of brain ECs and NC-driven effects. Brain ECs were incubated at 37 °C with 10 ng/mL TNFα (overnight treatment) and 200 µM CBE (72 h treatment) to simulate GBA deficiency, or 10 ng/mL TNFα (overnight treatment) alone as a GBA-normal control. Then, cells were incubated with biotynilated Ab against ICAM-1, washed to remove unbound Ab, followed by the addition of streptadivin conjugated quantum dot (QD)-633 and washed to remove unbound materials. Subsequently, cells were incubated or not with anti-ICAM-1 NCs (containing HAse as a model enzyme) for a 5-min binding pulse, washed to remove unbound NCs,

and analysed by TIRF microscopy. (A) Representative images of cells, where inserts show the projections of individual receptor trajectories. Scale bar microscopy picture = 5 µm, scale bar insert = 2 µm. (B) Histogram of immediate diffusion coefficients of individual receptor trajectories. Dashed line = threshold below which receptors are considered immobile, based on the calculated diffusion of QDs fixed on glass (97% immobilised QDs are below threshold). (C) Frequency of the immobile fraction in the absence and presence of NCs. (D) Frequency of the moment scale spectrum (MMS) slopes calculated from the immediate diffusion coefficients in the mobile fraction in the absence or presence of NCs (<0.2 = confined, 0.2-0.5 = subdiffusive, >0.5 = free). Dots represent individual cells. This experiment was performed by Dr Enric Gutierrez Martinez in Prof Maria Garcia-Parajo's laboratory at the Institute of Catalonia for Photonic Sciences (ICFO), Barcelona.

The increased mobility of ICAM-1 in GBA deficiency was unexpected due to the increased order of membrane caused by GlcCer accumulation[510,511], lowering membrane fluidity and thus decreasing receptor mobility. Nevertheless, ICAM-1 mobility might be increased through the interaction with other membrane constituents, namely tetraspanins. Tetraspanins are a family of transmembrane proteins crucial for the organisation of membrane microdomains enriched in tetraspanins that govern a myriad of cellular processes such as adhesion, endocytosis, and cell-cell fusion[536]. Although there is not yet any evidence for the direct interaction with membrane lipids, ICAM-1 colocalises with tetraspanins under inflammation conditions in tetraspanin-enriched microdomains, so called endothelial adhesive platforms, an organisational change independent of receptor activation[537,538]. Different interactions between lipids and tetraspanins have been described. For instance, tetraspanin-enriched microdomains associate with and depend on cholesterol[539–542], with tetraspanin CD9 showing increased lateral mobility under increased membrane cholesterol levels[543]. Furthermore, tetraspanins also interact with gangliosides with implications for their function, organisation, and mobility on the membrane[544–548]. Tetraspanin CD82 increases its lateral mobility under ganglioside depletion, whereas tetraspanins CD9 and CD81 are unaffected[548]. Generally, plasma lipid homeostasis is disturbed in GBA deficiency far beyond the original aberrant accumulation of GlcCer, with yet mostly unknown consequences. For example, GlcCer accumulation results in the secondary accumulation of other lipids such as ceramides[507,512], phosphatidylglycerol[507], and cholesterol[515,549]. Furthermore, ganglioside GM3 is highly elevated in plasma of GD patients[550]. Taken together, given the ample changes in lipid composition in GBA-deficient cells, the known interaction of ICAM-1 with tetraspanins, and the interaction of tetraspanins with several plasma membrane lipids whose membrane concentrations are affected by GBA deficiency, an effect of GBA deficiency on ICAM-1 lateral diffusion is likely mediated through tetraspanins. Interestingly,

tetraspanin CD9, whose lateral mobility is increased by cholesterol accumulation[543] such as in GBA deficiency[515,549], is a key regulator of ICAM-1 clustering[538]. Yet whether the lateral mobility of ICAM-1 is in fact modulated through tetraspanins and the secondary accumulation of membrane lipids in a cellular model remain unknown and should be subject to further investigation.

Furthermore, the increased confinement of ICAM-1 is likely the result of an increased total number of receptors engaged with NCs. A higher number of ICAM-1 molecules can be engaged in two ways; firstly, by an increase in the total number of NCs per cell and secondly, by an increased interaction of ICAM-1 molecules per NC. Given the equal total binding of NCs to GBA-deficient and GBA-normal cells (figure 7.7B), which excludes the first explanation, the total number of ICAM-1 interacting with the same NC is likely increased by the increased lateral mobility observed for ICAM-1 in GBA deficiency. This might be because given the usually more confined nature of ICAM-1 (figure 7.8A-B), only a restricted number of ICAM-1 molecules can be accessible to a single NC interacting through its Ab coat. Due to the increased lateral mobility of ICAM-1 in GBA-deficient cells (figure 7.8A-B) each ICAM-1 molecule on average can travel greater distances and, thus, cover a bigger surface area on the cell which would lead to a generally greater engagement of ICAM-1 molecules with the same total number of NCs (figure 7.8D). Furthermore, anti-ICAM-1 NCs with higher valency, thus able to engage with more ICAM-1 molecules per particle, show higher downstream signalling and subsequent uptake[149]. Similarly, a higher total engagement of ICAM-1 molecules per NC, as seen by the increased receptor confinement, are in line with the observed increased uptake in GBA-deficient cells (figure 7.7A).

In conclusion, the increased lateral mobility of ICAM-1 in GBA-deficient brain ECs is possibly the result of a lipid-mediated increased lateral mobility of tetraspanins, e.g., tetraspanin CD9 with which ICAM-1 associates, and likely results in greater engagement of ICAM-1 with anti-ICAM-1 NCs, explaining the observed increase in confined receptors, thereby increasing downstream signalling and ultimately uptake, in line with aforementioned findings.

7.2.5. The effect of GBA Deficiency on Lysosomal Trafficking and Reuptake

As described in other chapters, the lysosome is a prominent intracellular destination for NC trafficking and a prominent alternative route to transcytosis. GBA deficiency was shown to decrease transcytosis *via* all pathways comparably, with anti-ICAM-1 NCs being the most promising given its higher number of NCs transcytosed. Surprisingly, GBA deficiency increased endocytosis of anti-ICAM-1 NCs, likely mediated by GlcCer accumulation and/or increased ICAM-1 lateral mobility, whereas it did not affect the total binding. Given these seemingly incongruent results, the effect of GBA deficiency on lysosomal trafficking as a prominent alternative destination was assessed.

To this end, using confocal microscopy, the colocalisation of red-fluorescent dextran-stained lysosomes with green-fluorescent anti-ICAM-1 NCs was assessed at different time points (figure 7.9). Lysosomal trafficking was significantly higher in GBA-deficient cells compared to GBA-normal cells at all time points tested, increasing trafficking by 1.5-, 3.6-, 1.8-, 2.0-, and 1.5-fold at 0.5 h, 1 h, 3 h, 5 h, and 24 h, respectively. Using regression, GBA deficiency was found to decrease the trafficking half-time more than 2-fold, from 3.4 h to 1.5 h (figure 7.9).

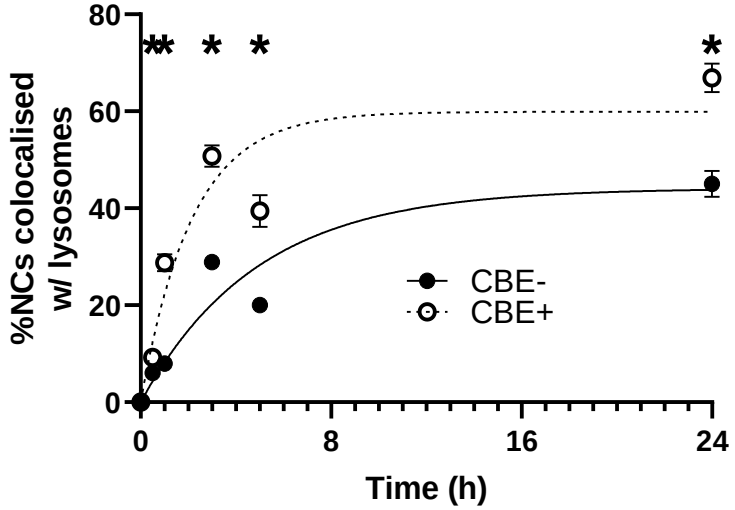

Figure 7.9 Lysosomal trafficking of anti-ICAM-1 NCs in GBA-normal *vs.* GBA-deficient brain ECs. Brain ECs were incubated at 37 °C with 10 ng/mL TNFα (overnight treatment) and 200 μM CBE (72 h treatment) to simulate GBA deficiency, or 10 ng/mL TNFα (overnight treatment) alone as GBA-normal control. Prior to the incubation with NCs, lysosomes were stained with 0.5 mg/mL 10 kDa Texas Red dextran, washed to remove extracellular dextran, and further incubated to allow for complete lysosomal trafficking of dextran. Then, cells were incubated with FITC-

labelled anti-ICAM-1 NCs (v2), washed to remove non-bound NCs, and further incubated (if applicable) in NC-free cell medium up to 24 h. At chase, cells were fixed and analysed by fluorescent microscopy. Lysosomal trafficking was determined by colocalisation of green NCs with red lysosomes (green + red = yellow). Data are shown as average ± SEM. Statistics: Student's t-test, *p<0.05.

This increase suggests a change in cargo trafficking from transcytosis towards predominant lysosomal trafficking. Similar changes in intracellular trafficking have been described in GBA-deficient fibroblasts and macrophages, where lactosylceramide, a substrate that is usually targeted to the Golgi apparatus upon endocytosis, was shown to be mistargeted to lysosomes[515,551]. The mechanism by which GBA deficiency induces a changed intracellular trafficking remain unknown, but was shown to be dose dependent[515]. Furthermore, altered intracellular trafficking of cargo has also been shown as a result of sphingomyelin accumulation in ASM deficiency (see Chapter 6). Thus, it is possible that there is an underlying mechanism that affects trafficking due to the accumulation of several types of membrane lipids, or the observed effect is not induced by GlcCer itself but other membrane lipids that also accumulate in both, GD, and PD. For example, both GBA deficiency and ASM deficiency, lead to the secondary accumulation of different membrane lipids including cholesterol[515,549], whose altered membrane concentrations, excess or depletion, have also been shown to result in predominant lysosomal trafficking of cargo[552].

Additionally, since there is a strong likelihood that NCs can undergo reuptake due to incomplete or slow detachment from the basolateral side of cells after transcytosis (see Chapter 5), the effect of GBA deficiency on the uptake of anti-ICAM-1 NCs from the basolateral side of brain ECs was assessed (figure 7.10). This was significantly quicker in GBA-deficient compared to GBA-normal cells (figure 7.10), with 61.3% *vs.* 26.2% at 0.5 h and 95.7% and 82.8% at 5 h, respectively.

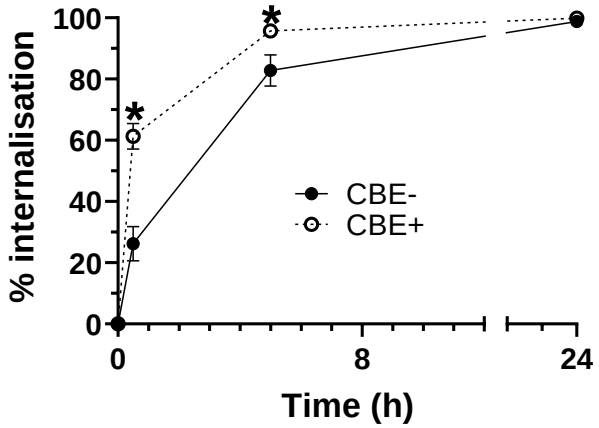

Figure 7.10 Internalisation of anti-ICAM-1 NCs from the basolateral side of GBA-normal *vs.* GBA-deficient brain ECs. Brain ECs were incubated at 37 °C with 10 ng/mL TNFα (overnight treatment) and 200 µM CBE (72 h treatment) to simulate GBA deficiency, or 10 ng/mL TNFα (overnight treatment) alone as GBA-normal control. Then, cells were incubated with FITC-labelled anti-ICAM-1 NCs (v2) for a 30-min binding pulse, washed to remove non-bound NCs, fixed, and counterstained with red secondary Ab to distinguish between intracellular (green only) and cell-bound (green + red = yellow) NCs. Analysis by fluorescence microscopy. Data are average ± SEM. (*p<0.05, Student's t-test).

These findings are comparable to the findings of the increased uptake of anti-ICAM-1 NCs from the apical side of the cell (figure 7.7A), indicating that the mechanism by which CAM-mediated endocytosis is increased in GBA deficiency operates similarly on both apical and basolateral sides of brain ECs (see section 7.2.4 and 7.2.5). It can be hypothesised that the same mechanisms governing the increase of CAM-mediated endocytosis from the apical and the basolateral side would also increase the reuptake of transcytosed NCs with subsequent lysosomal trafficking, further increasing cellular retainment of NCs (figure 7.11). This hypothesis would be in line with the overall increased lysosomal trafficking of anti-ICAM-1 NCs in GBA-deficient cells (figure 7.9). Although the exact lysosomal trafficking route that is affected in GBA-deficient brain ECs, apical-to-lysosome, or basolateral-to-lysosome, cannot be distinguished from results shown in the present work, the overall increase in lysosomal trafficking of anti-ICAM-1 NCs in GBA-deficient cells offers a satisfactory explanation for the decreased transcytosis rate despite the increased uptake rate of anti-ICAM-1 NCs in GBA-deficient brain ECs.

In conclusion, these results show that GBA deficiency significantly increases lysosomal trafficking, absolute and rate, and thus cellular retention of the NCs.

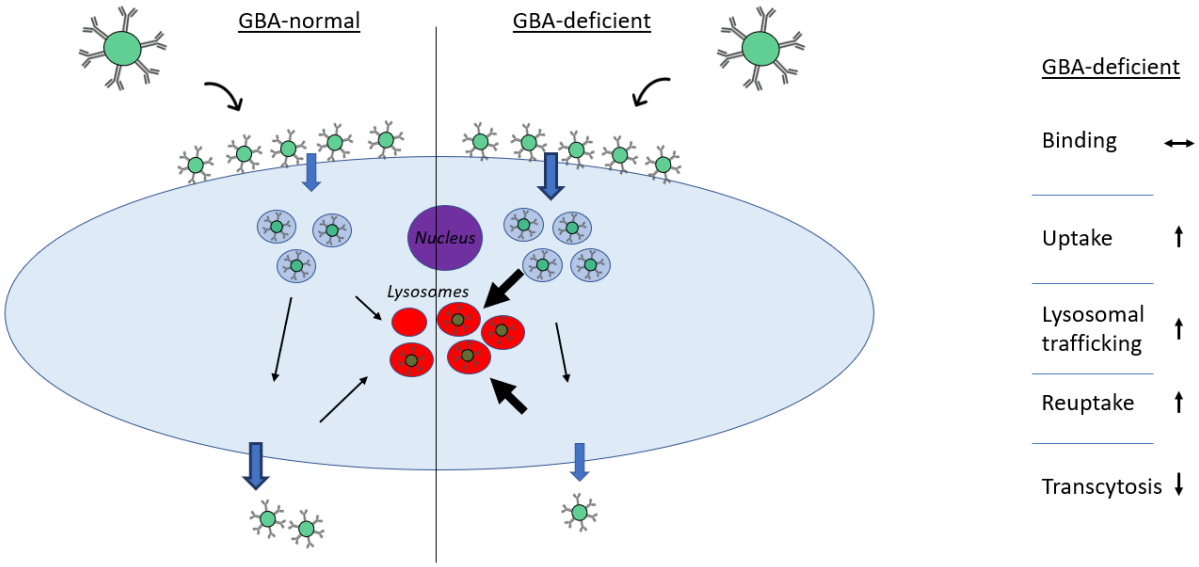

Figure 7.11 Model for the effects of GBA deficiency on anti-ICAM-1 NC transport by brain ECs. GBA-deficiency did not affect the binding of anti-ICAM-1 NCs to brain ECs, whereas the NC uptake was significantly increased. Furthermore, NC transcytosis was significantly decreased under disease conditions in favour of a significantly increased lysosomal trafficking. Interestingly, NC uptake was also significantly faster from the BL side of cells, probably facilitating reuptake following transcytosis, which would be in line with decreased transcytosis and increased lysosomal trafficking.

7.3. Conclusion

Nanomedicine offers an interesting alternative for ERT in GD patients with neuronopathic symptoms, for which effective treatment is currently lacking, and some PD patients may also benefit from this strategy. Nevertheless, disease-specific alterations on the cellular level might affect the transport machinery and alter NC trafficking. Therefore, a more detailed understanding of GBA deficiency pathology and its effects on receptor-mediated transport are paramount towards the development of therapeutic NCs for these diseases. Using a chemically induced GBA deficiency BBB model, the transport of NCs targeted to different pathways was tested and found to be reduced, and anti-ICAM-1 NCs were identified as the best option given the highest number of NCs crossing the barrier via this means. Focussing on this promising candidate, GBA deficiency was shown to increase NC uptake, likely due to GBA deficiency-related changes to cell morphology and signalling and/or an increased receptor-NC engagement brought about by an increased lateral mobility of ICAM-1 under this disease condition. Furthermore, a shift from transcytosis to predominant lysosomal trafficking was observed in GBA deficiency, explaining the

decreased transcytosis despite the increased endocytosis (see figure 7.11). Interestingly, anti-ICAM-1 NCs showed increased endocytosis not only from the apical but also from the basolateral side of brain ECs, which might further explain the decreased transcytosis and increased lysosomal trafficking due to a facilitated reuptake of transcytosed NCs with subsequent lysosomal trafficking. The present results highlight the importance of disease-specific alterations of cell machinery and transport for the development of novel therapeutic NCs. Furthermore, anti-ICAM-1 NCs were identified as the most promising candidate for the development of ERT for neuronopathic GD.

Chapter 8: CONCLUDING REMARKS

8.1. Overall summary

In summary, this project examined (1) the fabrication and characterisation of NCs suitable to target brain ECs to improve therapeutic enzyme delivery and models to address all other questions in this dissertation (Chapter 4), (2) the mechanism of CAM-mediated transcytosis with a special focus on the effect of targeting valency on lysosomal trafficking and basolateral reuptake following transcytosis (Chapter 5), (3) the effect of ASM deficiency on NC transport by brain ECs aimed for NPD ERT (Chapter 6), and (4) the effect of GBA deficiency on NC transport by brain ECs aimed for GD and perhaps PD ERT (Chapter 7).

With regards to the fabrication and characterisation of NCs to target brain ECs and deliver therapeutic enzymes (Chapter 4), I was able to prepare NCs of around 200 nm diameter with favourable physicochemical properties using a clinically relevant material, PLGA. These NCs were successfully loaded with a model therapeutic enzyme, HAse, and functionalised with targeting Abs, similar to previously described NCs[148,171,175,301]. Furthermore, PLGA NCs could be loaded with therapeutic enzyme in two different ways, *via* surface adsorption or *via* encapsulation. All NCs delivered significantly more enzyme to relevant target cells compared to free enzyme, thus proving the ability of the fabricated NC to not only load but also deliver enzyme, in line with results from the literature[171,172,174,187,302] Whereas the enzyme loading was significantly higher by encapsulation, this loading mode also significantly increased the size of NCs, which might be a limiting factor for drug delivery due to size restrictions of certain endocytosis pathways[553], such as clathrin-mediated endocytosis or caveolae-mediated endocytosis, with 100-200 nm[528] and 100 nm[65], respectively. Nevertheless, size restrictions are less of a concern for the CAM-pathway which has been reported to endocytose cargo of different sizes up to 5 µm[160,161,164]. Indeed, despite their larger size, PLGA NCs loaded *via* encapsulation delivered significantly more HAse than PLGA NCs loaded *via* surface adsorption, concluding that that formulation might offer the highest therapeutic benefit. Additionally, given the degradation of PLGA NCs by cells[324,325], non-degradable PS NCs were prepared and showed comparable characteristics to PLGA NCs, as described elsewhere[148,171,175,301]. Thus, these formulations were used as models in subsequent

transport studies to prevent confounding results arising from NC degradation simultaneous to transport. Furthermore, certain NC surface properties could be altered specifically without affecting other NC features, such as for the fabrication of three distinct targeting valencies, the number of targeting moieties displayed on the surface of a NC, or the selection of non-specific coating vs. coatings to target cell-surface markers associated with CAM-, clathrin-, or caveolae-mediated endocytosis. These model formulations showed specific targeting after iv injection in mice, for which their successful fabrication enabled me to study the rest of the questions in the present work. NC stability, an important parameter to ensure quality experimental results and reproducibility, was found to be good under storage conditions up to 21 days, with only minimal changes in size and PDI, verifying earlier findings[172,174], as well as under experimental physiological-like conditions, also in line with previous results[174]. These data validated the NCs' aptness for further experimental tests and, thus, provided me with the basis to study the remaining questions in the present work.

With regards to Chapter 5, the data obtained enhanced our understanding of the complex interplay between simultaneously happening trafficking events and identified a novel trafficking route of targeted NCs in brain EC monolayers using anti-ICAM-1 NCs. Several studies had shown the non-linear relationship between cargo avidity and transcytosis across brain ECs, with intermediate avidity cargo showing more efficient transcytosis compared to low and high avidity cargoes[170,375,376,386]. Whereas a complex relationship between targeting valency, defining avidity, and binding and uptake, transcytosis, and lysosomal trafficking had been seen to play a role[170], the mechanistic relationship between those trafficking routes remained unknown. In this chapter I demonstrated that NC transcytosis and lysosomal trafficking happen simultaneously in brain ECs, with the latter showing a direct relationship with targeting valency at early time points. Given the retention of high avidity cargo in and around ECs, possibly due to insufficient detachment following transcytosis[350,370–375,386], the question arose of what might happen to that cargo. To address this question, I first confirmed the possibility of binding and uptake of anti-ICAM-1 NCs from the basolateral side of brain ECs, which showed a slightly increased uptake rate compared to apical uptake. Then, I incubated brain EC monolayer with green-fluorescent NCs from the apical side and used a red-fluorescent fluid phase marker in the basolateral side to

determine reuptake of transcytosed NCs by fluorescence colocalisation. NCs were found to undergo reuptake following transcytosis, with high-valency (v3) NCs showing significantly higher reuptake rates compared to intermediate-valency (v2) NCs, in line with lower transcytosis efficiency for v3 formulations[170]. To get an idea of the subsequent intracellular trafficking, cells were incubated with NCs from the basolateral side of brain ECs. Lysosomal trafficking was shown to be quicker from the basolateral side compared to the apical side of cells, suggesting that lysosomal degradation is the preferred route following reuptake. Given this "secondary round" of lysosomal trafficking, the influence of targeting valency on lysosomal trafficking was assessed for a longer period of time. Interestingly, the direct relationship between targeting valency and lysosomal trafficking at early time points changed to a bell-shaped relationship at later time points. The mechanistic insight into the intricate interplay of concomitant intracellular transport events were paramount for understanding results obtained in Chapter 3 and Chapter 4, as discussed below.

Chapter 6 and Chapter 7 data deepened our understanding on the effect of ASM deficiency and GBA deficiency on the transport of targeted NCs. ASM deficiency increased the receptor expression of ICAM-1 and PV1, whereas TfR was not affected. Furthermore, only the binding of anti-ICAM-1 NCs was increased, in line with the increased expression, with no change for the other two NCs. On the other hand, the uptake of anti-ICAM-1 NCs was decreased from the apical side of cells, probably due to the involvement of ASM in ICAM-1-mediated endocytosis[161], which, compensated by the increased binding, resulted in comparable levels of intracellular NCs compared to control condition. Furthermore, the lysosomal trafficking rate was increased for all NCs, in line with similar findings in the literature[410,453,454]. With regards to transcytosis in ASM deficiency, trafficking rates were increased for anti-ICAM-1 NCs and anti-PV1 NCs, whereas anti-TfR NCs were unaffected. Interestingly, the uptake of anti-ICAM-1 NCs was also decreased from the basolateral side of cells, probably decreasing reuptake, and thus offering a possible explanation for the observed increase in transcytosis rate. Furthermore, the transcytosis efficacy was either decreased or not affected in ASM deficiency, with anti-ICAM-1 NCs showing the most promising results of all NCs tested due to the highest total number of NCs transcytosed, offering the best drug delivery across the BBB in that condition.

Based on the knowledge that stark differences in receptor expression governed transcytosis efficiency in ASM deficiency, independently from other more subtle disease-specific alterations, the receptor expression in GBA deficiency was first assessed and found to slightly increase ICAM-1 expression, whereas it did not change TfR or PV1 expression. Then, the transcytosis efficiency was directly assessed and found to be decreased in GBA deficiency for all NCs, with anti-ICAM-1 NCs again showing the highest absolute transcytosis, making it the most promising candidate for drug delivery in that condition. This is why anti-ICAM-1 NCs were chosen to further investigate and better understand the specific effects of GBA deficiency on NC transport. Interesting, in contrary to ASM deficiency, the uptake of anti-ICAM-1 NCs was significantly increased in GBA deficiency, whereas the binding was not affected. Furthermore, the receptor mobility was found to be increased, which might increase the interaction between NCs and receptors, possibly explaining the observed increased uptake. Furthermore, the lysosomal trafficking rate was found to be significantly increased, such as already observed in ASM deficiency, offering a possible explanation for the decreased transcytosis efficiency. Interestingly, not only the uptake from the apical but also from the basolateral side of cells was found to be increased, suggesting an increased reuptake of NCs in GBA deficiency, thus offering an additional explanation for the observed decreased transcytosis efficiency.

The common increased lysosomal trafficking rate for all NCs observed in ASM deficiency as well as GBA deficiency might be explained by common effectors in both diseases. One example is ceramide, the hydrophobic backbone of all complex sphingolipids[554], which is produced by both enzymes (figure 1.5). The deficient ceramide levels might either have a direct effect on lysosomal trafficking or by disturbing the synthesis of other sphingolipids. Furthermore, decreased ceramide levels might also stimulate complementary ceramide synthesis pathways. For instance, the salvage pathway uses sphingolipids from the plasma membrane to produce ceramide in late endosomes and lysosomes[535], which might explain the increased lysosomal trafficking observed in both LSDs. Another example is cholesterol, whose secondary accumulation has been observed in both diseases[212,515,549], which may contribute to increased lysosomal trafficking[552]. Unlike common findings on lysosomal transport, NC endocytosis and transcytosis of anti-ICAM-1 NCs were affected differently by both enzyme deficiencies. Counterintuitively, ASM deficiency

increased the transcytosis rate despite the observed decrease in endocytosis rate, whereas GBA deficiency decreased the transcytosis rate despite the observed increase in endocytosis rate. Importantly, both enzyme deficiencies altered the uptake rates at both sides of the cell, thus altering internalisation and reuptake alike. Hence, the decreased reuptake in ASM deficiency might explain the increased transcytosis rate, and *vice versa* for GBA deficiency.

Ultimately, this study highlights the importance of understanding the intricate interplay of different trafficking routes, the effect of NC properties as such as targeting valency on the interaction with cells, and specific disease effects on NC trafficking to guide the development of novel effective nanotherapeutics.

8.2. Current limitations and future steps

Results in the present work pose several open questions that could give rise to further experimental work in continuation to the present dissertation.

For instance, the present results have important implications for the development of a NC for the successful delivery of ERT into the CNS of patients with neuronopathic GD or NPD, who currently lack adequate treatment. For this study, ASM- and GBA-deficiency were chemically induced using imipramine and CBE, respectively. Although these models might not represent all pathological mechanisms of NPD and GD accurately, it offers a tuneable and reproducible disease model in terms of the enzyme activity reduction and substrate accumulation, adequate for an initial proof-of-concept study such as performed in the present investigation. For instance, one published study chose the chemically-induced GBA deficiency model over patient material to study the effect of glycosphingolipid accumulation on intracellular trafficking due to the lack of aberrant trafficking in GD patient macrophages, in which they were interested[515]. However, taking the example of GD, despite CBE being a standard drug for the induction of GBA deficiency, a broad spectrum of treatments has been used in research, e.g. in mice with concentrations ranging from 50 µM to 100 mM and incubation times between 2 h and 60 days[520]. These parameters likely influence the kinetics of substrate accumulation and, therefore, the downstream effects. Illustrating this, *in vivo* findings from a Fabry mouse model showed that substrate accumulation

was not a static process but changed over time, highlighting the importance of the treatment protocol[555]. Due to this, this study would benefit from future validation using other GD and NPD models. For instance, genetic mutations either introduced into healthy cells or by using patient cells or tissue could represent interesting alternatives. Whereas introducing genetic mutations into healthy cells by cloning might also inflict other relevant unwanted changes, using patient derived cells might be more representative regarding disease. Nevertheless, easily obtainable samples such as commonly used patient's fibroblasts[187,288,508,515,556,289,301,326,409,427,482,484,485] might have little relevance regarding GD or NPD neuropathology. Additionally, disease severity and residual enzyme activity can drastically vary among different mutations and patients[557], for which different patient-derived models might also result in high variability. In addition, pluripotent stem cells (iPS) have proven a valuable model that has increasingly gained attention in LDS research in recent years. This is because of their patient origin, them carrying relevant mutations, and their theoretical versatility to enable differentiation into any cell type, such as brain ECs or neurons, making this the most accurate model to study NC transport across the BBB[558]. Nevertheless, the high cost and lengthy protocols associated to working with iPS cells were outside the scope of the present work, but definitely deserve attention in the future.

Another limitation concerns NC targeting to PV1. PV1 is a EC-specific structural protein essential for the formation of endothelial diaphragms, e.g. at the neck of caveolae[559]. Therefore, PV1 targeting could theoretically provide specific targeting and transport via caveolae-mediated endocytosis[560,561]. Yet, caveolae-mediated transport is speculated not to play a role in healthy brain endothelium due to its specific downregulation via the expression of the Mfsd2a, specifically expressed in BBB-containing blood vessels[562,563]. Mfsd2a is a lipid transporter, likely a flippase[563,564], situated at the apical side of brain ECs which transports the essential omega-3 fatty acid docosahexaenoic acid (DHA)[565]. It is hypothesised that Mfsd2a increases the levels of DHA, known to disrupt caveolae in brain ECs[566], on the inner leaflet of brain EC's membranes, thereby dispersing cholesterol and caveolin-1, essential structural molecules for caveolae, consequently inhibiting their formation[563], with unknown consequences for PV1 and PV1 targeting. In caveolin-1 knock-out mice, an increased clathrin- and dynamin-independent internalisation and lysosomal degradation of PV1 has been seen in the lungs[567]. Importantly, neither the transcription nor the

translation of PV1 was affected in this scenario[567]. These results suggest how the lack of structures to form diaphragms decreases the localisation of PV1 at the cell membrane and favours its internalisation and lysosomal degradation[567]. Thus, the dispersion of cholesterol and caveolin-1 by DHA in healthy brain ECs might have similar effects on PV1. Nevertheless, this new potential equilibrium of PV1 expression and increased turnover might provide another targeting strategy to lysosomes, yet it is unlikely to provide efficient transcytosis given the physiological underlying mechanism of PV1 removal from the cell surface due to lack of function. Importantly, although foetal bovine serum (FBS) contains relatively high levels of more than 1% DHA[568] as compared to most other sera, it only provides less than 5% of different essential fatty acids such as DHA available to cells in the body at medium a concentration of 10%[569], as used in the present work. Therefore, it is possible that DHA levels present in the complete cell medium are not sufficient for proper inhibition of caveolae-mediated transport by Mfsd2a, which is why DHA should be considered to be supplemented in further studies. On the other hand, in the diseased brain, e.g. as a result of ischemic stroke, caveolae transport shows increased activity through a yet unknown mechanism[84,570], yet not much is known about the status of caveolae-mediated transport at the BBB in neuronopathic LSDs which might be altered, too, given the disease-associated neurologic injury, probably activating caveolae-mediated transport and thus enabling drug targeting *via* this pathway. Thus, further investigation is needed to assess the status of caveolae-mediated transport in LSDs to evaluate the possibility of targeting this pathway for ERT of neuronopathic symptoms of LSDs.

With respect to future steps, the results obtained *in vitro* comparing the three endocytosis pathways, identifying the CAM-mediated pathway as the most promising for ERT in neuronopathic LSD, should be verified in a more relevant model such as *in vivo* in mice. There are several important differences between studying NC transport *in vitro* such as in the present work or *in vivo*. Firstly, the general conditions for targeting differ in e.g., static incubation *vs.* flow/shear stress in the general circulation and lower serum levels complete cell medium than blood. Furthermore, the presence of different cell types will affect targeting on the one hand by quickly altering NC concentrations in blood through e.g., clearance by macrophages, or by changing the behaviour of the target cell through complex interactions with other cells such as astrocytes or

pericytes. This is why *in vivo* experiments give crucial information about biodistribution, important for therapeutic efficacy, which cannot be obtained using *in vitro* models.

Secondly, the understanding of the current results should be deepened by performing additional experiments with the current *in vitro* models. The intracellular trafficking of NCs targeted to all three pathways and the state of their cellular machinery should be completed for both diseases to gain a better understanding of the disease specific effects of LSDs on NC transport. As for the increased lateral mobility of ICAM-1 in GBA deficiency, the literature supports the idea that tetraspanins are the mediator between the lipid accumulation and the increased mobility of the receptor. To verify this hypothesis, cells should be treated with CBE to induce GBA deficiency and thus lipid accumulation, yet without TNFα-activation to preclude the association of ICAM-1 with tetraspanins such as CD9. A lack of increased lateral mobility would support the involvement of tetraspanins, which could additionally be tested by further colocalisation studies. As for the results on anti-ICAM-1 NCs in GBA deficient cells, the mediator(s) responsible for the increased uptake should be identified. To this end, cellular ceramide levels in GBA-normal *vs.* GBA-deficient cells could be quantified by mass spectrometry to assess whether there might be a general increase or visualised using anti-ceramide Ab to verify local accumulation around endocytosis sites. Alternatively, it could be assessed whether GlcCer has a direct effect on NC endocytosis by inhibiting the enzyme, GSC, that produces GlcCer from ceramide (figure 1.5). To this end, the uptake of anti-ICAM-1 NCs cells could be studied with and without a specific GSC inhibitor. A decreased uptake would suggest the direct involvement of GlcCer in CAM-mediated uptake, which could then further be corroborated by assessing the colocalisation of GCS with anti-ICAM NCs, such as has been done for ASM[161].

Thirdly, based on the present results, NC formulations could be further optimised to achieve maximum drug delivery. To this end, the delivery of therapeutic enzyme into and across healthy and diseased BBB models could be assessed for targeted PLGA NCs loaded *via* encapsulation or surface coating to elucidate the best loading method for drug delivery. Furthermore, given the interesting results in this work and others on the influence of NC targeting valency (Chapter 2) in combination with the compelling results on the influence of LSDs (Chapter 3 and Chapter 4) on NC trafficking, further studies could assess whether negative effects of disease can be

counteracted with altered valency, e.g., increasing the targeting valency, thereby increasing uptake, when targeting ASM-deficient cells, showing decreased uptake *via* the CAM-pathway. In this way, the full potential of the present work could be harvested to fine tune NC characteristics to improve nanotherapeutic delivery.

Lastly, some of the current models should be verified or could be improved. For instance, although in line with the mistargeting of lactosylceramide to lysosomes[453,454,515,551], results from this study showing an increased lysosomal trafficking of anti-ICAM NCs should be taken with care due to the lysosomal marker used. Dextran, usually trafficked to lysosomes, as verified by Lamp-1 colocalisation[172], where it accumulates due to the cells inability to degrade it[172], get stuck in the early endosomal pathway given the accumulation of macromolecules in lysosomes and thus not reach the lysosomal compartments. Therefore, the colocalisation of dextran with more reliable lysosomal markers such as LAMP-1 should verify the lysosomal trafficking of dextran. Furthermore, instead of chemically induced disease models such as used in the present work, more relevant patient material could be used to further study

Furthermore, instead of chemically induced disease models such as used in the present work, more relevant patient material could be used to further the effects of LSDs on NC trafficking and to verify current results. iPS cells pose a compelling model due to its patient origin carrying relevant gene mutations, theoretically enabling to differentiate the iPS cells to any cell type, such as brain ECs or neurons, making this the most accurate model to study NC transport across the BBB[558].

Alternatively, more realistic *in vitro* models such as microfluidic chips allowing for shear stress and co-cultures with different BBB cell types such as ACs, PVs, and/or neurons might allow for more realistic cellular architecture and therefore be a valuable tools to improve on the currently used systems.

8.3. Final conclusions

1. Targeted NCs were prepared from clinically relevant PLGA or non-degradable PS as a model for transport studies, capable of loading therapeutic enzyme *via* encapsulation or

surface coating. Targeting valencies and targeted receptor were varied without affecting other physicochemical properties (size, PDI, ζ-potential), allowing the study the effects of these targeting properties on NC trafficking.

2. ICAM-1 targeted NCs delivered a model therapeutic enzyme, HAse, to brain ECs *in vitro*, increasing the amount of enzyme delivered intracellularly compared to non-targeted enzyme. These NCs penetrate the brain *in vivo* in a mouse model, while providing peripheral targeting to other organs such as the lungs, which is required for LSD treatment, thus representing a promising strategy.

3. ICAM-1 targeted NCs were found to traffic from the apical side to both lysosomes and transcytosis in brain ECs *in vitro.* Then, a fraction of NCs was re-internalized from the basolateral side after transcytosis, which could also traffic to lysosomes.

4. Both basolateral re-internalisation as well as lysosomal trafficking of ICAM-1 targeted NCs depended directly on NC targeting valency. The simultaneous influence of apical and basolateral events caused the overall bell-shape dependency of transcytosis and inverted bell-shape curve of lysosomal trafficking on NC valency, previously observed, and verified here, where NCs with intermediate targeting valency offered the most efficient transcytosis.

5. ASM deficiency, which associates with NPD, affected the trafficking of NCs targeted to ICAM-1, TfR, and PV1 differently, with ICAM-1 targeted NCs being the most promising candidate to deliver ERT across the BBB due to the overall highest absolute number of NCs transcytosed, thus offering the highest potential for drug delivery.

6. GBA deficiency, which associates with GD and PD, decreased the transcytosis of NCs targeted to ICAM-1, TfR, and PV1 across brain ECs, with anti-ICAM-1 NCs being delivered in highest absolute levels, offering the highest potential for ERT delivery into the GD brain.

7. ASM deficiency increased the transcytosis rate of NCs targeted to ICAM-1, whereas GBA deficiency increased the transcytosis rate of NCs targeted to ICAM-1, which is likely the result of a respectively decreased and increased re-internalisation rate.

8. Both ASM deficiency and GBA deficiency increased the trafficking rate of NCs targeted to ICAM-1, TfR, and PV1 to lysosomes in brain ECs which can serve to not only deliver ERT across but also into the BBB to treat the diseased brain and diseased endothelium alike.

9. A better understanding of the intricate interplay of simultaneous trafficking events at the BBB and their alterations in specific pathologies is paramount for the successful development of novel nanotherapeutics to treat brain disease.

Appendix

Funding acknowledgements

This work was supported by awards to S.M. from the Spanish Ministry of Science and Innovation (EXPLORA SAF2017-91909-EXP and RTI2018–101034-B-I00 (MICIE/FEDER)), and the CERCA Program (Generalitat de Catalunya), as well as a fellowship to M.L from the InPhiNIT Predoctoral Fellowship program (LCF/BQ/DI18/11660018) from Fundación La Caixa and Horizon 2020 Marie Sklodowska-Curie (grant 713673).

Publications

Manthe RL, Loeck M, Bhowmick T, Solomon M, Muro S. "*Intertwined mechanisms define transport of anti-ICAM nanocarriers across the endothelium and brain delivery of a therapeutic enzyme"*. J Control Release. May 2020. doi.org/10.1016/j.jconrel.2020.05.009.

Muntimadugu E, Silva-Abreu M, Vives G, Loeck M, Pharm V, Solomon M, Muro S. "*Comparision between nanoparticle encapsulation and surface-loading for lysosomal enzyme replacement therapy".* Int. J. Mol. Sci. April 2022. doi.org/10.3390/ijms23074034.

Solomon M, Loeck M, Silva-Abreu M, Moscoso R, Bautista R, Vigo M, Muro S. "*Implications of transcytosis alterations on blood-brain barrier transport of nanotherapeutics for lysosomal storage disorders"*. J Control Release (revised article under second review round).

Loeck M, Vigo M, Muro S. "*Effect of acid sphingomyelinase deficiency in type A Niemann Pick disease on the transport of therapeutic nanocarriers across the blood-brain barrier".* (In preparation).

Loeck M, Gutierrez-Martinez E, Solomon M, Placci M, Selvadoss A, Garcia-Parajo M, Muro S. "*Effect of glucocerebrosidase deficiency relative to Gaucher and Parkinson's diseases on the blood-brain barrier transport of therapeutic nanocarriers".* (In preparation).

International and national conference, symposium, and seminars

Loeck M, Tump M, Muro S. (July 2019). "*Pathological Alterations Affect the Expression and Drug-Targeting of Transcytosis Receptors in Cellular Models of the Blood-Brain Barrier".* ICMS-IBEC Symposium 2019, Institute for Bioengineering of Catalunya (IBEC), Barcelona, Spain. Poster presentation.

Manthe RL, Loeck M, Bhowmick T, Solomon M, Muro S. (June 2020) "*Intertwined mechanisms define transport of anti-ICAM nanocarriers across the endothelium and brain delivery of a therapeutic enzyme*". CRS Annual Meeting 2020, Virtual format. Poster presentation.

Manthe RL, Loeck M, Bhowmick T, Solomon M, Muro S. (October 2020) "*Role of Valency on the Ability of ICAM-1-Targeted Nanoparticles to Effectively Cross the Blood-Brain Barrier and Deliver Therapeutic Enzymes in Cellular and Animal Models*". 13th IBEC symposium 2020, IBEC, Barcelona, Spain. Poster and flash presentation.

Loeck M, Gutierrez-Martinez E, Solomon M, Vives G, Garcia-Parajo M, Muro S. "*Glucocerebrosidase Deficiency Alters Plasmalemma Nano-Scale Domains and Transcytosis of Therapeutic Nanocarriers by Brain Endothelial Cells*". 14th IBEC symposium 2021, IBEC, Barcelona, Spain. Poster presentation.

Loeck M, Selvadoss A, Solomon M, Muro S. (May 2022) "*Different Neurological Disorders Alter Differently Brain Endothelial Transcytosis of Drug Nanocarriers*". 13th International Symposium on Polymer Therapeutics 2022, Valencia, Spain. Poster presentation.

International Mobility

Five weeks stay in Dr. Silvia Muro laboratory in the Fischell Institute for Biomedical Devices & the Institute for Bioscience and Biotechnology Research of the University of Maryland at College Park, MD, USA.

Ethical & Regulatory Compliance

All experiments described in this document were performed under compliance with all national and EU legislation, regulations, and ethical standards. All activities complied with all fundamental ethical codes and were regularly assessed and implemented, following the basic ethical principles described in the "Charter of Fundamental Rights" of the European Union (EU) (2000/C 364/01, www.europarl.europa.eu/charter/default_en.htm). All ethical items relative to research, training, and conduct were based on guidelines and procedures in place within Institute for Bioengineering of Catalonia (IBEC), Barcelona's Science Park (PCB), and University of Barcelona (UB).

Cells

This proposal involved human cells aimed to *in vitro* tests, including human endothelial cells from the umbilical vein and brain microvasculature, as well as astrocytes and pericytes. These cells were obtained from commercial vendors, i.e., Innoprot, Cultek and Lonza as described in Section 3.2. These vendors adhere to all ethical standards when acquiring specimens for their collections, which are procured, stored, and distributed according to applicable guidelines and regulations, which involve full consent, protection of human subjects and donor anonymity. These cells are numerically catalogued, from which the only information available is the type of cell, passage, and whether they were from a single donor or pooled from several donors. None of these cells were provided with personally-identifiable data, for which this project did not involve human subjects.

Vertebrate animals

Assays with mice were conducted to test circulation and biodistribution of targeted NCs, the status of the BBB permeability, and BBB transport of NCs injected i.v, all shown in Chapter 4. These studies were performed under Generalitat de Catalunya Project 11109, registry 9030/135780/2020, approved on 24/11/2020, which was designed in compliance with the 3R principle (Replacement, Reduction, and Refinement), through improvement of methods to minimize pain and involving the minimal indispensable number of animals to reach specific goals unattainable otherwise. As it can be appreciated from this dissertation, abundant *in vitro* cellular models were implemented to minimize the use of animals. However, the adequacy of the studied

NCs to target the BBB *in vivo* needed to be validated in animal models because this reflects the true interplay of the biophysiological factors such as circulation, clearance, body biodistribution, brain accumulation, etc. Wildtype C57Bl/6 mice were chosen to be able to compare results from this project with previous publications from Muro laboratory, which were based on this species and strain. This was also relevant because future studies will aim to compare data obtained in this wildtype animal with mice that are well-known models of LSDs, such as the ASM knockout mouse. This model is also based on a C57Bl/6 background, which justifies our selection. Mice were commercially obtained from Charles Rivers in compliance with all regulatory protocols. A total of 5 mice were used per condition, as this was estimated to render statistically significant results based on previous experience and statistical analysis. Additionally, similar numbers of males and females were used to best represent both sexes, since targeted NCs are aimed to both. Animals were housed and monitored and injected in approved PCB facilities. I received formal training through the UB course "Curs de Formació del personal usuari d'animals d'experimentació per a les funcions de cura, eutanàsia, realització de procediments, I disseny de projectes I procediments (funcions a, b, c i d) en rosegadors i peixos" in 2019 and obtained the approval by the Generalitat de Catalunya to manipulate mice under supervision by authorized PCB personnel. Animals were injected and kept under anaesthesia with 100 mg/kg ketamine and 1 mg/kg medetomidine every 30 min for the full procedure and through euthanasia by cervical dislocation, under the approved protocol described above. Animals were also regularly monitored for appearance of symptoms of pain or distress, and sacrifice at humane times if required. According to Annex VIII of the Directive 2010/63/EU of the European Parliament and of the Council, the designed procedures in this project were classified as mild to moderate pain. All procedures performed were consistent with the recommendations and guidelines of the Federation of European Laboratory Animal Science Associations (FELASA).

Environmental & health safety

1. Synthesis and use of nanomaterials: Nanocarriers (NCs) composed of PLGA, or polystyrene were used. Poystyrene nanoparticles were purchased from PolySciences, while PLGA nanoparticles were synthesized and characterized in the laboratory. For this task, I followed the Code of Conduct for Responsible Nanosciences and Nanotechnologies Research, following the

European Commission Recommendation (07/02/2008). In particular, health, safety and environmental measures were adopted, as well as good practices in terms of classification and labelling. The Health and Safety Department at IBEC guaranteed the compliance with safety-related rules in our laboratory.

The doses used in experiments (approx. 10^7-10^{10} particles/ml in cell culture or 10^{11}-10^{13} particles/kg of mouse body weight) are to be used. This very small amount of NCs was expected not to cause any harm either to the environment or researchers. But still and making use of the prevention principle currently applied to nanomaterials, any waste or residue related with the nanoparticle experiments was processed with maximal care. NCs were handled mostly in liquid form with a few exceptions, and under a chemical hood as much as possible, thus minimizing the risk of inhalation. The use of gloves, lab coat and goggles are mandatory in the laboratory and further provided protection against the contact of nanomaterials with the skin and eyes. The chemical products and solvents used for the fabrication of the NCs were manipulated using the same means of protection as those provided for the use of other common chemicals and supervised by IBEC.

2. Ionizing/non-ionizing radiation & chemical hazards: The use of radioactive materials (^{125}I), microscopy lasers, and chemical reagents (fixatives, solvents, etc.) may imply health and safety concerns, for which adequate safety measures were put in place to avoid or minimize any potential risk, guided by institutional authorities ensuring safety compliance. For instance, amounts of radioactive materials used are well below the minimum acceptable as safe for human health. In fact, the amounts used are officially considered as no radioactive. Nevertheless, experiments involving these materials were carried out using designated chemical hoods, shields, monitoring equipment, discarding bins, storage units, and PPE. I was required to receive specific training to handle radioactive materials, as well as using the adequate means of protection. An authorized supervisor (Dr. Agustí Munté, supervisor of IR-PCB) was responsible for ensuring that work was performed under good practices guidelines and using adequate safety measures. All activities were performed within dedicated and monitored facilities in PCB, which has the relevant operating authorisations from the Generalitat de Catalunya and the Spanish Nuclear

Security Council (CNS), complying with national legislation regarding radiological working areas and radiological protection (Royal Decrees 1836/1999 and 783/2001, respectively).

All other materials and equipment used in this project fully complied with the respective EU and ISO safety standards. Therefore, no further risks were involved during the course of the project.

Bibliography

1. Feigin, V. L. *et al.* The global burden of neurological disorders: translating evidence into policy. *Lancet Neurol.* **19**, 255–265 (2020).

2. Ray Dorsey, E. *et al.* Global, regional, and national burden of Parkinson's disease, 1990–2016: a systematic analysis for the Global Burden of Disease Study 2016. *Lancet Neurol.* **17**, 939–953 (2018).

3. Vos, T. *et al.* Global, regional, and national incidence, prevalence, and years lived with disability for 328 diseases and injuries for 195 countries, 1990-2016: a systematic analysis for the Global Burden of Disease Study 2016. *Lancet (London, England)* **390**, 1211–1259 (2017).

4. Wang, H. *et al.* Global, regional, and national life expectancy, all-cause mortality, and cause-specific mortality for 249 causes of death, 1980-2015: a systematic analysis for the Global Burden of Disease Study 2015. *Lancet (London, England)* **388**, 1459–1544 (2016).

5. The Circulatory System – Human Nutrition. https://pressbooks.bccampus.ca/nutr1100/chapter/the-cardiovascular-system/.

6. Godwin, L., Tariq, M. A. & Crane, J. S. Histology, Capillary. *StatPearls* (2022).

7. Dejana, E. Endothelial cell-cell junctions: happy together. *Nat. Rev. Mol. Cell Biol.* **5**, 261–270 (2004).

8. Blasig, I. E. & Haseloff, R. F. Tight junctions and tissue barriers. *Antioxid. Redox Signal.* **15**, 1163–1166 (2011).

9. Komarova, Y. A., Kruse, K., Mehta, D. & Malik, A. B. Protein interactions at endothelial junctions and signaling mechanisms regulating endothelial permeability. *Circ. Res.* **120**, 179 (2017).

10. Rapoport, S. I. Opening of the blood-brain barrier by acute hypertension. *Exp. Neurol.* **52**, 467–479 (1976).

11. Sharma, H. S. Blood-CNS barrier, neurodegeneration and neuroprotection: recent therapeutic advancements and nano-drug delivery. *J. Neural Transm.* **118**, 3–6 (2011).

12. Haseloff, R. F., Blasig, I. E., Bauer, H. C. & Bauer, H. In search of the astrocytic factor(s) modulating blood-brain barrier functions in brain capillary endothelial cells in vitro. *Cell. Mol. Neurobiol.* **25**, 25–39 (2005).

13. Wolburg, H., Noell, S., Wolburg-Buchholz, K., MacK, A. & Fallier-Becker, P. Agrin, aquaporin-4, and astrocyte polarity as an important feature of the blood-brain barrier. *Neuroscientist* **15**, 180–193 (2009).

14. Nadal, A., Fuentes, E., Pastor, J. & Mcnaughton, P. A. Plasma albumin is a potent trigger of calcium signals and DNA synthesis in astrocytes. *Proc. Natl. Acad. Sci. U. S. A.* **92**, 1426

(1995).

15. Abbott, N. J., Patabendige, A. A. K., Dolman, D. E. M., Yusof, S. R. & Begley, D. J. Structure and function of the blood-brain barrier. *Neurobiol. Dis.* **37**, 13–25 (2010).

16. Saint-Pol, J., Gosselet, F., Duban-Deweer, S., Cells, G. P.- & 2020, undefined. Targeting and crossing the blood-brain barrier with extracellular vesicles. *mdpi.com*.

17. Koepsell, H. Glucose transporters in brain in health and disease. *Pflugers Arch.* **472**, 1299 (2020).

18. Banks, W. A. Blood-brain barrier as a regulatory interface. *Forum Nutr.* **63**, 102–110 (2010).

19. Kadry, H., Noorani, B. & Cucullo, L. A blood–brain barrier overview on structure, function, impairment, and biomarkers of integrity. *Fluids Barriers CNS* **17**, 69 (2020).

20. Archie, S. R., Al Shoyaib, A. & Cucullo, L. Blood-Brain Barrier Dysfunction in CNS Disorders and Putative Therapeutic Targets: An Overview. *Pharmaceutics* **13**, (2021).

21. Razzak, R. A., Florence, G. J. & Gunn-Moore, F. J. Approaches to CNS Drug Delivery with a Focus on Transporter-Mediated Transcytosis. *Int. J. Mol. Sci.* **20**, (2019).

22. Saraiva, C. *et al.* Nanoparticle-mediated brain drug delivery: Overcoming blood-brain barrier to treat neurodegenerative diseases. *J. Control. Release* **235**, 34–47 (2016).

23. Pardridge, W. M. Biopharmaceutical drug targeting to the brain. *J. Drug Target.* **18**, 157–167 (2010).

24. Begley, D., Pontikis, C. & Scarpa, M. Lysosomal storage diseases and the blood-brain barrier. *Curr. Pharm. Des.* **14**, 1566–1580 (2008).

25. Aird, R. B. A study of intrathecal, cerebrospinal fluid-to-brain exchange. *Exp. Neurol.* **86**, 342–358 (1984).

26. Dong, X. Current strategies for brain drug delivery. *Theranostics* vol. 8 1481–1493 (2018).

27. Pardridge, W. M. Blood–brain barrier delivery. *Drug Discov. Today* **12**, 54–61 (2007).

28. Fung, L. K., Shin, M., Tyler, B., Brem, H. & Saltzman, W. M. Chemotherapeutic drugs released from polymers: distribution of 1,3-bis(2-chloroethyl)-1-nitrosourea in the rat brain. *Pharm. Res.* **13**, 671–682 (1996).

29. Day-Lollini, P. A., Stewart, G. R., Taylor, M. J., Johnson, R. M. & Chellman, G. J. Hyperplastic changes within the leptomeninges of the rat and monkey in response to chronic intracerebroventricular infusion of nerve growth factor. *Exp. Neurol.* **145**, 24–37 (1997).

30. Patel, M. M., Goyal, B. R., Bhadada, S. V., Bhatt, J. S. & Amin, A. F. Getting into the brain: approaches to enhance brain drug delivery. *CNS Drugs* **23**, 35–58 (2009).

31. Lang, A. E. *et al.* Randomized controlled trial of intraputamenal glial cell line-derived neurotrophic factor infusion in Parkinson disease. *Ann. Neurol.* **59**, 459–466 (2006).

32. Muro, S. Strategies for delivery of therapeutics into the central nervous system for treatment of lysosomal storage disorders. *Drug Deliv. Transl. Res.* **2**, 169–186 (2012).

33. Dhuria, S. V., Hanson, L. R. & Frey, W. H. Intranasal delivery to the central nervous system: mechanisms and experimental considerations. *J. Pharm. Sci.* **99**, 1654–1673 (2010).

34. Benedict, C. *et al.* Intranasal insulin improves memory in humans. *Psychoneuroendocrinology* **29**, 1326–1334 (2004).

35. Born, J. *et al.* Sniffing neuropeptides: a transnasal approach to the human brain. *Nat. Neurosci.* **5**, 514–516 (2002).

36. Westin, U. *et al.* Transfer of morphine along the olfactory pathway to the central nervous system after nasal administration to rodents. *Eur. J. Pharm. Sci.* **24**, 565–573 (2005).

37. Burgess, A. & Hynynen, K. Drug delivery across the blood-brain barrier using focused ultrasound. *Expert Opin. Drug Deliv.* **11**, 711 (2014).

38. Salahuddin, T. S., Johansson, B. B., Kalimo, H. & Olsson, Y. Structural changes in the rat brain after carotid infusions of hyperosmolar solutions. An electron microscopic study. *Acta Neuropathol.* **77**, 5–13 (1988).

39. Neuwelt, E. *et al.* Strategies to advance translational research into brain barriers. *Lancet Neurol.* **7**, 84–96 (2008).

40. Stewart, P. A. Endothelial vesicles in the blood-brain barrier: Are they related to permeability? *Cell. Mol. Neurobiol.* **20**, 149–163 (2000).

41. Muro, S., Koval, M. & Muzykantov, V. Endothelial endocytic pathways: gates for vascular drug delivery. *Curr. Vasc. Pharmacol.* **2**, 281–299 (2004).

42. Rodriguez-Boulan, E., Kreitzer, G., Molecular, A. M.-N. reviews & 2005, undefined. Organization of vesicular trafficking in epithelia. *nature.com* (2005) doi:10.1038/nrm1593.

43. and, D. B.-I. journal of clinical pharmacology & 2009, undefined. The endosomal network. *europepmc.org*.

44. Thompson, A. *et al.* Recycling endosomes of polarized epithelial cells actively sort apical and basolateral cargos into separate subdomains. *Mol. Biol. Cell* **18**, 2687–2697 (2007).

45. Haqqani, A. S. *et al.* Endosomal trafficking regulates receptor-mediated transcytosis of antibodies across the blood brain barrier. *J. Cereb. Blood Flow Metab.* **38**, 727–740 (2018).

46. Traub, L. M. Regarding the amazing choreography of clathrin coats. *PLoS Biol.* **9**, (2011).

47. Kaksonen, M., Toret, C. P. & Drubin, D. G. A modular design for the clathrin- and actin-mediated endocytosis machinery. *Cell* **123**, 305–320 (2005).

48. Taylor, M. J., Perrais, D. & Merrifield, C. J. A high precision survey of the molecular dynamics of mammalian clathrin-mediated endocytosis. *PLoS Biol.* **9**, (2011).

49. Carroll, S. Y. *et al.* Analysis of yeast endocytic site formation and maturation through a regulatory transition point. *Mol. Biol. Cell* **23**, 657–668 (2012).

50. Schmid, E. M. & McMahon, H. T. Integrating molecular and network biology to decode endocytosis. *Nature* **448**, 883–888 (2007).

51. Kaksonen, M. & Roux, A. Mechanisms of clathrin-mediated endocytosis. *Nat. Rev. Mol. Cell Biol. 2018 195* **19**, 313–326 (2018).

52. Cocucci, E., Aguet, F., Boulant, S. & Kirchhausen, T. The first five seconds in the life of a clathrin-coated pit. *Cell* **150**, 495–507 (2012).

53. Ford, M. G. J. *et al.* Curvature of clathrin-coated pits driven by epsin. *Nat. 2002 4196905* **419**, 361–366 (2002).

54. Kadlecova, Z. *et al.* Regulation of clathrin-mediated endocytosis by hierarchical allosteric activation of AP2. *J. Cell Biol.* **216**, 167–179 (2017).

55. Kelly, B. T. *et al.* Clathrin adaptors. AP2 controls clathrin polymerization with a membrane-activated switch. *Science* **345**, 459–463 (2014).

56. Messa, M. *et al.* Epsin deficiency impairs endocytosis by stalling the actin-dependent invagination of endocytic clathrin-coated pits. *Elife* **3**, 1–25 (2014).

57. Miller, S. E. *et al.* CALM regulates clathrin-coated vesicle size and maturation by directly sensing and driving membrane curvature. *Dev. Cell* **33**, 163–175 (2015).

58. Sun, Y., Martin, A. C. & Drubin, D. G. Endocytic internalization in budding yeast requires coordinated actin nucleation and myosin motor activity. *Dev. Cell* **11**, 33–46 (2006).

59. Dawson, J. C., Legg, J. A. & Machesky, L. M. Bar domain proteins: a role in tubulation, scission and actin assembly in clathrin-mediated endocytosis. *Trends Cell Biol.* **16**, 493–498 (2006).

60. Sousa, R. & Lafer, E. M. The role of molecular chaperones in clathrin mediated vesicular trafficking. *Front. Mol. Biosci.* **2**, (2015).

61. Boado, R. J. Brain-derived peptides increase blood-brain barrier GLUT1 glucose transporter gene expression via mRNA stabilization. *Neurosci. Lett.* **255**, 147–150 (1998).

62. Duffy, K. R., Pardridge, W. M. & Rosenfeld, R. G. Human blood-brain barrier insulin-like growth factor receptor. *Metabolism.* **37**, 136–140 (1988).

63. Mayor, S. & Pagano, R. E. Pathways of clathrin-independent endocytosis. *Nat. Rev. Mol. Cell Biol.* **8**, 603–612 (2007).

64. Pulgar, V. M. Transcytosis to cross the blood brain barrier, new advancements and challenges. *Front. Neurosci.* **13**, 1019 (2019).

65. Schnitzer, J. E. Caveolae: from basic trafficking mechanisms to targeting transcytosis for tissue-specific drug and gene delivery in vivo. *Adv. Drug Deliv. Rev.* **49**, 265–80 (2001).

66. Rothberg, K. G. *et al.* Caveolin, a protein component of caveolae membrane coats. *Cell* **68**, 673–682 (1992).

67. Hill, M. M. *et al.* PTRF-cavin, a conserved cytoplasmic protein required for caveola formation and function. *Cell* **132**, 113 (2008).

68. Hayer, A., Stoeber, M., Bissig, C., Traffic, A. H.- & 2010, undefined. Biogenesis of caveolae: stepwise assembly of large caveolin and cavin complexes. *Wiley Online Libr.* **11**, 361–382 (2010).

69. Liu, L. & Pilch, P. F. A Critical Role of Cavin (Polymerase I and Transcript Release Factor) in Caveolae Formation and Organization. *J. Biol. Chem.* **283**, 4314–4322 (2008).

70. Vinten, J., Johnsen, A. H., Roepstorff, P., Harpøth, J. & Tranum-Jensen, J. Identification of a major protein on the cytosolic face of caveolae. *Biochim. Biophys. Acta - Biomembr.* **1717**, 34–40 (2005).

71. McMahon, K. A. *et al.* SRBC/cavin-3 is a caveolin adapter protein that regulates caveolae function. *EMBO J.* **28**, 1001–1015 (2009).

72. Parton, R. G., Tillu, V. A. & Collins, B. M. Caveolae. *Curr. Biol.* **28**, R402–R405 (2018).

73. Stoeber, M. *et al.* Oligomers of the ATPase EHD2 confine caveolae to the plasma membrane throughassociation with actin. *EMBO J.* **31**, 2350 (2012).

74. Morén, B. *et al.* EHD2 regulates caveolar dynamics via ATP-driven targeting and oligomerization. *Mol. Biol. Cell* **23**, 1316 (2012).

75. Hansen, C. G., Howard, G. & Nichols, B. J. Pacsin 2 is recruited to caveolae and functions in caveolar biogenesis. *J. Cell Sci.* **124**, 2777–2785 (2011).

76. Kostan, J. *et al.* Direct interaction of actin filaments with F-BAR protein pacsin2. *EMBO Rep.* **15**, 1154–1162 (2014).

77. Senju, Y., Itoh, Y., Takano, K., Hamada, S. & Suetsugu, S. Essential role of PACSIN2/syndapin-II in caveolae membrane sculpting. *J. Cell Sci.* **124**, 2032–2040 (2011).

78. Vasile, E., Simionescu, M. & Simionescu, N. Visualization of the binding, endocytosis, and transcytosis of low-density lipoprotein in the arterial endothelium in situ. *J. Cell Biol.* **96**, 1677–1689 (1983).

79. Nistor, A. & Simionescu, M. Uptake of low density lipoproteins by the hamster lung: Interactions with capillary endothelium. *Am. Rev. Respir. Dis.* **134**, 1266–1272 (1986).

80. Ghitescu, L., Fixman, A., Simionescu, M. & Simionescu, N. Specific binding sites for

albumin restricted to plasmalemmal vesicles of continuous capillary endothelium: Receptor-mediated transcytosis. *J. Cell Biol.* **102**, 1304–1311 (1986).

81. Bendayan, M. & Rasio, E. A. Transport of insulin and albumin by the microvascular endothelium of the rete mirabile. *J. Cell Sci.* **109**, 1857–1864 (1996).

82. Schenk, G. J. & de Vries, H. E. Altered blood–brain barrier transport in neuro-inflammatory disorders. *Drug Discovery Today: Technologies* vol. 20 5–11 (2016).

83. Sorets, A. G., Rosch, J. C., Duvall, C. L. & Lippmann, E. S. Caveolae-mediated transport at the injured blood–brain barrier as an underexplored pathway for central nervous system drug delivery. *Curr. Opin. Chem. Eng.* **30**, 86–95 (2020).

84. Zhou, M. *et al.* Caveolae-Mediated Endothelial Transcytosis across the Blood-Brain Barrier in Acute Ischemic Stroke. *J. Clin. Med.* **10**, (2021).

85. Xiao, M., Xiao, Z. J., Yang, B., Lan, Z. & Fang, F. Blood-Brain Barrier: More Contributor to Disruption of Central Nervous System Homeostasis Than Victim in Neurological Disorders. *Front. Neurosci.* **14**, 764 (2020).

86. Duncan, R. The dawning era of polymer therapeutics. *Nat. Rev. Drug Discov.* **2**, 347–360 (2003).

87. Tewabe, A., Abate, A., Tamrie, M., Seyfu, A. & Siraj, E. A. Targeted Drug Delivery — From Magic Bullet to Nanomedicine: Principles, Challenges, and Future Perspectives . *J. Multidiscip. Healthc.* **14**, 1711–1724 (2021).

88. Panyam, J. & Labhasetwar, V. Biodegradable nanoparticles for drug and gene delivery to cells and tissue. *Adv. Drug Deliv. Rev.* **55**, 329–347 (2003).

89. BAZAK, R., HOURI, M., ACHY, S. EL, HUSSEIN, W. & REFAAT, T. Passive targeting of nanoparticles to cancer: A comprehensive review of the literature. *Mol. Clin. Oncol.* **2**, 904 (2014).

90. Orii, K. O. *et al.* Defining the Pathway for Tat-mediated Delivery of β-Glucuronidase in Cultured Cells and MPS VII Mice. *Mol. Ther.* **12**, 345 (2005).

91. Jones, A. T. Gateways and tools for drug delivery: endocytic pathways and the cellular dynamics of cell penetrating peptides. *Int. J. Pharm.* **354**, 34–38 (2008).

92. Rosenfeld, M. G., Kreibich, G., Popov, D., Kato, K. & Sabatini, D. D. Biosynthesis of lysosomal hydrolases: their synthesis in bound polysomes and the role of co- and post-translational processing in determining their subcellular distribution. *J. Cell Biol.* **93**, 135 (1982).

93. Hwa, J. L., Zhang, Y., Zhu, C., Duff, K. & Pardridge, W. M. Imaging brain amyloid of Alzheimer disease in vivo in transgenic mice with an Abeta peptide radiopharmaceutical. *J. Cereb. Blood Flow Metab.* **22**, 223–231 (2002).

94. Wu, D. & Pardridge, W. M. Neuroprotection with noninvasive neurotrophin delivery to

the brain. *Proc. Natl. Acad. Sci. U. S. A.* **96**, 254 (1999).

95. Murciano, J.-C. C. *et al.* ICAM-directed vascular immunotargeting of antithrombotic agents to the endothelial luminal surface. *Blood* **101**, 3977–3984 (2003).

96. Shuvaev, V. V., Dziubla, T., Wiewrodt, R. & Muzykantov, V. R. Streptavidin-biotin crosslinking of therapeutic enzymes with carrier antibodies: nanoconjugates for protection against endothelial oxidative stress. *Methods Mol. Biol.* **283**, 3–19 (2004).

97. Veronese, F. M. & Morpurgo, M. Bioconjugation in pharmaceutical chemistry. *Farmaco* **54**, 497–516 (1999).

98. Manthe, R. L. & Muro, S. Lysosomes and Nanotherapeutics: Diseases, Treatments, and Side Effects. 261–305 (2014) doi:10.1142/9789814520652_0025.

99. Pudlarz, A. & Szemraj, J. Nanoparticles as carriers of proteins, peptides and other therapeutic molecules. *Open Life Sci.* **13**, 285–298 (2018).

100. Kraft, J. C., Freeling, J. P., Wang, Z. & Ho, R. J. Y. Emerging research and clinical development trends of liposome and lipid nanoparticle drug delivery systems. *J. Pharm. Sci.* **103**, 29–52 (2014).

101. Torchilin, V. P. Multifunctional nanocarriers. *Adv. Drug Deliv. Rev.* **58**, 1532–1555 (2006).

102. Moghimi, S. M. & Szebeni, J. Stealth liposomes and long circulating nanoparticles: critical issues in pharmacokinetics, opsonization and protein-binding properties. *Prog. Lipid Res.* **42**, 463–478 (2003).

103. Minko, T., Pakunlu, R. I., Wang, Y., Khandare, J. J. & Saad, M. New generation of liposomal drugs for cancer. *Anticancer. Agents Med. Chem.* **6**, 537–552 (2006).

104. Leite, E. A. *et al.* Encapsulation of cisplatin in long-circulating and pH-sensitive liposomes improves its antitumor effect and reduces acute toxicity. *Int. J. Nanomedicine* **7**, 5259 (2012).

105. Witoonsaridsilp, W., Paeratakul, O., Panyarachun, B. & Sarisuta, N. Development of Mannosylated Liposomes Using Synthesized N-Octadecyl-d-Mannopyranosylamine to Enhance Gastrointestinal Permeability for Protein Delivery. *AAPS PharmSciTech* **13**, 699 (2012).

106. Werle, M., Makhlof, A. & Takeuchi, H. Carbopol-lectin conjugate coated liposomes for oral peptide delivery. *Chem. Pharm. Bull. (Tokyo).* **58**, 432–434 (2010).

107. Kim, E.-M. & Jeong, H.-J. Liposomes: Biomedical Applications. *Chonnam Med. J.* **57**, 27 (2021).

108. Dianzani, C. *et al.* Drug Delivery Nanoparticles in Skin Cancers. *Biomed Res. Int.* **2014**, (2014).

109. Rana, S., Bajaj, A., Mout, R. & Rotello, V. M. Monolayer coated gold nanoparticles for delivery applications. *Adv. Drug Deliv. Rev.* **64**, 200 (2012).

110. Ghosh, P., Han, G., De, M., Kim, C. K. & Rotello, V. M. Gold nanoparticles in delivery applications. *Adv. Drug Deliv. Rev.* **60**, 1307–1315 (2008).

111. Piludu, M., Medda, L., Monduzzi, M. & Salis, A. Gold Nanoparticles: A Powerful Tool to Visualize Proteins on Ordered Mesoporous Silica and for the Realization of Theranostic Nanobioconjugates. *Int. J. Mol. Sci.* **19**, (2018).

112. Chung, Y. H., Cai, H. & Steinmetz, N. F. Viral nanoparticles for drug delivery, imaging, immunotherapy, and theranostic applications. *Adv. Drug Deliv. Rev.* **156**, 214 (2020).

113. LeBowitz, J. H. *et al.* Glycosylation-independent targeting enhances enzyme delivery to lysosomes and decreases storage in mucopolysaccharidosis type VII mice. *Proc. Natl. Acad. Sci. U. S. A.* **101**, 3083 (2004).

114. Prince, W. S. *et al.* Lipoprotein receptor binding, cellular uptake, and lysosomal delivery of fusions between the receptor-associated protein (RAP) and alpha-L-iduronidase or acid alpha-glucosidase. *J. Biol. Chem.* **279**, 35037–35046 (2004).

115. Pettinato, M. C. Introduction to Antibody-Drug Conjugates. *Antibodies* **10**, (2021).

116. Discher, D. E. & Eisenberg, A. Polymer vesicles. *Science* **297**, 967–973 (2002).

117. Hans, M., Materials, A. L.-C. O. in S. S. and & 2002, undefined. Biodegradable nanoparticles for drug delivery and targeting. *Elsevier*.

118. Essa, D., Kondiah, P. P. D., Choonara, Y. E. & Pillay, V. The Design of Poly(lactide-co-glycolide) Nanocarriers for Medical Applications. *Front. Bioeng. Biotechnol.* **8**, 48 (2020).

119. Kapoor, D. N. *et al.* PLGA: a unique polymer for drug delivery. *Ther. Deliv.* **6**, 41–58 (2015).

120. Operti, M. C. *et al.* PLGA-based nanomedicines manufacturing: Technologies overview and challenges in industrial scale-up. *Int. J. Pharm.* **605**, 120807 (2021).

121. Li, Y. P. *et al.* PEGylated PLGA nanoparticles as protein carriers: synthesis, preparation and biodistribution in rats. *J. Control. Release* **71**, 203–211 (2001).

122. Li, J., Rothstein, S. N., Little, S. R., Edenborn, H. M. & Meyer, T. Y. The effect of monomer order on the hydrolysis of biodegradable poly(lactic-co-glycolic acid) repeating sequence copolymers. *J. Am. Chem. Soc.* **134**, 16352–16359 (2012).

123. Parikh, J. K., Vallabhbhai, S., Engineer, C., Parikh, J. & Raval, A. Review on hydrolytic degradation behavior of biodegradable polymers from controlled drug delivery system. *researchgate.net* **25**, 79–85 (2011).

124. Makadia, H., Polymers, S. S.- & 2011, undefined. Poly Lactic-co-Glycolic Acid (PLGA) as Biodegradable Controlled Drug Delivery Carrier. *mdpi.com* **3**, 1377–1397 (2011).

125. Sun, X. *et al.* Poly(Lactic-co-Glycolic Acid): Applications and Future Prospects for Periodontal Tissue Regeneration. *mdpi.com* doi:10.3390/polym9060189.

126. Lü, J. M. *et al.* Current advances in research and clinical applications of PLGA-based nanotechnology. *Expert Rev. Mol. Diagn.* **9**, 325 (2009).

127. Gentile, P., Chiono, V., … I. C.-I. journal of & 2014, undefined. An Overview of Poly(lactic-co-glycolic) Acid (PLGA)-Based Biomaterials for Bone Tissue Engineering. *mdpi.com* **15**, 15 (2014).

128. Wicki, A., Witzigmann, D., Balasubramanian, V. & Huwyler, J. Nanomedicine in cancer therapy: Challenges, opportunities, and clinical applications. *J. Control. Release* **200**, 138–157 (2015).

129. Muro, S. New biotechnological and nanomedicine strategies for treatment of lysosomal storage disorders. *Wiley Interdiscip. Rev. Nanomed. Nanobiotechnol.* **2**, 189 (2010).

130. Alcalá-Alcalá, S., Benítez-Cardoza, C. G., Lima-Muñoz, E. J., Piñón-Segundo, E. & Quintanar-Guerrero, D. Evaluation of a combined drug-delivery system for proteins assembled with polymeric nanoparticles and porous microspheres; characterization and protein integrity studies. *Int. J. Pharm.* **489**, 139–147 (2015).

131. Torchilin, V. Intracellular delivery of protein and peptide therapeutics. *Drug Discov. Today Technol.* **5**, e95–e103 (2008).

132. Xie, J., Lee, S. & Chen, X. Nanoparticle-based theranostic agents. *Adv. Drug Deliv. Rev.* **62**, 1064 (2010).

133. Pisal, D. S., Kosloski, M. P. & Balu-Iyer, S. V. DELIVERY OF THERAPEUTIC PROTEINS. *J. Pharm. Sci.* **99**, 2557 (2010).

134. Saito, N. *et al.* Carbon nanotubes: biomaterial applications. *Chem. Soc. Rev.* **38**, 1897–1903 (2009).

135. Atanase, L. I. Micellar Drug Delivery Systems Based on Natural Biopolymers. *Polymers (Basel).* **13**, 1–33 (2021).

136. Delie, F. & Blanco-Príeto, M. J. Polymeric Particulates to Improve Oral Bioavailability of Peptide Drugs. *Mol. A J. Synth. Chem. Nat. Prod. Chem.* **10**, 65 (2005).

137. Vila, A., Sánchez, A., Tobío, M., Calvo, P. & Alonso, M. J. Design of biodegradable particles for protein delivery. *J. Control. Release* **78**, 15–24 (2002).

138. Stayton, P. S. *et al.* 'Smart' delivery systems for biomolecular therapeutics. *Orthod. Craniofac. Res.* **8**, 219–225 (2005).

139. Shuvaev, V. V., Brenner, J. S. & Muzykantov, V. R. Targeted endothelial nanomedicine for common acute pathological conditions. *J. Control. Release* **219**, 576 (2015).

140. Yoo, J. W., Irvine, D. J., Discher, D. E. & Mitragotri, S. Bio-inspired, bioengineered and biomimetic drug delivery carriers. *Nat. Rev. Drug Discov.* **10**, 521–535 (2011).

141. El-Sayed, M. E. H., Hoffman, A. S. & Stayton, P. S. Smart polymeric carriers for enhanced intracellular delivery of therapeutic macromolecules. *Expert Opin. Biol. Ther.* **5**, 23–32

(2005).

142. Albanese, A., Tang, P. S. & Chan, W. C. W. The Effect of Nanoparticle Size, Shape, and Surface Chemistry on Biological Systems. *http://dx.doi.org/10.1146/annurev-bioeng-071811-150124* **14**, 1–16 (2012).

143. Amoozgar, Z. & Yeo, Y. Recent advances in stealth coating of nanoparticle drug delivery systems. *Wiley Interdiscip. Rev. Nanomed. Nanobiotechnol.* **4**, 219 (2012).

144. Moghimi, S. M., Hunter, A. C. & Murray, J. C. Nanomedicine: current status and future prospects. *FASEB J.* **19**, 311–330 (2005).

145. Papademetriou, I. T., Garnacho, C., Schuchman, E. H. & Muro, S. In vivo performance of polymer nanocarriers dually-targeted to epitopes of the same or different receptors. *Biomaterials* **34**, 3459–66 (2013).

146. Kim, J. *et al.* Co-coating of receptor-targeted drug nanocarriers with anti-phagocytic moieties enhances specific tissue uptake versus non-specific phagocytic clearance. *Biomaterials* **147**, 14–25 (2017).

147. Calderon, A. J. *et al.* Optimizing endothelial targeting by modulating the antibody density and particle concentration of anti-ICAM coated carriers. *J. Control. Release* **150**, 37–44 (2011).

148. Muro, S. *et al.* Endothelial targeting of high-affinity multivalent polymer nanocarriers directed to intercellular adhesion molecule 1. *J. Pharmacol. Exp. Ther.* **317**, 1161–1169 (2006).

149. Serrano, D., Manthe, R. L., Paul, E., Chadha, R. & Muro, S. How Carrier Size and Valency Modulate Receptor-Mediated Signaling: Understanding the Link between Binding and Endocytosis of ICAM-1-Targeted Carriers. *Biomacromolecules* **17**, 3127–3137 (2016).

150. Aird, W. Endothelial biomedicine. (2007).

151. Morral-Ruiz, G. *et al.* Multifunctional polyurethane-urea nanoparticles to target and arrest inflamed vascular environment: A potential tool for cancer therapy and diagnosis. *J. Control. RELEASE* **171**, 163–171 (2013).

152. Springer, T. A. Traffic signals for lymphocyte recirculation and leukocyte emigration: the multistep paradigm. *Cell* **76**, 301–314 (1994).

153. Yang, L. *et al.* ICAM-1 regulates neutrophil adhesion and transcellular migration of TNF-alpha-activated vascular endothelium under flow. *Blood* **106**, 584–592 (2005).

154. Rothlein, R., Dustin, M. L., Marlin, S. D. & Springer, T. A. A human intercellular adhesion molecule (ICAM-1) distinct from LFA-1. *J. Immunol.* **137**, 1270–4 (1986).

155. Heemskerk, N., Van Rijssel, J. & Van Buul, J. D. Rho-GTPase signaling in leukocyte extravasation: an endothelial point of view. *Cell Adh. Migr.* **8**, 67–75 (2014).

156. Wee, H., Oh, H. M., Jo, J. H. & Jun, C. D. ICAM-1/LFA-1 interaction contributes to the

induction of endothelial cell-cell separation: implication for enhanced leukocyte diapedesis. *Exp. Mol. Med. 2009 415* **41**, 341–348 (2009).

157. Rahman, A. & Fazal, F. Hug tightly and say goodbye: role of endothelial ICAM-1 in leukocyte transmigration. *Antioxid. Redox Signal.* **11**, 823–839 (2009).

158. Grassmé, H., Riehle, A., Wilker, B. & Gulbins, E. Rhinoviruses Infect Human Epithelial Cells via Ceramide-enriched Membrane Platforms *. *J. Biol. Chem.* **280**, 26256–26262 (2005).

159. Muro, S. *et al.* Control of intracellular trafficking of ICAM-1-targeted nanocarriers by endothelial Na^+/H^+ exchanger proteins. *Am. J. Physiol. Cell. Mol. Physiol.* **290**, L809–L817 (2006).

160. Muro, S. *et al.* A novel endocytic pathway induced by clustering endothelial ICAM-1 or PECAM-1. *J. Cell Sci.* **116**, 1599–609 (2003).

161. Serrano, D., Bhowmick, T., Chadha, R., Garnacho, C. & Muro, S. Intercellular adhesion molecule 1 engagement modulates sphingomyelinase and ceramide, supporting uptake of drug carriers by the vascular endothelium. *Arterioscler. Thromb. Vasc. Biol.* **32**, 1178–85 (2012).

162. Garnacho, C. *et al.* RhoA activation and actin reorganization involved in endothelial CAM-mediated endocytosis of anti-PECAM carriers: critical role for tyrosine 686 in the cytoplasmic tail of PECAM-1. *Blood* **111**, 3024 (2008).

163. Ghaffarian, R., Roki, N., Abouzeid, A., Vreeland, W. & Muro, S. Intra- and trans-cellular delivery of enzymes by direct conjugation with non-multivalent anti-ICAM molecules. *J. Control. Release* **238**, 221–230 (2016).

164. Muro, S. *et al.* Control of endothelial targeting and intracellular delivery of therapeutic enzymes by modulating the size and shape of ICAM-1-targeted carriers. *Mol. Ther.* **16**, 1450–1458 (2008).

165. Muro, S., Gajewski, C., Koval, M. & Muzykantov, V. R. ICAM-1 recycling in endothelial cells: a novel pathway for sustained intracellular delivery and prolonged effects of drugs. *Blood* **105**, 650–658 (2005).

166. Muzykantov, V. R. Biomedical aspects of targeted delivery of drugs to pulmonary endothelium. *Expert Opin. Drug Deliv.* **2**, 909–926 (2005).

167. Ghaffarian, R., Bhowmick, T. & Muro, S. Transport of nanocarriers across gastrointestinal epithelial cells by a new transcellular route induced by targeting ICAM-1. *J. Control. Release* **163**, 25–33 (2012).

168. Hsu, J., Bhowmick, T., Burks, S. R., Kao, J. P. Y. & Muro, S. Enhancing biodistribution of therapeutic enzymes in vivo by modulating surface coating and concentration of ICAM-1-targeted nanocarriers. *J. Biomed. Nanotechnol.* **10**, 345–354 (2014).

169. Bhowmick: ICAM-1-targeted nanocarriers provide efficient... - Google Académico. https://scholar.google.com/scholar_lookup?journal=Journal+of+Controlled+Release,+Na

tional+Harbor,+Maryland,+USA&title=ICAM-1-targeted+nanocarriers+provide+efficient+targeting,+transport+across+the+BBB,+and+uniform+distribution+and+effects+of+therapeutic+enzymes+in+the+brain,+Controlled+Release+Society&author=T+Bhowmick&author=J+Hsu&author=R+Dhami&author=SR+Burks&author=JPY+Kao&publication_year=2011&pages=34&.

170. Manthe, R. L. *et al.* Intertwined mechanisms define transport of anti-ICAM nanocarriers across the endothelium and brain delivery of a therapeutic enzyme. *J. Control. Release* **324**, 181–193 (2020).

171. Garnacho, C., Dhami, R., Solomon, M., Schuchman, E. H. & Muro, S. Enhanced Delivery and Effects of Acid Sphingomyelinase by ICAM-1-Targeted Nanocarriers in Type B Niemann-Pick Disease Mice. *Mol. Ther.* **25**, 1686–1696 (2017).

172. Hsu, J., Northrup, L., Bhowmick, T. & Muro, S. Enhanced delivery of α-glucosidase for Pompe disease by ICAM-1-targeted nanocarriers: comparative performance of a strategy for three distinct lysosomal storage disorders. *Nanomedicine* **8**, 731–9 (2012).

173. Muro, S. *et al.* Slow intracellular trafficking of catalase nanoparticles targeted to ICAM-1 protects endothelial cells from oxidative stress. *Am. J. Physiol. Physiol.* **285**, C1339–C1347 (2003).

174. Hsu, J. *et al.* Enhanced endothelial delivery and biochemical effects of alpha-galactosidase by ICAM-1-targeted nanocarriers for Fabry disease. *J. Control. Release* **149**, 323–331 (2011).

175. Garnacho, C. *et al.* Delivery of acid sphingomyelinase in normal and niemann-pick disease mice using intercellular adhesion molecule-1-targeted polymer nanocarriers. *J. Pharmacol. Exp. Ther.* **325**, 400–408 (2008).

176. Anselmo, A. C. *et al.* Exploiting shape, cellular-hitchhiking and antibodies to target nanoparticles to lung endothelium: Synergy between physical, chemical and biological approaches. *Biomaterials* **68**, 1–8 (2015).

177. Choi, K. S. *et al.* Inflammation-Specific T1 Imaging Using Anti-Intercellular Adhesion Molecule 1 Antibody-Conjugated Gadolinium Diethylenetriaminepentaacetic Acid: *http://dx.doi.org/10.2310/7290.2007.00005* **6**, 75–84 (2007).

178. Park, S. *et al.* Self-assembled nanoplatform for targeted delivery of chemotherapy agents via affinity-regulated molecular interactions. *Biomaterials* **31**, 7766–7775 (2010).

179. Hamilton, A. J. *et al.* Intravascular ultrasound molecular imaging of atheroma components in vivo. *J. Am. Coll. Cardiol.* **43**, 453–460 (2004).

180. Weller, G. E. R., Villanueva, F. S., Tom, E. M. & Wagner, W. R. Targeted ultrasound contrast agents: in vitro assessment of endothelial dysfunction and multi-targeting to ICAM-1 and sialyl Lewisx. *Biotechnol. Bioeng.* **92**, 780–788 (2005).

181. Ghaffarian, R., Pérez-Herrero, E., Oh, H., Raghavan, S. R. & Muro, S. Chitosan-Alginate

Microcapsules Provide Gastric Protection and Intestinal Release of ICAM-1-Targeting Nanocarriers, Enabling GI Targeting in Vivo. *Adv. Funct. Mater.* **26**, 3382–3393 (2016).

182. Bloemen, P. G. M. *et al.* Adhesion molecules: a new target for immunoliposome-mediated drug delivery. *FEBS Lett.* **357**, 140–144 (1995).

183. Sakhalkar, H. S. *et al.* Leukocyte-inspired biodegradable particles that selectively and avidly adhere to inflamed endothelium in vitro and in vivo. *Proc. Natl. Acad. Sci. U. S. A.* **100**, 15895–15900 (2003).

184. Chittasupho, C. *et al.* ICAM-1 targeting of doxorubicin-loaded PLGA nanoparticles to lung epithelial cells. *Eur. J. Pharm. Sci.* **37**, 141–150 (2009).

185. Rollerova, E. *et al.* Polymeric nanoparticles - Targeted drug delivery systems for treatment of CNS disorders and their possible endocrine disrupting activities. *Endocr. Regul.* **45**, 49–60 (2011).

186. Bondy, S. C. Nanoparticles and colloids as contributing factors in neurodegenerative disease. *Int. J. Environ. Res. Public Health* **8**, 2200–2211 (2011).

187. Muro, S., Schuchman, E. H. & Muzykantov, V. R. Lysosomal enzyme delivery by ICAM-1-targeted nanocarriers bypassing glycosylation- and clathrin-dependent endocytosis. *Mol. Ther.* **13**, 135–141 (2006).

188. Clark, A. J. L. *et al.* Biosynthetic human insulin in the treatment of diabetes. A double-blind crossover trial in established diabetic patients. *Lancet (London, England)* **2**, 354–357 (1982).

189. Leader, B., Baca, Q. J. & Golan, D. E. Protein therapeutics: a summary and pharmacological classification. *Nat. Rev. Drug Discov. 2007 71* **7**, 21–39 (2008).

190. Vecchio, I., Tornali, C., Bragazzi, N. L. & Martini, M. The Discovery of Insulin: An Important Milestone in the History of Medicine. *Front. Endocrinol. (Lausanne).* **9**, 613 (2018).

191. Barton, N. W. *et al.* Replacement therapy for inherited enzyme deficiency--macrophage-targeted glucocerebrosidase for Gaucher's disease. *N. Engl. J. Med.* **324**, 1464–1470 (1991).

192. Barton, N. W. *et al.* Dose-dependent responses to macrophage-targeted glucocerebrosidase in a child with Gaucher disease. *J. Pediatr.* **120**, 277–280 (1992).

193. Mason, H. S., Warzecha, H., Mor, T. & Arntzen, C. J. Edible plant vaccines: applications for prophylactic and therapeutic molecular medicine. *Trends Mol. Med.* **8**, 324–329 (2002).

194. Wurm, F. & Bernard, A. Large-scale transient expression in mammalian cells for recombinant protein production. *Curr. Opin. Biotechnol.* **10**, 156–159 (1999).

195. Zoller, M. J. New molecular biology methods for protein engineering. *Curr. Opin. Biotechnol.* **2**, 526–531 (1991).

196. Brannigan, J. A. & Wilkinson, A. J. Protein engineering 20 years on. *Nat. Rev. Mol. Cell Biol. 2002 312* **3**, 964–970 (2002).

197. Grabowski, G. A. *et al.* Enzyme therapy in type 1 Gaucher disease: Comparative efficacy of mannose- terminated glucocerebrosidase from natural and recombinant sources. *Ann. Intern. Med.* **122**, 33–39 (1995).

198. Rupa, P. & Mine, Y. Immunological comparison of native and recombinant egg allergen, ovalbumin, expressed in Escherichia coli. *Biotechnol. Lett.* **25**, 1917–1924 (2003).

199. Reichert, J. M. Trends in development and approval times for new therapeutics in the United States. *Nat. Rev. Drug Discov. 2003 29* **2**, 695–702 (2003).

200. Usmani, S. S. *et al.* THPdb: Database of FDA-approved peptide and protein therapeutics. *PLoS One* **12**, (2017).

201. Singh, R., Singh, S. & Lillard, J. W. Past, Present, and Future Technologies for Oral Delivery of Therapeutic Proteins. *J. Pharm. Sci.* **97**, 2497 (2008).

202. Amsden, B. G. & Goosen, M. F. A. Transdermal delivery of peptide and protein drugs: An overview. *AIChE J.* **41**, 1972–1997 (1995).

203. Scheuch, G., Siekmeier, R., Scheuch, G. & Siekmeier, R. NOVEL APPROACHES TO ENHANCE PULMONARY. *researchgate.net* (2007).

204. Brasnjevic, I., Steinbusch, H. W. M., Schmitz, C. & Martinez-Martinez, P. Delivery of peptide and protein drugs over the blood-brain barrier. *Prog. Neurobiol.* **87**, 212–251 (2009).

205. Platt, F. M., d'Azzo, A., Davidson, B. L., Neufeld, E. F. & Tifft, C. J. Lysosomal storage diseases. *Nat. Rev. Dis. Prim. 2018 41* **4**, 1–25 (2018).

206. Ballabio, A. & Gieselmann, V. Lysosomal disorders: from storage to cellular damage. *Biochim. Biophys. Acta* **1793**, 684–696 (2009).

207. Platt, F. M., Boland, B. & van der Spoel, A. C. The cell biology of disease: lysosomal storage disorders: the cellular impact of lysosomal dysfunction. *J. Cell Biol.* **199**, 723–734 (2012).

208. Kingma, S. D. K., Bodamer, O. A. & Wijburg, F. A. Epidemiology and diagnosis of lysosomal storage disorders; challenges of screening. *Best Pract. Res. Clin. Endocrinol. Metab.* **29**, 145–157 (2015).

209. Fuller, M., Meikle, P. J. & Hopwood, J. J. Epidemiology of lysosomal storage diseases: an overview. *Fabry Dis. Perspect. from 5 Years FOS* (2006).

210. Beck, M. Treatment strategies for lysosomal storage disorders. *Dev. Med. Child Neurol.* **60**, 13–18 (2018).

211. Muro, S., Schuchman, E. H. & Muzykantov, V. R. No Title. *Mol. Ther.* **13**, (2006).

212. Breiden, B. & Sandhoff, K. Mechanism of Secondary Ganglioside and Lipid Accumulation in Lysosomal Disease. *Int. J. Mol. Sci.* **21**, (2020).

213. Vembar, S. S. & Brodsky, J. L. One step at a time: endoplasmic reticulum-associated degradation. *Nat. Rev. Mol. Cell Biol.* **9**, 944–957 (2008).

214. Kornfeld, S. Trafficking of lysosomal enzymes in normal and disease states. *J. Clin. Invest.* **77**, 1–6 (1986).

215. Sun, M. *et al.* Mucolipidosis type IV is caused by mutations in a gene encoding a novel transient receptor potential channel. *Hum. Mol. Genet.* **9**, 2471–2478 (2000).

216. Peake, K. B. & Vance, J. E. Defective cholesterol trafficking in Niemann-Pick C-deficient cells. *FEBS Lett.* **584**, 2731–2739 (2010).

217. Mancini, G. M. S., Havelaar, A. C. & Verheijen, F. W. Lysosomal transport disorders. *J. Inherit. Metab. Dis.* **23**, 278–292 (2000).

218. Bartke, N. & Hannun, Y. A. Bioactive sphingolipids: metabolism and function. *J. Lipid Res.* **50**, S91–S96 (2009).

219. Purpura, D. P. & Suzuki, K. Distortion of neuronal geometry and formation of aberrant synapses in neuronal storage disease. *Brain Res.* **116**, 1–21 (1976).

220. Staubach, S. & Hanisch, F. G. Lipid rafts: signaling and sorting platforms of cells and their roles in cancer. *http://dx.doi.org/10.1586/epr.11.2* **8**, 263–277 (2014).

221. Sobota, J. A., Bäck, N., Eipper, B. A. & Mains, R. E. Inhibitors of the V0 subunit of the vacuolar H+-ATPase prevent segregation of lysosomal- and secretory-pathway proteins. *J. Cell Sci.* **122**, 3542–3553 (2009).

222. Raychowdhury, M. K. *et al.* Molecular pathophysiology of mucolipidosis type IV: pH dysregulation of the mucolipin-1 cation channel. *Hum. Mol. Genet.* **13**, 617–627 (2004).

223. Lloyd-Evans, E. *et al.* Niemann-Pick disease type C1 is a sphingosine storage disease that causes deregulation of lysosomal calcium. *Nat. Med.* **14**, 1247–1255 (2008).

224. Gabandé-Rodríguez, E., Boya, P., Labrador, V., Dotti, C. G. & Ledesma, M. D. High sphingomyelin levels induce lysosomal damage and autophagy dysfunction in Niemann Pick disease type A. *Cell Death Differ.* **21**, 864–875 (2014).

225. Korkotian, E. *et al.* Elevation of Intracellular Glucosylceramide Levels Results in an Increase in Endoplasmic Reticulum Density and in Functional Calcium Stores in Cultured Neurons *. *J. Biol. Chem.* **274**, 21673–21678 (1999).

226. Tessitore, A. *et al.* GM1-ganglioside-mediated activation of the unfolded protein response causes neuronal death in a neurodegenerative gangliosidosis. *Mol. Cell* **15**, 753–766 (2004).

227. Jeyakumar, M., Dwek, R. A., Butters, T. D. & Platt, F. M. Storage solutions: treating lysosomal disorders of the brain. *Nat. Rev. Neurosci.* **6**, 713–725 (2005).

228. Simons, K. & Gruenberg, J. Jamming the endosomal system: lipid rafts and lysosomal storage diseases. *Trends Cell Biol.* **10**, 459–462 (2000).

229. Schulze, H. & Sandhoff, K. Lysosomal lipid storage diseases. *Cold Spring Harb. Perspect. Biol.* **3**, 1–19 (2011).

230. Teixeira, C. A. *et al.* Early axonal loss accompanied by impaired endocytosis, abnormal axonal transport, and decreased microtubule stability occur in the model of Krabbe's disease. *Neurobiol. Dis.* **66**, 92 (2014).

231. Pastores, G. M. & Hughes, D. A. Non-neuronopathic lysosomal storage disorders: Disease spectrum and treatments. *Best Pract. Res. Clin. Endocrinol. Metab.* **29**, 173–182 (2015).

232. Hoffmann, B. & Mayatepek, E. Neurological manifestations in lysosomal storage disorders - from pathology to first therapeutic possibilities. *Neuropediatrics* **36**, 285–289 (2005).

233. McGovern, M. M., Aron, A., Brodie, S. E., Desnick, R. J. & Wasserstein, M. P. Natural history of Type A Niemann-Pick disease: possible endpoints for therapeutic trials. *Neurology* **66**, 228–232 (2006).

234. Rosenbloom, B. E. & Weinreb, N. J. Gaucher disease: a comprehensive review. *Crit. Rev. Oncog.* **18**, 163–175 (2013).

235. Zimran, A. & Elstein, D. Management of Gaucher disease: enzyme replacement therapy. *Pediatr. Endocrinol. Rev.* **12 Suppl 1**, 82–7 (2014).

236. Herder, M. What Is the Purpose of the Orphan Drug Act? *PLoS Med.* **14**, (2017).

237. Boudes, P. F. Clinical studies in lysosomal storage diseases: Past, present, and future. *Rare Dis. (Austin, Tex.)* **1**, e26690 (2013).

238. Hall, A. K. & Carlson, M. R. The current status of orphan drug development in Europe and the US. *Intractable rare Dis. Res.* **3**, 1–7 (2014).

239. S. Seregin, S. & Amalfitano, A. Gene therapy for lysosomal storage diseases: progress, challenges and future prospects. *Curr. Pharm. Des.* **17**, 2558–2574 (2011).

240. Colella, P. & Mingozzi, F. Gene Therapy for Pompe Disease: The Time is now. *Hum. Gene Ther.* **30**, 1245–1262 (2019).

241. Suzuki, Y. Emerging novel concept of chaperone therapies for protein misfolding diseases. *Proc. Jpn. Acad. Ser. B. Phys. Biol. Sci.* **90**, 145 (2014).

242. Sawkar, A. R. *et al.* Gaucher disease-associated glucocerebrosidases show mutation-dependent chemical chaperoning profiles. *Chem. Biol.* **12**, 1235–1244 (2005).

243. Yam, G. H.-F., Zuber, C. & Roth, J. A synthetic chaperone corrects the trafficking defect and disease phenotype in a protein misfolding disorder. *FASEB J.* **19**, 12–18 (2005).

244. Kirkegaard, T. *et al.* Hsp70 stabilizes lysosomes and reverts Niemann-Pick disease-

associated lysosomal pathology. *Nature* **463**, 549–553 (2010).

245. Platt, F. M. & Jeyakumar, M. Substrate reduction therapy. *Acta Paediatr.* **97**, 88–93 (2008).

246. Solomon, M. & Muro, S. Lysosomal enzyme replacement therapies: Historical development, clinical outcomes, and future perspectives. *Advanced Drug Delivery Reviews* vol. 118 109–134 (2017).

247. Diaz, G. A. *et al.* One-year results of a clinical trial of olipudase alfa enzyme replacement therapy in pediatric patients with acid sphingomyelinase deficiency. *Genet. Med.* **23**, 1543–1550 (2021).

248. Anderson, L. J. *et al.* Long-term effectiveness of enzyme replacement therapy in adults with Gaucher disease: results from the NCS-LSD cohort study. *J. Inherit. Metab. Dis.* **37**, 953–960 (2014).

249. Friedman, B. A. *et al.* A Comparison of the Pharmacological Properties of Carbohydrate Remodeled Recombinant and Placental-Derived β-Glucocerebrosidase: Implications for Clinical Efficacy in Treatment of Gaucher Disease. *Blood* **93**, 2807–2816 (1999).

250. Ioannou, Y. A., Bishop, D. F. & Desnick, R. J. Overexpression of human alpha-galactosidase A results in its intracellular aggregation, crystallization in lysosomes, and selective secretion. *J. Cell Biol.* **119**, 1137 (1992).

251. Anson, D. S. *et al.* Correction of human mucopolysaccharidosis type-VI fibroblasts with recombinant N-acetylgalactosamine-4-sulphatase. *Biochem. J.* **284**, 789 (1992).

252. Van Hove, J. L. K., Yang, H. W., Wu, J. Y., Brady, R. O. & Chen, Y. T. High-level production of recombinant human lysosomal acid alpha-glucosidase in Chinese hamster ovary cells which targets to heart muscle and corrects glycogen accumulation in fibroblasts from patients with Pompe disease. *Proc. Natl. Acad. Sci. U. S. A.* **93**, 65 (1996).

253. McVie-Wylie, A. J. *et al.* BIOCHEMICAL AND PHARMACOLOGICAL CHARACTERIZATION OF DIFFERENT RECOMBINANT ACID α-GLUCOSIDASE PREPARATIONS EVALUATED FOR THE TREATMENT OF POMPE DISEASE. *Mol. Genet. Metab.* **94**, 448 (2008).

254. Grubb, J. H. *et al.* Chemically modified β-glucuronidase crosses blood–brain barrier and clears neuronal storage in murine mucopolysaccharidosis VII. *Proc. Natl. Acad. Sci. U. S. A.* **105**, 2616 (2008).

255. Bielicki, J., Hopwood, J. J., Wilson, P. J. & Anson, D. S. Recombinant human iduronate-2-sulphatase: correction of mucopolysaccharidosis-type II fibroblasts and characterization of the purified enzyme. *Biochem. J.* **289**, 241 (1993).

256. Unger, E. G., Durrant, J., Anson, D. S. & Hopwood, J. J. Recombinant alpha-L-iduronidase: characterization of the purified enzyme and correction of mucopolysaccharidosis type I fibroblasts. *Biochem. J.* **304**, 43 (1994).

257. Kakkis, E. D., Matynia, A., Jonas, A. J. & Neufeld, E. F. Overexpression of the human

lysosomal enzyme alpha-L-iduronidase in Chinese hamster ovary cells. *Protein Expr. Purif.* **5**, 225–232 (1994).

258. Wraith, J. E. *et al.* Enzyme replacement therapy for mucopolysaccharidosis I: a randomized, double-blinded, placebo-controlled, multinational study of recombinant human alpha-L-iduronidase (laronidase). *J. Pediatr.* **144**, 581–588 (2004).

259. Murray, J. M. *et al.* Nonclinical safety assessment of recombinant human acid sphingomyelinase (rhASM) for the treatment of acid sphingomyelinase deficiency:the utility of animal models of disease in the toxicological evaluation of potential therapeutics. *Mol. Genet. Metab.* **114**, 217–225 (2015).

260. Berg, T. *et al.* Purification and characterization of recombinant human lysosomal alpha-mannosidase. *Mol. Genet. Metab.* **73**, 18–29 (2001).

261. Ohsawa, M. *et al.* Establishment of immortalized Schwann cells from Sandhoff mice and corrective effect of recombinant human beta-hexosaminidase A on the accumulated GM2 ganglioside. *J. Hum. Genet.* **50**, 460–467 (2005).

262. Matzner, U. *et al.* Enzyme replacement improves nervous system pathology and function in a mouse model for metachromatic leukodystrophy. *Hum. Mol. Genet.* **14**, 1139–1152 (2005).

263. Espejo-Mojica, Á. J. *et al.* Human recombinant lysosomal enzymes produced in microorganisms. **116**, 13–23 (2015).

264. Edelmann, M. J. & Maegawa, G. H. B. CNS-Targeting Therapies for Lysosomal Storage Diseases: Current Advances and Challenges. *Front. Mol. Biosci.* **7**, 291 (2020).

265. Brooks, D. A., Kakavanos, R. & Hopwood, J. J. Significance of immune response to enzyme-replacement therapy for patients with a lysosomal storage disorder. *Trends Mol. Med.* **9**, 450–453 (2003).

266. Wang, J. *et al.* Neutralizing antibodies to therapeutic enzymes: considerations for testing, prevention and treatment. *Nat. Biotechnol.* **26**, 901 (2008).

267. Hollak, C. E. M. & Linthorst, G. E. Immune response to enzyme replacement therapy in Fabry disease: impact on clinical outcome? *Mol. Genet. Metab.* **96**, 1–3 (2009).

268. Kishnani, P. S. *et al.* Immune response to enzyme replacement therapies in lysosomal storage diseases and the role of immune tolerance induction. *Mol. Genet. Metab.* **117**, 66–83 (2016).

269. Banugaria, S. G. *et al.* Persistence of high sustained antibodies to enzyme replacement therapy despite extensive immunomodulatory therapy in an infant with Pompe disease: Need for agents to target antibody-secreting plasma cells. *Mol. Genet. Metab.* **105**, 677 (2012).

270. Brooks, D. A., King, B. M., C. Crawley, A., Byers, S. & Hopwood, J. J. Enzyme replacement therapy in Mucopolysaccharidosis VI: evidence for immune responses and altered

efficacy of treatment in animal models. *Biochim. Biophys. Acta* **1361**, 203–216 (1997).

271. Matzner, U. *et al.* Non-inhibitory antibodies impede lysosomal storage reduction during enzyme replacement therapy of a lysosomal storage disease. *J. Mol. Med. (Berl).* **86**, 433–442 (2008).

272. Turner, C. T., Hopwood, J. J. & Brooks, D. A. Enzyme replacement therapy in mucopolysaccharidosis I: altered distribution and targeting of alpha-L-iduronidase in immunized rats. *Mol. Genet. Metab.* **69**, 277–285 (2000).

273. Barbey, F. & Livio, F. Safety of enzyme replacement therapy. *Fabry Dis. Perspect. from 5 Years FOS* (2006).

274. Concolino, D., Deodato, F. & Parini, R. Enzyme replacement therapy: efficacy and limitations. *Ital. J. Pediatr.* **44**, (2018).

275. Kim, J. *et al.* IgE-mediated anaphylaxis and allergic reactions to idursulfase in patients with Hunter syndrome. *Allergy* **68**, 796–802 (2013).

276. Miebach, E. Management of infusion-related reactions to enzyme replacement therapy in a cohort of patients with mucopolysaccharidosis disorders. *Int. J. Clin. Pharmacol. Ther.* **47 Suppl 1**, (2009).

277. Brady, R. O. Enzyme replacement therapy: conception, chaos and culmination. *Philos. Trans. R. Soc. B Biol. Sci.* **358**, 915 (2003).

278. Desnick, R. J. & Schuchman, E. H. Enzyme replacement and enhancement therapies: lessons from lysosomal disorders. *Nat. Rev. Genet.* **3**, 954–966 (2002).

279. Gritti, A. Gene therapy for lysosomal storage disorders. *Expert Opin. Biol. Ther.* **11**, 1153–1167 (2011).

280. Urayama, A., Grubb, J. H., Sly, W. S. & Banks, W. A. Mannose 6-Phosphate Receptor–mediated Transport of Sulfamidase Across the Blood–brain Barrier in the Newborn Mouse. *Mol. Ther.* **16**, 1261 (2008).

281. Shapiro, L. J., Hall, C. W., Leder, I. G. & Neufeld, E. F. The relationship of alpha-L-iduronidase and Hurler corrective factor. *Arch. Biochem. Biophys.* **172**, 156–161 (1976).

282. Stahl, P., Rodman, J. S. & Schlesinger, P. Clearance of lysosomal hydrolases following intravenous infusion. Kinetic and competition experiments with beta-glucuronidase and N-acetyl-beta-D-glucosaminidase. *Arch. Biochem. Biophys.* **177**, 594–605 (1976).

283. Achord, D. T., Brot, F. E., Bell, C. E. & Sly, W. S. Human beta-glucuronidase: in vivo clearance and in vitro uptake by a glycoprotein recognition system on reticuloendothelial cells. *Cell* **15**, 269–278 (1978).

284. Hickman, S., Shapiro, L. J. & Neufeld, E. F. A recognition marker required for uptake of a lysosomal enzyme by cultured fibroblasts. *Biochem. Biophys. Res. Commun.* **57**, 55–61 (1974).

285. Zhao, K. W. & Neufeld, E. F. Purification and characterization of recombinant human alpha-N-acetylglucosaminidase secreted by Chinese hamster ovary cells. *Protein Expr. Purif.* **19**, 202–211 (2000).

286. Boven, PhD, L. A. *et al.* Gaucher cells demonstrate a distinct macrophage phenotype and resemble alternatively activated macrophages. *Am. J. Clin. Pathol.* **122**, 359–369 (2004).

287. Zhu, Y., Li, X., Schuchman, E. H., Desnick, R. J. & Cheng, S. H. Dexamethasone-mediated up-regulation of the mannose receptor improves the delivery of recombinant glucocerebrosidase to Gaucher macrophages. *J. Pharmacol. Exp. Ther.* **308**, 705–711 (2004).

288. Cardone, M. *et al.* Abnormal mannose-6-phosphate receptor trafficking impairs recombinant alpha-glucosidase uptake in Pompe disease fibroblasts. *Pathogenetics* **1**, 6 (2008).

289. Dhami, R. & Schuchman, E. H. Mannose 6-phosphate receptor-mediated uptake is defective in acid sphingomyelinase-deficient macrophages: implications for Niemann-Pick disease enzyme replacement therapy. *J. Biol. Chem.* **279**, 1526–1532 (2004).

290. Rappaport, J., Garnacho, C. & Muro, S. Clathrin-mediated endocytosis is impaired in type A-B Niemann-Pick disease model cells and can be restored by ICAM-1-mediated enzyme replacement. *Mol. Pharm.* **11**, 2887–2895 (2014).

291. Zhao, H. *et al.* Polymer-based nanoparticles for protein delivery: Design, strategies and applications. *J. Mater. Chem. B* **4**, 4060–4071 (2016).

292. Johnston, A. P. R. *et al.* Targeting cancer cells: controlling the binding and internalization of antibody-functionalized capsules. *ACS Nano* **6**, 6667–6674 (2012).

293. Bertrand, N., Wu, J., Xu, X., Kamaly, N. & Farokhzad, O. C. Cancer Nanotechnology: The impact of passive and active targeting in the era of modern cancer biology. *Adv. Drug Deliv. Rev.* **66**, 2 (2014).

294. Muro, S. Challenges in design and characterization of ligand-targeted drug delivery systems. *J. Control. Release* **164**, 125 (2012).

295. Hamid Akash, M. S., Rehman, K. & Chen, S. Natural and synthetic polymers as drug carriers for delivery of therapeutic proteins. *Polym. Rev.* **55**, 371–406 (2015).

296. Cao, S. jun *et al.* Nanoparticles: Oral Delivery for Protein and Peptide Drugs. *AAPS PharmSciTech* **20**, 1–11 (2019).

297. Lee, H. J. *et al.* α-Galactosidase delivery using 30Kc19-human serum albumin nanoparticles for effective treatment of Fabry disease. *Appl. Microbiol. Biotechnol.* **100**, 10395–10402 (2016).

298. Giannotti, M. I., Esteban, O., Oliva, M., García-Parajo, M. F. & Sanz, F. pH-responsive polysaccharide-based polyelectrolyte complexes as nanocarriers for lysosomal delivery of therapeutic proteins. *Biomacromolecules* **12**, 2524–2533 (2011).

299. Sarrazin, S., Wilson, B., Sly, W. S., Tor, Y. & Esko, J. D. Guanidinylated Neomycin Mediates Heparan Sulfate–dependent Transport of Active Enzymes to Lysosomes. *Mol. Ther.* **18**, 1268 (2010).

300. Ltd, N., Mühlstein, A., Gelperina, S., Kreuter, J. & Kreuter, J. Development of nanoparticle-bound arylsulfatase B for enzyme replacement therapy of mucopolysaccharidosis VI. *Pharmazie* **68**, 549–554 (2013).

301. Grosso, A. Del *et al.* Brain-targeted enzyme-loaded nanoparticles: A breach through the blood-brain barrier for enzyme replacement therapy in Krabbe disease. *Sci. Adv.* **5**, (2019).

302. Garnacho, C. & Muro, S. ICAM-1 targeting, intracellular trafficking, and functional activity of polymer nanocarriers coated with a fibrinogen-derived peptide for lysosomal enzyme replacement. *J. Drug Target.* **25**, 786–795 (2017).

303. Muntimadugu, E. *et al.* Comparison between Nanoparticle Encapsulation and Surface Loading for Lysosomal Enzyme Replacement Therapy. *Int. J. Mol. Sci.* **23**, 4034 (2022).

304. Hsu, J., Rappaport, J. & Muro, S. Specific binding, uptake, and transport of ICAM-1-targeted nanocarriers across endothelial and subendothelial cell components of the blood-brain barrier. *Pharm. Res.* **31**, 1855–66 (2014).

305. Papademetriou, J. *et al.* Comparative binding, endocytosis, and biodistribution of antibodies and antibody-coated carriers for targeted delivery of lysosomal enzymes to ICAM-1 versus transferrin receptor. *J. Inherit. Metab. Dis.* **36**, 467–77 (2013).

306. Degan, D. *et al.* The Role of Inflammation in Neurological Disorders. *Curr. Pharm. Des.* **24**, 1485–1501 (2018).

307. Hurwitz, R., Ferlinz, K. & Sandhofl, K. The tricyclic antidepressant desipramine causes proteolytic degradation of lysosomal sphingomyelinase in human fibroblasts. *Biol. Chem. Hoppe. Seyler.* **375**, 447–450 (1994).

308. Rempel, B. P. & Withers, S. G. Covalent inhibitors of glycosidases and their applications in biochemistry and biology. *Glycobiology* **18**, 570–586 (2008).

309. Beutler, E. Gaucher Disease, Molecular Biology of. *Encycl. Mol. Cell Biol. Mol. Med.* (2006) doi:10.1002/3527600906.MCB.200300022.

310. Muro, S., Muzykantov, V. R. & Murciano, J. C. Characterization of endothelial internalization and targeting of antibody-enzyme conjugates in cell cultures and in laboratory animals. *Methods Mol. Biol.* **283**, 21–36 (2004).

311. Gao, H. *et al.* Ligand modified nanoparticles increases cell uptake, alters endocytosis and elevates glioma distribution and internalization. *Sci. Rep.* **3**, (2013).

312. Lachmann, R. H. Enzyme replacement therapy for lysosomal storage diseases. *Curr. Opin. Pediatr.* **23**, 588–593 (2011).

313. First therapy to treat two types of Niemann-Pick disease, a rare genetic metabolic disorder | European Medicines Agency. https://www.ema.europa.eu/en/news/first-therapy-treat-two-types-niemann-pick-disease-rare-genetic-metabolic-disorder.

314. Brady, R. O. & Schiffmann, R. Enzyme-replacement therapy for metabolic storage disorders. *Lancet Neurol.* **3**, 752–756 (2004).

315. Li, X. *et al.* Nano carriers for drug transport across the blood-brain barrier. *J. Drug Target.* **25**, 17–28 (2017).

316. Nabar, G. M. *et al.* Micelle-templated, poly(lactic-co-glycolic acid) nanoparticles for hydrophobic drug delivery. *Int. J. Nanomedicine* **13**, 351 (2018).

317. Barichello, J. M., Morishita, M., Takayama, K. & Nagai, T. Encapsulation of hydrophilic and lipophilic drugs in PLGA nanoparticles by the nanoprecipitation method. *Drug Dev. Ind. Pharm.* **25**, 471–476 (1999).

318. Lu, Y. *et al.* Engineering a 'PEG-g-PEI/DNA nanoparticle-in- PLGA microsphere' hybrid controlled release system to enhance immunogenicity of DNA vaccine. *Mater. Sci. Eng. C. Mater. Biol. Appl.* **106**, (2020).

319. Salvalaio, M. *et al.* Targeted Polymeric Nanoparticles for Brain Delivery of High Molecular Weight Molecules in Lysosomal Storage Disorders. *PLoS One* **11**, (2016).

320. Galliani, M. *et al.* Cross-Linked Enzyme Aggregates as Versatile Tool for Enzyme Delivery: Application to Polymeric Nanoparticles. *Bioconjug. Chem.* **29**, 2225–2231 (2018).

321. Villaseñor, R., Lampe, J., Schwaninger, M. & Collin, L. Intracellular transport and regulation of transcytosis across the blood–brain barrier. *Cellular and Molecular Life Sciences* vol. 76 1081–1092 (2019).

322. Zhang, N., Wang, J., Bing, T., Liu, X. & Shangguan, D. Transferrin receptor-mediated internalization and intracellular fate of conjugates of a DNA aptamer. *Mol. Ther. - Nucleic Acids* **27**, 1249–1259 (2022).

323. Wu, C. *et al.* Endosomal/lysosomal location of organically modified silica nanoparticles following caveolae-mediated endocytosis. *RSC Adv.* **9**, 13855 (2019).

324. Wu, L., Zhang, J. & Watanabe, W. Physical and chemical stability of drug nanoparticles. *Adv. Drug Deliv. Rev.* **63**, 456–469 (2011).

325. Muthu, M. S. & Feng, S. S. Pharmaceutical stability aspects of nanomedicines. *https://doi.org/10.2217/nnm.09.75* **4**, 857–860 (2009).

326. Frederick, Z., James, A. & E Dale, A. Lysosomal reacidification via degradation of PLGA nanoparticles in a lipotoxic cardiomyopathy model. *Front. Bioeng. Biotechnol.* **4**, (2016).

327. Zeng, J., Martin, A., Han, X., Shirihai, O. S. & Grinstaff, M. W. Biodegradable plga nanoparticles restore lysosomal acidity and protect neural pc-12 cells against mitochondrial toxicity. *Ind. Eng. Chem. Res.* **58**, 13910–13917 (2019).

328. Bourdenx, M. *et al.* Nanoparticles restore lysosomal acidification defects: Implications for Parkinson and other lysosomal-related diseases. *Autophagy* **12**, 472 (2016).

329. Hsu, J., Hoenicka, J. & Muro, S. Targeting, endocytosis, and lysosomal delivery of active enzymes to model human neurons by ICAM-1-targeted nanocarriers. *Pharm. Res.* **32**, 1264–78 (2015).

330. Natowicz, M. R. *et al.* Clinical and Biochemical Manifestations of Hyaluronidase Deficiency. *N. Engl. J. Med.* **335**, 1029–1033 (1996).

331. Stern, R. & Jedrzejas, M. J. The Hyaluronidases: Their Genomics, Structures, and Mechanisms of Action. *Chem. Rev.* **106**, 818 (2006).

332. Wiseman, M. E. & Frank, C. W. Antibody adsorption and orientation on hydrophobic surfaces. *Langmuir* **28**, 1765–1774 (2012).

333. Andrian, T., Delcanale, P., Pujals, S. & Albertazzi, L. Correlating Super-Resolution Microscopy and Transmission Electron Microscopy Reveals Multiparametric Heterogeneity in Nanoparticles. *Nano Lett.* **21**, 5360–5368 (2021).

334. Goodman, C. M., McCusker, C. D., Yilmaz, T. & Rotello, V. M. Toxicity of gold nanoparticles functionalized with cationic and anionic side chains. *Bioconjug. Chem.* **15**, 897–900 (2004).

335. Xia, T., Kovochich, M., Liong, M., Zink, J. I. & Nel, A. E. Cationic polystyrene nanosphere toxicity depends on cell-specific endocytic and mitochondrial injury pathways. *ACS Nano* **2**, 85–96 (2008).

336. Fleischer, C. C. & Payne, C. K. Nanoparticle–CellInteractions: Molecular Structureof the Protein Corona and Cellular Outcomes. *Acc. Chem. Res.* **47**, 2651 (2014).

337. Verma, A. & Stellacci, F. Effect of Surface Properties on Nanoparticle–Cell Interactions. *Small* **6**, 12–21 (2010).

338. Papademetriou, I., Tsinas, Z., Hsu, J. & Muro, S. Combination-targeting to multiple endothelial cell adhesion molecules modulates binding, endocytosis, and in vivo biodistribution of drug nanocarriers and their therapeutic cargoes. *J. Control. Release* **188**, 87–98 (2014).

339. Ansar, M., Serrano, D., Papademetriou, I., Bhowmick, T. K. & Muro, S. Biological functionalization of drug delivery carriers to bypass size restrictions of receptor-mediated endocytosis independently from receptor targeting. *ACS Nano* **7**, 10597–611 (2013).

340. Park, S. J. Protein–Nanoparticle Interaction: Corona Formation and Conformational Changes in Proteins on Nanoparticles . *Int. J. Nanomedicine* **15**, 5783–5802 (2020).

341. Mishra, R. K. *et al.* Biological effects of formation of protein corona onto nanoparticles. *Int. J. Biol. Macromol.* **175**, 1–18 (2021).

342. Abdelwahed, W., Degobert, G., Stainmesse, S. & Fessi, H. Freeze-drying of nanoparticles: Formulation, process and storage considerations. *Adv. Drug Deliv. Rev.* **58**, 1688–1713 (2006).

343. Fonte, P. *et al.* Effect of cryoprotectants on the porosity and stability of insulin-loaded PLGA nanoparticles after freeze-drying. *Biomatter* **2**, 329 (2012).

344. Ken-ichi, I., Sumie, Y. & Yasushi, T. The effects of additives on the stability of freeze-dried β-galactosidase stored at elevated temperature. *Int. J. Pharm.* **71**, 137–146 (1991).

345. Allison, S. D., Chang, B., Randolph, T. W. & Carpenter, J. F. Hydrogen bonding between sugar and protein is responsible for inhibition of dehydration-induced protein unfolding. *Arch. Biochem. Biophys.* **365**, 289–298 (1999).

346. Manthe, R. L. *et al.* Δ-Tocopherol effect on endocytosis and its combination with enzyme replacement therapy for lysosomal disorders: A new type of drug interaction? *J. Pharmacol. Exp. Ther.* **370**, 823–833 (2019).

347. Bosch, M. E. & Kielian, T. Neuroinflammatory paradigms in lysosomal storage diseases. *Front. Neurosci.* **9**, 417 (2015).

348. Cataldi, M., Vigliotti, C., Mosca, T., Cammarota, M. R. & Capone, D. Emerging Role of the Spleen in the Pharmacokinetics of Monoclonal Antibodies, Nanoparticles and Exosomes. *Int. J. Mol. Sci.* **18**, (2017).

349. Tsoi, K. M. *et al.* Mechanism of hard-nanomaterial clearance by the liver. *Nat. Mater. 2016 1511* **15**, 1212–1221 (2016).

350. Guzman-Martinez, L. *et al.* Neuroinflammation as a common feature of neurodegenerative disorders. *Front. Pharmacol.* **10**, 1008 (2019).

351. Erley, C. M. *et al.* Plasma clearance of iodine contrast media as a measure of glomerular filtration rate in critically ill patients. *Crit. Care Med.* **29**, 1544–1550 (2001).

352. Cabezón, I. *et al.* Trafficking of Gold Nanoparticles Coated with the 8D3 Anti-Transferrin Receptor Antibody at the Mouse Blood-Brain Barrier. *Mol. Pharm.* **12**, 4137–4145 (2015).

353. Joshi, S., Meyers, P. M. & Ornstein, E. Intracarotid Delivery of Drugs: The Potential and the Pitfalls. *Anesthesiology* **109**, 543 (2008).

354. Daneman, R. & Prat, A. The blood-brain barrier. *Cold Spring Harb. Perspect. Biol.* **7**, a020412 (2015).

355. Oh, P. *et al.* Live dynamic imaging of caveolae pumping targeted antibody rapidly and specifically across endothelium in the lung. *Nat. Biotechnol.* **25**, 327 (2007).

356. Pardridge, W. M. Drug transport across the blood–brain barrier. *J. Cereb. Blood Flow Metab.* **32**, 1959 (2012).

357. Niewoehner, J. *et al.* Increased Brain Penetration and Potency of a Therapeutic Antibody Using a Monovalent Molecular Shuttle. *Neuron* **81**, 49–60 (2014).

358. Clague, M. J. & Hammond, D. E. Membrane Traffic: Catching the Lysosome Express. doi:10.1016/j.cub.2006.05.009.

359. Wei, Z., Su, W., Lou, H., Duan, S. & Chen, G. Trafficking pathway between plasma membrane and mitochondria via clathrin-mediated endocytosis. *J. Mol. Cell Biol.* **10**, 539–548 (2018).

360. Geng, Y. *et al.* Shape effects of filaments versus spherical particles in flow and drug delivery. *Nat. Nanotechnol.* **2**, 249 (2007).

361. Herd, H. *et al.* Nanoparticle Geometry and Surface Orientation Influences Mode of Cellular Uptake. *ACS Nano* **7**, 1961–1973 (2013).

362. Merkel, T. J. *et al.* The Effect of Particle Size on the Biodistribution of Low-modulus Hydrogel PRINT Particles. *J. Control. Release* **162**, 37 (2012).

363. Mitragotri, S. In drug delivery, shape does matter. *Pharm. Res.* **26**, 232–234 (2009).

364. Simone, E. A., Dziubla, T. D. & Muzykantov, V. R. Polymeric carriers: Role of geometry in drug delivery. *Expert Opinion on Drug Delivery* vol. 5 1283–1300 (2008).

365. Duncan, R. & Richardson, S. C. W. Endocytosis and intracellular trafficking as gateways for nanomedicine delivery: opportunities and challenges. *Mol. Pharm.* **9**, 2380–2402 (2012).

366. Gunawan, R. C. & Auguste, D. T. Immunoliposomes That Target Endothelium In Vitro Are Dependent on Lipid Raft Formation. *Mol. Pharm.* **7**, 1569–1575 (2010).

367. Kawano, K. & Maitani, Y. Effects of Polyethylene Glycol Spacer Length and Ligand Density on Folate Receptor Targeting of Liposomal Doxorubicin In Vitro. *J. Drug Deliv.* **2011**, 1–6 (2011).

368. Stefanick, J. F., Ashley, J. D., Kiziltepe, T. & Bilgicer, B. A systematic analysis of peptide linker length and liposomal polyethylene glycol coating on cellular uptake of peptide-targeted liposomes. *ACS Nano* **7**, 2935–2947 (2013).

369. Wang, B., Galliford, C. V. & Low, P. S. Guiding principles in the design of ligand-targeted nanomedicines. *Nanomedicine (Lond).* **9**, 313–330 (2014).

370. Johnsen, K. B., Burkhart, A., Thomsen, L. B., Andresen, T. L. & Moos, T. Targeting the transferrin receptor for brain drug delivery. *Prog. Neurobiol.* **181**, (2019).

371. Koneru, T. *et al.* Transferrin: Biology and Use in Receptor-Targeted Nanotherapy of Gliomas. *ACS omega* **6**, 8727–8733 (2021).

372. Alata, W., Paris-Robidas, S., Emond, V., Bourasset, F. & Calon, F. Brain uptake of a fluorescent vector targeting the transferrin receptor: a novel application of in situ brain perfusion. *Mol. Pharm.* **11**, 243–253 (2014).

373. Manich, G. *et al.* Study of the transcytosis of an anti-transferrin receptor antibody with a Fab' cargo across the blood-brain barrier in mice. *Eur. J. Pharm. Sci.* **49**, 556–564 (2013).

374. Moos, T. & Morgan, E. H. Restricted transport of anti-transferrin receptor antibody (OX26) through the blood-brain barrier in the rat. *J. Neurochem.* **79**, 119–129 (2001).

375. Yu, Y. J. *et al.* Boosting brain uptake of a therapeutic antibody by reducing its affinity for a transcytosis target. *Sci. Transl. Med.* **3**, (2011).

376. Webster, C. I. *et al.* Enhanced delivery of IL-1 receptor antagonist to the central nervous system as a novel anti-transferrin receptor-IL-1RA fusion reverses neuropathic mechanical hypersensitivity. (2016) doi:10.1097/j.pain.0000000000000810.

377. Thom, G. *et al.* Enhanced Delivery of Galanin Conjugates to the Brain through Bioengineering of the Anti-Transferrin Receptor Antibody OX26. *Mol. Pharm.* **15**, 1420–1431 (2018).

378. Yu, Y. J. *et al.* Therapeutic bispecific antibodies cross the blood-brain barrier in nonhuman primates. *Sci. Transl. Med.* **6**, (2014).

379. Bien-Ly, N. *et al.* Transferrin receptor (TfR) trafficking determines brain uptake of TfR antibody affinity variants. *J. Exp. Med.* **211**, 233–244 (2014).

380. Sade, H. *et al.* A Human Blood-Brain Barrier Transcytosis Assay Reveals Antibody Transcytosis Influenced by pH-Dependent Receptor Binding. *PLoS One* **9**, e96340 (2014).

381. Haqqani, A. S. *et al.* Intracellular sorting and transcytosis of the rat transferrin receptor antibody OX26 across the blood-brain barrier in vitro is dependent on its binding affinity. *J. Neurochem.* **146**, 735–752 (2018).

382. Zhao, P. *et al.* Enhanced anti-angiogenetic effect of transferrin receptor-mediated delivery of VEGF-trap in a glioblastoma mouse model. *MAbs* **14**, (2022).

383. Arguello, A. *et al.* Molecular architecture determines brain delivery of a transferrin receptor-targeted lysosomal enzyme. *J. Exp. Med.* **219**, (2022).

384. Fakhari, A., Baoum, A., Siahaan, T. J., Le, K. B. & Berkland, C. Controlling ligand surface density optimizes nanoparticle binding to ICAM-1. *J. Pharm. Sci.* **100**, 1045–1056 (2011).

385. Wiley, D. T., Webster, P., Gale, A. & Davis, M. E. Transcytosis and brain uptake of transferrin-containing nanoparticles by tuning avidity to transferrin receptor. *Proc. Natl. Acad. Sci. U. S. A.* **110**, 8662–8667 (2013).

386. Zern, B. J. *et al.* Reduction of nanoparticle avidity enhances the selectivity of vascular targeting and PET detection of pulmonary inflammation. *ACS Nano* **7**, 2461–2469 (2013).

387. Tian, X. *et al.* On the shuttling across the blood-brain barrier via tubule formation: Mechanism and cargo avidity bias. *Sci. Adv.* **6**, 4397–4424 (2020).

388. Anraku, Y. *et al.* Glycaemic control boosts glucosylated nanocarrier crossing the BBB into the brain. *Nat. Commun.* **8**, (2017).

389. Li, W., Chen, Z., Chin, I., Chen, Z. & Dai, H. The Role of VE-cadherin in Blood-brain Barrier Integrity Under Central Nervous System Pathological Conditions. *Curr. Neuropharmacol.*

16, 1375–1384 (2018).

390. Ghaffarian, R. & Muro, S. Distinct subcellular trafficking resulting from monomeric vs multimeric targeting to endothelial ICAM-1: Implications for drug delivery. *Mol. Pharm.* **11**, 4350–4362 (2014).

391. Randolph, G. J. & Furie, M. B. Mononuclear phagocytes egress from an in vitro model of the vascular wall by migrating across endothelium in the basal to apical direction: role of intercellular adhesion molecule 1 and the CD11/CD18 integrins. *J. Exp. Med.* **183**, 451–462 (1996).

392. OMIM Entry - # 257200 - NIEMANN-PICK DISEASE, TYPE A. https://omim.org/entry/257200.

393. OMIM Entry - # 607616 - NIEMANN-PICK DISEASE, TYPE B. https://www.omim.org/entry/607616.

394. Vanier, M. T. Niemann–Pick diseases. *Handb. Clin. Neurol.* **113**, 1717–1721 (2013).

395. Schuchman, E. H. & Desnick, R. J. Types A and B Niemann-Pick Disease. *Mol. Genet. Metab.* **120**, 27 (2017).

396. Berry-Kravis, E. Niemann-Pick Disease, Type C: Diagnosis, Management and Disease-Targeted Therapies in Development. *Semin. Pediatr. Neurol.* **37**, 100879 (2021).

397. Quinn, P. J. Sphingolipid symmetry governs membrane lipid raft structure. *Biochim. Biophys. Acta* **1838**, 1922–1930 (2014).

398. Abe, A. & Shayman, J. A. Sphingolipid Catabolism. *Encycl. Biol. Chem. Second Ed.* 287–292 (2013) doi:10.1016/B978-0-12-378630-2.00462-X.

399. Breiden, B. & Sandhoff, K. Acid Sphingomyelinase, a Lysosomal and Secretory Phospholipase C, Is Key for Cellular Phospholipid Catabolism. *Int. J. Mol. Sci. 2021, Vol. 22, Page 9001* **22**, 9001 (2021).

400. Wasserstein, M. P. *et al.* The natural history of type B Niemann-Pick disease: results from a 10-year longitudinal study. *Pediatrics* **114**, (2004).

401. Hollak, C. E. M. *et al.* Acid sphingomyelinase (Asm) deficiency patients in The Netherlands and Belgium: disease spectrum and natural course in attenuated patients. *Mol. Genet. Metab.* **107**, 526–533 (2012).

402. McGovern, M. M. *et al.* A prospective, cross-sectional survey study of the natural history of Niemann-Pick disease type B. *Pediatrics* **122**, (2008).

403. McGovern, M. M. *et al.* Morbidity and mortality in type B Niemann-Pick disease. *Genet. Med.* **15**, 618–623 (2013).

404. Pavlů-Pereira, H. *et al.* Acid sphingomyelinase deficiency. Phenotype variability with prevalence of intermediate phenotype in a series of twenty-five Czech and Slovak patients. A multi-approach study. *J. Inherit. Metab. Dis.* **28**, 203–227 (2005).

405. Wasserstein, M. P. *et al.* Acid sphingomyelinase deficiency: prevalence and characterization of an intermediate phenotype of Niemann-Pick disease. *J. Pediatr.* **149**, 554–559 (2006).

406. McGovern, M. M., Avetisyan, R., Sanson, B. J. & Lidove, O. Disease manifestations and burden of illness in patients with acid sphingomyelinase deficiency (ASMD). *Orphanet J. Rare Dis.* **12**, 1–13 (2017).

407. Breilyn, M. S., Zhang, W., Yu, C. & Wasserstein, M. P. Plasma lyso-sphingomyelin levels are positively associated with clinical severity in acid sphingomyelinase deficiency. *Mol. Genet. Metab. Reports* **28**, 100780 (2021).

408. Van Meer, G., Voelker, D. R. & Feigenson, G. W. Membrane lipids: where they are and how they behave. *Nat. Rev. Mol. Cell Biol. 2008 92* **9**, 112–124 (2008).

409. Stieger, B., Steiger, J. & Locher, K. P. Membrane lipids and transporter function. *Biochim. Biophys. Acta - Mol. Basis Dis.* **1867**, 166079 (2021).

410. Casares, D., Escribá, P. V. & Rosselló, C. A. Membrane Lipid Composition: Effect on Membrane and Organelle Structure, Function and Compartmentalization and Therapeutic Avenues. *Int. J. Mol. Sci.* **20**, (2019).

411. Rappaport, J., Manthe, R. L., Solomon, M., Garnacho, C. & Muro, S. A Comparative Study on the Alterations of Endocytic Pathways in Multiple Lysosomal Storage Disorders. *Mol. Pharm.* **13**, 357–368 (2016).

412. Rappaport, J., Manthe, R. L., Garnacho, C. & Muro, S. Altered clathrin-independent endocytosis in type A Niemann-Pick disease cells and rescue by ICAM-1-targeted enzyme delivery. *Mol. Pharm.* **12**, 1366–1376 (2015).

413. Chen, C. S., Patterson, M. C., Wheatley, C. L., O'Brien, J. F. & Pagano, R. E. Broad screening test for sphingolipid-storage diseases. *Lancet* **354**, 901–905 (1999).

414. Puri, V. *et al.* Cholesterol modulates membrane traffic along the endocytic pathway in sphingolipid-storage diseases. **1**, 386–388 (1999).

415. Puri, V. *et al.* Clathrin-dependent and -independent internalization of plasma membrane sphingolipids initiates two Golgi targeting pathways. *J. Cell Biol.* **154**, 535 (2001).

416. EU/3/01/056 | European Medicines Agency. https://www.ema.europa.eu/en/medicines/human/orphan-designations/eu-3-01-056.

417. Roces, D. P. *et al.* Efficacy of enzyme replacement therapy in alpha-mannosidosis mice: a preclinical animal study. *Hum. Mol. Genet.* **13**, 1979–1988 (2004).

418. Ou, L., Herzog, T., Koniar, B. L., Gunther, R. & Whitley, C. B. High-Dose Enzyme Replacement Therapy in Murine Hurler Syndrome. *Mol. Genet. Metab.* **111**, 116 (2014).

419. Baldo, G., Giugliani, R. & Matte, U. Lysosomal enzymes may cross the blood–brain-barrier by pinocytosis: Implications for Enzyme Replacement Therapy. *Med. Hypotheses* **82**, 478–

480 (2014).

420. Blanz, J. *et al.* Reversal of peripheral and central neural storage and ataxia after recombinant enzyme replacement therapy in alpha-mannosidosis mice. *Hum. Mol. Genet.* **17**, 3437–3445 (2008).

421. Crawley, A. C., King, B., Berg, T., Meikle, P. J. & Hopwood, J. J. Enzyme replacement therapy in alpha-mannosidosis guinea-pigs. *Mol. Genet. Metab.* **89**, 48–57 (2006).

422. Matzner, U. *et al.* Enzyme replacement improves nervous system pathology and function in a mouse model for metachromatic leukodystrophy. *Hum. Mol. Genet.* **14**, 1139–1152 (2005).

423. Matzner, U. *et al.* Enzyme replacement improves ataxic gait and central nervous system histopathology in a mouse model of metachromatic leukodystrophy. *Mol. Ther.* **17**, 600–606 (2009).

424. Dunder, U. *et al.* Enzyme replacement therapy in a mouse model of aspartylglycosaminuria. *FASEB J.* **14**, 361–367 (2000).

425. Lee, W. C. *et al.* Enzyme replacement therapy results in substantial improvements in early clinical phenotype in a mouse model of globoid cell leukodystrophy. *FASEB J.* **19**, 1549–1551 (2005).

426. Polito, V. A. *et al.* Correction of CNS defects in the MPSII mouse model via systemic enzyme replacement therapy. *Hum. Mol. Genet.* **19**, 4871–4885 (2010).

427. Vogler, C. *et al.* From the Cover: Overcoming the blood-brain barrier with high-dose enzyme replacement therapy in murine mucopolysaccharidosis VII. *Proc. Natl. Acad. Sci. U. S. A.* **102**, 14777 (2005).

428. Study to Investigate CSL112 in Subjects With Acute Coronary Syndrome - Full Text View - ClinicalTrials.gov. https://clinicaltrials.gov/ct2/show/NCT03473223.

429. Schultz, M. L. *et al.* Synthetic high-density lipoprotein nanoparticles for the treatment of Niemann-Pick diseases. *BMC Med.* **17**, 1–18 (2019).

430. McGovern, M. M. *et al.* Novel first-dose adverse drug reactions during a phase I trial of olipudase alfa (recombinant human acid sphingomyelinase) in adults with Niemann-Pick disease type B (acid sphingomyelinase deficiency). *Genet. Med.* **18**, 34–40 (2016).

431. Aldosari, M. H. *et al.* Liposome-targeted recombinant human acid sphingomyelinase: Production, formulation, and in vitro evaluation. *Eur. J. Pharm. Biopharm.* **137**, 185–195 (2019).

432. Bui, T. M., Wiesolek, H. L. & Sumagin, R. ICAM-1: A master regulator of cellular responses in inflammation, injury resolution, and tumorigenesis. *J. Leukoc. Biol.* **108**, 787–799 (2020).

433. Moos, T., Nielsen, T. R., Skjørringe, T. & Morgan, E. H. Iron trafficking inside the brain. *J.*

Neurochem. **103**, 1730–1740 (2007).

434. Smirnov, I. M., Bailey, K., Flowers, C. H., Garrigues, N. W. & Wesselius, L. J. Effects of TNF-α and IL-1β on iron metabolism by A549 cells and influence on cytotoxicity. *Am. J. Physiol. - Lung Cell. Mol. Physiol.* **277**, 257–263 (1999).

435. Gan, L. *et al.* TNF-α Up-Regulates Protein Level and Cell Surface Expression of the Leptin Receptor by Stimulating Its Export via a PKC-Dependent Mechanism. *Endocrinology* **153**, 5821–5833 (2012).

436. Tsuji, Y., Miller$, L. L., Mille&, S. C., Torti, S. V & Tortill, F. M. Tumor necrosis factor-alpha and interleukin 1-alpha regulate transferrin receptor in human diploid fibroblasts. Relationship to the induction of ferritin heavy chain. *J. Biol. Chem.* **266**, 7257–7261 (1991).

437. Nezu, M., Iwagaki, H., Aoki, H., Tanaka, N. & Orita, K. Tumour necrosis factor-alpha upregulates transferrin receptors in K 562 cells. *J. Int. Med. Res.* **22**, 145–152 (1994).

438. Harel, E. *et al.* Enhanced transferrin receptor expression by proinflammatory cytokines in enterocytes as a means for local delivery of drugs to inflamed gut mucosa. *PLoS One* **6**, (2011).

439. Nanami, M. *et al.* Tumor necrosis factor-α-induced iron sequestration and oxidative stress in human endothelial cells. *Arterioscler. Thromb. Vasc. Biol.* **25**, 2495–2501 (2005).

440. Wasserman, S. M. *et al.* Gene expression profile of human endothelial cells exposed to sustained fluid shear stress. *Physiol. Genomics* **12**, 13–23 (2003).

441. Sydor, S. *et al.* Acid sphingomyelinase deficiency in Western diet-fed mice protects against adipocyte hypertrophy and diet-induced liver steatosis. *Mol. Metab.* **6**, 416–427 (2017).

442. Bartoll, A. *et al.* Inhibition of fatty acid amide hydrolase prevents pathology in neurovisceral acid sphingomyelinase deficiency by rescuing defective endocannabinoid signaling. doi:10.15252/emmm.201911776.

443. Duivenvoorde, L. P. M., Louisse, J., Pinckaers, N. E. T., Nguyen, T. & van der Zande, M. Comparison of gene expression and biotransformation activity of HepaRG cells under static and dynamic culture conditions. *Sci. Reports 2021 111* **11**, 1–12 (2021).

444. Beckmann, N., Sharma, D., Gulbins, E., Becker, K. A. & Edelmann, B. Inhibition of acid sphingomyelinase by tricyclic antidepressants and analogons. *Front. Physiol.* **5**, (2014).

445. Brenner, J. S. *et al.* Mechanisms that determine nanocarrier targeting to healthy versus inflamed lung regions. *Nanomedicine* **13**, 1495–1506 (2017).

446. Myerson, J. W. *et al.* Flexible Nanoparticles Reach Sterically Obscured Endothelial Targets Inaccessible to Rigid Nanoparticles. *Adv. Mater.* **30**, 1802373 (2018).

447. Myerson, J. W. *et al.* Non-affinity factors modulating vascular targeting of nano- and

microcarriers. *Adv. Drug Deliv. Rev.* **99**, 97–112 (2016).

448. Choudhury, H. *et al.* Transferrin receptors-targeting nanocarriers for efficient targeted delivery and transcytosis of drugs into the brain tumors: a review of recent advancements and emerging trends. *Drug Deliv. Transl. Res.* **8**, 1545–1563 (2018).

449. Wang, Z., Tiruppathi, C., Cho, J., Minshall, R. D. & Malik, A. B. Delivery of nanoparticle-complexed drugs across the vascular endothelial barrier via caveolae. *IUBMB Life* **63**, 659–667 (2011).

450. Lutz, S. E. *et al.* Caveolin1 Is Required for Th1 Cell Infiltration, but Not Tight Junction Remodeling, at the Blood-Brain Barrier in Autoimmune Neuroinflammation. *Cell Rep.* **21**, 2104–2117 (2017).

451. Knowland, D. *et al.* Stepwise recruitment of transcellular and paracellular pathways underlies blood-brain barrier breakdown in stroke. *Neuron* **82**, 603–617 (2014).

452. Botos, E. *et al.* Caveolin-1 is transported to multi-vesicular bodies after albumin-induced endocytosis of caveolae in HepG2 cells. *J. Cell. Mol. Med.* **12**, 1632 (2008).

453. Brown, M. S. & Goldstein, J. L. A receptor-mediated pathway for cholesterol homeostasis. *Science* **232**, 34–47 (1986).

454. Mundy, D. I., Li, W. P., Luby-Phelps, K. & Anderson, R. G. W. Caveolin targeting to late endosome/lysosomal membranes is induced by perturbations of lysosomal pH and cholesterol content. **23**, (2012).

455. Choudhury, A., Sharma, D. K., Marks, D. L. & Pagano, R. E. Elevated endosomal cholesterol levels in Niemann-Pick cells inhibit rab4 and perturb membrane recycling. *Mol. Biol. Cell* **15**, 4500–4511 (2004).

456. Te Vruchte, D. *et al.* Accumulation of glycosphingolipids in Niemann-Pick C disease disrupts endosomal transport. *J. Biol. Chem.* **279**, 26167–26175 (2004).

457. Rodal, S. K. *et al.* Extraction of cholesterol with methyl-beta-cyclodextrin perturbs formation of clathrin-coated endocytic vesicles. *Mol. Biol. Cell* **10**, 961–974 (1999).

458. OMIM Entry - # 231000 - GAUCHER DISEASE, TYPE III; GD3. https://www.omim.org/entry/231000.

459. OMIM Entry - # 230900 - GAUCHER DISEASE, TYPE II; GD2. https://omim.org/entry/230900.

460. OMIM Entry - # 230800 - GAUCHER DISEASE, TYPE I; GD1. https://www.omim.org/entry/230800.

461. Avenali, M., Blandini, F. & Cerri, S. Glucocerebrosidase Defects as a Major Risk Factor for Parkinson's Disease. *Front. Aging Neurosci.* **12**, 97 (2020).

462. Bohra, V. & Nair, V. Gaucher's disease. *Indian J. Endocrinol. Metab.* **15**, 182 (2011).

463. Mistry, P. K. *et al.* A reappraisal of Gaucher disease-diagnosis and disease management algorithms. *Am. J. Hematol.* **86**, 110–115 (2011).

464. Di Rocco, M. *et al.* A new severity score index for phenotypic classification and evaluation of responses to treatment in type I Gaucher disease. *Haematologica* **93**, 1211–1218 (2008).

465. Weinreb, N. J. *et al.* A validated disease severity scoring system for adults with type 1 Gaucher disease. *Genet. Med.* **12**, 44–51 (2010).

466. Davies, E. H., Surtees, R., Devile, C., Schoon, I. & Vellodi, A. A severity scoring tool to assess the neurological features of neuronopathic Gaucher disease. doi:10.1007/s10545-007-0595-x.

467. Cerezyme | European Medicines Agency. https://www.ema.europa.eu/en/medicines/human/EPAR/cerezyme.

468. Vpriv | European Medicines Agency. https://www.ema.europa.eu/en/medicines/human/EPAR/vpriv.

469. Elelyso | European Medicines Agency. https://www.ema.europa.eu/en/medicines/human/EPAR/elelyso.

470. Zavesca | European Medicines Agency. https://www.ema.europa.eu/en/medicines/human/EPAR/zavesca.

471. Cerdelga | European Medicines Agency. https://www.ema.europa.eu/en/medicines/human/EPAR/cerdelga.

472. Weinreb, N. J. *et al.* Effectiveness of enzyme replacement therapy in 1028 patients with type 1 Gaucher disease after 2 to 5 years of treatment: a report from the Gaucher Registry. *Am. J. Med.* **113**, 112–119 (2002).

473. Zimran, A. *et al.* Phase 1/2 and extension study of velaglucerase alfa replacement therapy in adults with type 1 Gaucher disease: 48-month experience. *Blood* **115**, 4651–4656 (2010).

474. Van Dussen, L., Biegstraaten, M., Hollak, C. E. M. & Dijkgraaf, M. G. W. Cost-effectiveness of enzyme replacement therapy for type 1 Gaucher disease. *Orphanet J. Rare Dis.* **9**, 51 (2014).

475. Wenstrup, R. J. *et al.* Effect of enzyme replacement therapy with imiglucerase on BMD in type 1 Gaucher disease. *J. Bone Miner. Res.* **22**, 119–126 (2007).

476. Sechi, A. *et al.* Long term effects of enzyme replacement therapy in an Italian cohort of type 3 Gaucher patients. *Mol. Genet. Metab.* **113**, 213–218 (2014).

477. Goker-Alpan, O. *et al.* Cognitive outcome in treated patients with chronic neuronopathic Gaucher disease. *J. Pediatr.* **153**, (2008).

478. Vellodi, A. *et al.* Management of neuronopathic Gaucher disease: Revised

recommendations. *J. Inherit. Metab. Dis.* **32**, 660–664 (2009).

479. Gaucher Disease Types 2 & 3 | National Gaucher Foundation. https://www.gaucherdisease.org/about-gaucher-disease/what-is/type-2-3/.

480. Ceravolo, F. *et al.* Combination therapy in a patient with chronic neuronopathic Gaucher disease: a case report. *J. Med. Case Rep.* **11**, 1–5 (2017).

481. Capablo, J. L. *et al.* Neurologic improvement in a type 3 Gaucher disease patient treated with imiglucerase/miglustat combination. *Epilepsia* **48**, 1406–1408 (2007).

482. Cox-Brinkman, J. *et al.* Potential efficacy of enzyme replacement and substrate reduction therapy in three siblings with Gaucher disease type III. doi:10.1007/s10545-008-0873-2.

483. Schiffmann, R. *et al.* Randomized, controlled trial of miglustat in Gaucher's disease type 3. *Ann. Neurol.* **64**, 514–522 (2008).

484. Barrias, C. C., Lamghari, M., Granja, P. L., Sá Miranda, M. C. & Barbosa, M. A. Biological evaluation of calcium alginate microspheres as a vehicle for the localized delivery of a therapeutic enzyme. *J. Biomed. Mater. Res. A* **74**, 545–552 (2005).

485. Do, M. A., Levy, D., Brown, A., Marriott, G. & Lu, B. Targeted delivery of lysosomal enzymes to the endocytic compartment in human cells using engineered extracellular vesicles. *Sci. Rep.* **9**, (2019).

486. Kyun, O. L. *et al.* Improved intracellular delivery of glucocerebrosidase mediated by the HIV-1 TAT protein transduction domain. *Biochem. Biophys. Res. Commun.* **337**, 701–707 (2005).

487. Koshkaryev, A., Thekkedath, R., Pagano, C., Meerovich, I. & Torchilin, V. P. Targeting of lysosomes by liposomes modified with octadecyl-rhodamine B. *J. Drug Target.* **19**, 606 (2011).

488. Thekkedath, R., Koshkaryev, A. & Torchilin, V. P. Lysosome-targeted octadecyl-rhodamine B-liposomes enhance lysosomal accumulation of glucocerebrosidase in Gaucher's cells in vitro. *Nanomedicine (Lond).* **8**, 1055 (2013).

489. Pardridge, W. M. Molecular Trojan horses for blood-brain barrier drug delivery. *Curr. Opin. Pharmacol.* **6**, 494–500 (2006).

490. Ding, B. Sen, Dziubla, T., Shuvaev, V. V., Muro, S. & Muzykantov, V. R. Advanced drug delivery systems that target the vascular endothelium. *Mol. Interv.* **6**, 98–112 (2006).

491. Bloem, B. R., Okun, M. S. & Klein, C. Parkinson's disease. *Lancet* **397**, 2284–2303 (2021).

492. Pringsheim, T., Jette, N., Frolkis, A. & Steeves, T. D. L. The prevalence of Parkinson's disease: A systematic review and meta-analysis. *Mov. Disord.* **29**, 1583–1590 (2014).

493. Nonnekes, J., Post, B., Tetrud, J. W., William Langston, J. & Bloem, B. R. MPTP-induced parkinsonism: an historical case series. *thelancet.com* (2018) doi:10.1089/neu.2017.5139.

494. Armstrong, M., Jama, M. O.- & 2020, undefined. Diagnosis and treatment of Parkinson disease: a review. *jamanetwork.com* (2020) doi:10.1001/jama.2019.22360.

495. Santos García, D. *et al.* Non-motor symptoms burden, mood, and gait problems are the most significant factors contributing to a poor quality of life in non-demented Parkinson's disease patients: Results from the COPPADIS Study Cohort. *Parkinsonism Relat. Disord.* **66**, 151–157 (2019).

496. Gaenslen, A., Swid, I., Liepelt-Scarfone, I., Godau, J. & Berg, D. The patients' perception of prodromal symptoms before the initial diagnosis of Parkinson's disease. *Mov. Disord.* **26**, 653–658 (2011).

497. Lancet, P. M. C. G.-T. & 2014, undefined. Long-term effectiveness of dopamine agonists and monoamine oxidase B inhibitors compared with levodopa as initial treatment for Parkinson's disease (PD MED): a. *Elsevier*.

498. Levodopa/Carbidopa/Entacapone Orion | European Medicines Agency. https://www.ema.europa.eu/en/medicines/human/EPAR/levodopa-carbidopa-entacapone-orion.

499. Brooks, D. J. Dopamine agonists: their role in the treatment of Parkinson's disease. *J. Neurol. Neurosurg. Psychiatry* **68**, 685–689 (2000).

500. Alborghetti, M. & Nicoletti, F. Different Generations of Type-B Monoamine Oxidase Inhibitors in Parkinson's Disease: From Bench to Bedside. *Curr. Neuropharmacol.* **17**, 861 (2019).

501. Gomez-Inhiesto, E. *et al.* Direct Cost of Parkinson's Disease: A Real-World Data Study of Second-Line Therapies. *Parkinsons. Dis.* **2020**, (2020).

502. Skrahina, V. *et al.* The Rostock International Parkinson's Disease (ROPAD) Study: Protocol and Initial Findings. *Mov. Disord.* **36**, 1005–1010 (2021).

503. Brockmann, K. *et al.* GBA-associated Parkinson's disease: Reduced survival and more rapid progression in a prospective longitudinal study. *Mov. Disord.* **30**, 407–411 (2015).

504. Kim, S. *et al.* GBA1 deficiency negatively affects physiological α-synuclein tetramers and related multimers. *Proc. Natl. Acad. Sci. U. S. A.* **115**, 798–803 (2018).

505. Sardi, S. P. *et al.* Augmenting CNS glucocerebrosidase activity as a therapeutic strategy for parkinsonism and other Gaucher-related synucleinopathies. *Proc. Natl. Acad. Sci. U. S. A.* **110**, 3537–3542 (2013).

506. Sardi, S. P. *et al.* CNS expression of glucocerebrosidase corrects α-synuclein pathology and memory in a mouse model of Gaucher-related synucleinopathy. *Proc. Natl. Acad. Sci. U. S. A.* **108**, 12101–12106 (2011).

507. Behl, T. *et al.* Cross-talks among GBA mutations, glucocerebrosidase, and α-synuclein in GBA-associated Parkinson's disease and their targeted therapeutic approaches: a comprehensive review. *Transl. Neurodegener. 2021 101* **10**, 1–13 (2021).

508. Ryan, E., Seehra, G., Sharma, P. & Sidransky, E. GBA1 -associated parkinsonism: New insights and therapeutic opportunities. *Curr. Opin. Neurol.* **32**, 589–596 (2019).

509. Hein, L. K., Meikle, P. J., Hopwood, J. J. & Fuller, M. Secondary sphingolipid accumulation in a macrophage model of Gaucher disease. *Mol. Genet. Metab.* **92**, 336–345 (2007).

510. Fuller, M. *et al.* Glucosylceramide accumulation is not confined to the lysosome in fibroblasts from patients with Gaucher disease. *Mol. Genet. Metab.* **93**, 437–443 (2008).

511. Batta, G. *et al.* Alterations in the properties of the cell membrane due to glycosphingolipid accumulation in a model of Gaucher disease. *Sci. Reports 2017 81* **8**, 1–13 (2018).

512. Varela, A. R. P. *et al.* Pathological levels of glucosylceramide change the biophysical properties of artificial and cell membranes. *Phys. Chem. Chem. Phys.* **19**, 340–346 (2016).

513. Varela, A. R. P. *et al.* Effect of glucosylceramide on the biophysical properties of fluid membranes. *Biochim. Biophys. Acta - Biomembr.* **1828**, 1122–1130 (2013).

514. Hattersley, K. J., Hein, L. K. & Fuller, M. Lipid composition of membrane rafts, isolated with and without detergent, from the spleen of a mouse model of Gaucher disease. *Biochem. Biophys. Res. Commun.* **442**, 62–67 (2013).

515. Hein, L. K., Duplock, S., Hopwood, J. J. & Fuller, M. Lipid composition of microdomains is altered in a cell model of Gaucher disease. *J. Lipid Res.* **49**, 1725 (2008).

516. Bratosin, D. *et al.* A cytometric study of the red blood cells in Gaucher disease reveals their abnormal shape that may be involved in increased erythrophagocytosis. *Cytom. Part B - Clin. Cytom.* **80 B**, 28–37 (2011).

517. Sillence, D. J. *et al.* Glucosylceramide modulates membrane traffic along the endocytic pathway. *J. Lipid Res.* **43**, 1837–1845 (2002).

518. Newburg, D. S., Yatziv, S., McCluer, R. H. & Raghavan, S. beta-Glucosidase inhibition in murine peritoneal macrophages by conduritol-B-epoxide: an in vitro model of the Gaucher cell. *Biochim. Biophys. Acta* **877**, 121–126 (1986).

519. Prence, E., Chaturvedi, P. & Newburg, D. In vitro accumulation of glucocerebroside in neuroblastoma cells: A model for study of Gaucher disease pathobiology. *undefined* (1996) doi:10.1002/(SICI)1097-4547(19960201)43:3.

520. Newburg, D. S., Shea, T. B., Yatziv, S., Raghavan, S. S. & McCluer, R. H. Macrophages exposed in vitro to conduritol B epoxide resemble Gaucher cells. *Exp. Mol. Pathol.* **48**, 317–323 (1988).

521. Farfel-Becker, T., Vitner, E. B. & Futerman, A. H. Animal models for Gaucher disease research. *Dis. Model. Mech.* **4**, 746 (2011).

522. Kuo, C. L. *et al.* In vivo inactivation of glycosidases by conduritol B epoxide and cyclophellitol as revealed by activity-based protein profiling. *FEBS J.* **286**, 584–600 (2019).

523. Wang, J., Min, J., Eghtesadi, S. A., Kane, R. S. & Chilkoti, A. Quantitative Study of the Interaction of Multivalent Ligand-Modified Nanoparticles with Breast Cancer Cells with Tunable Receptor Density. *ACS Nano* **14**, 372–383 (2020).

524. Csizmar, C. M. *et al.* Multivalent Ligand Binding to Cell Membrane Antigens: Defining the Interplay of Affinity, Valency, and Expression Density. *J. Am. Chem. Soc.* **141**, 251–261 (2019).

525. van Eijk, M. *et al.* Differential expression of the EGF-TM7 family members CD97 and EMR2 in lipid-laden macrophages in atherosclerosis, multiple sclerosis and Gaucher disease. *Immunol. Lett.* **129**, 64–71 (2010).

526. Lefebvre, T. *et al.* Involvement of hepcidin in iron metabolism dysregulation in Gaucher disease. *Haematologica* **103**, 587–596 (2018).

527. Caré, B. R. & Soula, H. A. Impact of receptor clustering on ligand binding. *BMC Syst. Biol.* **5**, 1–13 (2011).

528. Jarvis, G. E. & Thompson, A. J. Evidence for an effect of receptor density on ligand occupancy and agonist EC 50. *Sci. Rep.* **9**, (2019).

529. Kiss, A. L. & Botos, E. Endocytosis via caveolae: alternative pathway with distinct cellular compartments to avoid lysosomal degradation? *J. Cell. Mol. Med.* **13**, 1228 (2009).

530. Kaksonen, M. & Roux, A. Mechanisms of clathrin-mediated endocytosis. *Nat. Rev. Mol. Cell Biol. 2018 195* **19**, 313–326 (2018).

531. Liu, A. P., Aguet, F., Danuser, G. & Schmid, S. L. Local clustering of transferrin receptors promotes clathrin-coated pit initiation. **191**, 1381–1393 (2010).

532. Guo, L., Zhang, H., Hou, Y., Wei, T. & Liu, J. Plasmalemma vesicle-associated protein: A crucial component of vascular homeostasis. *Exp. Ther. Med.* **12**, 1639 (2016).

533. Vitner, E. B., Farfel-Becker, T., Eilam, R., Biton, I. & Futerman, A. H. Contribution of brain inflammation to neuronal cell death in neuronopathic forms of Gaucher's disease. *Brain* **135**, 1724–1735 (2012).

534. Pandey, M. K. *et al.* Gaucher disease: Chemotactic factors and immunological cell invasion in a mouse model. *Mol. Genet. Metab.* **111**, 163–171 (2014).

535. Doherty, G. J. & McMahon, H. T. Mechanisms of Endocytosis. *http://dx.doi.org/10.1146/annurev.biochem.78.081307.110540* **78**, 857–902 (2009).

536. Etienne-Manneville, S. *et al.* ICAM-1-coupled cytoskeletal rearrangements and transendothelial lymphocyte migration involve intracellular calcium signaling in brain endothelial cell lines. *J. Immunol.* **165**, 3375–3383 (2000).

537. Kitatani, K., Idkowiak-Baldys, J. & Hannun, Y. A. The sphingolipid salvage pathway in ceramide metabolism and signaling. *Cell. Signal.* **20**, 1010–1018 (2008).

538. Lang, T. & Hochheimer, N. Tetraspanins. *Curr. Biol.* **30**, R204–R206 (2020).

539. Barreiro, O. *et al.* Endothelial adhesion receptors are recruited to adherent leukocytes by inclusion in preformed tetraspanin nanoplatforms. *J. Cell Biol.* **183**, 527 (2008).

540. Franz, J. *et al.* Nanoscale Imaging Reveals a Tetraspanin-CD9 Coordinated Elevation of Endothelial ICAM-1 Clusters. *PLoS One* **11**, e0146598 (2016).

541. Israels, S. J. & McMillan-Ward, E. M. Platelet tetraspanin complexes and their association with lipid rafts. *Thromb. Haemost.* **98**, 1081–1087 (2007).

542. Delaguillaumie, A. *et al.* Tetraspanin CD82 controls the association of cholesterol-dependent microdomains with the actin cytoskeleton in T lymphocytes: relevance to co-stimulation. *J. Cell Sci.* **117**, 5269–5282 (2004).

543. Silvie, O. *et al.* Cholesterol contributes to the organization of tetraspanin-enriched microdomains and to CD81-dependent infection by malaria sporozoites. *J. Cell Sci.* **119**, 1992–2002 (2006).

544. Zimmerman, B. *et al.* Crystal structure of a full-length human tetraspanin reveals a cholesterol-binding pocket. *Cell* **167**, 1041 (2016).

545. Espenel, C. *et al.* Single-molecule analysis of CD9 dynamics and partitioning reveals multiple modes of interaction in the tetraspanin web. *J. Cell Biol.* **182**, 765 (2008).

546. Odintsova, E. *et al.* Gangliosides play an important role in the organization of CD82-enriched microdomains. *Biochem. J.* **400**, 315 (2006).

547. Todeschini, A. R., Dos Santos, J. N., Handa, K. & Hakomori, S. I. Ganglioside GM2/GM3 complex affixed on silica nanospheres strongly inhibits cell motility through CD82/cMet-mediated pathway. *Proc. Natl. Acad. Sci. U. S. A.* **105**, 1925–1930 (2008).

548. Todeschini, A. R., Dos Santos, J. N., Handa, K. & Hakomori, S. I. Ganglioside GM2-tetraspanin CD82 complex inhibits met and its cross-talk with integrins, providing a basis for control of cell motility through glycosynapse. *J. Biol. Chem.* **282**, 8123–8133 (2007).

549. Odintsova, E., Voortman, J., Gilbert, E. & Berditchevski, F. Tetraspanin CD82 regulates compartmentalisation and ligand-induced dimerization of EGFR. *J. Cell Sci.* **116**, 4557–4566 (2003).

550. Fernandez, L. *et al.* CD82 and Gangliosides Tune CD81 Membrane Behavior. *Int. J. Mol. Sci. 2021, Vol. 22, Page 8459* **22**, 8459 (2021).

551. SUOMI, W. D. & AGRANOFF, B. W. Lipids of the spleen in Gaucher's disease. *J. Lipid Res.* **6**, 211–219 (1965).

552. Ghauharali-van der Vlugt, K. *et al.* Prominent increase in plasma ganglioside GM3 is associated with clinical manifestations of type I Gaucher disease. *Clin. Chim. Acta.* **389**, 109–113 (2008).

553. Sillence, D. J. Glucosylceramide modulates endolysosomal pH in Gaucher disease. *Mol. Genet. Metab.* **109**, 194–200 (2013).

554. Hortsch, R. *et al.* Glycolipid Trafficking in Drosophila Undergoes Pathway Switching in Response to Aberrant Cholesterol Levels. *Mol. Biol. Cell* **21**, 778 (2010).

555. Rejman, J., Oberle, V., Zuhorn, I. S. & Hoekstra, D. Size-dependent internalization of particles via the pathways of clathrin-and caveolae-mediated endocytosis. *Biochem. J.* **377**, 159–169 (2004).

556. Castro, B. M., Prieto, M. & Silva, L. C. Ceramide: A simple sphingolipid with unique biophysical properties. *Prog. Lipid Res.* **54**, 53–67 (2014).

557. Shu, L. & Shayman, J. A. Caveolin-associated accumulation of globotriaosylceramide in the vascular endothelium of alpha-galactosidase A null mice. *J. Biol. Chem.* **282**, 20960–20967 (2007).

558. Donida, B. *et al.* Nanoparticles containing β-cyclodextrin potentially useful for the treatment of Niemann-Pick C. **43**, 586–601 (2020).

559. Torralba, M. A. *et al.* Identification and characterization of a novel mutation c.1090G>T (G325W) and nine common mutant alleles leading to Gaucher disease in Spanish patients. *Blood Cells. Mol. Dis.* **27**, 489–495 (2001).

560. Santos, D. M. & Tiscornia, G. Induced Pluripotent Stem Cell Modeling of Gaucher's Disease: What Have We Learned? *Int. J. Mol. Sci.* **18**, (2017).

561. Stan, R. V., Tkachenko, E. & Niesman, I. R. PV1 Is a Key Structural Component for the Formation of the Stomatal and Fenestral Diaphragms. *Mol. Biol. Cell* **15**, 3615 (2004).

562. Shuvaev, V. V. *et al.* Targeting superoxide dismutase to endothelial caveolae profoundly alleviates inflammation caused by endotoxin. *J. Control. Release* **272**, 1–8 (2018).

563. Marchetti, G. M. *et al.* Targeted drug delivery via caveolae-associated protein PV1 improves lung fibrosis. *Commun. Biol.* **2**, (2019).

564. Ben-Zvi, A. *et al.* Mfsd2a is critical for the formation and function of the blood-brain barrier. *Nature* **509**, 507–511 (2014).

565. Andreone, B. J. *et al.* Blood-brain barrier permeability is regulated by lipid transport-dependent suppression of caveolae-mediated transcytosis. *Neuron* **94**, 581 (2017).

566. Quek, D. Q. Y., Nguyen, L. N., Fan, H. & Silver, D. L. Structural Insights into the Transport Mechanism of the Human Sodium-dependent Lysophosphatidylcholine Transporter MFSD2A. *J. Biol. Chem.* **291**, 9383–9394 (2016).

567. Nguyen, L. N. *et al.* Mfsd2a is a transporter for the essential omega-3 fatty acid docosahexaenoic acid. *Nature* **509**, 503–506 (2014).

568. Li, Q. *et al.* Docosahexaenoic acid affects endothelial nitric oxide synthase in caveolae. *Arch. Biochem. Biophys.* **466**, 250–259 (2007).

569. Tkachenko, E. *et al.* Caveolae, fenestrae and transendothelial channels retain PV1 on the surface of endothelial cells. **7**, (2012).

570. Stoll, L. L. & Spector, A. A. Changes in serum influence the fatty acid composition of established cell lines. *In Vitro* **20**, 732–738 (1984).

571. Else, P. L. The highly unnatural fatty acid profile of cells in culture. *Prog. Lipid Res.* **77**, 101017 (2020).

572. Zhao, Y. L., Song, J. N. & Zhang, M. Role of caveolin-1 in the biology of the blood-brain barrier. *Rev. Neurosci.* **25**, 247–254 (2014).